

Optical frequency comb metrology  
from infrared to extreme ultraviolet  
wavelengths

Optical frequency comb metrology from infrared to extreme ultraviolet wavelengths

Tjeerd Jan Pinkert

Tjeerd Jan Pinkert

VRIJE UNIVERSITEIT

Optical frequency comb metrology from infrared to extreme ultraviolet  
wavelengths

ACADEMISCH PROEFSCHRIFT

ter verkrijging van de graad Doctor aan  
de Vrije Universiteit Amsterdam,  
op gezag van de rector magnificus  
prof.dr. F.A. van der Duyn Schouten,  
in het openbaar te verdedigen  
ten overstaan van de promotiecommissie  
van de Faculteit der Exacte Wetenschappen  
op woensdag 7 oktober 2015 om 15.45 uur  
in de aula van de universiteit,  
De Boelelaan 1105

door

Tjeerd Jan Pinkert

geboren te Zwolle

promotor: prof.dr. K.S.E. Eikema

Optical frequency comb metrology  
from infrared to extreme ultraviolet  
wavelengths

Tjeerd Jan Pinkert

This thesis was approved by the members of the reviewing committee:

prof. dr. J. F. de Boer  
(Vrije Universiteit, Amsterdam)

prof. dr. K.-J. Boller  
(Universiteit Twente, Enschede)

dr. F. J. M. Harren  
(Radboud Universiteit, Nijmegen)

prof. dr. K. H. K. J. Jungmann  
(University of Groningen, Groningen)

dr. G. Santarelli  
(LP2N/CNRS/IOGS, Université de Bordeaux, Talence, France)

The work described in this thesis was supported by:



© 2015, Tjeerd Jan Pinkert  
All rights reserved.

The illustration on the cover is based on equation (2.42) and shows frequency-comb signals in the time domain. The phase and amplitude of each comb mode have been randomised with increasing ranges for each graph. Each cover shows ten unique frequency-comb signals that have been calculated and placed randomly on the page according to a certain algorithm.

ISBN: 978-94-6259-786-0

Printed by: Ipskamp Drukkers B.V.

# Contents

1	Introduction	1
1.1	Matter . . . . .	1
1.2	Light . . . . .	2
1.3	Time . . . . .	3
1.4	Combining matter, light and time . . . . .	5
1.5	Outline of the thesis . . . . .	7
2	Theoretical backgrounds	9
2.1	Time and frequency . . . . .	9
2.2	Electromagnetic waves . . . . .	14
2.3	Frequency combs . . . . .	19
2.4	Light source characterisation with frequency comb lasers . . . . .	25
2.5	Frequency comb spectroscopy . . . . .	28
2.6	Direct frequency comb spectroscopy in the XUV . . . . .	35
2.7	The helium atom . . . . .	43
2.8	Systematic effects in atomic spectroscopy . . . . .	48
3	Towards narrow line width frequency comb lasers	55
3.1	Narrow line width CW lasers . . . . .	56
3.2	Auxiliary devices for use with narrow linewidth lasers . . . . .	61
4	Towards hybrid mode-locked quantum dot frequency comb lasers	69
4.1	Introduction . . . . .	69
4.2	Description of the HMLQDL and the experimental setup for optical injection . . . . .	70
4.3	CW injection of the HMLQDL . . . . .	71
4.4	Characterization of the generated frequency comb . . . . .	77
4.5	Discussion of the physical processes in the modulator . . . . .	82
4.6	Conclusions and outlook . . . . .	83
5	Tunability and phase stability of XUV frequency comb lasers	85
5.1	Widely tunable extreme UV frequency comb generation . . . . .	85
5.2	Appendix: Estimation of the phase jitter of the Ramsey comb in the XUV . . . . .	89
6	Frequency comb metrology on helium groundstate transitions	99
6.1	Extreme Ultraviolet Frequency Comb Metrology . . . . .	99
6.2	Appendix: Description of the systematic effects . . . . .	106

7	Effect of soil temperature on optical frequency transfer through unidirectional dense-wavelength-division-multiplexing fibre-optic links	115
7.1	Introduction	115
7.2	Theory: frequency stability of the fibre link and soil temperature	117
7.3	Experimental methods	119
7.4	Measurements and simulations	122
7.5	Conclusions and outlook	132
8	Outlook	135
8.1	High-precision spectroscopy in the XUV	135
8.2	Semiconductor frequency comb laser sources	136
8.3	Time and frequency transfer techniques	136

Appendices to the thesis

A	Equations, notations and derivations	141
B	A historical overview of the ionisation energy of helium	149
C	Private communication G. W. F. Drake	165
	Bibliography	167
	List of publications	185
	Summary	187
	Samenvatting	189
	Dankwoord	193





*Vanity of vanities, saith the Preacher, vanity of vanities; all is vanity.*

(Ecclesiastes 1:2)



# 1. Introduction

## 1.1 Matter

*“In the beginning God created the heaven and the earth.”* (Gen 1:1) [1]

With the act of creation, matter was brought into existence. It is exactly the material world that is the subject of the natural sciences. Mankind has ever wondered about the rich abundance and variety of phenomena observed in the world. And humans have used the ability of the conscious mind to observe, relate, abstract, model and manipulate, even to shape the material world to their own liking and advantage.

Ideas about the composition of the material world already existed in Antiquity. The Greek had various ideas about matter: some philosophers believed it consisted of the four elements (e.g. Aristotle), while other philosophical schools (e.g. Democritus) upheld a theory of atoms, indivisible building blocks of the natural world. In the course of time the natural philosophical method of observations leading to quantifiable theories and testing of theoretical predictions by measurement, of which Roger Bacon [2] can be seen as a founder, has come to prevail as a source of obtaining scientific knowledge about the world.

Early chemists like Lavoisier [3] and Mendeleev [4] composed tables of chemical elements that seemed to have the same chemical properties. The ordering of Mendeleev was especially successful in predicting the character of “missing” elements. Already earlier Dalton had proposed an atomic theory with which chemical reaction ratios could be explained. Through these experiments the idea that matter indeed exists of “indivisible” particles, atoms, was established around 1900.

Some questions however remained to be answered, like those about how charges were distributed in atoms. Through further experiments by, among others, Thomson [5] and Rutherford [6] various of the proposed atomic models could be excluded, leading to the idea that atoms consisted of a positively charged core with negatively charged electrons bound to the core through electrical forces. Charge seemed to be quantised (Millikan [7, 8]) and it was proposed that particles, like the electron, could behave like waves (de Broglie [9, 10]). In 1913 Bohr proposed the idea that electrons in the atom have quantised energies [11] now coined the old quantum theory. Around the 1930 the new quantum mechanics of Schrödinger [12] had explained many observations that previous theories could not explain satisfactorily.

The new quantum theory became the basis for more advanced field theories. Atoms were found to exist of protons (Rutherford [13]), neutrons (Chadwick [14]) and electrons, which themselves can exist of yet more fundamental particles like quarks, leptons and gluons. The current standing field theory of particles, the so called standard model [15], has been very successful in ex-

plaining the latest experiments in the field of high-energy physics [16,17]. Although many physical observations can be explained by the standard model, it is far from a complete theory of physics, because for example it does not include gravitation. Physicists therefore continue their search for a more unified theory.

## 1.2 Light

*“And God said, Let there be light: and there was light.”* (Gen 1:3) [1]

This biblical passage has been restated by Roy J. Glauber as “let there be quantum electrodynamics” [18]. Light is of vital importance to mankind. Not only does it allow us to see whereas darkness veils our eyes. Light allows for plant growth and as such agriculture, providing food for mankind. Light is a source of energy, both direct, for example as heat radiation, and indirect via wind or fossil fuels, used for industrial activity ever since early human societies exist [19]. Our voyage of discovery of creation would not be possible without light.

Already in antiquity people have tried to unravel the mysteries of light [20, 21]. The Greek already proposed the idea of light travelling in straight lines with which the workings of mirrors of various sorts could be explained. As early as Ptolemaeus the notion of index of refraction was present, and the apparent and true positions of stars were discussed. Further developments of the optical theories via Ibn al-Haitham (Alhazen) [22] reached Europe and the early renaissance scientists like Roger Bacon took knowledge of them. Knowledge about the making of lenses and a more and more refined mathematical description of optics lead to the discovery and refinement of the telescope (Zacharias Jansen) and microscope (Antonie van Leeuwenhoek). These instruments allowed for far reaching discoveries in the solar system and in the microbiological world.

Sir Isaac Newton and Christian Huygens, two contemporaries, held very different views on optical phenomena. Newton favoured a theory of light corpuscles. Huygens on the contrary first proposed the idea that light can travel as spherical waves and that these waves, by interference, can account for various observed phenomena. The classical theory of light comes to its greatest height in the field theory of Maxwell [23]. However, Maxwell’s theory can not fully describe the radiation spectrum emitted by a so called “black body” of a given temperature. In order to explain the black body spectrum, Max Planck [24] had to assume that light exists of discrete energy packets where the energy relates to the wavelength of the light “quanta”, an assumption established by Einstein [25, 26].

The quantum revolution and the testing of these quantum theories of light, consequently lead to the development of the modern field theories. Around 1948 the quantised field theories had resulted in the theory of quantum electrodynamics (QED), a relativistic quantised theory of the electromagnetic field and its interactions with matter, by Tomonaga, Schwinger and

Feynman [27]. This theory is known today as one of the best tested physical theories. It describes electrical interactions so well that it has yet to be disproved.

The quantum-optical description of the light-matter interaction required to describe spontaneous emission and amplified radiation [28,29] also lead to the development of the maser and the laser. Over time the stability and accuracy of the radiated light frequencies became better controllable. Lasers could be optically locked to narrow absorption resonances in molecular gases, such as CO<sub>2</sub> [30], methane [31] and acetylene [32]. Other options for laser frequency stabilisation are locking to etalons [33], for example by the Pound-Drever-Hall [34] locking method. Continuous wave lasers locked to highly stable resonators based on ultra-high reflection mirrors are now mainstream and can reach a fractional frequency stability better than 10<sup>-15</sup> in one second [35].

One more crucial development in laser physics took place that plays an important role in the usability of highly stable lasers for the highest accuracy optical frequency measurements. The development of the titanium sapphire mode-locked laser and the discovery that it can be used as a frequency comb laser [36,37]. Many of the properties of these mode-locked lasers were already known, but the practical implementation as a frequency comb laser was hampered by the fact that the combs frequency offset from zero, also called carrier-envelope offset frequency, could not be determined yet.

The offset frequency from zero of frequency combs can only be measured by beating the sum frequencies (via “frequency doubling”) of the low optical frequencies with the high optical frequencies of the mode-locked laser. It took however until around 1999 before the spectrum from a mode-locked laser could be made to span more than an octave of frequencies in a fully coherent way [36,37]. This became technically possible by means of non-linear optical interactions in the small core of photonic crystal fibres [38,39].

Since this time a frequency comb laser is an asset that cannot be missed in a serious optical metrology lab. Frequency comb lasers are now available at various wavelength ranges (Ti:Sapphire (500-1000 nm), Er<sup>3+</sup>-fibre (500-2000 nm), Yb<sup>3+</sup>-fibre (1030 nm centre wavelength) Th<sup>3+</sup>-fibre (2000 nm centre wavelength) and include both solid-state and fibre based lasers.

### 1.3 Time

*“Let there be lights in the firmament of the heaven to divide the day from the night; and let them be for signs, and for seasons, and for days, and years:”* (Gen 1:14) [1]

During the history of mankind, the constellation of stars and movement of the planets and asteroids visible by eye, have been observed and used in various calendar systems. It is well known that among others the Egyptians [40–42], Hebrews [43, 44], Assyrians [45], Babylonians [45, 46], Persians [47, 48], Indians [49], Chinese [50–53], Inca [54], Aztec [55], Mayans [56, 57], Celts [58–61],

and Greek [62] have all used calendars of some sort based on the positions of the sun, moon and stars.

In general the first clocks, devices that keep time within a day, are thought to be sundials and water clocks, of which the existence dates back to at least 1500 BC [63, 64]. Such clocks are accurate enough to keep reasonable track of time within a day, for example to determine working hours. At least from the early 1300's on, knowledge about building mechanical clocks existed in Italy [63]. Christiaan Huygens was the first to use the isochronous movement of the pendulum to improve the accuracy of the clocks [65].

The most accurate pendulum clock, designed and built around 1921, is almost certainly the (Shortt-)Synchronome free pendulum clock, which was commercially available. This clock combines a master pendulum made of invar (a metal designed to have a zero expansion point at room temperature) in a vacuum tank. This is combined with an electrical drive acting only once every  $n$  swings and an electrical readout with an electrically synchronised slave pendulum for the time readout piece [65].

The development of electrically driven clocks also made progress and the piezoelectric properties of the quartz crystal, discovered in 1880 [65, 66], appeared to be well suited for application in electrical precision oscillators. Today these (low cost) quartz oscillators are used as time or frequency standards in many electronic devices<sup>1</sup>. High-performance quartz oscillators of the BVA SC-cut type [67] form the flywheel of the most accurate of the modern primary time standards.

A whole new era of timekeeping started around the 1950's when the macroscopic properties of the rate defining elements were replaced by the properties of the building blocks of matter itself, atoms. Driven by the advances in microwave electronics and quantum mechanics, a combination of both fields yields unprecedented stability and accuracy in microwave spectroscopy. In particular due to the development of the molecular and atomic beam spectroscopy methods of Rabi [68] and Ramsey [69, 70]. Frequencies of electronic transitions under investigation have less frequency instability than the state of the art oscillators used in the laboratories [71]. This was recognised in 1967 when the hyperfine transition in the ground state of the caesium atom was made the new SI standard for the second [72, 73]. Caesium beam clocks are readily available from industry, while caesium fountain clocks form the pinnacle of microwave clock technology and are employed only at larger standards institutes such as NIST, PTB, Syrte and others to realise the SI second and international atomic time with the highest accuracy.

New developments in the field of lasers and ultracold ions and atoms by means of various types of traps presented the stage for a new type of atomic clock [74], the optical clock. At the moment two types of optical atomic clocks

---

<sup>1</sup>Quartz oscillators are all evasive in our modern world and found in devices ranging from wristwatches, photo camera's, magnetron ovens, mobile phones, radio's, computer equipment, and many many other electronic devices.

are employed for ultra-high precision; the ion clock [75–77], and the lattice clock [78–80]. In an atomic ion clock a single ion is used to define the clock frequency, while in a lattice clock many neutral atoms are used. Both clock types reach stabilities and accuracies that are more than an order of magnitude better than that of the best caesium standards. At present there is not one preferred clock type and the construction and operation of even better optical atomic clocks is in full progress.

Optical clocks have little value when the optical readout frequency can not be directly used, e.g. for direct clock comparisons. Frequency comb lasers are typically used as a gearbox between the microwave and optical domain to link the accuracy and stability of microwave atomic standards to the optical domain [36, 37], and in reverse to down convert the frequency of optical atomic clocks to the radio frequency domain [81–83] where electronic (counting) equipment is readily available.

## 1.4 Combining matter, light and time

In this thesis the three topical fields of physics, matter, light and time come together. Light is used to express properties of matter in the unit time in the spectroscopic experiments reported on. Matter is used in (frequency comb) lasers to generate light with accurately controlled frequencies. In this way properties of one physical quantity are expressed in another, forming systems of units and constants.

The Convention du Mètre treaty instituted le Bureau international des poids et mesures (BIPM) in Sèvres, France, which has determined the measurement standards for the base units of in the international system of units (SI<sup>2</sup>). The relation of the SI units to various other units and constants measured and used in physics is defined by the Committee on Data for Science and Technology (CODATA) Task Group on Fundamental Constants, and a consistent set of constants is currently defined as the 2010 CODATA set [84].

Time, and thus its inverse, frequency, is the most accurately determined of the seven base units. Thus properties of matter that can be expressed in and measured as frequencies can be determined most accurately, even when the values of the CODATA constants used in the conversions are less accurate and may change in the future.

One of the uses of these frameworks of units and constants is found in the comparison of theory and measurement. The helium atom for example, of which some ground state transitions have been measured with outstanding accuracy, can be modelled to a certain extent and the model also provides values for these transitions. The comparison of theory and measurement, can then be used for two purposes.

First, if the values of the constants are accurate enough, a theory can be tested. If it fails to predict a well established measurement outcome, it is likely to be incomplete.

---

<sup>2</sup>Le système international d'unités, abbreviated SI.

Second, if there is hardly any doubt about the validity of a theory, and a highly accurate measurement becomes available, the value of constants used in the theory can be derived from such measurements. On the other hand, if different measurements of the same constant give conflicting results, the theoretical framework might again be incomplete. Such a state has for example arisen with recent determinations of the proton charge radius [85, 86] in two distinguished experiments.

A measurement can be as accurate as the measured value of the base units it is based on, or more accurate if it is a ratio measurement. In practice measurements may be hampered by instrumental limitations, fundamental physical limitations of the measurement method used, or limited accuracy of measured constants. Construction of reliable and accurate precision measurement equipment and testing of internal consistency thereof is of great importance to obtain progress in the field of metrology.

As far as the development of measurement equipment goes, this thesis describes the results of an experiment to create semiconductor frequency comb lasers (chapter 4). Current frequency comb lasers are relatively bulky and can be hard to operate, especially outside an optical laboratory. Another aspect is that the price of frequency comb lasers is quite high. Therefore an approach to create (relatively) cheap semiconductor frequency comb laser sources has a certain appeal.

Semiconductor lasers are favoured both because mass production can be cheap and because such sources can be integrated with driver electronics and non-linear optics on a single chip if needed. In the experiment described in this thesis we have tried to use hybridly mode-locked quantum-dot lasers as frequency comb sources. Although a high quality frequency comb could be generated, there is certainly a long way to go for this particular laser type before comb generation becomes turn key.

An other area where the development of measurement equipment was performed is that of narrow CW semiconductor diode lasers. Such lasers with optical frequencies in the telecommunication range can be readily purchased, but require high-end electronics and appropriate thermal control to have both high feedback speeds on the generated laser frequency and sufficiently low thermal frequency drift to keep drift control applicable. These have been developed, which is reported on in Chapter 3. Frequency doubling of these stable CW lasers to frequencies in the Ti:Sapphire frequency comb laser spectrum for the purpose of optical locking has been demonstrated. For this purpose a high power  $\text{Er}^{3+}$  doped fibre amplifier capable of producing up to 4 Watt of optical power at the fundamental wavelength ( $\sim 1550$  nm) was built and frequency doubling achieved.

In the field of precision measurements itself, this thesis reports on extreme ultraviolet ( $\sim 51.5$  nm) spectroscopy performed on optical dipole transitions in helium from the atomic ground state. The energy difference between the electronic levels in the atom has been measured by excitation with two pulses of a frequency comb laser that were converted to the extreme ul-

traviolet (XUV). We have been able to improve the best determination of the ground state energy of the helium atom [87] with almost an order of magnitude. This determination is more accurate than the most accurate theoretical determination (using QED theory) at present [88] and the results agree with regard to the combined error. QED shifts are largest in the  $s$ -states (e.g. the ground state of helium), scale with the nuclear charge  $Z$  to fourth and higher powers while decreasing with increasing principle quantum number  $n$ . The outcome of the experiment can therefore be used as a reference for QED theory.

To show the wavelength tuning capabilities of the measurement method used in the XUV experiment, we have performed a demonstration experiment where the XUV radiation was generated over wide wavelength ranges in the XUV, using various atomic species as frequency detector. As a side effect of this demonstration, the pulse to pulse phase jitter of the XUV frequency comb laser has been assessed to be around 0.4 radian in the XUV, hardly dependent on the generated wavelength.

And finally in chapter 7 an experiment is described where the stability of narrow line width laser light ( $\sim 1559.79$  nm) is transferred over an optical fibre of  $2 \times 298$  km between the VU, Amsterdam and KVI, Groningen. The frequency instabilities introduced in this long haul fibre connection due to soil temperature changes could be detected and appropriately modelled. Because atomic Rb frequency standards were present at both ends of the fibre, these two primary lab standards have been compared using the transmitted optical carrier frequency. Currently even higher accuracies are achieved in our laboratory using Hz level actively stabilised optical frequency transfer systems.

## 1.5 Outline of the thesis

To summarise: In chapter 2 of the thesis, the theoretical basis of the work discussed in the subsequent chapters is described. Chapter 3 discusses some of the devices built with the purpose of optical frequency dissemination over fibre channels and for optical locking the frequency comb lasers. Chapter 4 treats some of the research on novel frequency comb sources based on hybridly mode locked quantum dot semiconductor lasers. Chapter 5 describes the results on the tunability of the XUV frequency comb system at the VU, while chapter 6 shows the results of the ground state energy determination of helium with this XUV laser system. Chapter 7 describes our experiments on the determination of the passive stability of the glass-fibre link between Amsterdam and Groningen, and describes part of the models needed to understand the stability that can be reached in the long term on such fibre links. Chapter 8 concludes the thesis with an outlook.



## 2. Theoretical backgrounds

The main themes of this thesis are atomic spectroscopy and frequency metrology by use of various laser sources. In this chapter the foundations of these themes, needed to understand the contents of this thesis, are therefore recalled. First the modern definitions of time and frequency are recalled, together with the theoretical means for the study of frequency stability.

Then the principles of electromagnetic waves, frequency combs and in particular frequency comb lasers will be treated. After the introduction of the frequency comb, various direct frequency comb measurement principles will be discussed. The determination of the frequency and frequency stability of CW laser and frequency comb laser radiation by means of CW lasers will be recalled, and the principles of direct frequency comb spectroscopy by means of the Ramsey method is treated.

In order to understand how frequency comb sources can be generated in short wavelength regions like the extreme ultra-violet (XUV) down to  $\sim 51$  nm the physics of high-order harmonic generation (HHG) in gas sources is discussed too. A practical treatment of the phase stability of HHG depending on the intensity stability of the fundamental is given together with an overview of the XUV direct frequency comb spectroscopy setup used to perform spectroscopy on helium ground state transitions.

The last part of this chapter deals with phase stability in HHG used in chapter 5, a primer on helium energy calculations and finally a discussion of systematic effects in the helium spectroscopy discussed in chapter 6.

### 2.1 Time and frequency

A revolution in the measurable accuracy of the established value of the second has been the change from the astronomically determined ephemeris time, based on the solar system artefact, defined during the 1956 meeting of the CIPM [89]<sup>1</sup>, as,

La seconde est la fraction  $1/31\,556\,925,9747$  de l'année tropique pour 1900 janvier 0 à 12 heures de temps des éphémérides,

to atomic time, based on the believe in the exact equality of atoms of equal proton number,  $Z$ , and mass number,  $A$ , defined during the CGPM meeting in 1967 [72] as,

---

<sup>1</sup>The second based on ephemeris time is a replacement of the conventional second. The conventional second had been taken as the  $1/86\,400^{\text{th}}$  part of the mean solar day, which is slightly longer than the ephemeris second, the latter being a more stable measure of time. Therefore the adoption of the ephemeris second is the main cause for the introduction of the leap second in UTC [90].

1. L'unité de temps du Système international d'unités est la seconde définie dans les termes suivants:  
« La seconde est la durée de 9 192 631 770 périodes de la radiation correspondant à la transition entre les deux niveaux hyperfins de l'état fondamental de l'atome de césium 133 ».
2. La Résolution 1 adoptée par le Comité international des poids et mesures à sa session de 1956 et la Résolution 9 de la Onzième Conférence générale des poids et mesures sont abrogées.

Thus the second is defined by the energy corresponding to  $\Delta v(^{133}\text{Cs})_{\text{hfs}} = 9\,192\,631\,770$  oscillation periods of radiation corresponding to the transition between the two hyperfine levels of the ground state of the  $^{133}\text{Cesium}$  atom when the atom is at rest and measured at a temperature of 0 K [72, 91, 92].

International Atomic Time (Temps Atomique International, TAI) is defined as an average of more than 400 clocks worldwide. Coordinated Universal Time (Temps Universel Coordonné, UTC) is related to TAI, but occasional leap seconds are introduced to correct for the difference between the ephemeris time and mean solar time [90, 93], and changes in the Earth's motion as measured in UT1 [94, 95], which can be related to Sol crossing the Greenwich meridian defining a local noon [96], or more accurately formulated, to the Greenwich Mean Siderial Time (GMST) [94]. For this purpose changes in the earth orientation in the celestial frame are closely monitored by the International Earth Rotation Service (IERS). This information is also of major importance for astronomers and space agencies (e.g. for the tracking of satellites). Fluctuations in the earth rotation rate and orientation of the rotational axis are e.g. caused by irregular motions of the Sun, Moon, Mercuri and Venus and seasonal variations due to the global weather [93].

### 2.1.1 Time and frequency definition

In the mathematical language of physics time is commonly denoted as  $t$  [s] and is counted in seconds ( $t \in \mathbb{R}$ ). Since the absolute zero time can not be determined accurately in the present state of the physical theory, one typically treats time as a relative measure and often applies a coordinate transformation to set  $t = 0$  at an arbitrary but calculation-wise convenient point, e.g. the start of a measurement.

Let us define a period of time as

$$T = t_1 - t_0 \tag{2.1}$$

where  $t_0$  is the time at the beginning of this period and  $t_1$  the time at the end of the period. We say that  $T$  has lasted 1 second [s] if we counted exactly 9 192 631 770 oscillations between the named hyperfine levels of the  $^{133}\text{Cs}$  atom at rest at 0 K without any external perturbations. Frequency  $f$  can now be defined as

$$f = \frac{1}{T} [\text{Hz}], \tag{2.2}$$

and is commonly understood as the number of occasions of a certain event (not necessarily an integer number), that took place in one second. This can, for example, be the number of swings of a pendulum or periods of a periodically changing voltage.

The simplest mathematical periodic functions are the sine and cosine. Fourier theory (see e.g. [97]) tells us that all other functions can be decomposed and written as a sum of sine and cosine functions. In the case of real valued time signals the argument of the sine and cosine functions is an instantaneous phase term that evolves in time, typically denoted as  $\varphi(t)$  and is measured in radians. The instantaneous frequency of a signal at time  $t$  can now be defined as

$$v(t) = \frac{1}{2\pi} \frac{d\varphi(t)}{dt}. \quad (2.3)$$

The average or nominal frequency of a periodic signal is typically designated as  $\nu_0$ . We can now define a sinusoidal signal as

$$s(t) = A_0 \cos(2\pi\nu_0 t + \varphi_0), \quad (2.4)$$

where  $A_0$  is a scaling factor for the amplitude and  $\varphi_0$  is the phase offset of the cosine function.

### 2.1.2 Noise on signals

Physical signals always suffer from noise, in the final limit related to the Heisenberg uncertainty relations for physical quantities. For example, electrical signals suffer from noise arising from the discretised charge of the electrons. The so called “shot noise” in transistors for example, is related to the trapping of electrons in irregularities in the crystal lattice at boundary layers in the transistor structure at random times. The same holds for light fields where the photon statistics define the minimal noise present on an optical signal.

A sinusoidal signal with inclusion of noise can be written as

$$s(t) = (A_0 + \varepsilon_A(t)) \cos(2\pi\nu_0 t + \varphi_0 + \varepsilon_\varphi(t)), \quad (2.5)$$

where  $\varepsilon_A$  is the amplitude error in time and  $\varepsilon_\varphi$  is the phase error in time<sup>2</sup>. These errors can be characterised in terms of their statistical properties. For the rest of this thesis the  $\varepsilon_A(t)$  term will be assumed to be negligible. It is important to note that amplitude noise can degrade the spectral purity of a source and that it can be converted to phase noise e.g. via non-linear processes. It must always be assured that amplitude noise does not have a significant influence on a phase measurement.

The phase error can now be rewritten to a frequency error  $\Delta v(t)$  as

$$\Delta v(t) = \frac{1}{2\pi} \frac{d\varepsilon_\varphi(t)}{dt} \quad (2.6)$$

---

<sup>2</sup>Note that  $\varepsilon_A(t)$  is more commonly written in the literature as  $\varepsilon(t)$  and  $\varepsilon_\varphi(t)$  is commonly written as  $\varphi(t)$ , the same symbol that is used for the full phase signal, see e.g. [98], which can then easily cause confusion.

from which the dimensionless parameter instantaneous fractional frequency deviation  $y(t)$  can be defined as

$$y(t) = \frac{\Delta v(t)}{v_0}. \quad (2.7)$$

### 2.1.3 Noise characterisation in the frequency domain

From this point on, one can start to define the relation between the time and frequency domain representation of phase noise [99, 100]. By assuming that  $\Delta v(t)$  is a stationary process for which we can define the average (denoted as  $\langle \dots \rangle$ ) of the auto-correlation function

$$R_{\Delta v}(\tau) = \langle \Delta v(t)\Delta v(t - \tau) \rangle, \quad (2.8)$$

the two-sided  $S_{\Delta v}^{(TS)}(f)$  and single-sided  $S_{\Delta v}(f)$  spectral density function of the frequency deviations can now be defined as

$$S_{\Delta v}^{(TS)}(f) = \int_{-\infty}^{\infty} R_{\Delta v}(\tau) e^{-i2\pi f\tau} d\tau \quad (2.9)$$

$$S_{\Delta v}(f) = 2S_{\Delta v}^{(TS)}(f), \quad \text{for } 0 \leq f < \infty, \quad \text{otherwise zero.} \quad (2.10)$$

This measure can be transformed into a spectral density of  $y$  and  $\varepsilon_\varphi$  as follows

$$S_y(f) = \frac{1}{v_0^2} S_{\Delta v}(f), \quad (2.11)$$

$$S_{\varepsilon_\varphi}(f) = \frac{1}{f^2} S_{\Delta v}(f). \quad (2.12)$$

Noise encountered in oscillators can be expressed in powers  $\alpha$  of  $f$  in the spectral domain

$$S_y(f) = h_\alpha f^\alpha, \quad (2.13)$$

where  $h_\alpha$  describes the noise level and  $\alpha$  is characteristic for the type of noise. Table 2.1 describes the most commonly encountered types of noise and the equivalent values of  $\alpha$ . Further notice must be taken that the area below the  $S_y(f)$  curve corresponds to the signal power and must therefore be bounded by definition. In practice one can define a cut-off frequency  $f_h$  up to which the system description is valid (e.g. the Nyquist frequency for sampled systems) and write

$$S_y(f) = \begin{cases} \sum_{\alpha=-4}^2 h_\alpha f^\alpha, & 0 \leq f \leq f_h \\ 0, & f > f_h. \end{cases} \quad (2.14)$$

Noise type	$\alpha$	$S_y(f)$	$S_{\varepsilon_\varphi}(f)$
Random run frequency noise	-4	$h_{-4}f^{-4}$	$v_0^2 h_{-4} f^{-6}$
Flicker walk frequency noise	-3	$h_{-3}f^{-3}$	$v_0^2 h_{-3} f^{-5}$
Random walk frequency noise	-2	$h_{-2}f^{-2}$	$v_0^2 h_{-2} f^{-4}$
Flicker frequency noise	-1	$h_{-1}f^{-1}$	$v_0^2 h_{-1} f^{-3}$
White frequency noise	0	$h_0$	$v_0^2 h_0 f^{-2}$
Flicker phase noise	1	$h_1 f^1$	$v_0^2 h_1 f^{-1}$
White phase noise	2	$h_2 f^2$	$v_0^2 h_2$

Table 2.1: Noise types and their  $\alpha$  values for the spectral density of fractional frequency fluctuations and phase fluctuations.

### 2.1.4 Noise characterisation in the time domain

In the time domain an average frequency can be measured in a certain time interval  $T = \tau$ . The number of cycles  $n_k$  counted by a frequency counter starting at a certain time  $t_k$  is written as

$$\langle v(t) \rangle_{t_k, \tau} = v_0 + \frac{1}{\tau} \int_{t_k}^{t_k + \tau} \Delta v(t') dt' = \frac{n_k}{\tau}, \quad (2.15)$$

and the normalised average fractional frequency is typically denoted as

$$\bar{y}_k = \frac{1}{\tau} \int_{t_k}^{t_k + \tau} y(t') dt'. \quad (2.16)$$

Because no infinite number of average frequency samples are available, the ideal or true variance  $\sigma^2[\bar{y}_k] = \langle \bar{y}_k^2 \rangle$ , under the assumption of zero mean of  $y(t)$ , can not be measured. An approximation can be made by use of the sample variance, defined for  $N$  samples of  $\bar{y}_k$ ,  $k \in [1, N]$  for a measurement time  $\tau$  and a repetition time defined as  $t_{k+1} = t_k + T$ , closely following the definition of variance  $\sigma^2(x) = \langle (x - \langle x \rangle)^2 \rangle$  (see section A.1).

This estimator is biased and must thus be corrected according to the main noise types present at various  $\tau$ . which is an undesired property due to the fact that comparison among estimators for various measurements will be impossible. This is especially true because a comparison depends on the amount of frequency samples  $N$ . It is even so that for certain types of noise encountered in the characterisation of oscillators, the variance diverges when more measurement samples (increasing  $N$ ) are analysed.

Allan [99–101] therefore introduced the two-sample variance with zero dead-time which allows a meaningful comparison of frequency stability measurements performed in the time domain. Equation (A.2) serves as a basis, for which we set the sample size  $N = 2$ , and  $T = \tau$  such as to have no dead time. The equation for the so-called Allan variance can now be written as

$$\sigma_y^2(\tau) = \frac{1}{2} \langle (\bar{y}_2 - \bar{y}_1)^2 \rangle. \quad (2.17)$$

A possible estimator for the Allan variance based on  $m$  pairs of consecutive measurement samples  $\bar{y}_i, \bar{y}_{i+1}$  is [99]

$$\sigma_y^2(\tau) = \frac{1}{2(m-1)} \sum_{i=1}^{m-1} (\bar{y}_{i+1} - \bar{y}_i)^2. \quad (2.18)$$

The confidence intervals of this estimator for several values of  $\alpha$  as given by Lesage [102] are

$$E_\alpha \simeq \sigma_y(\tau) K_\alpha m^{-\frac{1}{2}}, \quad \text{for } m > 10, \quad (2.19)$$

with  $K_2 = K_1 = 0.99$ ,  $K_0 = 0.87$ ,  $K_{-1} = 0.77$  and  $K_{-2} = 0.75$ . Thus one needs to have (1) enough samples of the variance, and (2) needs to address the dominant type of noise at the given sample time  $\tau$ , before it is possible to estimate the error. For zero dead time measurements, sample times  $\tau = m\tau_0$  can be used by averaging the fractional frequency values over  $m$  consecutive samples.

The Allan deviation is a  $\chi_N^2$  distribution [103–105]. The calculation of the error should therefore be performed with methods appropriate for the  $\chi_N^2$  distribution, especially for estimates with small  $N$ . In general one must also take into account the dominant noise process as described by the power law model for the spectral density of the fractional frequency deviations  $S_y(f)$  in order to produce a non-biased estimator for the error on the distribution (see section A.2).

There are various modern alternatives to the Allan variance like Theoretical variance number 1 (Théo1 [106–108]) a biased removed version (ThéoBR [109]) and a hybrid (ThéoH [110,111]) bridging the gap between the Allan variance and (fast [112]) ThéoBR. Vernotte [113] approaches the non-stationary noises by use of the moments of the distribution, in order to give an estimation of the Allan variance and it's error for noise types that are not converging in the traditional approach. There exists a plethora of other measures of oscillator stability all suited to specific needs, see for example Riley [114] and references therein for an overview and as starting point.

The normal Allan variance, and it's square root the normal Allan deviation, will be used to depict frequency stability in this thesis because most people are accustomed with this traditional measure of frequency stability<sup>3</sup>.

## 2.2 Electromagnetic waves

Light, treated classically, will propagate as an electromagnetic wave. The Maxwell equations<sup>4</sup> together with material properties and, possibly, bound-

<sup>3</sup>Next to familiarity, ease of implementation and computational efficiency are other reasons to use this measure of frequency stability.

<sup>4</sup>See appendix A.3.

any conditions dictate which solutions of the wave equations

$$\begin{aligned} \nabla^2 \mathbf{E} - \mu_0 \varepsilon_0 \frac{\partial^2 \mathbf{E}}{\partial t^2} &= \frac{1}{\varepsilon_0} \nabla \rho_f + \mu_0 \frac{\partial \mathbf{J}_f}{\partial t} + \mu_0 \frac{\partial}{\partial t} (\nabla \times \mathbf{M}) \\ &+ \mu_0 \frac{\partial^2 \mathbf{P}}{\partial t^2} - \frac{1}{\varepsilon_0} \nabla (\nabla \cdot \mathbf{P}), \end{aligned} \quad (2.20a)$$

$$\begin{aligned} \nabla^2 \mathbf{H} - \mu_0 \varepsilon_0 \frac{\partial^2 \mathbf{H}}{\partial t^2} &= -\nabla \times \mathbf{J}_f - \frac{\partial}{\partial t} \nabla \times \mathbf{P} \\ &+ \mu_0 \varepsilon_0 \frac{\partial^2 \mathbf{M}}{\partial t^2} - \nabla (\nabla \cdot \mathbf{M}). \end{aligned} \quad (2.20b)$$

can be found. The electric field is denoted  $\mathbf{E}$ , the magnetic field  $\mathbf{H}$ , the free charge density  $\rho_f$ , the free current density  $\mathbf{J}_f$ , the magnetization  $\mathbf{M}$  and the polarization  $\mathbf{P}$ , and  $\varepsilon_0$  and  $\mu_0$  the permittivity and permeability of free space.

The focus will be on the wave equation of the electrical field in non magnetic dielectric (so, non-conducting) media, which has significance for the discussion of the frequency comb laser. The laser crystal, or a glass fibre are such materials, and are typically found inside the laser resonator.

### 2.2.1 Plane waves in dielectric matter

Rewriting the general wave equations (2.20), setting terms due to the magnetisation and free charges to zero, leads to the much simplified wave equations

$$\nabla^2 \mathbf{E} - \mu_0 \varepsilon_0 \frac{\partial^2 \mathbf{E}}{\partial t^2} = \mu_0 \frac{\partial^2 \mathbf{P}}{\partial t^2} - \frac{1}{\varepsilon_0} \nabla (\nabla \cdot \mathbf{P}), \quad (2.21a)$$

$$\nabla^2 \mathbf{H} - \mu_0 \varepsilon_0 \frac{\partial^2 \mathbf{H}}{\partial t^2} = -\frac{\partial}{\partial t} \nabla \times \mathbf{P}. \quad (2.21b)$$

The expression  $\nabla (\nabla \cdot \mathbf{P})$  in equation (2.21a), remains from  $\nabla \times \nabla \times \mathbf{E} = \nabla (\nabla \cdot \mathbf{E}) - \nabla^2 \mathbf{E}$ . The divergence of  $\mathbf{E}$  and therefore the divergence of  $\mathbf{P}$  can be shown to vanish in some cases, e.g. for transverse plane waves, or to be small, e.g. when the slowly varying envelope approximation applies [115], therefore this term is typically neglected.

The polarisation of a solid state medium is determined by the way electrons in the medium react to the electrical wave. There are typically several electronic resonances, and related resonance frequencies on which the electrons in the medium can vibrate and dissipate. The electrons in the medium can thus be described as harmonic oscillators driven by the electrical field giving rise to the polarisation term. Use of this model [116, 117] gives the (complex) refractive index of gasses as

$$\tilde{n}^2(\omega) = 1 + \frac{Ne^2}{\varepsilon_0 m_e} \left( \sum_j \frac{f_j}{\omega_j^2 - i\gamma_j \omega - \omega^2} \right), \quad (2.22)$$

where  $N$  is the number of contributing electrons per unit volume,  $e$  the electron charge,  $m_e$  the electron mass,  $f_j$  the oscillator strength of resonance  $j$  of an electron, with resonance frequency  $\omega_j$  and damping coefficient  $\gamma_j$ , which determines the losses through radiation and heating (forced coulombic motion of the atoms). In solid media the electrical field of neighbouring charges on the motion of the electrons has to be taken into account [117] which leads to

$$\frac{\tilde{\mathbf{n}}^2(\omega) - 1}{\tilde{\mathbf{n}}^2(\omega) + 2} = \frac{Ne^2}{3\varepsilon_0 m_e} \left( \sum_j \frac{f_j}{\omega_j^2 - i\gamma_j\omega - \omega^2} \right). \quad (2.23)$$

The relation between the (complex) refractive index and the permittivity ( $\varepsilon$ ) and permeability ( $\mu$ ) is defined as

$$\tilde{\mathbf{n}} \equiv \sqrt{\frac{\varepsilon\mu}{\varepsilon_0\mu_0}}. \quad (2.24)$$

Using the relation between the wave vector  $\tilde{\mathbf{k}}$  and the refractive index  $\tilde{\mathbf{n}}$

$$\tilde{\mathbf{k}} = \mathbf{k} + i\kappa = \frac{\omega}{c} \tilde{\mathbf{n}}, \quad (2.25)$$

the wave vector can be related to the material properties of the medium. It is thus seen that  $\kappa$  relates to the imaginary part of  $\tilde{\mathbf{n}}$  and  $\mathbf{k}$  relates to the real part of  $\tilde{\mathbf{n}}$ .

Returning to the wave equation (2.21a) the plane wave solution<sup>5</sup> can be written as

$$\begin{aligned} \mathbf{E}(\mathbf{r}, t) &= \frac{E_0}{2} e^{-\kappa \cdot \mathbf{r}} \left( e^{i(\mathbf{k} \cdot \mathbf{r} - \omega t + \varphi)} + e^{-i(\mathbf{k} \cdot \mathbf{r} - \omega t + \varphi)} \right) \hat{\mathbf{n}}, \\ &= E_0 e^{-\kappa \cdot \mathbf{r}} \cos(\mathbf{k} \cdot \mathbf{r} - \omega t + \varphi) \hat{\mathbf{n}}, \end{aligned} \quad (2.26)$$

where  $\hat{\mathbf{n}}$  is the unit polarisation vector,  $\kappa$  determines the attenuation due to dielectric losses, and the wave velocity is determined by the wave vector  $\mathbf{k}$ .

From the solution of the wave equation (2.21a) the speed of the wave in the medium, the phase velocity  $v_\varphi$ , can be related to the speed of the wave in free-space, denoted  $c = \frac{1}{\sqrt{\varepsilon_0\mu_0}} \equiv 299\,792\,458 \text{ m s}^{-1}$ , via the real part of the refractive index as

$$v_\varphi = \frac{c}{n} = \frac{\omega}{k}. \quad (2.27)$$

Neglecting dielectric losses, a valid assumption far away from electronic resonance frequencies in a medium, the refractive index becomes real and can be written as a Taylor expansion around a center frequency  $\omega_0$  in the

<sup>5</sup>See also equation (A.18).

usual way

$$\begin{aligned}
 n(\omega) &= n(\omega_0) + \left. \frac{\partial n}{\partial \omega} \right|_{\omega_0} (\omega - \omega_0) + \left. \frac{\partial^2 n}{2\partial \omega^2} \right|_{\omega_0} (\omega - \omega_0)^2 + \dots \\
 &= \sum_{m=0}^{\infty} \frac{n^{(m)}|_{\omega_0}}{m!} (\omega - \omega_0)^m.
 \end{aligned} \tag{2.28}$$

where  $n^{(m)} = \partial^m n / \partial \omega^m$ .

The wave vector itself (omitting the imaginary part and it's vector nature) can be expanded in a Taylor series as well

$$k(\omega) = \sum_{m=0}^{\infty} \frac{k^{(m)}|_{\omega_0}}{m!} (\omega - \omega_0)^m. \tag{2.29}$$

### 2.2.2 Waves with multiple frequency components

A superposition of plane electromagnetic waves all propagating in a common direction  $\hat{\mathbf{k}}$  but with a different frequencies  $\omega$ , around a central frequency  $\omega_0$  is described as

$$E(\mathbf{r}, t) = \frac{1}{2\pi} \int_{-\infty}^{\infty} A(\omega - \omega_0) \left( e^{i(\mathbf{k}\cdot\mathbf{r} - \omega t + \varphi)} + c.c. \right) d\omega, \tag{2.30}$$

where the part inside the integral is the frequency domain description of the signal with  $A(\omega - \omega_0)$  the spectral amplitude function. To shorten the notation the complex conjugate (*c.c.*) will be left out in the following.

To come to a time domain description the amplitude is written as  $A(\omega - \omega_0) = A(\omega)e^{-i\omega_0 t}$  through which we obtain

$$E(\mathbf{r}, t) = \frac{1}{2\pi} \int_{-\infty}^{\infty} A(\omega) e^{i(\mathbf{k}\cdot\mathbf{r} - \omega_0 t + \varphi)} e^{-i\omega t} d\omega. \tag{2.31}$$

Both frequency dependent functions  $\mathbf{k}$  and  $\varphi$  can be written as a constant at  $\omega_0$  and a deviation, yielding  $\mathbf{k}_0 + \delta\mathbf{k}(\omega)$  and  $\varphi_0 + \delta\varphi(\omega)$  and inserted in equation (2.31) to obtain

$$\begin{aligned}
 E(\mathbf{r}, t) &= \frac{1}{2\pi} \int_{-\infty}^{\infty} A(\omega) e^{i(\mathbf{k}_0\cdot\mathbf{r} + \delta\mathbf{k}\cdot\mathbf{r} - \omega_0 t + \varphi_0 + \delta\varphi(\omega))} e^{-i\omega t} d\omega \\
 &= \tilde{A}(\mathbf{r}, t) e^{i(\mathbf{k}_0\cdot\mathbf{r} - \omega_0 t)}.
 \end{aligned} \tag{2.32}$$

In the following the propagation of waves of equation (2.32) in a linear dielectric medium with the propagation direction along the  $z$  axis is treated. The propagation of a wave  $E_0(t)$  from  $z = 0$  to an arbitrary  $z$  can be described by use of a Greens function

$$E(z, t) = \int_{-\infty}^{\infty} E_0(\tau) G(t - \tau, z) d\tau. \tag{2.33}$$

where

$$G(t - \tau, z) = \frac{1}{2\pi} \int_{-\infty}^{\infty} e^{i\omega(t-\tau) - ikz} d\omega \quad (2.34)$$

is called the pulse propagator<sup>6</sup> as proposed by Marcuse [118] and referred to by Akhmanov [119] and subsequently Witte [120]. The wave vector,  $k$ , in this equation is frequency dependent, which will give rise to varying propagation behaviour in each order of its derivative.

Inserting the zero-order term of the expansion (2.29) into the propagator (2.34) one obtains  $\delta(t - \tau - n(\omega_0)z/c)$ . Propagating  $\mathbf{E}_0(t)$ , by use of the sifting property of the delta function in the convolution integral, then yields

$$\begin{aligned} \mathbf{E}(z, t) &= \int_{-\infty}^{\infty} \mathbf{E}_0(\tau) \delta(t - \tau - n(\omega_0)z/c) d\tau \\ \mathbf{E}(z, t) &= \mathbf{E}_0\left(t - \frac{n(\omega_0)}{c}z\right) \\ \mathbf{E}(z, t) &= \mathbf{E}_0\left(t - \frac{z}{v_\varphi}\right). \end{aligned} \quad (2.35)$$

As expected the field has moved with the speed of light in the medium.

The pulse propagator for the first order of  $k$  yields

$$\mathbf{E}(z, t) = e^{-i(k^{(0)} - k^{(1)}\omega_0)z} \mathbf{E}_0(t - k^{(1)}z). \quad (2.36)$$

The field now moves with a speed

$$v_g = \frac{1}{k^{(1)}} = \left. \frac{d\omega}{dk} \right|_{\omega_0}, \quad (2.37)$$

which is therefore commonly called the group velocity of a wave. The carrier  $\omega_0$  is shifted with respect to the shape of the  $\mathbf{E}_0(t)$ , and obtains an amount of carrier to envelope phase shift

$$\Delta\varphi = \omega_0 \left( \frac{1}{v_g} - \frac{1}{v_\varphi} \right) z = \frac{\omega_0^2}{c} \left. \frac{\partial n}{\partial \omega} \right|_{\omega_0} z. \quad (2.38)$$

The second order of  $k$  introduces pulse broadening, and additionally introduces a deviation of the instantaneous frequency of the carrier wave, usually referred to as chirp as is shown by Witte [121].

Under the assumption of an isotropic dielectric medium, e.g. a non-polarised crystal or a gas, the first non-linear term in the equation for the refractive index due to the electric field has a second order dependence on  $\mathbf{E}$  (linear in intensity), and the equation for the refractive index becomes

$$n(\omega, \mathbf{E}) = n_0(\omega) + n_2(\omega)\mathbf{E}^2. \quad (2.39)$$

---

<sup>6</sup>The term pulse propagator is actually a misnomer, since it describes the propagation of arbitrary electric fields in arbitrary matter.

This second order non-linear response of the refractive index is also referred to as the Kerr effect [122–125].

Inserting (2.39) into the equation for the carrier to envelope phase shift (2.38), one finds (to first order) an intensity dependence

$$\Delta\varphi = \frac{\omega_0^2}{c} \frac{\partial(n_0(\omega) + n_2(\omega)\mathbf{E}^2)}{\partial\omega} \Big|_{\omega_0} z, \quad (2.40)$$

of the carrier to envelope phase due to a non-linear material response [126].

## 2.3 Frequency combs

The concept of a frequency comb is quite common in electronics. For example, the harmonics of a square wave generator form a frequency comb and can be used as a (high) frequency reference. The usual characterisation of a frequency comb<sup>7</sup> in optics<sup>8</sup> is given by the frequency relation

$$f_m = f_0 + mf_{\text{rep}}, \quad m \in \mathbb{N} \quad (2.41)$$

where  $f_m$  is the frequency of mode  $m$ ,  $f_0$  is the offset frequency,  $f_{\text{rep}}$  is the repetition rate frequency, and  $\mathbb{N}$  are the natural numbers including 0. It is easily seen that this description is not a physically correct description of a frequency comb's output signal, but rather sets a restriction on the frequency content of the output signal. A broad variety of sources (confining the selection to electromagnetic wave emitters) ranging from e.g. electrical square wave generators via microwave harmonic generators [127] to various optical sources [36, 37, 128–134], adhere to these properties and can be called frequency combs.

Among the optical frequency comb sources, a distinction can be made between optical frequency comb generators and frequency comb lasers. The former devices typically generate a comb from a single frequency (CW) input signal, while the latter devices are laser sources whose output spectrum resembles an optical frequency comb<sup>9</sup>.

### 2.3.1 Frequency comb signals

The most general form of a physical frequency comb signal can be written as a sum of cosines with frequencies given by equation (2.41) and where to each mode  $m$  is assigned an amplitude  $A_m$  and a phase  $\varphi_m$ , as in

$$y(t) = \sum_{m=0}^{\infty} A_m \cos(2\pi(f_0 + mf_{\text{rep}})t + \varphi_m). \quad (2.42)$$

<sup>7</sup>The name frequency comb is due to the fact that this frequency relation depicted as impulse functions on a frequency axis resembles the image of a comb.

<sup>8</sup>The offset frequency  $f_0$  is typical for an optical frequency comb.

<sup>9</sup>Note that the word laser already implies an optical source, but no fundamental principle excludes other (electromagnetic) wave sources with a frequency comb output signal.

The frequency domain signal can be obtained via a Fourier transform as

$$Y(f) = \sum_{m=0}^{\infty} \frac{A_m}{2} \left[ e^{i\varphi_m} \delta(f - (f_0 + mf_{\text{rep}})) + e^{-i\varphi_m} \delta(f + (f_0 + mf_{\text{rep}})) \right], \quad (2.43)$$

where the mode amplitude and phase symmetries around zero on the frequency axis should be observed.

For certain configurations of the (usually neglected) parameters amplitude and phase of the frequency comb modes, the output of a frequency comb can become a train of pulses, in other configurations the output signal appears to be irregular, for some configurations (e.g. ones for with  $f_0 = 0$ ) it can still repeat itself each  $1/f_{\text{rep}}$ . For again other configurations a regular “pulse like” structure that quasi repeats at multiples of  $f_{\text{rep}}$  can be observed.

In an often used model, the spectral envelope function is taken to be a Gaussian function<sup>10</sup> shifted to a certain (optical) centre frequency  $f_c$  with a full width half maximum  $\Delta f$ . In this model description the spectral phase function  $\varphi(f)$  is zero. The outcome of this model is then used to get an idea about how the “pulse train” from a frequency comb source looks. Figure 2.1a) gives a graphical representation of this model description for very low mode numbers. This give a good impression of the main properties of the frequency comb signals for classes of comb parameters that resemble this simplified case.

It is easily seen that the time domain amplitude is the Fourier transform of the frequency domain amplitude and the width of the pulse in the time domain is exactly  $1/\Delta f$ . The carrier frequency is the central frequency  $f_c$  of  $A(f)$ . The carrier-envelope offset frequency was chosen to be  $\frac{1}{4}f_{\text{rep}}$  and thus the carrier slips  $2\pi$  underneath the envelope every 4 pulses.

It is generally not the case that the spectral phases  $\varphi_m$  are zero, or that the spectral amplitude function is a Gaussian, which can complicate the time domain signal significantly. One case can be seen in Fig 2.1b) which represents the same frequency comb as in Fig 2.1a) but now with a random spectral phase function. It is seen that the random spectral phase alters the time domain signal significantly. However, the time domain signal maintains it's periodicity due to the rational  $f_0/f_{\text{rep}}$  value. Strictly speaking the time domain envelope function will always be periodic with  $1/f_{\text{rep}}$ , but already in this case it is clear that the time-domain envelope function is not the direct Fourier transform of the spectral envelope function, but something more complex.

### 2.3.2 Frequency comb lasers

In the optical community the term frequency comb laser<sup>11</sup> usually refers to a self-referenced,  $f_0$  and  $f_{\text{rep}}$  stabilised mode-locked laser. It must be noted

<sup>10</sup> $A(f) = \exp \{ -4 \ln 2 [(f - f_c) / \Delta f]^2 \}$

<sup>11</sup>Several terms are used in literature such as: frequency comb, optical frequency synthesizer, femtosecond frequency comb, comb, femtosecond laser comb, femtosecond comb...which all more or less do not say what is exactly meant.

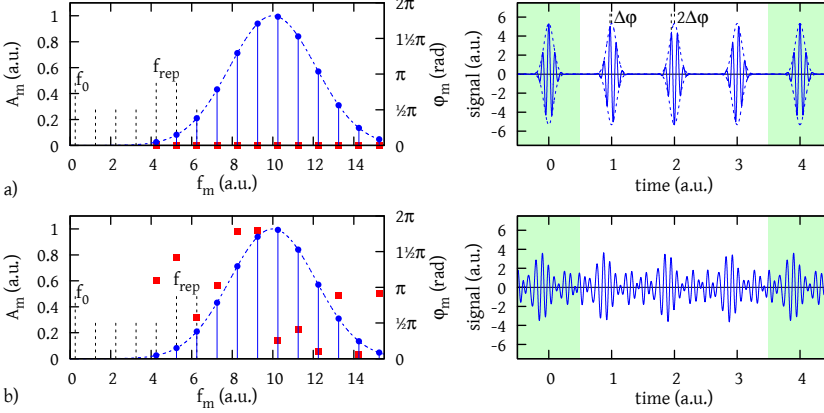


Figure 2.1: Frequency comb signals. a) Gaussian model in frequency (left) and time (right) domain with  $f_0 = 0.25$  and  $f_{\text{rep}} = 1.0$ , the spectral phase has been chosen 0. The blue lines (and dots) represent the frequency comb mode amplitudes and the frequency comb signal respectively. The blue dotted lines are the spectral and time-domain envelope functions. The red squares denote the values of the spectral phase of the comb modes. Note the carrier-envelope phase shift  $\Delta\phi = 2\pi f_0/f_{\text{rep}}$  in the time domain. The signal repeats itself with a period  $f_{\text{rep}}/f_0 = 4$ , the signals on the green backgrounds are exactly equal. b) Comb parameters  $f_{\text{rep}}$  and  $f_0$  and the spectral amplitude function have been chosen as in a), the spectral phase has been chosen random. This influences the time domain frequency comb signal significantly.

that the words self-referenced and stabilised dictate a severe limitation on the class of (mode-locked) lasers that qualify as frequency comb lasers.

### Properties of the laser resonator and medium

The properties of frequency comb laser light are strongly determined by the properties of the (materials in the) laser resonator. In the usual frequency comb laser, the fundamental transverse electromagnetic mode ( $\text{TEM}_{00}$ ) of the resonator is excited. The plane wave along the resonator length (the  $z$  coordinate) is written

$$\mathbf{E}(z, t) = E_0 \cos(kz - \omega t + \varphi_0) \hat{\mathbf{n}}, \quad (2.44)$$

where  $\hat{\mathbf{n}}$  is a normal vector denoting the direction of the  $\mathbf{E}$ -field transverse to the propagation direction  $z$ .

Given the phase velocity of light (2.27) in a material with refractive index  $n$ , independent of the frequency  $\omega$  of the light and a resonator of two mirrors with a spacing  $L$  (optical length  $nL$ ), the resonator is able to sustain multiple waves, where the value of the phase after one round trip is equal, which results in the frequency  $f_m$  of mode  $m$  of

$$f_m = \frac{cm}{n2L} \quad m \in \mathbb{N}. \quad (2.45)$$

Such a resonator can sustain a frequency comb with the properties

$$f_{\text{rep}} = \frac{c}{n2L} \quad \text{and} \quad f_0 = 0. \quad (2.46)$$

From equations (2.22) and (2.23) we have seen that the refractive index is not a constant but a function of frequency depending on the media in the laser resonator. Equation (2.45) dictates that the second- and higher-order derivatives in the Taylor expansion (2.28) of the refractive index around  $\omega_0$ , need to vanish in order to obtain an equidistant mode spacing around  $\omega_0$  in the resonator. A resonator with these properties is said to be dispersion compensated around  $\omega_0$ .

In the resonator of a frequency comb laser a significant portion of the spectral range at which lasing is possible needs to be dispersion compensated to support sustenance of a frequency comb output spectrum. An effect called “mode pulling”, where non-linear interactions like four wave mixing dictate the frequency of modes, enable frequency comb generation and sustenance in the non-dispersion compensated part of the resonator to a certain degree, giving rise to an increased width of the obtained frequency comb spectrum. In case of a dispersion compensated resonator, the group velocity of the wave envelope is constant and the envelope of the output wave of the laser repeats itself with frequency  $f_{\text{rep}}$ .

Equation (2.38) shows that the first derivative of  $n$  introduces a phase shift of the carrier with respect to the envelope of the wave along the resonator, and thus gives rise to a fixed carrier-to-envelope phase shift for each round trip. The frequency of this phase shift per round-trip time (expressed in its inverse  $f_{\text{rep}}$ ), is then given as

$$f_{\text{CEO}} = \frac{\Delta\varphi}{2\pi} f_{\text{rep}}. \quad (2.47)$$

The phase shift  $\Delta\varphi$ , which can be expressed as a value modulo  $2\pi$ , thus determines the so called carrier-envelope offset frequency,  $f_{\text{CEO}}$ , which is bound to the range  $f_{\text{CEO}} \in [0, f_{\text{rep}})$ . The offset frequency  $f_0$  in the frequency comb definitions equals the carrier-envelope offset frequency  $f_{\text{CEO}}$  in an optical frequency comb (both are used in literature).

A means of obtaining the carrier-envelope offset frequency is by use of non-linear interactions, through which multiples of the comb mode frequencies are obtained, that contain multiples of  $f_{\text{CEO}}$ . For example sum frequency generation in a  $\chi^{(2)}$  non-linear optical medium yields a comb structure in the doubled frequency region, where each mode acquires  $2f_{\text{CEO}}$ .

The carrier-envelope offset frequency can then be obtained by comparing the original comb spectrum at the high frequency side with nearly the same frequencies obtained by sum frequency mixing of modes at the low frequency side of the comb spectrum. This is done by interference of both types of modes on a photodiode, leading to a beat note at the difference frequency  $f_{\text{CEO}}$ . Note that the sum frequency modes around  $m$  interfere with

modes around  $2m$  in the original frequency comb spectrum, which requires a spectral width of more than an octave. This procedure is called self referencing (of  $f_{\text{CEO}}$ ) of a frequency comb, since no external frequency reference signal is required to determine  $f_{\text{CEO}}$ .

As mentioned above, a frequency comb laser is a laser of which the frequency comb is stabilised. This means that handles on both  $f_{\text{rep}}$  and  $f_{\text{CEO}}$  are needed. Control over  $f_{\text{rep}}$  can be obtained by control over the cavity length, or the refractive index (equation (2.45)), while control over  $f_{\text{CEO}}$  can be obtained via the intra-cavity laser intensity due to the third-order non-linear refractive index (equation (2.40)).

The accuracy of the frequency relations in frequency comb lasers have been tested to better than  $1 \times 10^{-19}$  [135, 136], showing an unprecedented potential for optical frequency measurements using frequency comb lasers.

### The role of the laser medium and mode locking

So far nothing has been said about the laser medium and its role in frequency comb lasers. In order to achieve lasing an optically active medium that can have population inversion is needed. In a frequency comb laser, such a medium should be relatively broadband to support a wide spectral output, and thus a comb that spans over a large spectral range. We already saw that self referencing  $f_{\text{CEO}}$  requires a frequency comb output over a spectral range that spans more than an octave of frequencies.

As can be seen from equation (2.43), two free but constant parameters, the amplitude  $A_m$  and the phase offset  $\varphi_m$  of the frequency comb modes exist. The spectral shape of these free parameter is crucial for the possible output signals of a frequency comb generator. In most frequency comb generators, the functions  $A(f)$  and  $\varphi(f)$  are slowly varying functions from mode to mode, where  $\varphi(f)$  is at most a linear function if the pulse is to be Fourier limited. A wide spectral amplitude function  $A(f)$  then allows for fast temporal amplitude changes  $a(t)$ , leading to a frequency comb output signal that exists of short pulses.

Note that a randomly varying but time constant value  $\varphi_m$  from mode to mode still yields a frequency comb, but gives rise to a quasi random temporal output signal. In the same way a randomly varying  $A_m$  leads to a quasi random output signal. Coherent control methods specifically use the freedom to manipulate (groups of)  $A_m$  and  $\varphi_m$ , to obtain favourable experimental behaviour (see e.g. Barmes [137]).

If the phase offset is equal for all modes

$$\varphi_m = C, \quad \forall m, \quad (2.48)$$

with  $C$  a constant modulo  $2\pi$ , then the output signal consists of a field envelope given by the Fourier transform of the frequency comb spectrum, with a carrier frequency given by the weighted average<sup>12</sup>, the ‘‘center’’, of the fre-

<sup>12</sup>The mode amplitudes are the weighting factors.

quency comb spectrum. The carrier will be shifted from repetition period to repetition period by the carrier-to-envelope phase shift. In general, the phase of the modes is not constant with frequency which introduces temporal field envelope changes and temporal carrier wave phase deviations.

Fixing of the free phase offset parameters  $\varphi_m$  to constant values is referred to as mode-locking. A time varying  $\varphi_m$  means that the mode frequencies are not constant<sup>13</sup>. Typically mode-locking is achieved via non-linear processes that favour the efficiency of the mode-locked state over a randomly fluctuating phase state of the comb source, thereby stabilizing to the mode-locked state. Examples of such non-linear processes are the Kerr effect, intensity induced birefringence, or saturable absorption [138].

Although it is commonly thought that the output of mode-locked lasers are (ultra-short) pulses, this is not necessarily the case. The phase offset  $\varphi_m$  needs only to be constant to create a frequency comb but can have an arbitrary value from mode to mode, which may lead to a quasi-random shape of the electrical field in the time domain as seen in Fig 2.1b. For example, the mode-locked quantum-dot lasers discussed in chapter 4 give only a slight intensity modulation on their output intensity in stead of clear pulses.

### 2.3.3 Optical frequency comb generators

Besides laser sources that act as frequency combs, other ways of generating optical frequency combs have been successfully pursued. One class of devices, pioneered by Kourogi [128], exist of a moderately high-finesse optical cavity, a CW input laser source and an active modulation device, e.g. an electro-optical phase modulator (EOM). The CW laser is set to the frequency of a mode of the optical cavity and the modulation frequency of the EOM is adjusted to the resonator mode spacing. Under these conditions a comb arises due to cross modulation of the light in the various cavity modes, as long as the losses stay relatively low, so that the lost photons can be replenished from the CW seed laser.

A second class of sources, pioneered by Vahala and Kippenberg [133, 139] consist of a high finesse ( $\mathcal{F} > 100\,000$ ) micro resonator where the light from a CW laser exhibits significant non-linear parametric interaction with the material. When the laser is brought in resonance with the cavity, the intracavity intensity becomes high enough that spontaneous four wave mixing populates other modes of the resonator seeded by vacuum fluctuations. However, the frequency combs generated in these devices need not necessarily be equidistant [133]. Recently various mechanisms through which the comb structures arise have been identified, which clarify in part why stable multipulsing and multiple coexisting frequency comb structure regions are possible in these devices [134, 140].

The way a frequency comb was generated in the quantum dot laser sources treated in chapter 4 resembles a Kourogi type optical frequency comb gen-

<sup>13</sup>Phase noise can be modelled by addition of noise to the free phase parameter.

erator. An important difference is that in this case the optical gain from the quantum-dot laser medium compensates for the loss mechanisms inside the device, instead of relying on a high-finesse cavity.

## 2.4 Light source characterisation with frequency comb lasers

Frequency comb lasers have enabled highly accurate calibration and characterisation of narrow band (optical mode bandwidth less than  $\frac{1}{2}f_{\text{rep}}$ ) light sources such as CW or other frequency comb lasers. The spectral properties of the light source are then translated to the RF domain by means of a heterodyne beat between the source and comb, which can be measured with conventional microwave measurement equipment such as spectrum analysers, counters and phase noise analysers.

### 2.4.1 Absolute CW laser frequency measurements

In order to determine the absolute frequency of a CW laser<sup>14</sup> a heterodyne beat is made between the output of a frequency comb laser and the output of a CW laser. The device used for this is called a “beat unit” and it typically first contains a means to obtain good spatial overlap between the two laser beams. The beam direction, divergence and location all need to be equal. In this case the electric fields overlap perfectly and a maximum interference signal is obtained along the beam path. If a photo diode is placed in the beam, intensity fluctuations  $I(t) = E^2(t)$  are detected which contain the sum and difference frequencies of the CW laser mode  $l$  (with frequency  $\omega_l$ ) and the frequency comb modes  $m$  (with frequency  $\omega_m$ ).

This is easily seen by working out the equation for the intensity expressed in electrical fields for the laser mode and a single frequency comb mode

$$I = E^2 = (E_l + E_m)^2 = E_l^2 + E_m^2 + 2E_lE_m, \quad (2.49)$$

where the cross term gives rise to sum and difference frequencies of the frequency comb modes and the CW laser mode. The frequency comb laser and CW laser modes themselves give rise to a DC component and frequency doubled component both of which contribute to a DC background signal. The cross term is written out as an example

$$E_l = E_{0,l} \cos(\omega_l t) \quad E_m = E_{0,m} \cos(\omega_m t), \quad (2.50)$$

$$E_l E_m = \frac{1}{2} E_{0,l} E_{0,m} \left( \cos(\omega_m + \omega_l t) + \cos(\omega_m - \omega_l t) \right). \quad (2.51)$$

The beating between the various frequency comb laser modes themselves gives rise to sum and difference frequencies (replace  $\omega_m$  with e.g.  $\omega_{m+1} =$

---

<sup>14</sup>These procedures are general and will work for arbitrary CW frequency determination with a frequency comb source.

$\omega_m + 2\pi f_{\text{rep}}$ ) at the lowest harmonics of  $f_{\text{rep}}$  up to the maximum detection frequency of the photo diode. The DC background formed by frequency comb laser modes not contributing to the desired beat signal can saturate the photo diode current and can therefore deteriorate the signal to noise ratio. These frequency comb laser modes are filtered out of the optical spectrum as much as possible before the heterodyne beat is detected, e.g. by use of a grating, lens and slit, or an interference filter. A sketch of a beat spectrum between a frequency comb laser and a CW laser is given in Fig. 2.2.

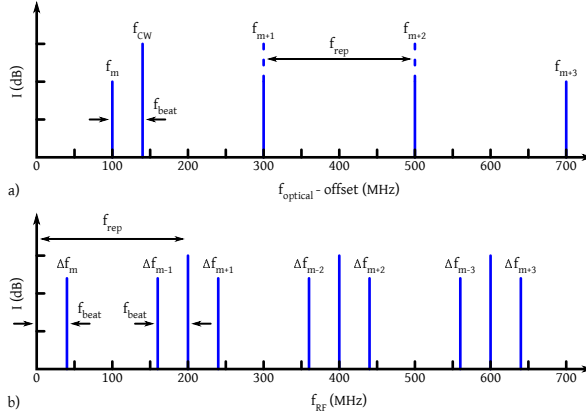


Figure 2.2: a) Part of the combined optical spectrum of a frequency comb laser and CW laser output, note the mode numbers  $m$ ,  $m + 1$ , etc. Only a small frequency range is shown at an offset in the optical spectrum, typically 100 – 400 THz. b) Microwave spectrum of the beat signal as recorded on a spectrum analyser, note the characteristic repeated pattern of positive and negative beat signals. The sequence is typically repeated up to the cutoff frequency of the photodiode. A single beat can be filtered out and used for measurement or feedback purposes. The labels  $\Delta f_m$ ,  $\Delta f_{m-1}$  etc. denote the comb modes from which the beat signals originate.

Typically only one of the heterodyne beat signals that lies in a countable or recordable frequency range is of interest. This beat signal, with frequency  $f_{\text{beat}}$ , is filtered out of the microwave spectrum and fed into the measurement equipment. The absolute frequency of the CW laser under investigation is given as

$$f_i = \pm f_{\text{CEO}} + m f_{\text{rep}} \pm f_{\text{beat}}, \quad (2.52)$$

where  $f_{\text{CEO}}$ ,  $f_{\text{rep}}$  and  $f_{\text{beat}}$  are microwave signals and  $m$  is the mode number of the frequency comb laser mode involved. To obtain the absolute frequency it is crucial to know the beat signs of  $f_{\text{CEO}}$  and  $f_{\text{beat}}$ , and the mode number  $m$ . If the CW laser under investigation has a relatively stable mode, the beat signs can be found by changing frequency  $f_{\text{rep}}$  or  $f_{\text{CEO}}$  while observing the change in frequency  $f_{\text{beat}}$ . Two mode numbers  $m$  can be found by repeating the measurement with a different  $f_{\text{rep}}$  and slight prior knowledge about the CW laser frequency. In this case two mode numbers  $m_1$  and  $m_2$  can be found by solving

$$f_{l_1} = \pm f_{\text{CEO}_1} + m_1 f_{\text{rep}_1} \pm f_{\text{beat}_1}, \quad (2.53a)$$

$$f_{l_2} = \pm f_{\text{CEO}_2} + m_2 f_{\text{rep}_2} \pm f_{\text{beat}_2}, \quad (2.53b)$$

$$|\Delta f_{l_1, l_2}| = |f_{l_1} - f_{l_2}| \equiv 0, \quad (2.53c)$$

which will have a unique solution in a frequency range  $n f_{\text{rep}_1}$  around the CW laser frequency, where

$$n = \frac{f_{\text{rep}_1}}{f_{\text{rep}_2} - f_{\text{rep}_1}} \quad (2.54)$$

for integer  $n$ , otherwise a unique solution exists. In general a variation of  $f_{\text{rep}}$  by about 0.1–1% suffices when the CW laser frequency does not drift too much (typically  $< 10$  kHz is sufficient) between the measurements. In practice measurement errors lead to non-integer mode number determinations and a non-zero outcome of the comparison (2.53c).

#### 2.4.2 Characterisation of frequency stability of CW lasers

Heterodyne beats provide the means to measure both the short term and long term characteristics of a CW laser. The border between short and long term lies somewhere around 1 second. A caveat for short term characterisation is that the laser with the largest phase noise, either the frequency comb laser or CW laser, determines the measurement limits of e.g. line width measurements directly on the beat note. Methods to fully overcome the limitations of the transfer laser, in this case the frequency comb laser, have been devised by Telle *et al.* [141]. These methods have not been used for this thesis, but are currently in development for future experiments. Some of the frequency comb laser limits, e.g. large phase noise on  $f_{\text{CEO}}$ , can be overcome in a simpler way by using a second CW laser as will be described below.

For the long term frequency stability behaviour of a CW laser, a simple counter connected to the RF output of the beat unit is used to record frequency changes of the laser, which include instabilities (e.g. due to temperature) in the measurement setup. If both the frequency comb laser and the counter are referenced to a common frequency reference, the only principle limitations to the measurement accuracy are then the signal to noise ratio of the system and the counter resolution. Short-term frequency fluctuations will typically average out in 10 to 100 seconds. Long-term measurements are usually displayed using an Allan deviation plot, where the two-sample Allan deviation is plotted as a function of the counter gate time.

The short term frequency (or phase) stability is often measured as a power spectral density recorded with a spectrum analyser if no significant amplitude noise is present. More specific phase noise measurement methods that are less susceptible to amplitude noise are available if required [142, 143]. If the frequency comb laser has a larger phase noise than the CW laser under investigation, a second, equally or more phase stable, CW laser can be used as

a reference laser. If no direct beat signal between the CW lasers is obtainable, the frequency comb laser can be used as a transfer oscillator, as long as the CW laser wavelengths lie within the wavelength range of the frequency comb laser output.

From the set of equations for the beat frequencies of two CW lasers  $l_1, l_2$  with a frequency comb laser

$$f_{\text{beat}_1} = f_{\text{CEO}} + m_1 f_{\text{rep}} - f_{l_1}, \quad (2.55a)$$

$$f_{\text{beat}_2} = f_{\text{CEO}} + m_2 f_{\text{rep}} - f_{l_2}, \quad (2.55b)$$

$$f_{\text{beat}_2} - f_{\text{beat}_1} = m_2 f_{\text{rep}} - f_{l_2} - m_1 f_{\text{rep}} + f_{l_1} \quad (2.55c)$$

it is seen that fluctuations in  $f_{\text{CEO}}$  are common to both beat signals and drop out when the difference frequency of the heterodyne beats is recorded. Frequency fluctuations of  $m_2 f_{\text{rep}}$  are  $m_2/m_1$  as large as frequency fluctuations of  $m_1 f_{\text{rep}}$ , and can be accounted for when the mode numbers  $m_1, m_2$  are known and the  $f_{\text{rep}}$  signal is recorded simultaneously with the beat signals. In this way the short term stability of CW lasers can be compared although the frequency comb laser can have significant phase noise on  $f_{\text{CEO}}$  and/or  $f_{\text{rep}}$ . As mentioned before, Telle [141] describes a method to directly account for the  $f_{\text{CEO}}$  and  $f_{\text{rep}}$  fluctuations using a frequency comb source as a transfer oscillator by using a direct digital synthesizer (DDS) as a fractional divider to compensate for the the difference in  $m_1$  and  $m_2$ .

### 2.4.3 Characterisation of frequency comb laser stability

The combination of two CW lasers with two frequency comb lasers, can be used in several ways in order to characterise the second frequency comb laser. Such an approach has been used to characterise the repetition rate stability of a generated optical frequency comb on a CW laser described in Chapter 4.

Leaving two CW lasers free running while recording the four beat signals with the two frequency comb lasers, will tell something about the mutual  $f_{\text{rep}}$  stability of the frequency comb lasers. Locking both CW lasers tightly to the first frequency comb laser while characterising the beats with a second frequency comb laser on the other hand, can tell something about the mutual  $f_{\text{CEO}}$  and  $f_{\text{rep}}$  stability through correlations in the beat signals. By measuring all the required beat notes simultaneously with fast photodiodes and a multichannel oscilloscope, the characterization can be carried out off-line on a computer system.

## 2.5 Frequency comb spectroscopy

The term frequency comb spectroscopy is used for a number of different ways of measuring spectra “with a frequency comb source”. In astrophysics spectrometers can be calibrated by means of optical frequency combs [144,145]. In traditional CW laser spectroscopy, improved accuracy can be obtained by calibration of a stabilised CW laser against an optical frequency comb [146–151]

in stead of using the traditional etalon together with, e.g. iodine absorption spectroscopy. A more advanced use of a frequency comb source is stabilisation of the phase or frequency of a CW laser against an optical frequency comb (see e.g. [152]), or by use of an optical frequency comb as a transfer oscillator against an ultra-stable laser source [141].

These measurement modes will be referred to as indirect frequency comb spectroscopy, because a frequency comb source is used to calibrate a CW source, but the output of the frequency comb source itself is not used as part of the spectroscopic method. Measurement modes where the output of a frequency comb source itself is used in the spectroscopic method are called direct frequency comb spectroscopy. The remainder of this section will treat various methods of direct optical frequency comb spectroscopy, and includes the application of direct frequency comb spectroscopy on a two level quantum system.

### 2.5.1 Direct frequency comb spectroscopy

One technologically quite advanced method of direct optical frequency comb spectroscopy capable of measuring complex spectra, is to send optical frequency comb light through a sample (e.g. an atomic or molecular gas) and then analyse the light in a Virtually Imaged Phased Array (VIPA) spectrometer [153] to obtain a spectroscopic fingerprint of the sample. In this case the intensity of each mode is separately recorded, and the spectrum shows up directly as absorption dips in the (calibrated) frequency comb laser intensity spectrum. Full spectral coverage is obtained by scanning  $f_{\text{rep}}$  and/or  $f_{\text{CEO}}$ . This method enables accurate spectroscopy, simultaneously covering a wide spectral range, which is particularly interesting for complex molecular spectra.

In case of a sample with a few transitions that are much narrower than  $f_{\text{rep}}$ , one can excite the sample with a single frequency comb, while changing  $f_{\text{CEO}}$  or  $f_{\text{rep}}$  to scan the comb modes over a given transition [137, 154]. The recorded signal is in this case the spectral convolution of the line shape of the comb laser mode and the line shape of the transition, which can be broadened by e.g. the Doppler effect, pressure, interaction time and others. The signal will typically be fluorescence from the excited state decay [154]. Other detection channels can be ionisation of the excited species [155] or, in case of a trapped sample, trap loss if the excited state is not trapped. Here the ultimate limit will be the natural line width of the transition, the amount of time available for the measurement on an atom or molecule, the intensity stability and the frequency accuracy and phase stability (in popular language, line width) of the frequency comb laser.

Another possibility for direct frequency comb spectroscopy is the use of two frequency comb laser systems as a Fourier transform spectrometer [156–158]. The lasers will operate with a slightly different  $f_{\text{rep}}$ . In this case light of one comb is used as a reference while the other comb is used to probe the

sample. Alternatively the sample can be placed in the combined beam path. The spectroscopic resolution is in this case limited by the coherence time of the modes of the two frequency comb lasers, which must be longer than the acquisition time ( $1/\Delta f_{\text{rep}}$ ). Fast acquisition times (many kHz) can be obtained. One of the interesting applications is the real time monitoring of the molecular composition of gasses in the so called finger print region of roughly between 3–20  $\mu\text{m}$ . This type of frequency comb spectroscopy is of interest for online monitoring of material composition in the output of chemical reactors, especially in drug synthesis processes and has a medical application in breath analysis for detection of diseases. There are different configurations possible of dual-comb spectroscopy, including Doppler-free spectroscopy [159–161].

### 2.5.2 The two-level atom model

In order to understand the electromagnetic interaction of the output of a frequency comb with a spectroscopic system under investigation, a short summary of the two-level atom model is given. The artificial two-level atom is, to first order, a good description of a real atomic or molecular electronic system, and is widely used e.g. as a basis for perturbation theory [162]. The two-level atom is used to numerically validate various systematic effects in the spectroscopy on ground state transitions in helium.

Let us consider an artificial atom with only two atomic states (e.g. as in [163–165]), the so called two-level atom, an electronic ground state wave function  $|g\rangle$ , with energy  $E_g$  and an electronic excited state wave function  $|e\rangle$  with energy  $E_e$ . The wave functions are orthogonal. The state of the atom is now written

$$|\psi(t)\rangle = C_g(t)e^{\frac{iE_g t}{\hbar}} |g\rangle + C_e(t)e^{\frac{iE_e t}{\hbar}} |e\rangle, \quad (2.56)$$

the state amplitudes  $C_g$  and  $C_e$  are normalised according to

$$|C_g(t)|^2 + |C_e(t)|^2 = 1, \quad (2.57)$$

which simply states that the probability of finding the atom in a superposition of the states at any given time  $t$  is 1.

The state vectors can be written explicitly as

$$|g\rangle = \begin{pmatrix} 1 \\ 0 \end{pmatrix}, \quad |e\rangle = \begin{pmatrix} 0 \\ 1 \end{pmatrix}. \quad (2.58)$$

For convenience the energy levels of this atom are chosen symmetrical around zero. The transition frequency between the levels is given as

$$\omega_0 = \frac{E_e - E_g}{\hbar}. \quad (2.59)$$

and thus the unperturbed Hamiltonian can be written as

$$\begin{aligned}\hat{H}_0 &= \frac{\hbar\omega_0}{2} \begin{pmatrix} -1 & 0 \\ 0 & 1 \end{pmatrix} \\ &= \frac{\hbar\omega_0}{2} (|e\rangle\langle e| - |g\rangle\langle g|)\end{aligned}\quad (2.60)$$

where  $|a\rangle\langle a| = \hat{P}_a$  is the projection operator of state  $a$ .

Together with the time dependent Schrödinger equation

$$i\hbar\frac{\partial\Psi}{\partial t} = \hat{H}\Psi, \quad (2.61)$$

with  $\Psi$  the position and time dependent wave function, the stage is set for interaction of a frequency comb laser signal with the two-level atom.

### 2.5.3 Optical Ramsey spectroscopy

To obtain the frequencies of helium ground state transitions with high accuracy, two pulses of a frequency comb laser were used similar to the method of Ramsey's microwave spectroscopy. In the latter case molecules fly through two regions of interaction with an oscillating magnetic field (Fig. 4 in [74]), while in optical Ramsey spectroscopy two laser pulses separated in time interact with the atom. The interaction of either a two-level system with a magnetic field or a two-level atom with an electric field belong topologically speaking to the  $SU(2)$  group [166, 167], which means that it is allowed to take the derivation of Ramsey for magnetic fields and make substitutions for interaction with an electric field.

Let a perturbation in the form of an electrical field  $\mathbf{E}(t)$ , here taken in the form  $\mathbf{E}(t) = \mathbf{E}_0 \cos(\omega t)$ , be able to change the state amplitudes through the dipole operator  $\hat{\mathbf{d}}$ , yielding an interaction Hamiltonian

$$\hat{H}' = V_{e1}(t) = -\hat{\mathbf{d}} \cdot \mathbf{E}(t). \quad (2.62)$$

The dipole operator  $\hat{\mathbf{d}}$  determines the wave function overlap of, and thus the coupling strength between the two states. In order to change the state amplitudes significantly, the frequency of the electrical field (determined by the energy  $\hbar\omega$  of the photons) should be within a small range around the transition frequency  $\omega_0$ . We take  $\hat{\mathbf{d}} \cdot \mathbf{E}_0$  to be real and substitute  $\hat{\mathbf{d}} \cdot \mathbf{E}_0 = \mathcal{V}$  in the following.

The full Hamiltonian is now written out as

$$\hat{H} = \hat{H}_0 + \hat{H}' = \begin{pmatrix} -\frac{\hbar\omega_0}{2} & -\mathcal{V} \cos(\omega t) \\ -\mathcal{V} \cos(\omega t) & \frac{\hbar\omega_0}{2} \end{pmatrix} \quad (2.63)$$

inserting in the Schrödinger equation (2.61) and explicitly writing out for ground and excited state gives

$$i\hbar \frac{\partial}{\partial t} C_g(t) e^{\frac{iE_g t}{\hbar}} = -\frac{\hbar\omega_0}{2} C_g(t) e^{\frac{iE_g t}{\hbar}} - \mathcal{V} \cos(\omega t) C_e(t) e^{\frac{iE_e t}{\hbar}} \quad (2.64a)$$

$$i\hbar \frac{\partial}{\partial t} C_e(t) e^{\frac{iE_e t}{\hbar}} = -\mathcal{V} \cos(\omega t) C_g(t) e^{\frac{iE_g t}{\hbar}} + \frac{\hbar\omega_0}{2} C_e(t) e^{\frac{iE_e t}{\hbar}} \quad (2.64b)$$

For a given input state, the time dependent Schrödinger equation with a given Hamiltonian  $\hat{H}$ , applied for a time  $\tau$  is the unitary transformation

$$|\Psi(t_0 + \tau)\rangle = e^{i\frac{\hat{H}}{\hbar}\tau} |\Psi(t_0)\rangle. \quad (2.65)$$

Ramsey [70] has derived the rotation of the initial state amplitudes  $C_g(t_0)$  and  $C_e(t_0)$  over an angle  $\theta$  after an interaction time  $t_0 + \tau$  as

$$\begin{aligned} C_g(t_0 + \tau) = & \left\{ \left[ i \cos \theta \sin \frac{1}{2} a \tau + \cos \frac{1}{2} a \tau \right] C_g(t_0) \right. \\ & \left. - \left[ i \sin \theta \sin \frac{1}{2} a \tau \cdot e^{i\omega t_0} \right] C_e(t_0) \right\} \\ & \cdot \exp \left\{ \frac{i}{2} \left[ \omega - \frac{E_g + E_e}{\hbar} \right] \tau \right\}, \quad (2.66a) \end{aligned}$$

$$\begin{aligned} C_e(t_0 + \tau) = & \left\{ - \left[ i \sin \theta \sin \frac{1}{2} a \tau \cdot e^{-i\omega t_0} \right] C_g(t_0) \right. \\ & \left. + \left[ -i \cos \theta \sin \frac{1}{2} a \tau + \cos \frac{1}{2} a \tau \right] C_e(t_0) \right\} \\ & \cdot \exp \left\{ -\frac{i}{2} \left[ \omega + \frac{E_g + E_e}{\hbar} \right] \tau \right\}, \quad (2.66b) \end{aligned}$$

where according to Ramsey [70]

$$\begin{aligned} \cos \theta &= \frac{\omega_0 - \omega}{a}, & \sin \theta &= \frac{2b}{a}, \\ a &= \sqrt{(\omega_0 - \omega)^2 + (2b)^2}, \end{aligned} \quad (2.67)$$

noting that Ramsey has defined the interaction Hamiltonian slightly different as

$$\hat{H}' = \begin{pmatrix} 0 & \hbar b e^{i\omega t} \\ \hbar b e^{-i\omega t} & 0 \end{pmatrix}, \quad (2.68)$$

using complex notation for the field.

Ramsey notes that the outcome will be that of the freely evolving wave functions of each state in case the interaction strength  $b$  is zero. The outcome of a Ramsey experiment can now be calculated by successive application of (2.66) with the result of the previous interaction inserted as the start

of the next interaction. The interactions consist of interaction for time  $\tau$  with the electric field, an field-free interaction for time  $T - \tau$  (where  $T = 1/f_{\text{rep}}$ ), and another interaction with the electric field for time  $\tau$ .

Let me shortly elaborate on the field as introduced into the equation by Ramsey [70]. We see from equation (1) in this reference that the assumption is made that the excitation field phase progresses uniformly with a frequency  $\omega$ . This is both true in the traditional microwave spectroscopy, where care has been taken to obtain an equal phase of the microwave fields in the interaction regions, and in optical spectroscopy where pulses are “cut out” of a CW laser source which is phase coherent over time  $T$ , while the frequency is varied. If the electric field of the pulses of a frequency comb source is used, the carrier has a single frequency and a fixed starting phase per pulse, and the effect of the carrier envelope offset phase shift (2.38) must be taken into account as an additional phase shift of the electric field of the second pulse. In this case the time between the pulses is being varied.

In order to come to a more contemporary notation and the description of Ramsey fringes observed in an experiment we write out the equations in matrix form while making substitutions (2.67), and substituting [165]

$$\omega_0 - \omega = \Delta, \quad \text{and } a = 2\Omega_R \quad (2.69)$$

In order to simplify the equations significantly, the Rotating Wave Approximation (RWA) is made, which excludes the fast rotating terms in the equations. A further simplification is made by the assumption that the atom is in the ground state ( $C_g(t_0) = 1, C_e(t_0) = 0$ ) before application of the first excitation period. Zinkstok [165] and Witte [121] introduce an additional phase  $\varphi$  between the pulses as well and show that the excited state amplitude after the second Ramsey pulse becomes

$$\begin{aligned} C_e(T + \tau) = \frac{2C_{e,\text{single}}}{\Omega_R} & \left\{ \cos\left(\frac{\omega T + \varphi}{2}\right) \cdot \right. \\ & \left[ \Omega_R \cos(\Omega_R \tau) \cos\left(\frac{\tau \Delta}{2}\right) + \frac{\Delta}{2} \sin(\Omega_R \tau) \sin\left(\frac{\tau \Delta}{2}\right) \right] \\ & - \sin\left(\frac{\omega T + \varphi}{2}\right) \cdot \\ & \left. \left[ \Omega_R \cos(\Omega_R \tau) \sin\left(\frac{\tau \Delta}{2}\right) - \frac{\Delta}{2} \sin(\Omega_R \tau) \cos\left(\frac{\tau \Delta}{2}\right) \right] \right\}. \quad (2.70) \end{aligned}$$

Under assumption of a low excitation rate ( $\mathcal{V} \ll \Delta, \Omega_R \approx \Delta/2$ ) the expression

for the excited state amplitude turns into

$$\begin{aligned}
C_e(T + \tau) &\approx \frac{4C_{e,\text{single}}}{\Delta} \left\{ \cos\left(\frac{\omega T + \varphi}{2}\right) \cdot \right. \\
&\quad \left. \frac{\Delta}{2} \left[ \cos^2\left(\frac{\Delta\tau}{2}\right) + \sin^2\left(\frac{\Delta\tau}{2}\right) \right] \right. \\
&\quad \left. - \sin\left(\frac{\omega T + \varphi}{2}\right) \frac{\Delta}{2} \sin(0) \right\} \\
&\approx 2C_{e,\text{single}} \cos\left(\frac{\omega T + \varphi}{2}\right)
\end{aligned} \tag{2.71}$$

yielding the equation for the transition probability  $|C_e(T + \tau)|^2$  as

$$P_{g,e} \approx 4 |C_{e,\text{single}}|^2 \cos^2\left(\frac{\omega T + \varphi}{2}\right). \tag{2.72}$$

The additional phase  $\varphi$  will in our case be  $\varphi_{\text{CEO}}$  to which, in case of the XUV spectroscopy, residual differential phase shifts on the fundamental, introduced by e.g. the amplifier, lenses and windows, are to be added.

### 2.5.4 Full repetition rate frequency comb spectroscopy

The interaction of frequency comb laser output with an atom can be viewed upon from various standpoints. One way of describing the interaction, which is commonly used, is to look at a frequency comb laser with a pulsed output field and describing the interaction with the atom in a picture in which each pulse can interfere with the atomic state vector, which then progresses at it's transition frequency in the mean time. If the carrier wave of the subsequent pulses is in phase with the transition frequency, each pulse can constructively interfere and a significant fraction of the upper state is populated after time  $t$ .

Zinkstok and Witte [168, 169] described the interaction of  $n$  pulses by the alternating application of the pulse operator  $\hat{\mathbf{M}}_{\text{pulse}}$  and the field free evolution operator  $\hat{\mathbf{M}}_{\text{free}}$  as in

$$|\psi_n\rangle = \hat{\mathbf{M}}_{\text{pulse},n} \cdot \hat{\mathbf{M}}_{\text{free}} \cdot \hat{\mathbf{M}}_{\text{pulse},n-1} \cdot \dots \cdot \hat{\mathbf{M}}_{\text{free}} \cdot \hat{\mathbf{M}}_{\text{pulse},1} |\psi_0\rangle, \tag{2.73}$$

in which the final state vector  $|\psi_n\rangle$  results from application of  $n$  pulses to the initial state vector  $|\psi_0\rangle$ . The case of only two pulses interacting with the atom, we retrieve the Ramsey signal as described in the previous section.

In the approximation of a weak interaction, the upper state population for an  $N$  pulse interaction can be derived [168, 169] as

$$|C_{e,N}|^2 = N^2 |C_{e,\text{single}}|^2 \left| \sum_{n=0}^{N-1} e^{in(\omega T + \varphi)} \right|^2. \tag{2.74}$$

Note that the excitation probability is linear in the intensity,  $I = |\mathbf{E}|^2$ , of the field used in the excitation. Witte proves that this equation can be regarded exact in the parameter range for the XUV spectroscopy on helium described in Chapter 6.

Another way of describing the interaction is that of an array of CW lasers all with their own spectral phase  $\varphi_m$  and a certain detuning from the transition frequency. The interaction of each frequency comb mode with the two-level atom leads to Rabi oscillations, that interfere to yield the final atomic inversion after an excitation time  $t$ . Time  $t$  can be limited by various factors, e.g. atoms moving through the beam or a trap time of an atomic ensemble [170, 171].

## 2.6 Direct frequency comb spectroscopy in the XUV

A frequency comb can be converted to shorter wavelengths using methods like frequency doubling and sum frequency mixing. The wavelength limit for these processes, in which one typically uses non-linear crystals, lies around 200 nm (BBO), although crystals with high non-linear index and transparency at lower wavelengths like KBBF and CBBF are being developed in China [172–174]. For even shorter wavelengths, one can use harmonic-generation or frequency mixing in gas sources, although the non-linear harmonic yield will decrease rapidly for higher orders. A special technique makes it possible to go to even shorter wavelengths and is called High-order Harmonic Generation (HHG) [175, 176].

At the time of writing, two methods for frequency comb generation in the extreme ultraviolet (XUV) are available that can generate enough XUV light for use in spectroscopic applications. The first method, used by the author, uses an optical parametric amplifier (OPA) to amplify pulses of a Ti:Sapphire frequency comb laser to the mJ level. Amplification in the OPA has a phase stability that is high enough to use in time-domain Ramsey spectroscopy [69, 177]. This method has led to, in our knowledge, the first direct frequency comb spectroscopy in the XUV region (wavelengths well below 100 nm) on the  $1s^2\ ^1S_0 - 1s\{4,5\}p\ ^1P_1$  transitions in neutral helium around 51.5 nm [155, 178]. Subsequently it was shown (see Chapter 5) that this method is not limited to a narrow wavelength range, but can be applied over a large range of wavelengths at several harmonic orders [179].

This technique was developed further by Jonas Morgenweg, who implemented variable delay double-pulse amplification [180]. In this case pulses can be amplified at multiples of the comb repetition time, without affecting the phase of the pulses (at a few mrad level). This means that not only one, but a series of Ramsey signals can be obtained for a wide range of time delays. Therefore this method is now called the “Ramsey-comb spectroscopy” [181, 182]. Because the phase shift (e.g. due to the OPCPA) is constant, it drops out of the analysis of the signals, leading to a strongly improved accuracy. Moreover, due to the increased time delay  $T$  now possible, the ac-

curacy also improves proportionally to this delay. More details can be found in [181, 182].

However, with this technique difficulties can arise due to phase deviations introduced in the HHG process by ionisation of the medium. In that case the phase shift is possibly not constant as a function of delay  $T$ . It is expected that this can be solved by using pulses spaced by more than  $\sim 150$  ns since the ionised gas sample is replaced completely with a non-ionised sample due to the pulsed gas beam.

The second method capable of producing enough XUV for spectroscopic applications [183] is based on the amplification of a full repetition rate frequency comb and subsequent intensity amplification by use of an enhancement cavity. A gas jet is placed in the focus of the enhancement cavity to enable HHG in the steady state plasma. The generated XUV can be coupled out of the cavity by means of a grating or a mirror with a centred hole [183–185].

### 2.6.1 High-order harmonic generation

Frequency conversion from the IR to the extreme ultraviolet (XUV), can be obtained through a high-order harmonic generation (HHG) process. To this end the amplified frequency comb laser beam is focused in a noble gas jet to produce a frequency comb at various harmonics of the fundamental frequency.

Most of the properties of the spectra generated during HHG can be understood by the so called “simple man’s model” or three step model proposed by Corkum [175]. A quantum mechanical description was then given by Lewenstein [176] confirming the appropriateness of the three step model. Seres [186] developed an extension to the model, which further explains unpredicted behaviour seen in some experiments as signs of parametric amplification, due to the transverse components of the electron current induced by the laser radiation.

In the “simple man’s model” the HHG process occurs in three steps (see Fig. 2.3). Due to the presence of the strong electrical laser field, the atomic potential is modified significantly, and an electron (actually an electron wave packet) can tunnel out of the atomic potential (step 1). The electron, now no longer bound to the atomic core, is accelerated away from and then back to the atomic core due to the strong electric field of the laser (step 2). The electron thereby gains energy due to the work done by the electric field. If the electron, on its re-encounter with the atom, recombines with the atomic core, the excess energy can be released as a high-energy (short wavelength) photon (step 3). Due to the fact that the whole process is driven by the electric field of the laser and energy is conserved, the generated radiation is coherent with the driving field.

The excess energy of the electron upon recombination can in most cases be expressed by the particularly simple equation (see [176])

$$U_{\text{excess}} \simeq 3.17U_p + 1.32I_p \quad (2.75)$$

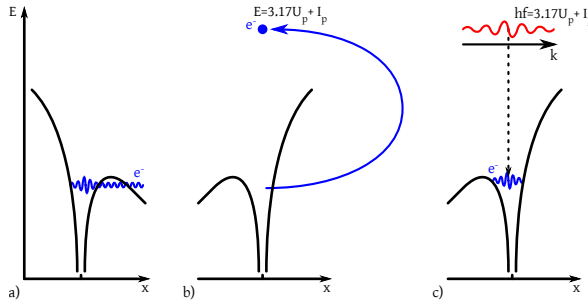


Figure 2.3: Illustration of the three steps in the high-order harmonic generation process. a) An electron tunnels out of the atomic core because of the deformed atomic potential caused by the driving field. b) The electron (now treated as a classical particle) is accelerated by the electrical field of the driving wave, it ends up with a certain excess energy at the position of the atom. c) The electron recombines. A high energy photon of  $\hbar\omega = 3.17U_p + I_p$  (depicted in red) is released due to conservation of energy.

where  $U_p$  is the ponderomotive energy and  $I_p$  is the ionisation potential of the atom, which is valid when  $I_p \ll U_p$ . The ponderomotive energy is given by

$$U_p = \frac{E^2}{4\omega^2} \quad (2.76)$$

and depends on the electrical field strength  $E$  and the angular frequency  $\omega$  of the light field. Only odd harmonics are generated due to the isotropic nature of the medium (typically a noble gas) in which HHG is performed. The first few harmonics rapidly decrease in intensity with harmonic order. These harmonics can still be described by the classical perturbative approach based on non-linear susceptibilities. Next a plateau region, where all harmonics have an almost equal intensity, extends up to  $U_{\text{excess}}$ . Higher harmonics fall off in intensity quickly. This curve is schematically depicted in Fig. 2.4.

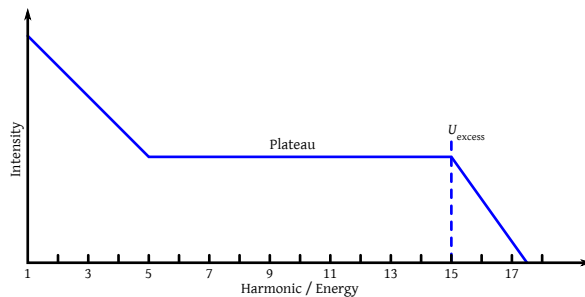


Figure 2.4: A sketch of a HHG spectrum, the line gives the intensity for the harmonics, but each harmonic need not have a wide spectrum, e.g. in the XUV spectroscopy experiments the spectral width of a harmonic order is typically between 6 nm for the fundamental and 0.1–0.2 nm for the cut-off harmonic at  $U_{\text{excess}}$  and is thus much narrower than the inter-harmonic spacing.

In particular the fact that the HHG process is highly coherent, means that a frequency comb at the fundamental frequency gets transferred to each of the harmonic orders  $M$  as

$$f_n = Mf_{\text{CEO}} + nf_{\text{rep}}, \quad (2.77)$$

where it is noted that the frequency spacing between the comb modes is not dependent on the harmonic order, but the offset frequency has changed. That  $f_{\text{rep}}$  should be independent of the harmonic order can be understood by realising that the pulse repetition rate at the harmonic order is not changed by the HHG process. However the carrier offset for each harmonic is multiplied by the harmonic order solely due to the fact that the phase of the generated harmonic evolves at  $M$  times the speed of the fundamental, which implies that the phase offset with respect to the envelope is shifted  $M$  times faster (illustrated in Fig. 2.5).

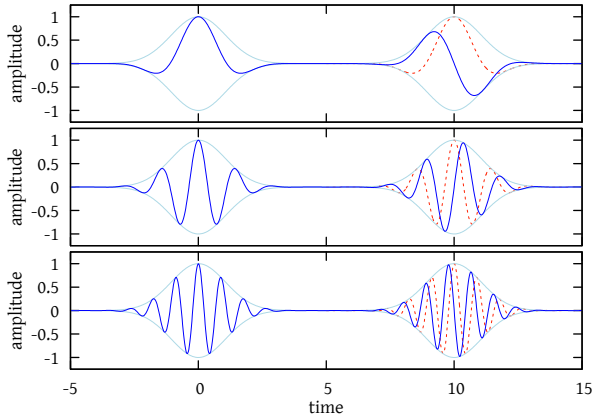


Figure 2.5: An illustration of the carrier envelope offset phase of the fundamental and the third and fifth harmonic. Time and amplitude are in arbitrary units. With the carrier envelope offset phase  $\Delta\varphi = 0.5\pi$  it is conveniently seen (note the flank of the carrier at the centre of the second pulse) that at the fundamental (top) the phase slip is 0.25 cycles, at the third harmonic (centre) it is 0.75 cycles and at the fifth harmonic (bottom) it is 1.25 which is equivalent to 0.25 cycles. The dotted insets shows the carrier of the first pulse in the second pulse.

The description of the ionisation step has been well established. Perelomov [187] and Ammosov [188] extend the seminal article about strong field ionisation by Keldysh [189] for AC electrical fields. Reiss (e.g. [190]) has done extensive work in this field as well.<sup>15</sup> Lewenstein [176], whom I will closely follow in presenting the basic theory behind HHG, restricts his treatment to a regime where the Keldysh parameter  $\gamma = \sqrt{I_p}/2U_p$  is smaller than one and where  $I_p$  is much larger than the photon energy  $\hbar\omega$ . Moreover  $U_p$  is comparable to, or larger than  $I_p$ , but  $U_p$  is still lower than the saturation level  $U_{\text{sat}}$

<sup>15</sup>An overview of the state of the field of above-threshold ionisation not long before Lewenstein can be found in [191].

where all atoms are ionised. This is exactly the regime used in the HHG generation in the XUV spectroscopy.

Starting with the time-dependent Schrödinger equation (2.61) with a potential function existing of the atomic core potential  $V_a(\mathbf{r})$  and a time dependent dipole potential (in atomic units, energy in units of photon energy)

$$V = V_a(\mathbf{r}) - \mathbf{r}E_0 \cos(\mathbf{k}\mathbf{r} - \omega t)\hat{\mathbf{x}}, \quad (2.78)$$

where  $E_0 \cos(\mathbf{k}\mathbf{r} - \omega t)\hat{\mathbf{x}}$  is the electrical field polarised in the  $x$  direction, the Schrödinger equation for the active electron is written out in the length gauge ( $\mathbf{k}\mathbf{r} \gg a_0$  with  $a_0$  the Bohr radius) as

$$i\frac{\partial}{\partial t}\Psi(\mathbf{r}, t) = \left(-\frac{1}{2}\nabla^2 + V_a(\mathbf{r}) - xE_0 \cos(\omega t)\right)\Psi(\mathbf{r}, t). \quad (2.79)$$

The wave vector  $\Psi$  consists of the (typically spherical) atomic ground state  $|0\rangle$  and kinetic momentum states  $|\mathbf{v}\rangle$  in the continuum. The core potential influence on the free electron and the coupling between bound states are neglected. The coupling between continuum states  $\langle\mathbf{v}|\mathbf{r}|\mathbf{v}'\rangle$  can partially be treated exactly [176]. The coupling between the ground state and a kinetic momentum state is given by the dipole matrix element

$$\mathbf{d}(\mathbf{v}) = \langle\mathbf{v}|\mathbf{r}|0\rangle. \quad (2.80)$$

The wave vector can now be written as

$$|\Psi(t)\rangle = e^{i\mu t} \left( a(t)|0\rangle + \int b(\mathbf{v}, t)|\mathbf{v}\rangle d^3\mathbf{v} \right), \quad (2.81)$$

where  $a(t) \simeq 1$  is the ground state amplitude and  $b(\mathbf{v}, t)$  the momentum state amplitudes. The Schrödinger equation can then be expressed in  $b(\mathbf{v}, t)$  and a solution found. Via introduction of a canonical momentum  $\mathbf{p} = \mathbf{v} - \mathbf{A}(t)$  with a vector potential  $\mathbf{A} = -E \sin(t) \cdot \hat{\mathbf{x}}$  and reducing the dipole matrix element to the  $x$  direction as  $\mathbf{d}(\mathbf{v}) \cdot \hat{\mathbf{x}} = d_x(\mathbf{v})$ , the equation for the  $x$  component of the time-dependent dipole moment  $x(t)$  (remember we work in a.u.) can be found as

$$\begin{aligned} x(t) = i \int_0^t dt' \int d^3\mathbf{p} \quad & E \cos(t') d_x(\mathbf{p} - \mathbf{A}(t')) \\ & \times d_x^*(\mathbf{p} - \mathbf{A}(t)) e^{-iS(\mathbf{p}, t, t')} \\ & + c.c., \quad (2.82) \end{aligned}$$

where  $d_x^*$  is the complex conjugate of  $d_x$  and

$$S(\mathbf{p}, t, t') = \int_t^{t'} \left( \frac{|\mathbf{p} - \mathbf{A}(t)|^2}{2} + I_p \right) dt'', \quad (2.83)$$

is the quasi-classical action.

Lewenstein interprets Eq. 2.82 in the following way. The term  $E \cos(t') d_x(\mathbf{p} - \mathbf{A}(t'))$  is the probability for the electron to appear in the continuum. The term  $e^{-iS(\mathbf{p}, t, t')}$  is a phase gained by the dipole with respect to the driving field due to the quasi-classical action while the electron is in the continuum. After it's roundtrip the electron recombines with the atom with an amplitude  $d_x^*(\mathbf{p} - \mathbf{A}(t))$ .

The gradient of the action with respect to the momentum equals the difference in position of the electron before and after the action took place. The stationary points of the action are thus

$$\nabla_{\mathbf{p}} S(\mathbf{p}, t, t') = \mathbf{r}(t) - \mathbf{r}(t') = 0, \quad (2.84)$$

which means that an electron leaving the atom at place  $\mathbf{r}$  is re-colliding with the atom at this same position. The electron is expelled into the continuum only in the vicinity of the atom and can only recombine in the vicinity of the atom, where vicinity roughly coincides with  $a_0$ , the Bohr radius.

Introducing the return time of the electron to the core as  $\tau = t - t'$  the integral of (2.82) can be solved by means of a saddle-point method. The stationary values of canonical momentum  $\mathbf{p}_{\text{st.}}$  and quasi-classical action  $S_{\text{st.}}(t, \tau)$  are

$$\mathbf{p}_{\text{st.}}(t, \tau) = \frac{E(\cos(t) - \cos(t - \tau))}{\tau} \quad (2.85)$$

and

$$\begin{aligned} S_{\text{st.}}(t, \tau) &= \frac{1}{2} \int_{t-\tau}^t dt'' (\mathbf{p}_{\text{st.}} - \mathbf{A}(t''))^2 \\ &= (I_p + U_p)\tau - 2U_p \frac{(1 - \cos(\tau))}{\tau} - U_p C(\tau) \cos(2t - \tau) \end{aligned} \quad (2.86)$$

with

$$C(\tau) = \sin(\tau) - \frac{4 \sin^2(\tau/2)}{\tau}. \quad (2.87)$$

The value  $2|C(\tau)|$  (Fig. 2.6) is the quantum equivalent of the kinetic energy gain ( $\Delta E_{\text{kin}}/U_p$ ) in the classical approach. This equation in essence shows the energy gain for electron paths of duration  $\tau$ .

Note that electrons can be out for several periods of the driving field. Upon each encounter with the parent ion, the electron can either recombine and produce harmonic radiation, or be scattered to a permanently ionised state (in which case it is lost for the HHG process). Another factor is diffusion processes that cause the wave function of long living electrons to spread out spatially, reducing the overlap with the core, so that they are effectively lost to the HHG process. The stationary point of the quasi classical action lies exactly there where electrons appear in the continuum with zero velocity.

In practice, radiation of two paths will be seen, the so called short ( $0 < \tau < \tau_{\text{peak}}$ ) and long path ( $\tau_{\text{peak}} < \tau < 2\pi$ ). From Eq. (2.87) it is also seen that

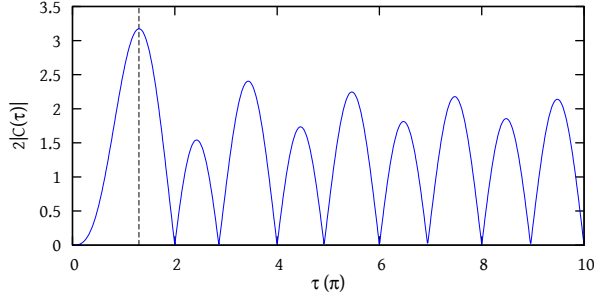


Figure 2.6: Graphical representation of  $2|C(\tau)|$ . It is seen that the function  $C(\tau)$  has its first minimum for  $\tau = 2\pi$ , which means that this is a minimum for the action  $S_{st.}(t, \tau)$ . Therefore the quantum paths contributing to the highest harmonics (highest value of  $C(\tau)$ ) have return times smaller than  $2\pi$ . Electron trajectory paths left of the dashed line are called “short” paths and to the right (up to  $2\pi$  for the energy maximum) “long paths”. The short and long paths join at the maximum excess energy  $2|C(\tau)| \approx 3.17$ .

there is only one return time, and thus one quantum path, at  $\tau_{\text{peak}} \approx 4.08$  where the emitted radiation has the highest energy as given by Eq. (2.75). For this return time the short and long quantum path join. Radiation generated by the short and long path show a different spatial distribution in the plane perpendicular to the propagation axis of the fundamental. Radiation generated from the short path is more collimated than radiation from the long path.

### 2.6.2 Intensity dependent phase shift of generated harmonics

The carrier phase of the generated harmonic radiation can be related to the long and short paths taken by the electrons in the HHG process [175, 176, 192–194]. The phase accumulated over such a path depends on the Gouy phase and the classical action integral  $S(\mathbf{p}, t, t')$  of the electron [192–194] and is therefore intensity dependent. The phase stability of the generated harmonic radiation thus depends on the intensity stability of the fundamental.

Lewenstein [193] shows that the intensity dependent phase of the generated harmonics can be approximated by a piecewise linear function while Salieres [192] describes the position dependent properties of the HHG process. The phase is most stable for harmonics generated in the region behind the focus, where phase matching favours the short path. It is in this region in the laser beam that frequency chirp due to the intensity dependence on the generated harmonic radiation is minimal.

The phase of the emitted XUV beam can, for the higher harmonics, be approximated by a linear relationship between the intensity of the fundamental and the phase of the harmonic generated [192–194], which is in essence equal to the atomic dipole phase. Corsi [194] has modelled and measured these phase coefficients for various intensities and noble gasses using the equation

$$\varphi_q^{ls}(r, t) = -\alpha_q^{ls} I(r, t) \quad (2.88)$$

where  $\alpha_q^{l,s}$  is a coefficient depending on the harmonic order  $q$  and the long or short quantum path, and  $I(r, t)$  is the intensity of the fundamental laser pulse. Since the coefficients  $\alpha$  are correlated to the return time of the electrons, the coefficients of the long and short paths will be equal for the harmonics generated at the cutoff. In practice, one can choose the phase matching conditions in the HHG such that either the long or short free electron path is favoured or such that harmonics on both paths are generated.

We have used these measured values to derive estimates of the phase stability of the HHG process used in atomic spectroscopy described in chapter 5.

### 2.6.3 Direct frequency comb spectroscopy in the XUV

We have applied the method of high-order harmonic generation to create an XUV frequency comb laser. As mentioned, the HHG process is coherent. If we use the pulses from a frequency comb laser as a driving field for HHG, the higher order harmonics have a fixed phase relation to the driving pulse. However, the peak intensity for HHG needs to be in the order of  $10^{14}$  W/cm<sup>2</sup>, and this means the output of a frequency comb laser needs significant amplification to be able to drive this process.

Witte and Zinkstok [121, 165] have built an optical parametric amplifier system that could amplify single few-cycle pulses from a pulse train emitted by a traditional Ti:Sapphire frequency comb laser to TW peak power (mJ pulse energy). The frequency comb laser that was used had a  $f_{\text{rep}}$  in the order of 100–200 MHz, while the amplifier amplified single pulses at a rate of about 30 Hz. Later, Renault [195], Kandula [196] and Gohle [155] modified this setup for relatively narrow band but phase stable amplification of pulse pairs (two consecutive pulses from the frequency comb seed laser) for Ramsey frequency comb spectroscopy.

This laser system, of which the details have been described elsewhere [121, 165, 195, 196], has been the basis for spectroscopy of ground state transitions in helium (Chapter 6) and the demonstration of the wide wavelength range this system can cover (Chapter 5) using various HHG gas targets like xenon and krypton.

The actual spectroscopy takes place in a crossed beam experiment, as shown in Fig. 2.7. After excitation of the atom with two frequency comb pulses, the excited state population is measured via ionisation of the excited atoms and detection of the ion signal by a channel electron multiplier tube on top of a time-of-flight mass spectrometer.

The relative XUV intensity in the excitation harmonic of the spectroscopy pulses is determined by analysis of the HGG radiation with an XUV monochromator and a photon multiplier tube. The full methodology has been described by Kandula [178, 196]

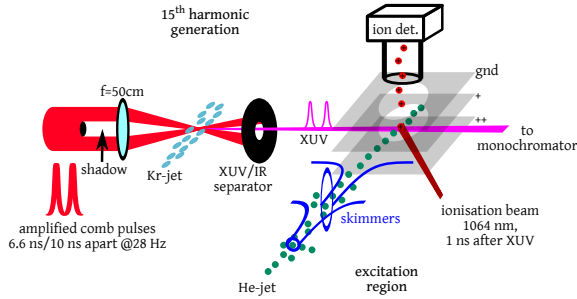


Figure 2.7: Overview of the HHG generation and XUV spectroscopy in a crossed beam experiment. The high-order harmonic generation takes place where the fundamental is focused in a gas jet. The phase matching is optimised for the generation of short-path harmonics. The XUV is separated from the fundamental by use of an aperture, in the image plane of a centred circular beam block placed in front of the focusing lens. The XUV radiation is then crossed with a skimmed helium beam and an ionisation beam (left over of the fundamental of the OPA pump system). Excited atoms are ionised and extracted in a time-of-flight mass spectrometer and ion counting system.

## 2.7 The helium atom

With the advent of quantum mechanics, the electronic properties of atoms could be described more accurately than by use of classical laws of electrodynamics (the “planetary” model [197], where electrons circulate around a nucleus). The quantum mechanical description of atoms was a major breakthrough, followed by another breakthrough when quantum electrodynamics (QED) theory was first applied in the late 1950s.

Unlike the hydrogen atom, helium cannot be described fully analytically. One needs to rely on perturbation theories in the mathematical approximation of the atomic properties. This is one reason why helium is such an interesting system. Continuously increasing accuracy of spectroscopic experiments has been the main driving force behind improvements in theoretical description of matter, leading to the development of quantum mechanics and field theories like QED. Another interesting aspect of helium is that it has two stable isotopes,  $^4\text{He}$  and  $^3\text{He}$ . A comparison of experimental outcomes can tell something about e.g. the nuclear size difference (charge radius).

In this section we recall some of the basics about the calculation of the electronic levels in helium. An extensive treatment of QED theory for helium unfortunately goes beyond the scope of this thesis.

The treatment of the helium atom would be trivial if it could be approximated as two electrons moving in the central field of the nucleus, without interaction with each other. In this case the Hamiltonian becomes a two electron version of the hydrogen Hamiltonian and is written

$$H = \sum_{i=1}^n \left( \frac{\mathbf{p}_i^2}{2m_e} - \frac{Ze^2}{4\pi\epsilon_0 r_i} \right) \quad (2.89)$$

with  $n = 2$  for the number of electrons in helium, and the proton number

$Z = 2$  which accounts for the core charge of helium. The wave function would in this case be a simple multiplication of the wave functions of hydrogen [198]

$$\psi = \prod_{i=1}^2 \psi_{n_i, l_i, m_i}(\mathbf{r}_i). \quad (2.90)$$

There are two problems with this approach, one, the electron is a fermion, in which case the wave function of the two-electron system must be antisymmetric, and two, the potential seen by one of the two electrons does not only include the core, it also includes the other electron.

The antisymmetric nature of the wave function gives rise to the existence of a spin singlet–triplet system of levels. Helium is special in the sense that these systems are almost completely decoupled for the lowest atomic levels. Helium is said to have an almost pure spin-orbit, or *LS*, coupling, which reflects itself in the notation of the atomic state (appendix A.6). This gives rise to very narrow transitions between these systems and makes that the lowest lying state of the triplet system has a lifetime of about  $8 \times 10^3$  seconds before it decays to the ground state via spontaneous emission. This type of long lived states are called metastable.

The electron – electron interaction can be treated as a perturbation on the non interacting system, which will shift the ground state energy to first order from  $-108.8$  eV (two times an electron bound to a  $2e$  charged core) by about 34 eV, without taking “screening” of the core potential by one electron “perceived” by the other electron into account. The first order perturbation calculation for the electron – electron interaction in the non-degenerate approximation uses the electron – electron potential

$$V_p = \frac{e^2}{4\pi\epsilon_0 |\mathbf{r}_1 - \mathbf{r}_2|} \quad (2.91)$$

where the energy of state  $k$ ,  $E_k$  is written as (see e.g. [199])

$$E_k^{(1)} = E_k^{(0)} + \langle \psi_k^{(0)} | V_p | \psi_k^{(0)} \rangle \quad (2.92)$$

with  $E_k^{(0)}$  the energy and  $\psi_k^{(0)}$  the wave function of the unperturbed state  $k$ . The first order energy shift for the electron – electron interaction in helium then yields

$$\begin{aligned} \Delta E_k^{(1)} &= E_k^{(1)} - E_k^{(0)} \\ &= \langle \psi_{100} | \langle \psi_{100} | \frac{e^2}{4\pi\epsilon_0 |\mathbf{r}_1 - \mathbf{r}_2|} | \psi_{100} \rangle | \psi_{100} \rangle \\ &\approx 34\text{eV}. \end{aligned} \quad (2.93)$$

where  $|\psi_{100}\rangle |\psi_{100}\rangle$  is the unperturbed ground state wave function according to equation 2.90.

The wave function  $\psi_k^{(1)}$  (with first-order correction) can now be reconstructed as [199]

$$\psi_k^{(1)} = \psi_k^{(0)} + \sum_{j \neq k} \frac{\langle \psi_j^{(0)} | V_p | \psi_k^{(0)} \rangle}{E_k^{(0)} - E_j^{(0)}} \psi_j^{(0)}. \quad (2.94)$$

This wave function is used to obtain the energy shift for the second-order perturbation

$$\Delta E_k^{(2)} = E_k^{(2)} - E_k^{(1)} = \sum_{j \neq k} \frac{\langle \psi_j^{(0)} | V_p | \psi_k^{(0)} \rangle}{E_k^{(0)} - E_j^{(0)}} \langle \psi_k^{(0)} | V_p | \psi_j^{(0)} \rangle, \quad (2.95)$$

which can be used again to calculate the second-order correction to the wave function.<sup>16</sup>

Surprisingly this approach of adding perturbations to the non-relativistic Schrödinger equation is still useful for the most accurate calculations on helium today. This is because there are no bound state solutions of the fully relativistic Dirac equation for helium. Modern approaches to approximate the energies of the states of helium and helium-like systems with high-accuracy will however start off with the time independent three-body Schrödinger equation

$$\left[ \frac{1}{2M} \mathbf{p}_N^2 + \sum_{i=1}^2 \left( \frac{\mathbf{p}_i^2}{2m_e} - \frac{Ze^2}{4\pi\epsilon_0 |\mathbf{r}_N - \mathbf{r}_i|} \right) + \frac{e^2}{4\pi\epsilon_0 |\mathbf{r}_1 - \mathbf{r}_2|} \right] \psi = E\psi, \quad (2.96)$$

which takes into account the shift of the centre of mass of the system due to the electron positions.

An approximation of the energy eigenvalues of this system can be given by the use of the Rayleigh-Ritz variational principle, with a suitable basis-set of trial functions, e.g. the Hylleraas basis set [200,201] proposed in 1928. The level energies can then be computed using

$$E_{\text{tr}} = \frac{\langle \psi_{\text{tr}} | H | \psi_{\text{tr}} \rangle}{\langle \psi_{\text{tr}} | \psi_{\text{tr}} \rangle}, \quad (2.97)$$

with  $\psi_{\text{tr}}$  the trial wave functions for the Hamiltonian  $H$ . The level energies thus found are but a start, corrections are computed for, among others, relativistic effects like fine structure and finite mass and e.g. higher-order spin

<sup>16</sup>The first- and second-order perturbation theory are used to derive equations for the Zeeman and Stark shifts of the electronic states of a two-level atom in Sec. 2.8, and are then calculated for ground state transitions in helium in Chapter 6.

dependent terms. The anomalous magnetic moment of the electrons and other quantum electrodynamic (QED) corrections are of particular interest. Such shifts are commonly known as the Lamb shift<sup>17</sup>, after Willis Eugene Lamb who measured these shifts for the first time on the 2S–2P transition in hydrogen. The QED corrections describe the influence of vacuum fluctuations on the atom.

In order to understand this influence we need the Heisenberg uncertainty principle [202] in quantum mechanics. The uncertainty principle states that the position  $q$  and momentum  $p$  of a particle can not be accurately measured at the same moment in time due to the noncommuting nature of observables in the Schrödinger equation. The product of the measured standard deviations ( $\Delta$ ) of the two conjugate quantities like position and momentum always relates as

$$\Delta q \Delta p \geq \frac{\hbar}{2}. \quad (2.98)$$

or for energy ( $E$ ) and time ( $t$ )

$$\Delta E \Delta t \geq \frac{\hbar}{2}. \quad (2.99)$$

The latter relation states that on short timescales (having a small  $\Delta t$ ) the energy of a system has a sizeable uncertainty.

Einstein has shown the equality of energy and mass (the famous  $E = mc^2$ ). The latter means that particles of a certain energy or mass are allowed to come into existence for a certain time (as long as  $\Delta E \Delta t < \hbar/2$ ), without violating the conservation law of energy. These are so called virtual particles, or vacuum fluctuations. It is Feynman who introduced a particularly simple way of describing the interactions between charged particles, the domain of QED, by means of diagrams that now bear his name. Note that for all interactions the common conservation laws hold.

Of these quantum electrodynamic processes the electron self-energy and the so called vacuum polarisation terms yield the largest contributions to the level energies of an atomic system. Feynman diagrams for these two terms are given in Fig. 2.8.

The self energy of the electron is given by creation and annihilation of a virtual photon, which gives momentum kicks to the electron upon creation and annihilation. The resulting motion gives an effective size to the otherwise point-like electron. This effective electron size reduces the interaction of the electron with the nucleus slightly compared to that of an ideal point-like particle. Because the normal way of solving the Schrödinger equation does not include this effective size of the electron, it can be included by treating it as a perturbation and it gives rise to a shift of the atomic energy levels.

In the same way the vacuum polarisation, in which a virtual photon converts into a virtual electron – positron pair that forms a dipole that shields

---

<sup>17</sup>The Lamb shift includes the relativistic shifts.

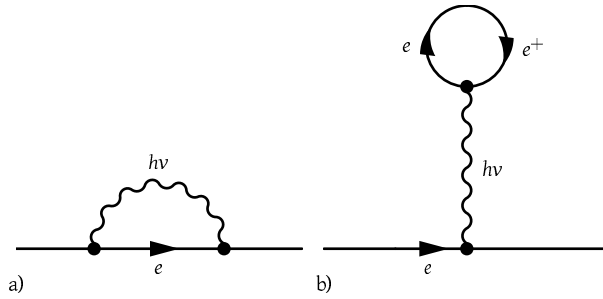


Figure 2.8: Feynman diagrams for the lowest order QED contributions. a) The electron self energy. b) The vacuum polarisation. Lines represent particles with mass, wiggly lines represent photons, dots interaction points, while the interaction sequence takes place in the order left to right.

in part the electrical interaction between the electron and the nucleus, gives rise to a shift in the atomic energy levels. Both effects are largest when the electron interacts stronger with the nucleus. This is the case in the *s* states (see A.6), especially those with the lowest principle quantum number. QED effects quickly decrease with higher principle quantum numbers and for higher orbital angular momentum states, since the probability of the electron to be inside the nucleus quickly decreases in these cases.

Contribution	Magnitude	Relative magnitude
Nonrelativistic energy	$Z^2$	1.0e+00
Mass polarization	$Z^2 \mu / M$	1.4e-04
Second-order mass polarization	$Z^2 (\mu / M)^2$	1.9e-08
Relativistic corrections	$Z^4 \alpha^2$	2.1e-04
Relativistic recoil	$Z^4 \alpha^2 \mu / M$	2.9e-08
Anomalous magnetic moment	$Z^4 \alpha^3$	1.6e-06
Hyperfine structure	$Z^3 g_I \mu_0^2$	9.5e-12
Lamb shift	$Z^4 \alpha^3 (\ln \alpha) + \dots$	-7.6e-06
Radiative recoil	$Z^4 \alpha^3 (\ln \alpha) \mu / M$	-1.0e-09
Higher order QED	$Z^5 \alpha^4 + \dots$	2.3e-08
Finite nuclear size	$Z^4 \langle \bar{r}_c / a_0 \rangle^2$	4.0e-09

Table 2.2: Relative magnitude of the various contributions of Table 1 in Drake *et al.* [203], relative to the Nonrelativistic energy (for  $Z = 2$ ). Because these values only indicate the size of the effects only two digits are displayed.

In order to get a feeling for the size of the various contributions to the total atomic energy in helium, the size of the various contributions of Table 1 of Drake [203] are displayed relative to the nonrelativistic energy of the atom in Table 2.2. Table 2.3 shows calculated correction values from Drake’s [203] Table 3 and 4 for the lowest levels of helium. This table contributes to an easy understanding of the order of magnitude of the various effects for the spectroscopist.

Contribution	$1^1S_0$	$2^1S_0$	$2^1P_1$
$\mu c^2 \alpha^2$	-5 945 405 676.717	-960 331 428.608	-814 736 669.940
$\mu c^2 \alpha^2 (\mu/M)_{\text{mp}}$	143 446.256	8 570.430	41 522.201
$\mu c^2 \alpha^2 (\mu/M)_{\text{mp}}^2$	-58.146	-16.772	-20.800
$\mu c^2 \alpha^4$	16 901.706	-11 969.811(1)	-14 022.122
$\mu c^2 \alpha^4 (\mu/M)_{\text{ms}}$	-154.761	-14.832	-8.509
$\mu c^2 \alpha^4 (\mu/M)_{\text{mp}}$	53.370	9.845	3.775
$\Delta E_{\text{nuc}}$	29.70(3)	1.995(2)	0.064
$\Delta E_{\text{QED}}$	41 284(36)	2 809.9(1.7)	48.0(1.0)
Total	-5 945 204 175(36)	-960 332 037.9(1.7)	-876 106 246.8(1.0)

Table 2.3: Contributions to the level energy according to Drake *et al.* [203]. Energies are given in MHz, multiplication with Plancks constant  $h$  gives the exact level energy. Contributions are: Non-relativistic reduced mass isotope shift  $\mu c^2 \alpha^2$ , nonrelativistic first order mass polarization correction  $\mu c^2 \alpha^2 (\mu/M)_{\text{mp}}$ , nonrelativistic second-order mass polarization correction  $\mu c^2 \alpha^2 (\mu/M)_{\text{mp}}^2$ , lowest order relativistic corrections  $\mu c^2 \alpha^4$ , relativistic finite mass correction due to mass scaling  $\mu c^2 \alpha^4 (\mu/M)_{\text{ms}}$ , relativistic finite mass correction due to mass polarization  $\mu c^2 \alpha^4 (\mu/M)_{\text{mp}}$ , finite nuclear size correction  $\Delta E_{\text{nuc}}$  and quantum electrodynamics shift  $\Delta E_{\text{QED}}$  up to largest contributions of order  $\mu c^2 \alpha^6$ .

A comprehensive overview of theoretical and calculational techniques for derivation of atomic energies are given in various chapters of [204] and more background can be obtained from the references therein. More recent theoretical developments can be found in [88, 205–208] in which e.g. QED perturbations have been fully calculated up to the sixth order of alpha [88]. A partial historical overview of measured and calculated ground state energies of helium is given in appendix B.

## 2.8 Systematic effects in atomic spectroscopy

In this section the theoretical basis used to calculate systematic effects that are present during the spectroscopic determination of the ground state energy of helium (Chapter 6 and its appendix) are recalled. In section 2.5.2 and 2.5.3 the two-level atom and atomic dipole transitions were introduced as a model atomic system. These approximations are a good approximation of a real atomic system like helium and can therefore be used to calculate various perturbations (systematic effects) that can occur in atomic systems during spectroscopic measurements.

### 2.8.1 Stark effect

Due to the presence of electrical fields during optical excitation of an atom, the atomic levels are shifted in energy. This is termed the Stark effect, since it was first observed by Stark [209] and experimentally treated by Epstein [210] in the old quantum theory. A treatment of the Stark effect in the new quantum theory [12] has been given by, among others, Schrödinger, Pauli and Epstein [211–213].

The presence of DC and AC electrical fields in our experiments, e.g. remnants of the extraction fields in the interaction zone, stray light and the excitation lasers (especially true in the case of Raman excitation), will cause energy shifts of the atomic states. Since these shifts can not always be determined experimentally by varying the laser intensity, it is useful to calculate these shifts in order to have a theoretical estimate, which can be compared to the experimental uncertainties.

The calculation of the DC and AC Stark shift, will loosely follow the books of Hertel [162] (from §8.5) and Sobelman [214] (from §7.1).

### The DC Stark effect

The induced dipole moment for a homogeneous electrical field, setting  $\mathbf{E} \parallel z$  which defines a quantization axis  $z$  on the atom, and given a radial potential and a single “Leuchtelektron”, is conveniently written in spherical coordinates as

$$H'(\mathbf{r}, t) = V_{\text{el}}(r, \theta, \varphi) = e\mathbf{r} \cdot \mathbf{E} = eErC_{10}(\theta, \varphi) = eErC_{10}(\theta), \quad (2.100)$$

with  $C_{10}(\theta, \varphi)$  the normalised spherical harmonic, there is no dependence of  $V_{\text{el}}(\mathbf{r})$  on  $\varphi$ .

Depending on the size of the perturbation we can distinguish linear and quadratic Stark effects. If the perturbation is much larger than the non-Coulomb part of the effective potential ( $\langle V_{\text{el}} \rangle \gg \langle V_{\text{nc}} \rangle$ ) in a multi-electron system the external electrical field will lift the L-degeneracy resulting in a linear Stark effect. If on the other hand, the non-Coulomb potential has already lifted the L-degeneracy ( $\langle V_{\text{nc}} \rangle \gg \langle V_{\text{el}} \rangle$ ), an additional external electrical field will have no effect in first order and will result in a quadratic Stark effect [215]. The latter is the case in helium.

The second-order DC Stark shift can be written (see section A.5) as

$$\Delta E_k^{(2)} = |eE|^2 \sum_{j \neq k} \frac{|z_{kj}|^2}{E_k^{(0)} - E_j^{(0)}}, \quad (2.101)$$

where  $z_{jk}$  is a measure for the strength of the transition. In order to calculate the Stark shift for one photon transitions in helium, we take the calculated transition probabilities from Theodosiou [216, 217]. Theodosiou defines the absorption oscillator strength from level  $\gamma J_i$  to  $\gamma J_k$  as

$$f_{ki} = \frac{2}{3} \Delta E \frac{|\langle \gamma SLJ_k || D || \gamma SLJ_i \rangle|^2}{2J_i + 1} \quad (2.102)$$

in which  $D = e\mathbf{r}$  is the dipole operator and  $2J_i + 1$  accounts for the multiplicity of the lower level. Combining equations (2.101) and (2.102) the total DC Stark shift of level  $k$  can now be calculated as the sum over all levels  $i$  that couple via

the dipole interaction. Additionally we take into account the different unit systems chosen by the authors.

$$\Delta E_k^{(2)} = \sum_i \pm |eE|^2 \frac{3(2J_i + 1)}{2m_e} \sum_{M_i=-J_i}^{J_i} \frac{f_{ki}}{\omega_{ki}^2} \begin{pmatrix} J_i & 1 & J_k \\ -M_i & q & M_k \end{pmatrix}, \quad (2.103)$$

with  $M$  the magnetic quantum number. The level shift is positive if level  $E_i < E_k$  and negative otherwise. The polarization of the light is included as  $q = 0 \pm 1$  in the three- $J$  symbol, and is 0 for linearly polarized light in the direction of the quantisation-axis ( $= z$ ),  $M_k = M_i$  since we only take into account the multiplicity of the lower state, that is, the multiplicity (see e.g. [218]) of the higher state is included in  $f_{ki}$ .

### The AC Stark effect

If we now define the AC electrical field as

$$\mathbf{E}(\mathbf{r}, t) = \frac{i}{2} E_0 \left( \mathbf{e} e^{i(\mathbf{kr}-\omega t)} - \mathbf{e}^* e^{-i(\mathbf{kr}-\omega t)} \right), \quad (2.104)$$

we apply the following approximation based on the fact that  $\lambda \gg r_{\text{atom}}$  which means  $\mathbf{kr} \ll 1$ ,

$$\mathbf{E}(\mathbf{r}, t) = \frac{i}{2} E_0 \left( \mathbf{e} e^{-i\omega t} - \mathbf{e}^* e^{i\omega t} \right). \quad (2.105)$$

Considering that the overall phase of the field is not important the perturbation of the electrical field now becomes

$$V = \mathbf{DE} = e\mathbf{rE} \quad (2.106)$$

Following the calculation for the DC Stark shift with our AC perturbation yields

$$\Delta E_k^{(2)} = \sum_i \pm \frac{1}{2} |eE_0|^2 \frac{3(2J_i + 1)}{2m_e} \sum_{M_i=-J_i}^{J_i} \frac{f_{ki}}{\omega_{ki}^2 - \omega^2} \begin{pmatrix} J_i & 1 & J_k \\ -M_i & q & M_k \end{pmatrix}, \quad (2.107)$$

where  $E_0$  is the peak field strength, and  $\omega$  is the frequency of the AC field, which is for example the frequency of the fundamental light in the HHG setup.

### 2.8.2 Zeeman effect

In the presence of a magnetic field  $\mathbf{B}$ , the atomic levels can shift depending on the polarization of the light and the sensitivity of the atomic level given by the Lande  $g$ -factor. The perturbation Hamiltonian for the Zeeman shift, when the quantisation axis is chosen along  $z$ , can be written for weak fields as

$$V_B = \langle \hat{V}_B \rangle = g_J \mu_B M_J B, \quad (2.108)$$

where  $g_J$  is the Lande g-factor,  $\mu_B$  is the Bohr magneton with a value of  $13.9962 \times 10^9 \text{ Hz T}^{-1}$ ,  $M_J$  is the angular momentum of the light, and  $B$  is the magnetic field. The Lande g-factor is defined as

$$g_J = \left( 1 + \frac{J(J+1) - L(L+1) + S(S+1)}{2J(1+J)} \right), \quad (2.109)$$

where  $L$ ,  $S$  and  $J$  are the angular momenta as given in equation (A.31).

### 2.8.3 Recoil effect

In order to fulfill the conservation of momentum during optical excitation of an atom, momentum is transferred from the photon to the atom as the photon is annihilated. The atom therefore gains momentum and additional energy is needed from the laser field to make up for increased kinetic energy of the atom. The recoil shift follows as<sup>18</sup>

$$f_{\text{recoil}} = \frac{hf_{\text{obs.}}^2}{2m_a c^2}, \quad (2.110)$$

where  $f_{\text{obs.}}$  is the observed frequency of the atomic transition including the recoil shift and  $m_a$  is the mass of the atom.

### 2.8.4 Doppler effect

If an atom has a velocity component in the propagation direction of the light beam used in a spectroscopy experiment, this will lead to a shift in the measured transition frequency, the so called Doppler shift. Doppler broadening of the atomic transition is caused when the velocity distribution of the atoms under investigation has a solid angle of components in the propagation direction of the light beam. A diverging light beam is another cause for Doppler broadening of an atomic transition.

A systematic Doppler shift can arise if the integral over the atomic density in the beam times the local Doppler shifts in the beam does not average to zero. The typical configuration of beam angles in a crossed beam experiment, as used in the spectroscopy on helium discussed in this thesis, is given in Fig. 2.9.

The Doppler shifted frequency  $f$ , for a source at infinite distance moving with velocity  $\mathbf{v}$  with respect to the observer, where the source is emitting a frequency  $f_0$  in the direction  $\mathbf{k}$ , is given by Einstein [219] (modified for a moving emitter and fixed observer) as

$$f = f_0 \gamma \left( 1 + \frac{\mathbf{k} \cdot \mathbf{v}}{2\pi f_0} \right), \quad (2.111)$$

and

$$\gamma = \frac{1}{\sqrt{1 - \left(\frac{v}{c}\right)^2}} \quad (2.112)$$

<sup>18</sup>See section 6.2.3 for more details.

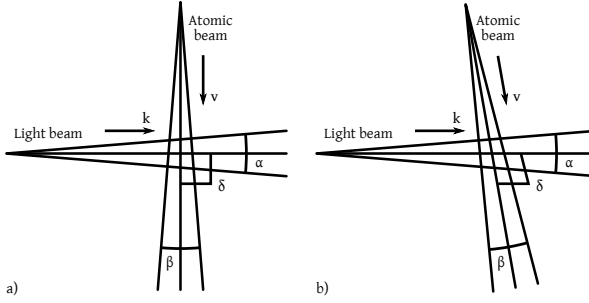


Figure 2.9: Sketch of the beam-angles involved in the calculation of the Doppler shift. a) The angle  $\delta$  between the light beam and the atomic beam is  $90^\circ$ . In this case the Doppler broadening will be caused by the angular spread of the light beam (in the far field representation with angle  $\alpha$ ), the angular spread of the atomic beam (angle  $\beta$ ) and its velocity distribution. b) The angle between the light beam and the atomic beam is not  $90^\circ$ . Next to the broadening described in a), a systematic frequency offset is present in the measured transition frequency, which depends on the angle  $\delta$  and the average atomic beam velocity.

where  $\gamma$  is the Lorentz factor,  $v = |\mathbf{v}|$ , and  $c$  the speed of light (in vacuum). Note the explicit mention of infinite distance in [219], which fixes the in-product, that is, the angle between direction of movement of the source and the direction of the line of sight between observer and source ( $\hat{\mathbf{r}} = -\hat{\mathbf{k}}$ ). If the source is relatively close to the observer, one needs to take changes in the angle into account too.

If, and only if,  $\mathbf{k} \cdot \mathbf{v} = 0$ , then the ratio  $f/f_0$  is  $\gamma$ . This will allow us to write Eq. (2.111) as a Taylor expansion [220] of

$$(1+x)^n = 1 + nx + \frac{n(n-1)}{2!}x^2 + \frac{n(n-1)(n-2)}{3!}x^3 + \dots, \quad (2.113)$$

which is mathematically valid for  $-1 < x^2 < 1$  and where we set

$$n = -\frac{1}{2} \quad (2.114)$$

$$x = -\left(\frac{v}{c}\right)^2, \quad (2.115)$$

to obtain the Taylor expansion of  $f/f_0 = \gamma$  as

$$f = f_0 \left\{ 1 + \frac{1}{2} \left(\frac{v}{c}\right)^2 + \frac{3}{8} \left(\frac{v}{c}\right)^4 + \dots \right\}. \quad (2.116)$$

Note that the condition for  $x$  is always fulfilled for particles with mass. This allows us to obtain the second [221] and higher-order Doppler shifts.

Equation (2.116) holds for emitted photons by the moving atom, therefore the sign of the shift for the received photons is exactly opposite and we obtain the relation for the Doppler shifts up to second order in  $\mathbf{v}$

$$f \simeq f_0 + \gamma \frac{\mathbf{k} \cdot \mathbf{v}}{2\pi} - \frac{f_0 v^2}{2c^2}, \quad (2.117)$$

where  $f_0$  is now the frequency observed by the atom and  $f$  the frequency of the photon sent to the atom. The factor  $\gamma$  in the expression for the first order Doppler shift is typically left out, the whole expression being a good approximation for low  $v$ .

The Doppler profile of the atomic beam is calculated by integration over the interaction volume for beam angles  $\beta$  and  $\alpha$  (Fig. 2.9), thus summing the Doppler shift multiplied by the excitation probability, which depends on the number of atoms and the intensity of the light, which themselves are functions that depend on the beam angles.

If the beam angles  $\beta$  and  $\alpha$  are small, the average Doppler shift is mainly dependent on the angle  $\delta$  between the beams, as long as the atomic and light beam have a symmetric radial distribution. For small angles  $\delta$  the Doppler shift is by good approximation proportional to the angle. This means that, in the typical skimmer configuration used, the Doppler shift is linear with the movement of a skimmer parallel with the laser beam for small angles  $\delta$ .

The second order Doppler effect not only causes a line shift but can also cause line shape distortion due to velocity spread in the atomic source. Since the second order Doppler effect is usually small, including the lineshape distortion only plays a role in experiments where the lineshape is resolved with a width smaller than the order of magnitude of the second order Doppler shift.



### 3. Towards narrow line width frequency comb lasers

In order to perform Hz level direct frequency comb spectroscopy, it is clear that the frequency comb laser itself should have line widths at least in the sub-kHz level regime. In typical high-resolution spectroscopy experiments one can still resolve an accurate frequency down to  $1 \times 10^{-3}$  of the measured line width if the spectroscopic conditions are known well enough [137, 222]. In self-referenced optical frequency comb lasers the line width is effectively limited by the feedback mechanisms available and the way in which feedback is applied to the system in order to fix the frequency of the comb modes.

Traditionally the locking of frequency combs is achieved by referencing to stable RF sources[36, 37, 131], which are in turn referenced to a stable and accurate frequency standard, traceable to the SI second. To obtain a frequency comb, both  $f_{\text{CEO}}$  and  $f_{\text{rep}}$  must be referenced to the clock. Typically one obtains an error signal for  $f_{\text{CEO}}$  and  $f_{\text{rep}}$  from a phase or phase-frequency comparator, which is then fed into a PID-controller. The output of the controller is fed back onto the laser. The feedback for  $f_{\text{CEO}}$ , which is controlled by the intracavity dispersion, is typically applied via the pump intensity, while feedback on  $f_{\text{rep}}$ , which is controlled by the optical cavity length of the laser, can be applied via a mirror mounted on a piezo-electric element.

For Ti:Sapphire frequency comb lasers,  $f_{\text{CEO}}$  can be locked to an RF source to millihertz bandwidth by controlling the pump intensity with an AOM. Fibre lasers usually have a rather noisy  $f_{\text{CEO}}$ , mostly due to pump laser noise and ASE [223]. Feedback speed can be limited by the upper laser level lifetime ( $\tau$ ), which can range up to  $\tau \simeq 8$  ms in  $\text{Er}^{3+}$ -doped fibre glasses [224]. Pump intensity control is in this case typically applied through variation of the pump laser diode injection current.

Several things are important to realise when locking  $f_{\text{rep}}$ . First of all, the phase noise on the harmonics  $m$  of the detected  $f_{\text{rep}}$  of a comb generator, scales with  $m^2$  [225]. Therefore it is useful to lock  $f_{\text{rep}}$  at a higher harmonic, limited by the available RF power in the harmonics in the photo diode signal and the availability of high-end RF sources (these typically have  $> 60$  dBc at  $> 1$  kHz offset depending on the frequency, see e.g. [226]). In this way the repetition rate noise is reduced by a factor  $n^2$ , where  $n$  is the harmonic used for the RF lock, for a given accuracy of the phase lock. It must be noted that with a very tight RF lock, generator noise can be imposed on  $f_{\text{rep}}$ , which can degrade the phase stability of the optical comb lines.

Second, how well  $f_{\text{rep}}$  can be locked depends on the environmental noise spectrum and the bandwidth of the piezo mirror assembly used. Better compensation is achieved with higher bandwidth and piezo mirror assemblies; bandwidths of 180 kHz and higher have been demonstrated [227].

In case of the Ti:Sapphire laser oscillator in our lab, an optical comb line width of 1.6 MHz [178] has been measured in the IR, resulting from a low feedback speed rf lock at the 60<sup>th</sup>–70<sup>th</sup> harmonic  $m$  of  $f_{\text{rep}}$  with a stable microwave generator. At the same time  $f_{\text{CEO}}$  was kept within a Hz from its RF reference.

For the Er<sup>3+</sup>-fibre frequency comb laser in our lab the  $f_{\text{CEO}}$  phase noise dominates the optical line width which is typically 60–400 kHz depending on the settings of the oscillator. The estimated contribution of the repetition rate servo to this mode linewidth, based on the measurement of  $f_{\text{rep}}$ , is in the order of 100kHz.

A further reduction of the comb line width is possible by locking the repetition rate of the frequency comb laser directly in the optical domain [228, 229]. A beat between a laser with a narrow line width at the Hz level (obtained by locking<sup>1</sup> to a high-finesse optical cavity [34, 35, 231]) and a comb mode is used to perform the optical locking of a comb laser. The CW laser must have a good short-term stability resulting in a narrow line width, while frequency drift can, for example, be compensated by using an AOM driven by a voltage controlled oscillator (VCO). In the following sections I will treat the development of narrow line width diode lasers and auxiliary devices built with the purpose of optically locking frequency comb lasers.

### 3.1 Narrow line width CW lasers

As a basis for our optical references, two semiconductor-based narrow line-width lasers (NLL) of the type Rio Planex [232] have been used, both in an integrated package with the electronics (brand name: RIO Orion), and with in-house developed electronics, featuring modulation bandwidths of up to 15 MHz (DC coupled) and 1.5 GHz (AC coupled). These lasers have a short term line width of < 3 kHz [232], but are very sensitive to injection current noise and thermal fluctuations.

#### 3.1.1 Thermal stabilization of narrow linewidth lasers

Although the Planex laser has an internal Peltier element for temperature stabilization, both the Planex and Orion are susceptible to environmental temperature fluctuations causing significant drift of the lasers. In case of the Orion and Planex, the day – night temperature cycle in the laboratory ( $\Delta T$  up to a few °C) causes a peak-peak frequency drift of > 150 MHz per day. This can still be corrected by modulation of the lasers injection current, but it is near the limit.

Larger changes in temperature can cause mode-hops due to the interaction of various wavelength selection mechanisms in the laser. These mode-hops are particularly intolerable when the laser is used in a dense wavelength division multiplexing (DWDM) optical communications network as in chapter 7, because of power changes > 10 dB. On the SURFnet fibre network, power

---

<sup>1</sup>Commonly using the optical equivalent of a locking technique developed by Pound [230].

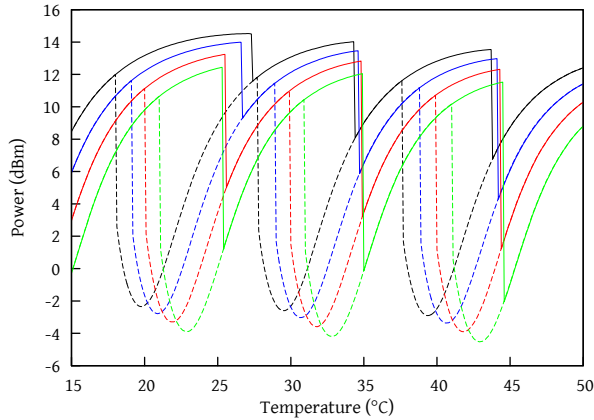


Figure 3.1: Output power vs. temperature of the Planex laser diode. Injection powers are 100 mA (black), 90 mA (blue), 80 mA (red), 70 mA (green). The solid lines indicate an increasing temperature, the dashed lines indicate a decreasing temperature.

fluctuations with a maximum of  $\pm 0.5$  dB are allowed on a DWDM channel in order not to disturb the data communication on neighbouring channels on same fibre. A measurement of the laser output power versus temperature is shown in Fig. 3.1 for different injection currents through the laser diode.

To avoid mode-hopping and improve the intrinsic frequency stability, the lasers have been mounted in a temperature stabilised environment. Acoustic feedback can also cause frequency fluctuations of these lasers. Measures to avoid acoustic coupling to the environment have been incorporated in the design of the temperature stabilisation system. The mechanical stabilisation system consists of a heavy aluminium box, covered on the inside with sound absorption foam. This foam acts as a spring suspension in which the thermal stabilisation system is mounted.

The thermal stabilisation system consists of an aluminium heat sink and a 20 mm thick extender coupled via a 80 W Peltier element to a 1 cm thick copper plate on which the laser is mounted. The heat sink and copper plate are thermally decoupled by thermal isolation foam. Air flow through the heat sink is provided by two slits in the box which allows for convection cooling.

The system is driven by a pulse-width modulated thermal controller, allowing for both heating and cooling of the copper block. The temperature stability of the copper block at the measurement position is better than 0.01 K. The original design shielded sound waves from the heat sink, but unfortunately this caused a high flow resistance in the air cooling circuit (see Fig. 3.2). A design change enabled a better air flow at the expense of reduced acoustic shielding.

After installation of the thermal insulation and stabilisation, the frequency drift of the Orion laser has been measured, and found to be within 3 MHz

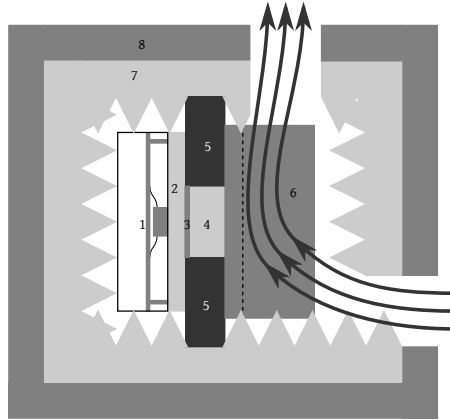


Figure 3.2: Side view of the Planex temperature stabilisation system. 1. Planex laser and driver electronics on Euro card format printed circuit board, placed inside an EMI shielding tin; 2. Copper heat spreader (1 cm thick plate  $10 \times 20$  cm); 3. Peltier element 80 W; 4. Aluminium heat conductor block  $5 \times 5 \times 4$  cm; 5. Thermal insulation foam (BASF Styrodur C); 6. Aluminium heat sink (vertical ribs); 7. Noise isolation material, also acts as damper and mount for thermal stabilisation assembly; 8. Aluminium casing (2 cm thick plates, outer dimensions  $l \times w \times h$ ) are  $34 \times 32 \times 22$  cm; Arrows represent the convection air flow for cooling.

over 4.5 days. The thermal drift rate of the Planex diode was initially about 40 MHz per day (20 MHz peak-peak) which is easily corrected for by modulation of the injection current. This large drift has been attributed to the fact that, although the laser diode itself had been temperature stabilised, the electronics were at this point still a commercial current and temperature driver (Thorlabs IDL200 and IDC200) undergoing the laboratory temperature changes. After replacement of the external electronics with in the house developed ones (see next section), the frequency drift of the Planex and Orion were of the same order.

### 3.1.2 Development of low noise current drivers

Low-noise current drivers for both low current (up to 150 mA) and high current (up to 1.5 A) have been developed in collaboration with the electronics department of the VU. Part of the inspiration for their design has been taken from [233, 234]. Initial measurements confirm that the current noise is on the order of what is required for the diode lasers to work in their narrow line width regime.

The driver electronics include both the laser current driver and thermal controller. The temperature and current can be set via a USB interface and a computer program. A DC-coupled current feedback circuit with a bandwidth  $> 15$  MHz is available, as well as an ultra-high frequency AC-coupled circuit, which can be driven at frequencies up to  $\sim 1.5$  GHz.

Figure 3.3 shows a Rio Planex laser diode built into the developed elec-



Figure 3.3: Low noise, high modulation-bandwidth laser-driver electronics including temperature stabilisation, developed in house at VU Bèta Elektronica. The Rio Planex laser diode is clearly visible in the middle as the rectangular electronics package marked RIO. Note that the electronics are built into an EMI enclosure and that filtered feed-throughs (right side, with the red leads soldered on) are used to connect the power supplies.

tronics printed circuit board. Details with regard to the electronics can be obtained via the VU Beta Electronics department.

A modified Allan deviation has been measured for both the Orion and the Planex laser (free running) and is shown in Fig. 3.4 together with the counted frequencies. The Allan deviation shows that the in house developed electronics performs less good at short time scales. This is possibly due to the high-bandwidth modulation circuits, which might cause additional injection current noise at shorter time scales (causing higher frequency fluctuations). The exact reasons for this behaviour should still be investigated. On the other hand it is clear from the locking behaviour of the VU electronics that, with the high-bandwidth modulation input, the laser can in principle be locked much tighter, e.g. to the frequency comb laser than the Orion package can.

### 3.1.3 Establishing the laser line width

The short term stability of the Orion and Planex lasers was established in a dual beat experiment using the  $\text{Er}^{3+}$ -fibre frequency comb laser. The heterodyne beats were measured with fibre coupled beat units. By shifting one of the lasers to around 70 MHz offset from a comb line and the other laser to around -20 MHz offset of a comb line, the sum and difference frequencies could be generated using a RF mixer. The  $f_{\text{CEO}}$  noise is cancelled in the difference frequency assuming that  $f_{\text{CEO}}$  is indeed equal for both beat signals. The estimated contribution of fractional  $f_{\text{rep}}$  noise on the measurement is in the order of 1 kHz, based on the two-sample variance for  $f_{\text{rep}}$  determined by the commercial fibre-comb software, which is less than the short term frequency variations of the CW lasers.

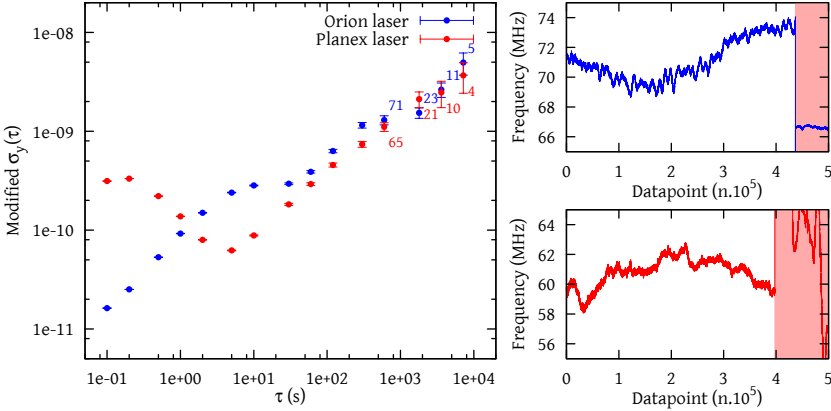


Figure 3.4: Comparison of frequency stability of the free-running temperature stabilised Planex (VU Electronics laser driver) and Orion laser packages. (left) The modified Allan deviation calculated from the counted frequencies (right). The additional numbers in the left graph represent the amount of statistical data available for calculation of the average and standard deviation (for  $n < 100$  data points). The frequency data with a red background was not taken into account since the frequency comb used went out of lock during the data taking.

Figure 3.5 (left part) shows an overview of the RF spectrum in which the widths of the sum (50 MHz) and difference (90 MHz) frequencies are clearly different due to the cancellation of  $f_{\text{CEO}}$  noise in the difference frequency. The 70 MHz peak is the beat with the frequency comb at 70 MHz which is not fully suppressed in the mixer output. In the right part of figure 3.5 the difference frequency line width is more clearly resolved. An upper bound on the linewidth of the laser was estimated to be 5 kHz by narrowing the RBW and observing a change in signal strength at RBW settings below 5 kHz. If both lasers have an equal line profile this means that their individual line widths are  $< 3.5$  kHz, which is slightly higher than specified in their data sheets ( $< 3$  kHz).

### 3.1.4 Long term locking stability of narrow linewidth lasers

Both narrow linewidth lasers have been locked to the  $\text{Er}^{3+}$ -fibre comb laser at offset frequencies of 60 and 70 MHz by means of a counting phase frequency detector. These signals were multiplied using an RF mixer to produce a difference frequency of 10 MHz absent of  $f_{\text{CEO}}$  noise. The difference frequency has been counted with a dead-time free counter in order to establish an upper bound on the long term system stability.

Since the frequency comb modes have a relatively high phase noise, the Orion, which has a modulation bandwidth of only 30 kHz, runs out of the counting range of the detectors relatively often. On the other hand, the locking speed of the Planex laser with in-house electronics (speed limited by the phase comparator electronics with a bandwidth of  $\approx 80$  kHz) is capable of

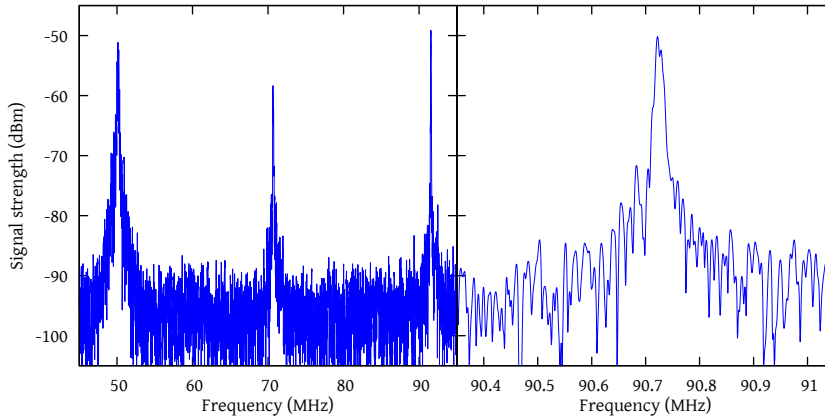


Figure 3.5: (left) Overview spectrum of the difference mixing between two narrow line width lasers, free running with respect to the  $\text{Er}^{3+}$ -fibre frequency comb laser. A clear difference in width between the sum frequency at 50 MHz and the difference frequency at 90 MHz can be observed (see text). The peak at 70 MHz is the residual signal of the beat at 70 MHz with the frequency comb laser. The analyser RBW and VBW settings are both 51 kHz. (right) A close up of the difference frequency signal at 90.7 MHz. The radio bandwidth and video bandwidth of the analyser were 10 kHz.

tracking the comb laser much better. In case of a silent lab (the comb laser being the most sensitive to acoustic noise), out-of-counting range conditions happened once every 10 minutes or so.

The obtained modified Allan deviation is shown in Fig. 3.6. This graph shows that the system noise limit, caused by locking of the narrow linewidth lasers, lies at relative frequency accuracies better than  $4 \times 10^{-18}$  at a few thousand seconds.

## 3.2 Auxiliary devices for use with narrow linewidth lasers

Several auxiliary devices for use with narrow linewidth laser sources and the  $\text{Er}^{3+}$ -fibre based frequency comb laser have been designed and built. Devices like fully fibre based beat units and photo diodes facilitate convenient comparison of CW lasers with the frequency comb laser. In order to distribute and double (for use with the Ti:Sapphire frequency comb lasers) the narrow linewidth laser light,  $\text{Er}^{3+}$  doped fibre amplifiers have been built to generate laser powers up to a few Watts. Acousto-optic modulator (AOM) based frequency shifters enable continuous tuning of the lasers over a relatively wide range, and can be used to scan  $f_{\text{rep}}$  of optically locked frequency comb lasers. Modern, referenced, low noise direct digital synthesizer (DDS) sources have been constructed to drive the AOMs with accurate and traceable frequencies.

### 3.2.1 Fibre coupled beat units and photo diodes

Beat units, used to make optical heterodyne beats between the frequency comb light and other light sources, based on free space optics are difficult

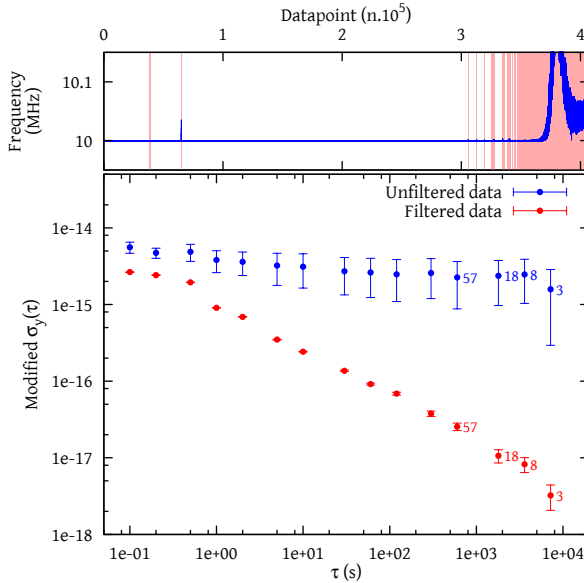


Figure 3.6: Modified Allan deviation of the locked lasers against each other. (top) The raw frequency data, while taking the data, the  $f_{\text{CEO}}$  signal has slowly decreased, data points  $>$  no.  $3.5 \times 10^5$  show where  $f_{\text{CEO}}$  has gone out of lock and this data has not been taken into account for the modified Allan deviations shown in the bottom graph. (bottom) Modified Allan deviations; The graph of the unfiltered dataset (blue points) includes 41 outlier points (0.012% of the data), shown by the red background area's between measurement 0 and  $3.5 \times 10^5$ . The outlier points are caused by external influences. The filtered dataset (red points) shows the noise floor of the system (there is a continuous range of  $> 2 \times 10^5$  measurements without disturbances, yielding a similar result as the filtered dataset).

to align and require constant attention to maintain a good signal to noise ratio. The oscillator outputs of the  $\text{Er}^{3+}$ -fibre based frequency comb are fibre coupled. One of the output ports is used to supply the frequency comb oscillator light as input for so called fibre beat-units.

The scheme of a beat unit that can work on a two international telecommunication union (ITU) DWDM channels is given in Fig. 3.7. A photograph of a two channel, double beat unit (2 independent beat signals per DWDM channel) is shown in Fig. 3.8. Spatial overlap of the frequency comb and CW laser light is readily provided for by the fibre optics. The unused comb spectrum is cut away by use of DWDM filters, that provide 100 GHz ( $\sim 0.8$  nm) wide spectral transmission windows centred on the ITU channel grid for optical communication networks. Because the remaining light is led into an output fibre, beat units for different DWDM channels can be cascaded.

The Menlo Systems frequency comb has a high-power oscillator output port available that was not used. The output power of this ports is approximately 27 mW in a  $\sim 80$  nm wide spectrum. Compared to the free space output of 200 mW in a 1000 nm wide spectrum after spectral broadening in

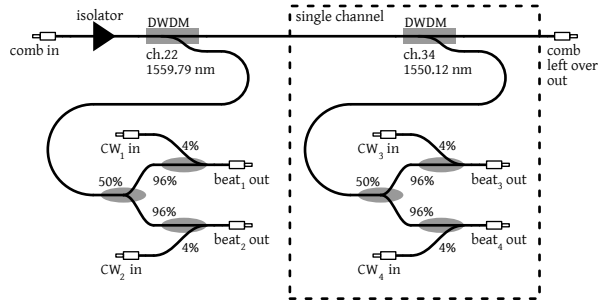


Figure 3.7: Schematic of a dual DWDM-channel double-output fibre coupled beat unit. The splitter ratio between comb and CW laser has been optimized for about 5mW of CW input and a typical signal to background of 40 dB is reached. Note that other channels can be cascaded on the “comb left over out” port or that this port can be used for other purposes like stable RF generation as is done in [235].

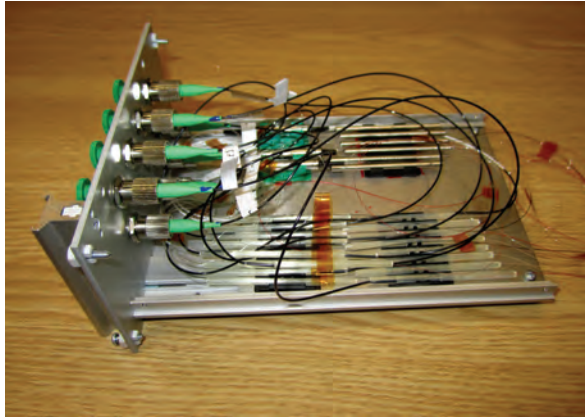


Figure 3.8: Photograph of the two DWDM-channel double-output fibre coupled beat units built into a rack mountable module. The fibre optical components are in the tubes mounted in the top part, while the splice protectors are mounted at the bottom.

a photonic crystal fibre, the spectral power is slightly higher. Taking into account additional losses due to splitting, non-ideal alignment (free-space frequency comb laser output only), polarisation effects and so on, this comparison between the fibre-coupled and free space output favours the fibre-coupled case, where at least four times as much power per comb mode is available to make a heterodyne beat.

In our implementation we make use of this fact to implement a double beat unit per DWDM channel, using the amount of frequency comb mode power per beat unit as efficient as possible by choosing a splitting ratio of 96% to combine the frequency comb light with 4% of the CW laser light. The combination ratio might not be the best yet for optimised signal to background

of the heterodyne beat [131, 236].

To exploit the fibre coupled nature of the beat units, photo diode units based on the Fujitsu FID3Z1LX have been developed. The FID3Z1LX is a typical 2.5 Gb/sec data communication receiver diode (responsivity 0.85 A/W, -3 dB low pass cut-off frequency 2.5 GHz) with a multi-mode fibre pigtail. Signals up to 6.5 GHz have actually been observed with these diodes. The multi-mode fibre might cause widening (amplitude or phase noise) of the RF signals due to multipath interference. These kind of effects have not (yet) been observed experimentally.

The resulting beat signals out of these fully fibre-coupled beat units have almost always more than 40 dB signal to background noise, which is more than sufficient for all our current experiments. We have not tried to further improve the signal to noise ratio by adjustment of the beat unit coupling ratios or by changing the photo diode electronics.

### 3.2.2 AOM frequency shifters and DDS-based RF sources

To obtain a complete spectrum in direct frequency comb spectroscopy, the comb modes that probe the spectrum need to be shifted by at least one  $f_{\text{rep}}$ . If a comb mode is locked to an ultra-stable laser, the repetition rate is virtually fixed (except for the drift of the ultra-stable laser). In order to obtain an optical source that can be accurately frequency shifted, acousto optic modulators (AOMs) can be used.

Normal fibre-coupled AOMs have a very limited frequency shift range, because of their construction. In order to obtain a large frequency tuning range with an AOMs, a free-space optical implementation after Donley [237] has been built.

The free space AOM unit is equipped with a fibre-coupled in and output. The acousto-optic modulators used (Brimrose model IPF-150-100-1550) have a centre frequency of 150 MHz, and a 3dB tuning range of 100 MHz with a peak efficiency of about 60 – 70 %. This means that a double-pass scan range of 200 MHz is available but with fairly poor overall efficiency of at best 28% at the centre frequency, and 8% at the edges, assuming 80% coupling efficiency into the output fibre. The output of the AOM units therefore needs amplification.

To drive the AOMs, ideally RF sources with a high spectral purity are used. Because the absolute frequency of the optical reference is shifted by the RF frequency, this frequency source needs to be referenced to the 10 MHz lab standard. The Analog Devices AD9912A direct digital synthesizers (DDSs), which is available on an evaluation board with a convenient USB interface, meets both specifications. Frequency doubling of a 10 MHz frequency reference provides a 20 MHz reference for the internal 1 GHz generator. Wideband background as well as nearby spurious signals are below 60 dBc as shown in Fig. 3.9. To obtain the 1.5 W RF power needed to drive the AOM, a single low-noise amplifier was used (Mini-Circuits ZHL-03-5WF).

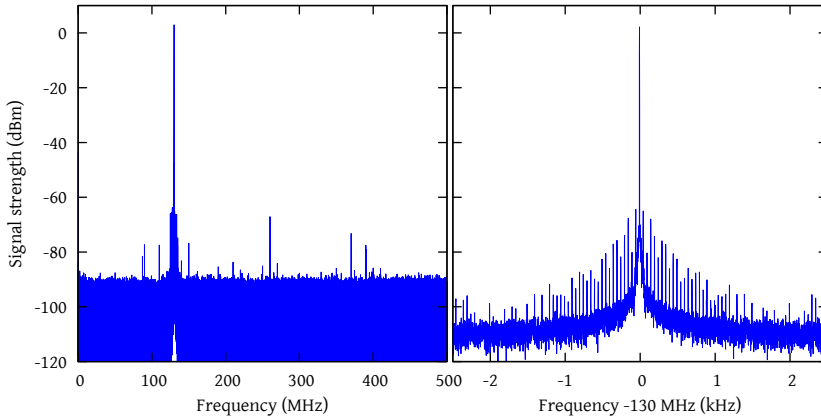


Figure 3.9: Spectral purity of the AD9912A DDS signal generator. a) Wide band spectrum, spurious signals are  $< 60$  dBc while the  $-3$  dB low pass filter frequency lies at 450 MHz. Spectrum analyser settings: RBW=3 kHz, VBW=10 kHz. b) Narrow band spectrum with near carrier spurious signals. Spectrum analyser settings: RBW=1Hz, VBW=1Hz,  $5\times$  averaged.

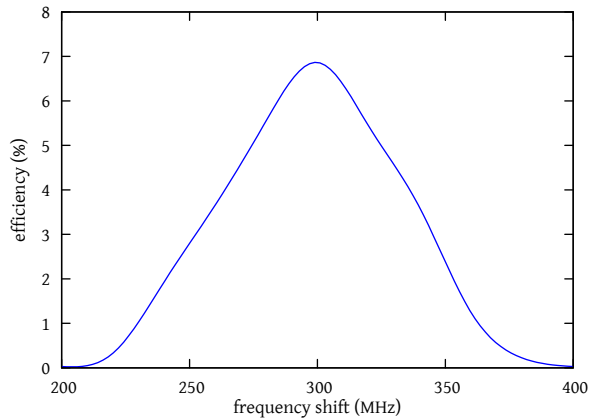


Figure 3.10: Efficiency of the fibre coupled AOM unit as a function of the induced optical frequency shift. Estimations are that the overall efficiency should be more than 2 times larger when the unit is better optimised.

The final fibre to fibre losses as a function of driver frequency are shown in Fig. 3.10. The optimal reachable efficiency is about 40%, given the numbers of the manufacturer and a coupling efficiency of 80% into the out-coupling fibre. In practice we have not reached these numbers. The maximum diffraction efficiency for the AOM was 47%, due to polarisation dependence of the AOM. During the measurements the in-coupling efficiency was only 41% which has been improved to about 80% in the mean time. The overall efficiency can thus be optimised further and a realistic value of 17.5% (50% dif-

fraction efficiency + 70% in-coupling efficiency) should be obtainable at the central AOM frequency.

The performance is sufficient to have a tuning range of about 96 MHz where the unit is usable in combination with a pre-amplifier. This frequency range is sufficient to optically lock and tune  $f_{\text{rep}}$  of the fibre frequency comb laser, and to lock and frequency tune  $f_{\text{rep}}$  of the Ti:Sapphire frequency comb lasers after additional amplification and frequency doubling.

### 3.2.3 $\text{Er}^{3+}$ -doped amplifiers

To compensate the losses introduced in the AOM units and distribution splitters,  $\text{Er}^{3+}$ -doped fibre amplifiers have been constructed. These amplifiers are used to reach (in telecommunication terms) relatively high power levels of about 160 mW with core pumped, and  $> 3$  W with cladding pumped fibres.

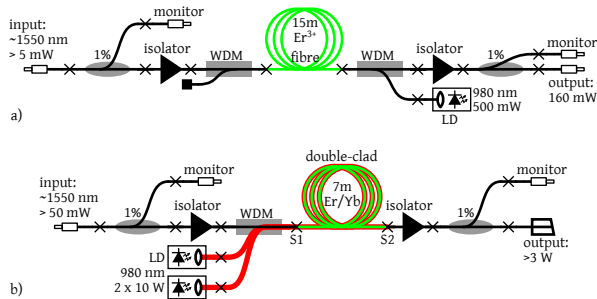


Figure 3.11: a)  $\text{Er}^{3+}$  core-pumped pre-amplifier design with a counter propagating pump. A WDM to couple the residual pump light from the amplifier section off the fibre has been implemented mainly as a precaution to protect the seed diodes. b) High power ( $> 4$  W)  $\text{Er}^{3+}$  cladding pumped amplifier design. Two special splices s1 and s2 have been made. Splice s1 was optimised to keep the pump light in the cladding and splice s2 was optimised to safely couple the remaining pump laser light out of the fibre (see main text for details). A co-propagating design was implemented because of the simpler construction and the possibility of high pump power left-overs guided in the core.

Figure 3.11a shows the design of the pre-amplifiers. A counter propagating core-pumped design has been chosen to achieve good efficiency. The first version of the amplifier had an active fibre (NUFERN EDFC-980-HP) of about 5 m length, based on the gain figures specified by the manufacturer. However, these figures turned out to be measured for amplification levels up to 1 mW. For high-power applications ( $> 1$  mW) the reachable gain of these fibres drops due to saturation effects. Based on the gain reached (at high powers) in the first implementation, the optimal fibre length was chosen to be  $\sim 15$  m, which is probably slightly too long still because of the counter propagating pump design.

These amplifiers are pumped by a single-mode 500 mW, 980 nm pump diode. For these diodes, two in-house developed 1.5 A diode current and TEC drivers have been built into a 19" rack housing together with the two fibre pre-amplifiers. If desired, optimisation of the amplifiers could be done using

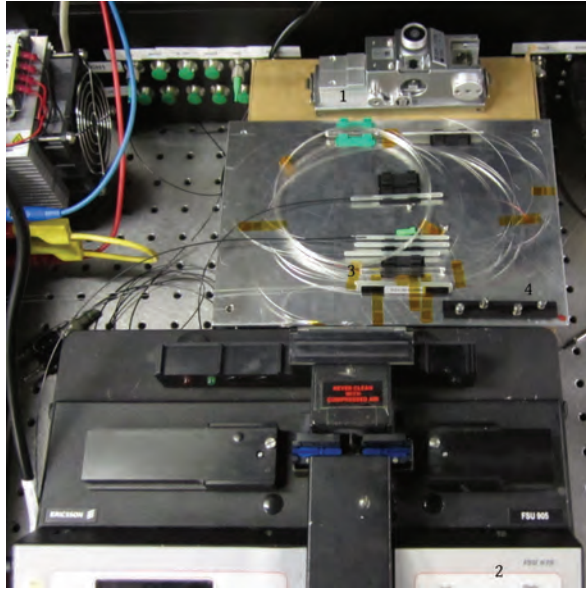


Figure 3.12:  $\text{Er}^{3+}$  cladding-pumped post-amplifier under construction. (1) The fibre-cleaver to obtain flat fibre end-faces in order to use the fusion splicer (2) to weld the fibres together. (3) S1 and (4) S2 are the special splices used in the double-clad amplifier design. Splice S1 is glued with UV curing glue into a glass capillary with a hole diameter of  $\sim 350 \mu\text{m}$  in order to obtain pump guiding in the cladding. Splice S2 is carefully clamped into a spring loaded aluminium holder with a V-groove to enable the safe transmission of pump light out of the fibre cladding at the splice.

the modelling methods devised by Giles and Desurvire [238–241] as a starting point, but the current performance is more than enough for the applications they are used for.

Figure 3.11b shows the design of the power amplifier. This amplifier uses a 7 meter long cladding-pumped Er/Yb co-doped gain fibre of type (NUFERN SM-EYDF-6/125-HE) which is suitable for high power applications up to tens of Watts. In this amplifier two special splices are used to connect the gain fibre to the pump combiner and output fibre section. Splice s1 is an air guided pump light section, mechanical stability is reached by gluing the fibre into the ends of a glass capillary with UV curing glue. Splice s2 is carefully clamped into a spring loaded anodised aluminium V-groove holder in order to dissipate left-over pump power safely around the splice area. In practice splice s2 works well and hardly any pump leftover is present in the core, although pump light is still present (visible with an IR viewer) over tens of centimetre in the cladding of the output fibre. The coupling to free space was made via a special FC/PC connector (Diamond-Kimberlit) incorporating a glass ferrule that acts as a beam expander.

A photograph of the power amplifier under construction is shown in Fig. 3.12. At the top of the photo the fibre-cleaver (1) is shown which we used to

obtain flat end-faces on the fibres in a controlled way. The fusion splicer (2) at the bottom of the photo is then used to weld the glass fibres together in order to enable low-loss fibre-to-fibre connections.

# 4. Towards hybrid mode-locked quantum dot frequency comb lasers

Abstract: We report on frequency comb generation at 1.5  $\mu\text{m}$  by injection of a CW laser in a hybridly<sup>1</sup> mode-locked InAs/InP two-section quantum-dot laser (HMLQDL). The generated comb has  $> 60$  modes spaced by  $\sim 4.5$  GHz and a -20 dBc width of  $> 100$  GHz (23 modes) at  $> 30$  dB signal to background ratio. Comb generation was observed with the CW laser (red) detuned more than 20 nm outside the HMLQDL spectrum, spanning a large part of the gain spectrum of the quantum dot material. It is shown that the generated comb is fully coherent with the injected CW laser and RF frequency used to drive the hybrid mode-locking. This method of comb generation is of interest for the creation of small and robust frequency combs for use in optical frequency metrology, high-frequency ( $> 100$  GHz) RF generation and telecommunication applications.

## 4.1 Introduction

Frequency comb lasers [36, 242] have been around since the early 2000's, enabling highly-accurate optical time and frequency measurements resulting in many applications [145, 153, 243, 244]. Integrated optical frequency comb lasers would pave the way to an even broader application of comb technology because of low fabrication and maintenance costs. Mode-locked quantum dot lasers (MLQDL) are interesting for this application as they have a broad gain bandwidth ( $> 100$  nm) required for short pulse generation [245–249]. Further on-chip integration with an optical amplifier, highly non-linear media for spectral broadening and an  $f$ - $2f$  interferometer (for carrier envelope offset frequency ( $f_{\text{CEO}}$ ) detection), and feedback electronics for orthogonal control of  $f_{\text{rep}}$  and  $f_{\text{CEO}}$  [250], could lead to fully integrated, self-referenced frequency comb laser designs.

Because of their small size, these lasers have pulse repetition rates ( $f_{\text{rep}}$ ) in the range of a GHz up to hundreds of GHz, which is a useful property for e.g. low-noise microwave generation [251, 252], accurate calibration of spectrometers [145], and optical arbitrary waveform generation [253]. Apart from metrology applications, high repetition rate frequency combs are of interest for telecommunication applications as highly stable pulse train emitters for applications such as optical time-domain multiplexing (OTDM) [254] or all-optical clock recovery [255]. With their wide optical spectrum and stabilized mode spacing, ultra-high repetition rate frequency combs are attractive for application in wavelength-division multiplexed (WDM) systems and also as

---

<sup>1</sup>Hybrid mode locking refers to the mode-locking scheme where the modelocking behaviour of a semiconductor is enhanced by electrically modulating an absorption section on the laser chip.

multi-wavelength light sources [256–259]. The coherence of frequency comb modes can be exploited in Coherent Optical Orthogonal Frequency Division Multiplexing (CO-OFDM) [260].

In this work we report on the generation of optical side bands (modes in the form of a frequency comb) on a CW diode laser injected into two-section InAs/InP (H)MLQDL devices [261, 262] working at  $1.5 \mu\text{m}$ . This frequency comb generation appears to be independent of the laser action and shows that the device works as an electro-optical modulator, producing equally spaced and coherent modes. The generated comb has been characterized using two narrow linewidth CW lasers and an  $\text{Er}^{3+}$ -fiber based frequency comb laser.

## 4.2 Description of the HMLQDL and the experimental setup for optical injection

The (H)MLQDL's used in this experiment are 9 mm long ( $f_{\text{rep}} \sim 4.5 \text{ GHz}$ ), two-section InAs/InP (100) Fabry-Pérot type ridge-waveguide devices, produced by metal-organic vapor-phase epitaxy [261–264]. The  $2 \mu\text{m}$  wide wave guides have been produced using reactive ion etching and the mirrors are formed by the cleaved facets ( $\sim 31\%$  reflectivity). The saturable absorber section had a length of  $360 \mu\text{m}$  (4%).

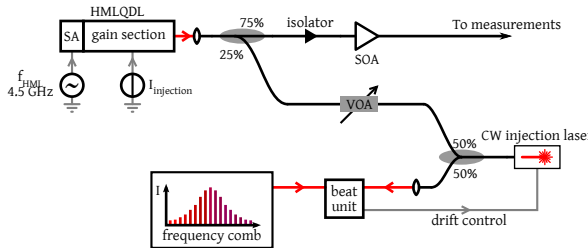


Figure 4.1: Setup for studies of CW injected QDL device behavior. HMLQDL: hybridly mode-locked quantum dot laser, SOA: semiconductor optical amplifier, FCL: frequency comb laser, VOA: variable optical attenuator, gray lines: electrical signals, red lines: free space optical path, black lines: fiber optics.

Figure 4.1 shows part of the setup used to investigate the behavior of the HMLQDL device when a CW laser is injected. The effects of hybrid mode-locking were reported previously [261]. The HMLQDL is mounted on a copper plate that is temperature stabilized to  $10^\circ\text{C}$  to optimize the gain. To prevent condensation, the setup is flushed with nitrogen gas. An Agilent N5181A RF generator with a frequency doubling setup and an amplifier (maximum output 25 dBm) was used to generate the hybrid mode-locking voltage (typically 6–11 V<sub>pp</sub>) that was applied to the SA section of the chip via a bias tee (no bias voltage applied) and a three point ground-signal-ground probe (coupling efficiency to SA section unknown).

The output of the laser was coupled into an anti-reflection coated lensed fiber using a piezo controlled three axis translation stage (estimated coupling loss 3–5 dB). Light of a CW laser (Toptica DL 100/pro, linewidth 100 kHz, power  $\sim 40$  mW, internal isolator) was adjusted in power with a variable attenuator (0–6.2 mW) and injected into the HMLQDL device via the 25% port of a fused fiber splitter/combiner. The standard single-mode fiber was manipulated to optimize the polarization of the injected light. The injection laser was optically locked to one of the modes of a Menlo Systems FC1500 Er<sup>3+</sup>-doped fiber frequency comb laser (FCL) to precisely control the optical injection frequency ( $f_{\text{injection}}$ ). The HMLQDL output (75% port) was sent through an optical isolator and amplified in a semiconductor optical amplifier (SOA, type JDS CQF 872/108C) to about 40mW in order to have sufficient optical power for further analysis. It has been checked that the SOA did not induce additional non-linear effects.

### 4.3 CW injection of the HMLQDL

As frequency comb applications benefit from narrow modes, injection locking of the (H)MLQDL to reduce the linewidth of the (H)MLQDL modes was attempted. No injection locking and related narrowing of the HMLQDL modes has been observed, presumably due to the low resonator Q (and resulting mode widths of  $> 100$  MHz) of the devices which makes it hard to influence these modes by narrow CW laser injection. However, narrow linewidth peaks were observed in the heterodyne spectrum which were independent of the HMLQDL's native mode structure but exhibited a spacing of  $f_{\text{HML}}$ .

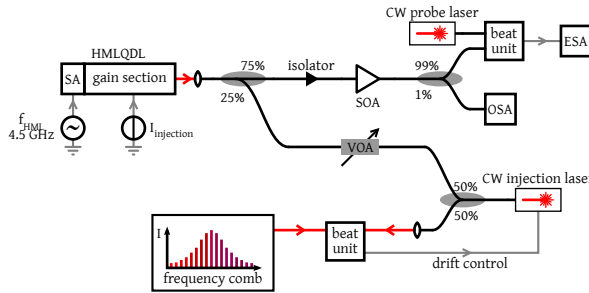


Figure 4.2: Setup used to characterize the mode structure of the QDL with CW laser injection. HMLQDL: hybridly mode-locked quantum dot laser, SOA: semiconductor optical amplifier, ESA: electrical spectrum analyzer, OSA: optical spectrum analyzer, FCL: frequency comb laser, VOA: variable optical attenuator, gray lines: electrical signals, red lines: free space optical path, black lines: fiber optics.

The setup of Fig. 4.2 was used where the probe laser is a Toptica DL 100/pro CW laser (tunable 1490–1590 nm). This probe laser was used to make a heterodyne beat with the output of the CW injected QDL. The CW injection laser was placed at an arbitrary wavelength of  $\sim 1515$  nm where native QDL modes are visible in the heterodyne spectrum. The probe laser was blue

detuned with respect to the injection laser with  $\sim 7.9$  GHz. The spectrum of this heterodyne beat was recorded with an Agilent 4440A electrical spectrum analyzer (ESA), showing the (optical) sum and difference frequencies between the QDL laser output and the probe laser in the frequency range recorded.

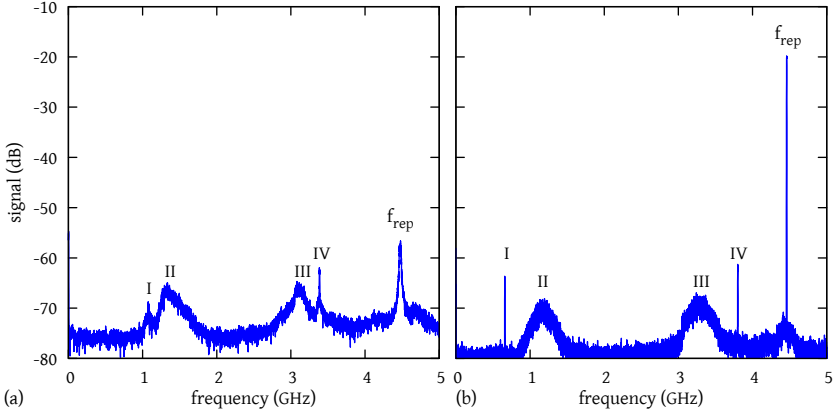


Figure 4.3: Optical heterodyne beat signals of the QDL light including the modulated CW injection laser with the probe laser measured with the electrical spectrum analyzer (ESA). The wavelength of the injection laser was tuned inside the (H)MLQDL's spectrum at  $\sim 1515$  nm. QDL modes are visible as broad peaks (II and III) at  $I_{injection} \sim 645$  mA. (a) Passively mode-locked QDL.  $f_{rep} \sim 4.5$  GHz, modes 1 (IV) and 2 (I) of the modulated CW injection laser are visible at  $\sim 3.4$  and  $\sim 1.1$  GHz. (b) Hybridly mode-locked QDL.  $f_{rep} = 4.46$  GHz, modes of the modulated CW injection laser are visible at  $\sim 3.8$  (IV) and  $\sim 0.7$  GHz (I).

Figure 4.3(a) shows the RF spectrum of the beat of the injected passively mode-locked laser with the probe laser. The direct beat between the injection and probe lasers (located at  $\sim 7.9$  GHz) is not visible in the recorded spectrum. The first two modulation side bands are visible at  $\sim 3.4$  (IV) and  $\sim 1.1$  GHz (I, negative beat sign) as narrow spikes, while native modes of the QDL (II and III) are visible as broad peaks around  $\sim 1.5$  and  $\sim 3$  GHz. The narrow spikes (I and IV) disappear when no CW laser light is injected, while the QDL modes stay the same. When the frequency of the injected laser is shifted, the narrow peaks shift the same amount in frequency. The frequency difference between the two narrow peaks is exactly the passive mode-locking frequency of the QDL. The appearance of narrow peaks, the spacing of these peaks and the shifting of the peaks together with (optical) frequency shifts of the injection laser are all clear signs of optical side-band generation on the injected CW laser.

A similar spectrum of the hybridly mode-locked QDL is shown in Fig. 4.3(b). Again the broad peaks ( $\sim 1.2$  (II) and  $\sim 3.2$  GHz (III)) are native QDL modes, while the narrow spikes at  $\sim 3.8$  (IV) and  $\sim 0.7$  GHz (I) are side bands of the modulated CW injection laser. The repetition rate ( $f_{rep}$ ) is now fixed by the RF generator at 4.46 GHz.

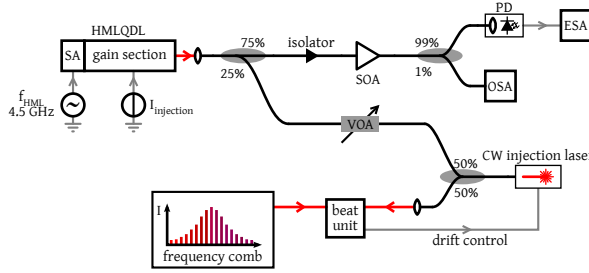


Figure 4.4: Setup used to investigate variation of  $I_{\text{injection}}$  and  $f_{\text{HML}}$ . HMLQDL: hybridly mode-locked quantum dot laser, SOA: semiconductor optical amplifier, PD: photo diode, ESA: electrical spectrum analyzer, OSA: optical spectrum analyzer, FCL: frequency comb laser, VOA: variable optical attenuator, gray lines: electrical signals, red lines: free space optical path, black lines: fiber optics.

A number of experiments was performed to further study the modulation imposed on the injected CW laser. It was noted that the modulation was present when the injected CW laser was tuned outside the QDL's spectrum as well, this effect was exploited to study the modulation with no interference of the native QDL spectrum.

#### 4.3.1 Characterization of the passively mode-locked QDL with an injected CW laser

The setup shown in Fig. 4.4 has been used to characterize the passively mode-locked QDL by recording the RF and optical spectra without (Fig. 4.5(a)) and with (Fig. 4.5(b)) the CW injection laser. About 1% of the SOA output was directed to an ANDO 6315A optical spectrum analyzer (OSA, resolution 0.05 nm), while the remaining 99% was split in two (this splitter is not drawn) and the light of one of the outputs was coupled into an EOT ET-3500 InGaAs photo diode (3 dB bandwidth > 10 GHz) to obtain RF spectra with the ESA. The injection current  $I_{\text{injection}}$  has been varied from 200 mA to 1000 mA in steps of 5 mA. For each value of  $I_{\text{injection}}$  an RF repetition rate spectrum and an optical spectrum of the laser were recorded. This setup has also been used to investigate the influence of the hybrid mode-locking frequency ( $f_{\text{HML}}$ ).

The results for the passively mode-locked QDL are shown in Fig. 4.5. For  $I_{\text{injection}}$  from  $\sim 540$  mA to  $\sim 760$  mA a relatively well defined passive mode-locking repetition rate frequency of  $\sim 4.45$  GHz is seen. In Fig. 4.5(b) broadening of the CW laser spectrum is visible for  $I_{\text{injection}} > 800$  mA. At  $I_{\text{injection}}$  higher than  $\sim 840$  mA there is no well defined peak found in the RF spectrum, the peaks at various low frequencies up to 2 GHz indicate Q-switching of the laser in this regime. The modulation (with varying current) of the spectral width (clearly seen between 0.5 and 0.8 A) in the optical spectrum and background noise in the RF spectrum, are attributed to the resonance condition of the CW laser in the QDL cavity. The index of refraction of the waveguide varies with the current density and temperature variations caused by changing the cur-

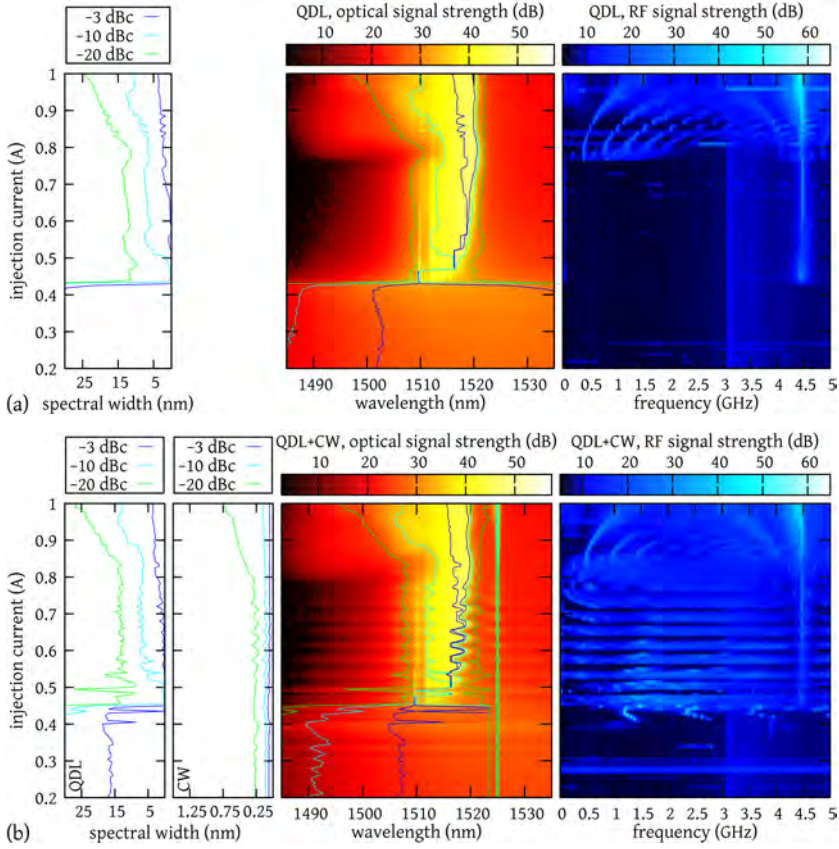


Figure 4.5: (a) Spectra of the passively mode-locked QDL. (b) Spectra of the passively mode-locked QDL with injected CW laser at  $\sim 1525$  nm. (left panel) Optical spectral widths of the QDL and the modulated CW injection laser at -3, -10 and -20 dB relative to the peak height. Optical (middle panel) and RF repetition rate (right panel) spectra of the passively mode-locked QDL. The injected optical power was 2.8 mW into the 25% port (Fig 4.4). The slight background step in the RF spectrum starting at  $\sim 3$  GHz and fading out to  $\sim 4$  GHz is an analyzer artefact.

rent density via  $I_{\text{injection}}$ . The spectral broadening of the injected CW laser, is attributed to a periodic modulation of the losses and refractive index of the SA section due to a fluctuating photo-current caused by the light pulses of the QDL traveling back and forth in the waveguide.

#### 4.3.2 Characterization of the hybridly mode-locked QDL with an injected CW laser

The injection of the QDL was repeated while hybridly mode-locking the QDL laser. The hybrid mode-locking (HML) frequency  $f_{\text{HML}}$  has been chosen for optimal HML at  $I_{\text{injection}} \sim 700$  mA. It's frequency lies in the vicinity of the passive mode-locking frequency (4.45 GHz). The injection current  $I_{\text{injection}}$  has

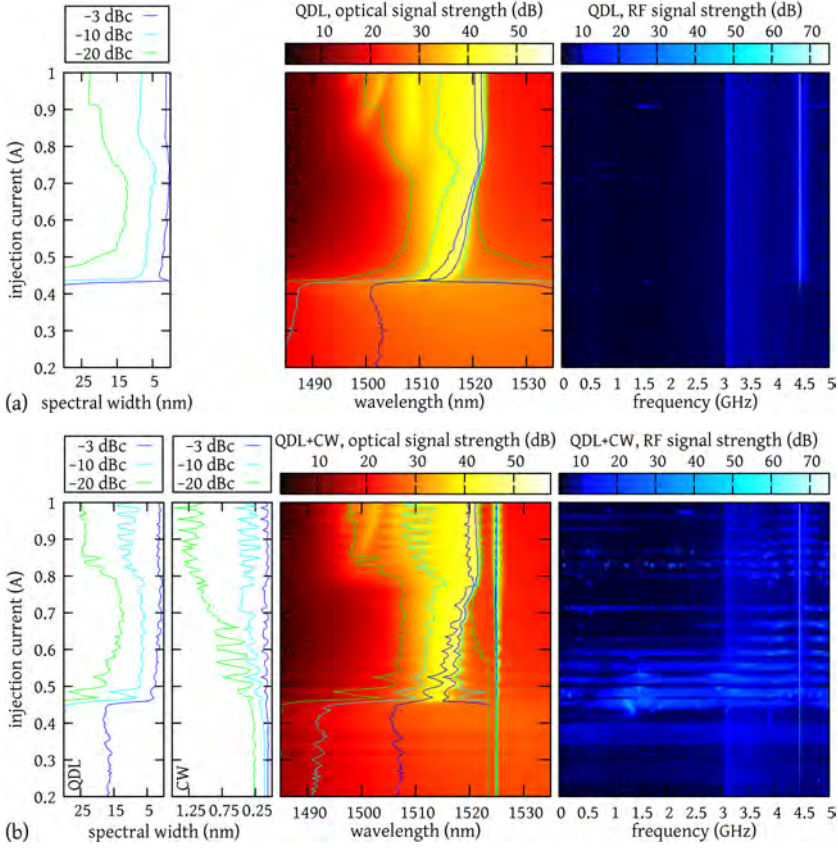


Figure 4.6: (a) Spectra of the hybridly mode-locked QDL. (b) Spectra of the hybridly mode-locked QDL with modulated CW injection laser at  $\sim 1525$  nm. (left panel) Optical spectral widths of the QDL and the injected CW laser at -3,-10 and -20 dB relative to the peak height. Optical (middle panel) and RF repetition rate (right panel) spectra of the hybridly mode-locked QDL. The injected optical power was 2.8 mW into the 25% port (Fig 4.4).

been varied from 200 mA to 1000 mA in steps of 5 mA, and for each value of the current an RF repetition rate and optical spectrum of the laser were recorded. In Fig. 4.6 and Fig. 4.7 the RF peak has been artificially broadened in frequency from the kHz resolution band width of the ESA to 10 MHz in order to make this peak visible in the RF spectra.

For below lasing threshold values of  $I_{\text{injection}}$  up to  $\sim 440$  mA the applied RF voltage to the SA section already causes modulation of the injected CW laser, which is visible as an enhanced RF peak in Fig. 4.6(b) in the RF spectrum. This is an indication that the SA section of the laser works as an electro-optical modulator (EOM) for amplitude and phase. In this case a signal to background ratio of  $> 20$  dB has been measured at  $7f_{\text{HML}}$  mode spacings from the injected CW laser.

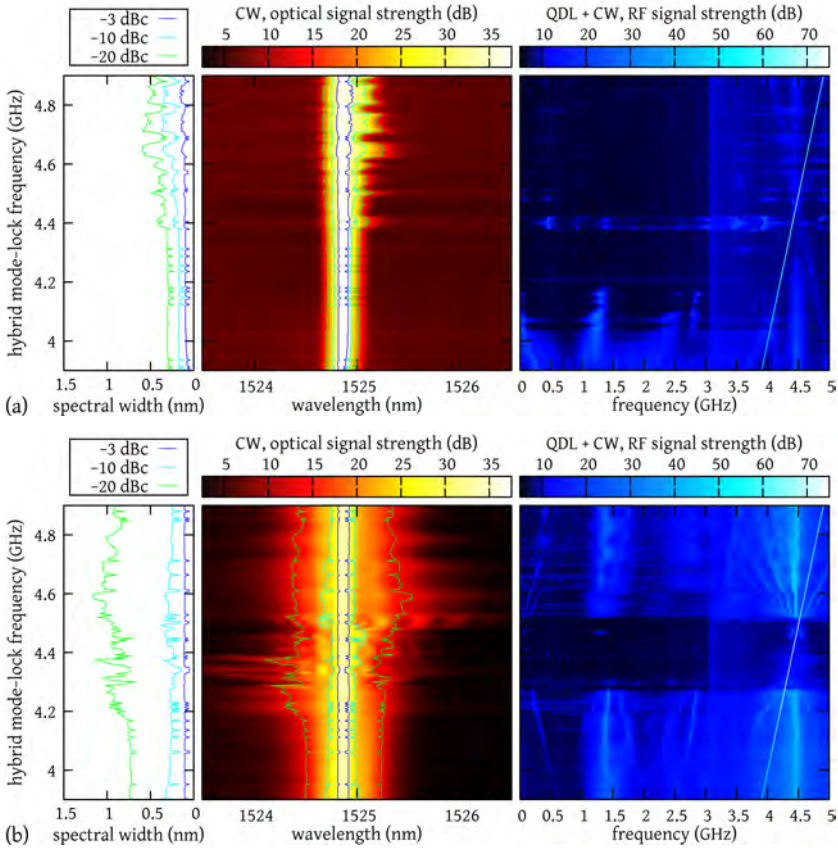


Figure 4.7: Spectral width of the modulated CW injection laser as a function of  $f_{\text{HML}}$ . Part (a) is for  $I_{\text{injection}} = 500$  mA, while part (b) shows the same for  $I_{\text{injection}} = 1000$  mA. (left panel) -3, -10 and -20 dB width of the modulated CW injection laser with respect to peak height. (middle panel) Optical spectrum of the modulated CW injection laser only. (right panel) RF repetition rate spectrum of the HMLQDL including the modulated CW injection laser. The injected optical power was 2.8 mW into the 25% port.

At  $I_{\text{injection}}$  above  $\sim 440$  mA the laser is properly hybridly mode-locked (spurious frequencies are more than 50 dB below the HML signal). Spectral broadening of the injected laser has been observed over the entire HMLQDL spectrum and up to  $\sim 25$  nm red detuned from the edge of the HMLQDL spectrum. The width of the modulation decreased when increasing the separation between the CW injection wavelength and the edge of the HMLQDL's spectrum. Both Fig. 4.5 and Fig. 4.6 show an increased modulation width with increasing  $I_{\text{injection}}$ . Hybrid mode-locking was found to increase the width of the modulation with regard to the passively mode-locked case.

### 4.3.3 Spectral width of the injected CW laser with varying $I_{\text{injection}}$ and $f_{\text{HML}}$

Since the laser itself undergoes only minor changes in its spectrum while varying the HMLQDL parameters, we will focus on the properties of the modulation imposed by the HMLQDL on the CW laser in the remainder of the article.

In the previous section the influence of  $I_{\text{injection}}$  on the width of the modulation was studied while  $f_{\text{HML}}$  was given a fixed value. To observe the influence of  $f_{\text{HML}}$  on the modulation of the CW laser, it has been varied from 3.9 to 4.9 GHz with a step size of 2 MHz for a fixed value of  $I_{\text{injection}}$  while recording the optical and RF repetition rate spectra. The results are shown in Fig. 4.7 for  $I_{\text{injection}} = 500$  mA and  $I_{\text{injection}} = 1000$  mA.

Varying  $f_{\text{HML}}$  at a low injection current of 500 mA shows various frequency ranges where the modulation depth is enhanced, mainly for frequencies above the passive mode-locking frequency. Note that the mode-locking frequency of the HMLQDL seems to follow  $f_{\text{HML}}$  over the full frequency range. This is however probably not the case, since the HMLQDL output and the modulated CW light on the detector both cause an RF peak, which masks the proper HML range of the QDL. A slightly enhanced background at the native repetition rate of the QDL up to  $\sim 4.3$  GHz and from  $\sim 4.5$  GHz are an indication that the QDL does not HML properly over the full frequency range, which is consistent with previous results for these lasers [261].

At a high injection current of 1000 mA the modulation depth is larger over the full  $f_{\text{HML}}$  range. The range for proper hybrid mode-locking however, is restricted as can be seen (Fig. 4.7(b), right panel) by strong spectral components around the natural QDL resonance frequency below  $f_{\text{HML}} \sim 4.2$  GHz and above  $f_{\text{HML}} \sim 4.5$  GHz, where the laser mode-locks at its native and hybrid frequencies. The asymmetry in the frequency range for hybrid mode-locking around the native mode-locking frequency has been observed in other HMLQDLs as well [265]. The intensity variations in the modulated injection laser spectrum as a function of wavelength for a certain  $f_{\text{HML}}$  can be a sign of self phase modulation due to gain saturation in the gain section of the HMLQDL.

An optimum in spectral width of the modulated CW laser was found for  $I_{\text{injection}} \sim 750$  mA and  $f_{\text{HML}} \sim 4.45$  GHz. This point approximately coincides with  $I_{\text{injection}}$  where the passively mode-locked QDL starts to give spurious frequencies in the RF spectrum, and where  $f_{\text{HML}}$  coincides with the passive mode-locking frequency at this value of  $I_{\text{injection}}$ . The largest spectral width of the modulated CW injection laser, determined at -20 dBc, was 1.27 nm with an injected power of 6.2 mW into the 25% port. The working point for further investigation was chosen at  $I_{\text{injection}} = 747.3$  mA and  $f_{\text{HML}} = 4.4532$  GHz.

## 4.4 Characterization of the generated frequency comb

In order to characterize the discrete modulation side-bands (these will be called comb modes from now on) imposed on the injected CW laser, high-

resolution optical spectra were taken to resolve the individual comb modes. To conclude the measurements on the generated frequency comb the optical coherence of the comb modes has been verified in an optical heterodyne-beat experiment with two CW lasers and an  $\text{Er}^{3+}$ -fiber frequency comb laser.

#### 4.4.1 High resolution optical spectra of the generated frequency comb

The setup of Fig. 4.2 has been used to acquire high-resolution optical spectra of the generated frequency comb. The CW probe laser was in this case an Agilent 8164A with 81600B tunable laser source (relative set accuracy  $< \pm 125$  MHz, linewidth  $\sim 100$  kHz, frequency stability within tens of MHz). The optical beat with the injection laser was used to characterize the generated comb. The frequencies of these comb modes are positioned at the optical injection frequency ( $f_{\text{injection}}$ ) modulo  $f_{\text{HML}}$ . The probe laser frequency was stepped through the generated comb spectrum in steps of 1–2 GHz.

With this setup optical spectra with high frequency resolution (120–600 kHz) have been measured, and a determination of the comb amplitude to background ratio could be derived from these spectra. About 1% of the light after the SOA was sent to the OSA for low resolution reference spectra, while 99% of the light was used to generate the optical heterodyne beat between the optically injected HMLQDL and the probe laser. The resulting RF spectra were measured with the ESA.

Once  $f_{\text{injection}}$  was established (in this case relative on the Agilent 81600B wavelength scale), the comb modes can be found and the peak height and signal to background ratio determined from the RF spectra by a fitting procedure. The radio band width (RBW) of the ESA was set at  $\geq 300$  kHz in order to properly record the RF power of the down converted optical modes in the photo diode signal.

Figure 4.8 shows the determined signal to background ratio for each side mode of the modulated CW laser. Mode position 0 equals  $f_{\text{injection}}$ . The average of the OSA spectra recorded during the high-resolution scan is given as a comparison (red line). The OSA wavelength scale has been calibrated with the Agilent 81600B and the peak value of the OSA was shifted to match the peak value of mode 0. The width of modulated CW laser from 0 to -20 dBc as seen on the OSA spectra can directly be compared with the width of the modulation in the high-resolution optical spectrum. The 30 dB signal to background ratio spans 23 modes, which is  $> 100$  GHz in the optical domain. These data show that we have generated a frequency comb existing of narrow modulation peaks, through modulation of the injected CW laser by the HMLQDL.

The occasional mode with a low signal to background ratio is possibly a sign of self phase modulation due to saturation in the gain section of the HMLQDL structure [266]. The asymmetry in the spectrum can be seen as a hint in this direction, as well as the fact that the modulation of the spectral intensity was observed when the power of the light coupled into the laser was relat-

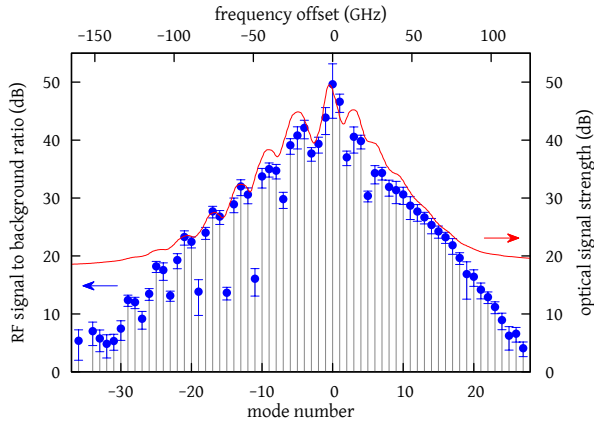


Figure 4.8: The signal to background ratio of each of the modes of the comb generated by the HM-LQDL on the CW injection laser. Each dot represents a mode of the comb. The error bars give the rms deviation. The average of the OSA spectra recorded during the probe laser scan is given by the red line. The gain profile of the quantum dot laser is nearly constant on the wavelength scale of this plot.

ively high, while  $I_{\text{injection}}$  was, at the same time, set for optimal modulation width. Despite the long measurement time causing significant deviation in the fiber in-coupling ( $> 5$  dB) which might have led to varying laser dynamics during the measurement, the generated comb was not much affected. The recorded OSA spectra show a slight variation over time. However, the correspondence of the high-resolution spectrum with the averaged OSA spectra show that these variations were not the prime cause of the reduced signal to background of some of the modes.

In a separate heterodyne beat measurement, using two Toptica DL 100/pro lasers as probe and injection laser, we determined the width of the comb modes on short time scales by use of the ESA. In this case the RBW of the ESA was set below the linewidth of the optical heterodyne beat, in order to resolve the width of the individual modes of the comb. The width of the heterodyne beat between the injection and probe laser was determined to be 140(60) kHz. The width of the heterodyne beat between comb mode 18 of the generated comb and the probe laser was 160(40) kHz, and the width of the heterodyne beat of comb mode 39 with the probe laser was 170(90) kHz. This means that there is no significant broadening of the generated comb modes with increasing mode number within the errors.

#### 4.4.2 Optical coherence of the generated frequency comb

The coherence of the generated comb was determined by an optical heterodyne experiment involving two CW lasers and an  $\text{Er}^{3+}$ -fiber frequency comb laser (FCL) as shown in Fig. 4.9. Two Toptica DL 100/pro CW diode lasers were used in this experiment. Beat frequencies ( $f_{\text{beat}}$ ) of both CW lasers with the

FCL were counted. The optical beat frequency of the second CW laser with a mode of the generated comb on the injected CW laser was also counted. The counters (Agilent 53132A) were synchronously gated using an external trigger and time gate. The FCL, ESA, counters and RF generator used to generate  $f_{\text{HML}}$  were all referenced to a rubidium atomic standard (Stanford Research Systems PRS10) phase-locked to a one pulse-per-second signal retrieved from the global positioning system.

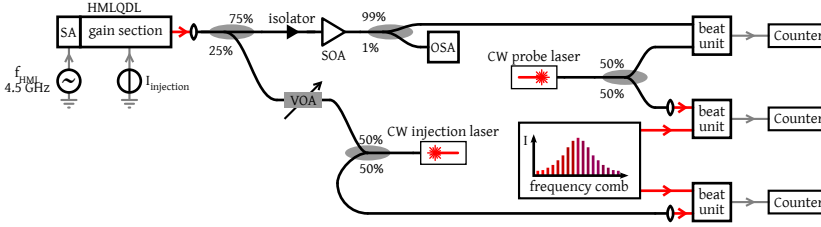


Figure 4.9: Setup used to characterize the coherence of the comb generated on the CW injection laser. HMLQDL: hybridly mode-locked quantum dot laser, SOA: semiconductor optical amplifier, OSA: optical spectrum analyzer, FCL: frequency comb laser, VOA: variable optical attenuator, gray lines: electrical signals, red lines: free space optical path, black lines: fiber optics.

Each mode of the QDL generated comb and fiber frequency comb laser can be described by  $f_n = f_{\text{CEO}} + n f_{\text{rep}}$ ,  $n \in \mathbb{N}$ , where  $f_{\text{CEO}}$  is the carrier envelope offset frequency,  $f_{\text{rep}}$  is the repetition rate frequency of the comb, and  $n$  the mode number of the comb mode. The frequency  $f_{\text{CW}}$  of a CW laser in an optical heterodyne measurement with a FCL can be expressed as:

$$f_{\text{CW}} = f_{\text{CEO}} + n \cdot f_{\text{rep}} + f_{\text{beat}}, \quad (4.1)$$

where  $n$  is the mode number of the optical comb mode with which the beat is made and  $f_{\text{beat}}$  is the RF beat frequency. Both  $f_{\text{CEO}}$  and  $f_{\text{beat}}$  can be positive or negative.

For two CW lasers and two FCLs (the HMLQDL generated comb being one of them) Eq. (4.2) and (4.3) can be written with  $m, n$  the mode numbers of the modes used for the optical heterodyne beats with comb<sub>1</sub> (FCL) and  $o, p$  for beats with comb<sub>2</sub> (QDL):

$$f_{\text{CW}_2} - f_{\text{CW}_1} = (n - m) \cdot f_{\text{repFCL}} + f_{\text{beatCW}_2, \text{FCL}} - f_{\text{beatCW}_1, \text{FCL}}, \quad (4.2)$$

$$f_{\text{CW}_2} - f_{\text{CW}_1} = (p - o) \cdot f_{\text{repQDL}} + f_{\text{beatCW}_2, \text{QDL}} - f_{\text{beatCW}_1, \text{QDL}}. \quad (4.3)$$

Note that  $f_{\text{CEO}}$  drops out of Eq. (4.2) and (4.3). Taking laser CW<sub>2</sub> as the injection laser,  $f_{\text{beatCW}_2, \text{QDL}} = 0$  since it acts as the central mode of the QDL generated comb. This is illustrated in Fig. 4.10. Equating Eq. (4.2) and (4.3) then gives:

$$\Delta f = (n - m) \cdot f_{\text{repFCL}} - (p - o) \cdot f_{\text{repQDL}} + f_{\text{beatCW}_2, \text{FCL}} - f_{\text{beatCW}_1, \text{FCL}} + f_{\text{beatCW}_1, \text{QDL}} \equiv 0, \quad (4.4)$$

where  $\Delta f$  is the measured deviation from 0 which is used to give a measure of the coherence of the generated comb. Measurement errors can be present when the S/N ratio of the heterodyne beats is too low, giving rise to false or missed counts. In the experiment the three optical beat notes were counted at various counter gate times. For this experiment the CW laser frequencies do not necessarily need to be locked, therefore the lasers were left free running.

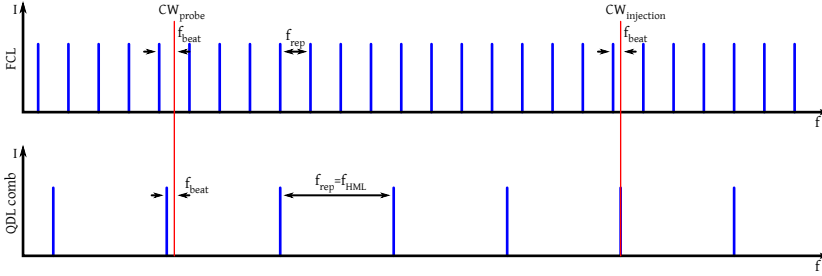


Figure 4.10: Illustration of the coherence measurement by using a frequency comb laser (FCL) and the generated QDL comb. The frequency difference between the CW lasers measured with both combs should be equal ( $\Delta f = 0$ ) if the combs are coherent at the time scale of the measurement. This can be determined using the mode number differences and measured beat frequencies ( $f_{\text{beat}}$ ).

Typical results of the measurements performed with the setup of Fig. 4.9 are shown in Fig. 4.11. The measured beat frequencies in the top part can vary with multiple MHz. The frequency deviation displayed in the bottom part of the graph was calculated from the data in the top part via Eq. (4.4). A measurement 14  $f_{\text{HML}}$  modes away from  $f_{\text{injection}}$ , corresponding to 249 modes frequency difference on the FCL gave deviations from Eq. (4.4) of  $-1.2(2.9)$  Hz at 2.0 s gate time (59 measurements),  $-0.1(2.6)$  Hz at 0.5 s gate time (61 measurements) and  $0.1(3.9)$  Hz at 0.1 s gate time (75 measurements).

The coherence of the generated comb modes has been measured up to mode 23 of the QDL comb. In this case the S/N ratio was  $\sim 25$  dB which leads to cycle slips and/or false counts. The mean of the  $\Delta f$  measurement sets is in this case at kHz level with typical rms-deviations within the sets of up to 100 Hz.

From the measurements it is clear that the comb generated by CW injection of a HMLQDL is strongly determined by the RF generator used for hybrid mode-locking and is at least tunable in  $f_{\text{rep}}$  over the range where proper hybrid mode-locking can be achieved. The  $f_{\text{CEO}}$  of the generated comb then only relies on the absolute frequency stability of the injected CW laser. Stable optical CW laser sources at  $1.5 \mu\text{m}$  can be achieved by optical locking of the CW laser on e.g. an acetylene line [267].

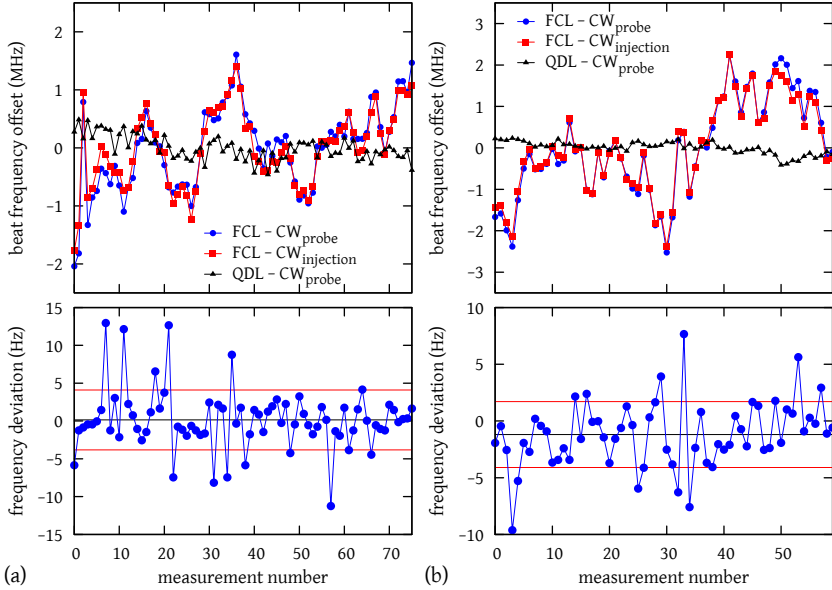


Figure 4.11: Optical heterodyne beat of 2 CW lasers with the FCL and QDL comb,  $S/N > 30$  dB at  $(p - o) = 14$ , confirming the coherence of the generated comb on the CW injection laser. (a) Frequency deviation  $\Delta f = 0.1(3.9)$  Hz at 0.1 s gate time. (b) Frequency deviation  $\Delta f = -1.2(2.9)$  Hz at 2.0 s gate time. (top part) Counted beat frequencies, offset from mean in MHz. (bottom part) Frequency deviation  $\Delta f$  for  $f_{\text{beat}}$ 's from the top part in Hz.

#### 4.5 Discussion of the physical processes in the modulator

The observation of coherent side mode generation from a CW laser that is injected into a HMLDQL naturally raises the question which processes could lead to the observed results. Especially in the hybridly mode-locked case it is clear that the modulation is caused by the modulation of the SA section of the QDL which acts as an electro-optical modulator (EOM). Amplitude modulation (via loss/gain) and phase modulation (via refractive index changes), can arise due to the electron-density changes in the SA section. The modulation strength might be enhanced by the quantum dot material [268]. It appears that the mode-locked laser action is not greatly influencing the side-mode generation and gives rise to the question if it is important at all for the workings of the device as an EOM.

In the case of the passively mode-locked laser, the observed small modulation depth of the injected laser can be caused by modulation of the photocurrent (loss/refractive index) in the SA section of the QDL because of the light pulse circulating in the laser, and by phase modulation via the quantum dot material. In case of hybrid mode-locking this light pulse is influenced by the alternating loss and gain during the RF cycle, which causes a much stronger modulation of the CW laser. Moreover, this modulated light is then

amplified in the gain section of the laser, which can give rise to non-linear optical effects if it is optically saturated. That the modulation is enhanced with gain can be seen from the increasing strength of the  $f_{\text{HML}}$  peak with increasing current in Fig. 4.6(b) below lasing threshold, and by the increasing width of the generated comb spectrum on the injection laser above threshold. The conclusion that gain plays a role is further supported by the fact that the width of the comb spectrum narrows when the wavelength of the injected laser is moved towards the edge of the gain spectrum of the QD material [245], where the modulation strength in the SA section and amplification in the gain section are smaller.

## 4.6 Conclusions and outlook

In this article, coherent modulation of a CW laser injected into a HMLQDL resulting in frequency comb generation has been demonstrated. Possible mechanisms behind this modulation have been proposed, however a full understanding is still lacking. Comb generation is possible in the gain spectrum of the QD material. The generated comb is decoupled from the HMLQDL laser action. The central frequency of the resulting comb can be changed by tuning the wavelength of the injected CW laser. Tuning of  $f_{\text{rep}}$  is provided by the hybrid mode-locking frequency of the QDL, while  $f_{\text{CEO}}$  can be tuned by using both  $f_{\text{rep}}$  and the absolute frequency of the CW injection laser. The 30 dB signal to background range of the generated modulation extended over 23 modes ( $> 100$  GHz). Phase coherence of the generated comb has been shown at the level of 0.1(3.9) Hz deviation for timescales of 0.1 to 0.5 seconds, at mode 14 ( $> 60$  GHz) from the injected laser (mode 0). It provides strong evidence for full coherence of the generated comb of which more than 60 modes could be resolved.

One of the applications of these generated coherent combs could be phase locking of telecommunication lasers on neighboring channels in dense wavelength division multiplexing (DWDM) optical networks. Another application could be harmonic generation of a GHz RF source by optical mode filtering of the generated comb, providing stable frequency sources at  $> 100$  GHz when the light is converted back to the RF by a fast photo diode. The generated comb could also be used as a basis for several telecommunication modulation schemes. We note however, that the comb flatness (3 dB bandwidth) needs improvement, see e.g. [259, 269], before this is feasible for some of the modulation schemes proposed in the introduction.

We conclude from this experiment that coherent narrow linewidth frequency comb generation and amplification is possible in the used InAs/InP quantum dot material. Modifications to the laser cavity like a high-Q resonator and intra-cavity dispersion control, can lead to narrow linewidth ( $< 100$  kHz), short pulse ( $< 100$  fs) frequency comb lasers, paving the way towards fully integrated, robust, narrow linewidth, self referenced semiconductor frequency comb lasers.

## Acknowledgments

The authors thank Sylwester Latkowski for helpful comments and discussions, and W. Kaenders of TOPTICA Photonics for making available the two DL 100/pro CW diode lasers used in the present experiment. This work was supported by the Netherlands Ministry of Economic affairs through a IOP Photonic Devices program grant as well as via the MEMPHIS (Merging Electronics and Micro & Nano-Photonics in Integrated Systems) program.

# 5. Tunability and phase stability of extreme ultraviolet frequency comb lasers

In Sec. 5.1 (published in Optics Letters [179]) an experiment is described demonstrating widely tunable extreme ultraviolet (XUV) frequency comb generation based on the Ramsey comb method. Some of the details of this experiment that were not published before are presented in Sec. 5.2, including an estimation to what short wavelengths the method could be feasible.

## 5.1 Widely tunable extreme UV frequency comb generation

**Abstract:** Extreme ultraviolet (XUV) frequency comb generation in the wavelength range of 51 to 85 nm is reported based on high-order harmonic generation of two consecutive IR frequency comb pulses that were amplified in an optical parametric chirped pulse amplifier. The versatility of the system is demonstrated by recording direct XUV frequency comb excitation signals in helium, neon and argon with visibilities of up to 61%.

### 5.1.1 Introduction to XUV frequency combs

Frequency comb (FC) lasers have become an important tool in many fields of physics, ranging from precision spectroscopy [36, 37], to attosecond science [270]. Typical FCs cover only the infrared to UV wavelengths due to the availability of laser materials and the use of low-order frequency conversion. Extension of FCs to much shorter wavelengths such as extreme ultraviolet ( $\lambda < 100$  nm) is pursued by several groups through high-harmonic generation (HHG). It has been shown that HHG can result in (to some degree) phase coherent up-conversion of ultrafast pulses. This has been shown for a single amplified pulse [271], an amplified pulse split in two (spatially or temporally) [271, 272], and for an infinite FC pulse train enhanced in a resonator cavity [184, 185, 273]. Alternatively, phase-coherent amplification of two or more FC pulses in combination with low and high harmonics has been demonstrated as well [155, 274, 275], and to the best of our knowledge only in this case could precision metrology in the XUV be shown [155].

In this Letter we demonstrate the versatility and tunability of the method based on FC amplification and up-conversion of only two FC pulses by recording XUV frequency comb (XFC) spectroscopic signals over ranges between 51 nm and 85 nm in helium, neon and argon. With two pulses the spectrum still peaks at the positions determined by the modes of the original FC, but now in the form of a cosine-like modulation. The broad 'modes' are not limiting the resolution, as the time between the pulses can be increased to reduce the mode distance and therefore increase the resolution (the mode spacing is inversely proportional to the delay of the pulses) [275]. After amplification and HHG in a gas jet, the XUV pulses are used to directly excite a transition in a

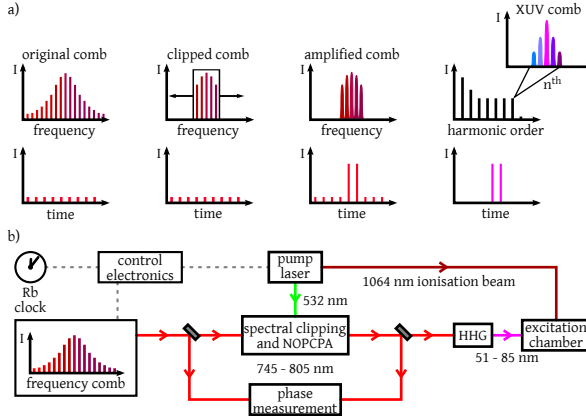


Figure 5.1: (a) Time and frequency domain structure in the XFC system. From left to right: FC output, spectrally clipped FC, amplified FC, FC after HHG. (b) The XFC spectroscopy system, where two FC pulses are amplified in the NOPCPA, upconverted by HHG for direct XFC spectroscopy.

noble gas. By changing the repetition rate of the FC in the IR, the modes in the XUV are scanned over the transition. This results in a cosine-like excitation spectrum, much like in Ramsey spectroscopy [69].

### 5.1.2 Overview of the frequency comb laser system

A schematic of the system can be seen in Fig. 5.1. The FC delivering the phase-coherent pulses is based on Ti:sapphire, with an average power of 800 mW and a pulse duration of less than 20 fs. The repetition-rate ( $f_{\text{rep}} = 150$  MHz) and carrier-envelope offset frequency ( $f_{\text{CEO}} = 37.5$  MHz) of the FC are referenced to a GPS-disciplined Rb clock. Amplification of two pulses from the FC takes place in a 3 stage non-collinear optical parametric chirped pulse amplifier (NOPCPA). The pump laser for this system has been designed to produce two 50 ps pulses of  $\approx 100$  mJ at 532 nm that are delayed carefully to match the time separation of the FC pulses. that carefully match the pulse time separation of the FC. Two FC pulses, each less than 0.5 nJ in energy and  $\approx 2$  ps long after the stretcher, are amplified in the NOPCPA system to 5 mJ using two beta-barium-borate (BBO) crystals. After re-compression in a grating compressor, 1–2 mJ per pulse is available for HHG.

To generate the XFC, the 6.1 mm diameter amplified IR beam is focused with a 50 cm lens into a pulsed noble gas jet (Kr for the 15<sup>th</sup> harmonic, Xe for 13<sup>th</sup> and lower harmonics). Only a single transition should be excited by the XFC, otherwise a reduction in contrast and uncontrolled shifts of the cosine-shaped signal can occur. The transition frequency can be obtained from this signal because a maximum occurs each time the transition comes into resonance with one of the XFC modes centered at  $f_m = qf_{\text{ceo}} + mf_{\text{rep}} + \Delta\phi_{\text{eff}}f_{\text{rep}}/2\pi$ . In this expression  $q$  is the harmonic order,  $m$  is the mode number, and  $\Delta\phi_{\text{eff}}$

is an effective differential phase shift at the transition frequency that takes phase shifts in the IR (e.g. due to the NOPCPA [177]) and the HHG process into account [155]. The XUV bandwidth (the XFC wavelength span,  $<0.1$  nm) is controlled by a slit in the Fourier plane of the stretcher, which limits the amplified spectrum in the IR to 6 nm for the helium and neon spectroscopy, and to 3 nm for the argon spectroscopy. The central XFC wavelength can be coarsely tuned by changing the position of the slit in the stretcher, selecting IR wavelengths between 805 to 740 nm at the fundamental.

The XUV light is crossed perpendicularly with a low divergence ( $<3$  mrad) pulsed atomic beam. Whenever one of the XFC modes comes into resonance, a peak in the excitation probability occurs. Excited atoms are detected via ionization with a 1064 nm pulse and a time-of-flight mass spectrometer. A channel electron multiplier is used to count the ions, while the XUV intensity of the harmonic used for excitation is measured with a grating monochromator and a photomultiplier.

### 5.1.3 Demonstration of wavelength tunability

The tunability of the system at the conditions required for XFC generation is demonstrated first by performing coarse spectroscopy on helium, neon and argon with a single up-converted pulse of the frequency comb's pulse train (which does not form a comb). By changing the IR intensity and the gas medium for HHG, the cutoff photon energy is tuned to the harmonic that is used for the spectroscopy (9<sup>th</sup> for Ar, 13<sup>th</sup> for Ne and 15<sup>th</sup> for He). In this way direct ionization due to XUV light of higher harmonic orders is minimized. To record these spectra, the ion signal was measured at each wavelength (with steps of 0.25–1 nm in the IR) for 500 laser shots while scanning the slit in the stretcher. Signal from ionization (10–20%) due to higher HHG orders was measured by blocking the ionization beam and subtracted from the signal.

Fig. 5.2 (lower part) shows these spectra of ground-state transitions in argon, neon and helium (the arrows indicate NIST database line positions for comparison [276]). In argon the transitions to the excited states  $3p^5(^2P_{3/2})4d[1/2]_1$  to  $3p^5(^2P_{1/2})6s[1/2]_1$  have been recorded. In neon excitation to  $2p^5(^2P_{3/2})5s[3/2]_1$  to  $2p^5(^2P_{3/2})7d[3/2]_1$  is shown and in helium the  $1snp\ ^1P_1, n \in \{4, \dots, 9\}$  series can be distinguished up to  $n = 9$ . The XUV scanning range was determined at the low energy side by the requirement that the 1064 nm beam could ionize the excited state.

### 5.1.4 Frequency comb spectroscopy at XUV wavelengths

To generate an XFC, a second amplified and up-converted pulse was added, and care was taken that the HHG process did not saturate ( $I_{IR} < 5 \times 10^{13}$  W/cm<sup>2</sup> for krypton, and a factor of 2 lower for HHG in xenon). In this manner two phase coherent XUV pulses are produced, leading to a cosine-modulated spectrum. The mode spacing in the XUV remains the same as that of the original FC in the infrared, which was close to  $f_{rep} = 150$  MHz. Given the XUV spec-

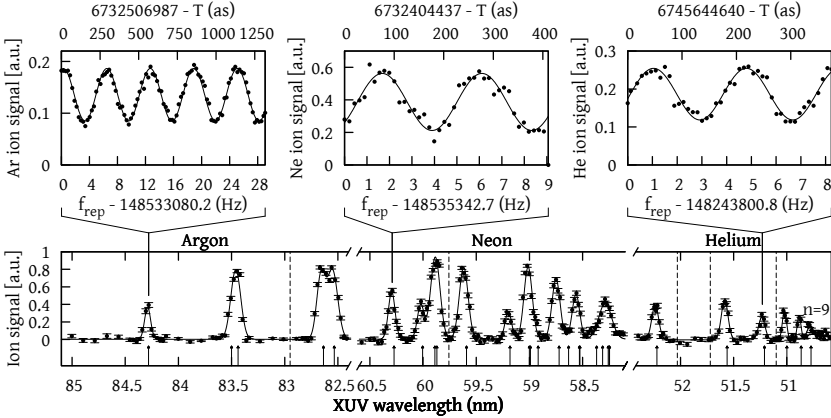


Figure 5.2: Single pulse (bottom) and double-pulse XFC (top) spectra of argon, neon and helium. The wavelength axis calibration in the lower part is obtained with an Ando AQ6315A spectrometer in the IR (accurate to 0.03–0.06 nm). The vertical dashed lines indicate separate measurements sessions, while the arrows indicate NIST database line positions [276] for comparison. The top row shows the XFC signal measured on the Ar  $3p^5(^2P_{3/2})4d[1/2]_1$  (contrast  $\approx 37\%$ ), Ne  $2p^5(^2P_{3/2})5s[3/2]_1$  (45%) and He  $1s6p$  (36%) state by scanning  $f_{\text{rep}}$  of the FC. For helium a mixture with neon was used to reduce Doppler broadening to 40 MHz.

tral width, there are approximately  $2.8 \times 10^4$ – $8.0 \times 10^4$  XFC modes present for a central wavelength of 85–51 nm. The slit in the stretcher was used to select a particular transition, and the repetition rate of the FC in the IR was then scanned to move the comb modes over the transition. The upper part in Fig. 5.2 shows this XFC signal recorded for selected transitions in helium, neon and argon. The signal (based on approximately 20000–40000 laser shots, binned into 20 groups per XFC excitation signal period) is normalized to the measured average XUV-intensity.

In [155] we demonstrated that from the XFC signal in helium (similar to that shown in Fig. 5.2), the transition frequencies can be obtained with up to 6 MHz accuracy at 51 nm. For the wavelength range presented here in argon and neon, at least a similar accuracy can be obtained experimentally, as all the systematic and statistical errors are expected to be smaller. However, a comparison with theory is hampered by a lack of sufficiently accurate calculations in Ne and Ar. Therefore we concentrate in this Letter on the tunability and contrast (defined as the signal amplitude over the average) of the XFC signal. This contrast is mostly influenced by Doppler broadening, lifetime of the excited state relative to the pulse delay, background from direct ionization by higher harmonics, and phase noise introduced in the NOPCPA (typically tens of mrad in the IR) and HHG. Phase shifts common to both pulses do not lead to a shift in the mode spectrum, or contrast reduction. However, a differential phase shift  $\Delta\varphi$ , changes the frequency of the modes according to  $\Delta f = f_{\text{rep}}\Delta\varphi/(2\pi)$ . HHG introduces an IR intensity dependent adiabatic phase shift in the emitted harmonics [176,194], and accompanying ionization

can also lead to phase shifts as large as 2 rad [155]. Because of these effects, phase noise due to variations in IR intensity, pulse intensity ratio and HHG medium density can reduce the contrast of the measured comb modulation. Doppler broadening is reduced for helium in the supersonic atomic beam by mixing it with neon and argon, leading to a helium velocity of 830(200) m/s and 500(250) m/s respectively [155].

The highest XFC signal contrasts (averaged over several measurements) were seen in helium (55% when seeded in argon) and argon (61%), while for neon a contrast of 43% was observed. Measurements on one transition varied up to 10% in contrast. We use a model assuming a Gaussian shape XUV phase noise and Doppler profile to obtain an estimation for the atomic beam divergence and XUV jitter from the measurements. This results in an atomic beam divergence of 2.4 mrad (FWHM) and an XUV phase jitter of 0.40(13), 0.46(9) and 0.41(10) cycles for the He, Ne and Ar measurements respectively. For helium almost a factor 2 lower XUV phase noise is expected based on the stability of the frequency comb (1.6 MHz mode line width) and NOPCPA pulse energy stability (6% rms). For argon measurements, even lower XFC noise is expected due to the lower harmonic (9th compared to 15th for helium). No clear correlation between the contrast and IR intensity, intensity jitter or harmonic order is observed in the measurements, which might indicate an underestimation of the influence of density variations in the HHG jet, or the bandwidth of the FC modes in the IR.

### 5.1.5 Conclusion and outlook

In conclusion, we have demonstrated widely tunable (51–85 nm) XUV comb generation and spectroscopy based on amplification and up-conversion of two frequency comb laser pulses. With the present setup continuous tuning down to 47 nm is possible, and with higher harmonics even 25 nm should be feasible with >10% contrast. However, the latter has not been tested due to a lack of suitable transitions. A sub-MHz accuracy should become possible by employing pulses with a bigger time separation, combined with further Doppler broadening reduction using e.g. a two-photon transition.

This work was supported by the FOM through its IPP program "Metrology with Frequency Comb Lasers", NWO through a VICI grant, the EU via FP7 JRA ALADIN, and by the Humboldt Foundation.

## 5.2 Appendix: Estimation of the phase jitter of the Ramsey comb in the XUV

In this section parts of sections 2.5.3, 2.8.4 and 2.6.1 will be used to model the contrast of the signals obtained from the helium, neon and argon spectroscopy. This model underlies the XUV phase stability calculations of which the results appeared in [179]. In this case, from a measured contrast a minimum XUV phase stability is calculated to obtain this contrast from the best estimates for certain experimental parameters. Relatively many assumptions have

been made, since exact properties, e.g. of the atomic beam, have not been separately measured due to the fact that the need for contrast calculations came up after the experiment was completed. Nevertheless, because the resulting XUV phase jitter is a worst-case estimation it provides valuable input for calculations to estimate Ramsey fringe contrasts at shorter wavelengths.

### 5.2.1 Modelling the Ramsey fringes

The Ramsey signal is modelled after equation (2.72) with a slight modification due to radiative decay of the excited atom, which is significant since the lifetime of the excited states (especially in He) is on the order of  $1/f_{\text{rep}}$  and should therefore be taken into account. We assume that the signal detection (ionisation pulse) takes place at a timescale  $\ll 1/f_{\text{rep}}$  (typically within 1 ns) after the second excitation pulse so that radiative decay after the second pulse can be neglected. The signal is therefore equal to

$$S(f_{\text{rep}}) = |c_{e,2 \text{ pulses}}|^2 = |c_{e,p_1}|^2 e^{-\frac{A_{21}}{f_{\text{rep}}}} + |c_{e,p_2}|^2 + 2 |c_{e,p_2}| |c_{e,p_1}| e^{-\frac{A_{21}}{2f_{\text{rep}}}} \cos \left\{ 2\pi \left( \frac{f_{\text{tr}} + f_{\text{CEO}}}{f_{\text{rep}}} \right) \right\}, \quad (5.1)$$

where  $c_{e,p_{1,2}}$  are the excitation amplitudes due to pulse 1 and 2 which are proportional to the pulse intensity,  $f_{\text{tr}}$  is the transition frequency, and  $A_{21}$  is the Einstein A coefficient which determines the spontaneous emission rate. Equation (5.1) gives the excitation probability immediately after the second pulse. Figure 5.3 shows the excitation rates for Einstein A coefficients near  $f_{\text{rep}}$ .

The contrast  $C$  of the Ramsey signal  $S$  is given as

$$C(S) = \frac{\max(S) - \min(S)}{\max(S) + \min(S)} \quad (5.2)$$

where  $\min(S)$  is the level of the minima and  $\max(S)$  is the level of the maxima of the signal. In the case that  $1/A_{21}$  (the decay time) is much faster than the pulse delay the contrast will be near zero, although an average excitation  $|c_{e,p_2}|^2$  of the atomic ensemble remains due to the second excitation pulse, as can be seen in Fig. 5.3. In the following simulations to determine the phase jitter, the parameter  $f_{\text{CEO}}$  is neglected as it has no influence on the contrast.

### 5.2.2 Modelling of the atomic beam properties

In order to determine the Doppler profile due to the atomic beam configuration of Fig. 2.9, the longitudinal velocity distribution along the laser beam needs to be known, as well as the atomic density profile.

The configuration of the valve and skimmers, determining the shape of the atomic beam, is given in Fig. 5.4. This configuration exists of a pulsed General Valve, a circular skimmer of 0.5 mm diameter and a slit skimmer with

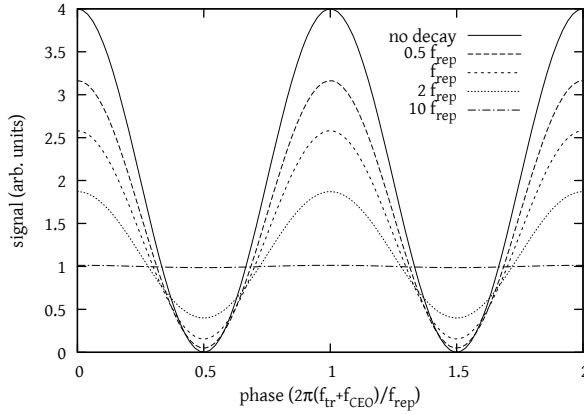


Figure 5.3: Ramsey signal as function of the phase  $2\pi(f_{\text{tr}} + f_{\text{CEO}})/f_{\text{rep}}$  for decay rates  $A_{21}$  in the order of  $f_{\text{rep}}$ . For increasing excited state decay rate the contrast decreases, although a certain amount of signal remains due to the second excitation pulse. The excitation amplitudes are normalised ( $c_{e,p1,2} = 1$ ).

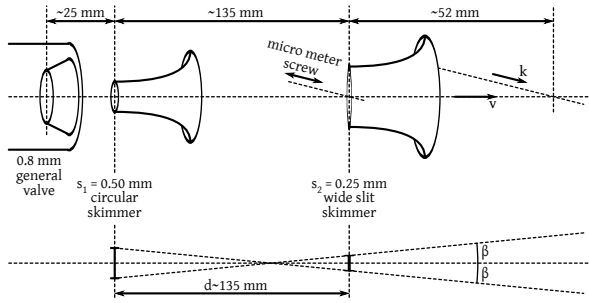


Figure 5.4: The atomic beam setup as used in the crossed beam XUV spectroscopy experiments. Two skimmers are used to obtain a beam with a narrow opening angle from a General Valve (electromagnetic valve). The maximum opening angle is given by the geometry as depicted in the bottom half of the figure. The second skimmer is a slit which can be moved by a micrometer to adjust the angle between the atomic and XUV beam for (near) Doppler-free excitation.

a width of 0.25 mm. This effectively creates a highly directional gas “screen”, where the maximum velocity in the direction of the XUV beam is limited by the transverse velocity component of the atomic beam due to the maximum possible beam half angle

$$\beta = \arctan\left(\frac{s_1 + s_2}{2d}\right) = \arctan\left(\frac{0.5 + 0.25}{2 \cdot 135}\right) = 2.8 \text{ mrad} \quad (5.3)$$

where  $s_{1,2}$  are the skimmer widths and  $d$  the distance between the skimmers. Thus the maximum full beam angle is  $2\beta = 5.6 \text{ mrad}$ .

A time-of-flight profile of the atomic beam, measured by scanning the pulsed valve opening time with respect to a single pulse excitation and ion-

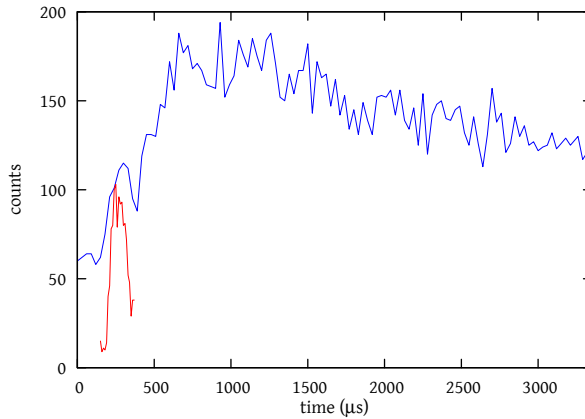


Figure 5.5: Time of flight (TOF) ion signal of the atomic beam obtained by scanning of the pulsed valve opening time with respect to the excitation, ionisation pulse pair. In this case a single pulse excitation is used in order to avoid a minimum on the Ramsey fringe. The long signal shows an initial scan, where the atoms scattering off the back of the chamber fill the whole beam path causing a large signal after 500  $\mu\text{s}$ . A second scan (red line) was repeated a day later with a higher resolution to get a better impression of the shape of the He pulse. The pulse length is in the order of 150  $\mu\text{s}$ .

isation sequence is depicted in Fig. 5.5. The duration of the supersonic expansion of the atomic beam is about 150  $\mu\text{s}$ . During the frequency comb excitation (ns time scale) we interact with only a fraction of the full atomic beam selecting a particular velocity class. Moreover the supersonic expansion leads to a higher forward velocity in the beam, but with a much narrower velocity distribution than a thermal beam. We therefore neglect this velocity distribution of the atomic beam in the contrast and XUV phase jitter analysis.

The exact beam velocities can not be derived from these measurements, but have been derived during the helium spectroscopy, by varying angle  $\delta$  (see Fig. 2.9) between the XUV and atomic beam and observing the shift of the helium transition frequency for a pure helium beam and mixtures of helium:neon and helium:argon (1:5). The measured beam speeds and the maximum transverse velocity are given in Table 5.1 as measured by Kandula [178]. The forward velocity is that of the supersonic gas expansion from the general valve (backing pressure 3 bar). For pure noble gasses used to record Ramsey fringes at other than 51 nm, the beam speed is assumed to be equal to that of the seeded helium beams.

The speed ratio for of forward velocity and transverse velocity component of the atomic beam is  $\beta$  for small beta. It should be noted that the Doppler shift is proportional to the angle at each position in the beam. The spectroscopy signal strength is proportional to the amount of atoms, which is also a function of the angular position. Therefore the first order Doppler profile

Gas	forward velocity (ms <sup>-1</sup> )	maximum transverse velocity (ms <sup>-1</sup> )
He	2000(320)	±11(1.8)
Ne	830(200)	±4.6(1.1)
Ar	500(250)	±2.8(1.4)

Table 5.1: The beam speeds for the supersonic helium beams seeded in the given seed gasses. The He:seed ratio is 1:5. We assume that the beam speed is determined by the seed gas. The size of the standard deviation is mainly due to the uncertainty in the velocity determination. The actual velocity spread in the supersonically expanding beam is expected to be much less.

will be proportional to the angular atomic density function.

$$f_{\text{Doppler}}(\beta) = \frac{f}{c}\beta v \quad (5.4)$$

$$I(f_{\text{Doppler}}) = N(f_{\text{Doppler}}) \quad (5.5)$$

where  $f$  is the laser frequency,  $\beta$  is the atomic beam angle,  $v$  the atomic velocity and  $c$  the speed of light,  $I(\beta)$  is the spectroscopy signal intensity which depends on the atomic density function  $N(\beta)$ .

The density functions proposed for  $N$  are the normalised rectangular, triangular or Gaussian functions

$$\text{rect}(w, x_0) = \{u(x - x_0 + w) - u(x - x_0 - w)\}, \quad (5.6a)$$

$$N_{\text{rect.}}(w, x_0) = \frac{1}{2w} \text{rect}(w, x_0), \quad (5.6b)$$

$$N_{\text{tr.}}(w, x_0) = \left\{ \frac{1}{w} - \frac{|x - x_0|}{w^2} \right\} \text{rect}(w, x_0), \quad (5.6c)$$

$$N_{\text{Gauss.}}(w, x_0) = \frac{2\sqrt{\ln 2}}{w\sqrt{\pi}} \exp \left\{ -4 \ln 2 \cdot \frac{(x_0 - x)^2}{w^2} \right\}, \quad (5.6d)$$

where  $u(x)$ , is the unit step function,  $w$  is the full-width half-maximum (FWHM) of the function, and  $x_0$  is the central position of the function. For the rectangular function  $w$  is actually half the width of the rectangle. This definition creates consistency with regard to the maximum atomic beam angle possible in the actual skimmer geometry, because the rectangular function would otherwise only fill half the possible beam angle of the other functions for a given  $w$ . The functions given in equations (5.6) are plotted in Fig. 5.6.

It is to be expected that under a uniform angular distribution for each position in the first skimmer, the atomic density behind the second skimmer should resemble a triangular function. However it could be likely that collisions of the atoms after the first skimmer might lead to a more uniform distribution, like a Gaussian shape, with the rectangular shape as a limiting case.

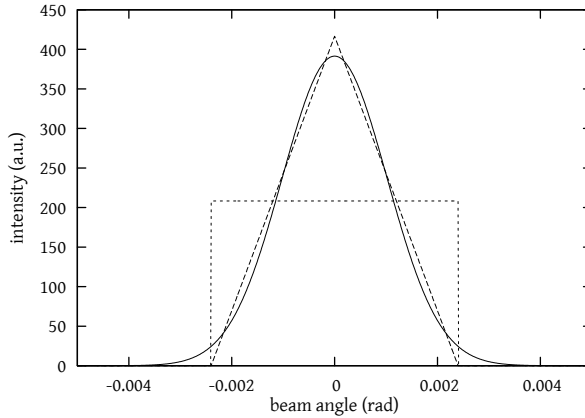


Figure 5.6: Doppler profiles used in the XUV phase jitter determination. The FWHM is 2.4 mrad, which is the value for which the XUV jitter values have been determined in Chapter 5.

The Doppler profiles of equation (5.5) act as filters on the Ramsey signals modelled, decreasing the contrast  $C$  of the Ramsey fringe. The reduction of contrast can be found by convolution of these functions with the Ramsey signal.

### 5.2.3 Modelling of the XUV phase jitter

The carrier phase difference between the first and second pulse used for the Ramsey spectroscopy depends on the intensity ratio of the amplified frequency comb pulses. There are two indistinguishable effects. The first effect is due to the phase dependence of the HHG process on the intensity via the classical action integral (equation (2.83)). The second effect is that of the refractive index difference in the HHG gas jet due to the electron density caused by ionisation of the gas by the first HHG pulse. This refractive index change causes a phase shift of the fundamental and, through the HHG process, also on the harmonics of the second frequency comb pulse.

The frequency shift  $\Delta f$  of the Ramsey fringe due to a phase offset  $\varphi$  of the second XUV pulse with respect to the first, is given as

$$\Delta f(\varphi) = \frac{\varphi}{2\pi} f_{\text{rep}} \quad (5.7)$$

where the phase offset is in radians.

The phase jitter process has been assumed to yield a normal probability density around a central fixed value (whose absolute value has been determined in the helium metrology experiment as part of the systematic effects). Thus equation (5.6d) with a FWHM  $w = \Delta f$  corresponding to a certain root mean square value of the phase jitter  $\varphi$  has been used to model this effect.

As with the Doppler profile, the phase jitter profile obtained via equations (5.7) and (5.6d) can be used as a filter that reduces the contrast of the Ramsey fringe.

### 5.2.4 Modelling of the spectroscopy signal

In order to model the spectroscopy signal and obtain a contrast as it is measured in the experiment, a background signal due to direct ionisation needs to be accounted for. This background signal is a more or less constant fraction of 1–20% of the average level of the ion signal, depending on the atomic species under investigation and the strength of the atomic transition.

The intensity of the fundamental is chosen such that the excitation harmonic (e.g. the 15<sup>th</sup>) is exactly at the cut-off frequency of the HHG process. The next higher harmonic, which typically lies above the first ionisation energy of the atom, can still be present at about 10% of the intensity of the excitation harmonic, and causes direct ionisation of the atoms under investigation. This leads to a background signal that cannot be separated from the Ramsey fringes.

The direct ionisation fraction is modelled by adding a constant background to the signal, according to the amount determined during the performed spectroscopy. The background fraction  $b$  is defined as

$$b = \frac{S_{\text{back.}}}{\langle S_{\text{spec.}} \rangle} \quad (5.8)$$

where  $S_{\text{back.}}$  is the absolute background signal level and  $\langle S_{\text{spec.}} \rangle$  is the average spectroscopy signal level.

The spectroscopy signal  $S_{\text{spec.}}$  is modelled by generating a Ramsey signal ( $S(f_{\text{rep}})$ ) according to equation (5.1). Doppler (equation (5.5)) and XUV jitter ((5.7)) are taken into account by convolution with the Ramsey signal, and the background fraction is added

$$S_{\text{spec.}} = S(f_{\text{rep}}) * I(f_{\text{Doppler}}) * I(f_{\text{XUV}}) + S_{\text{back.}}, \quad (5.9)$$

where  $*$  denotes a convolution. The contrast of the modelled signal can then be determined via equation (5.2) and used to make various estimations.

### 5.2.5 Estimation of the XUV phase jitter

To estimate the XUV phase jitter, the minimum value for the difference in contrast between experiment and simulation have been determined. A series of measurements have been selected in helium, neon and argon, although the neon and argon spectroscopy signals were never recorded with the intention of a phase jitter analysis in mind. The latter measurements therefore show a larger spread in both beam angles and XUV phase jitter, which are to some extent interchangeable in the model.

The calculated contrasts for varying atomic beam divergence and XUV phase jitter have been compared with contrasts obtained in the He, Ne and

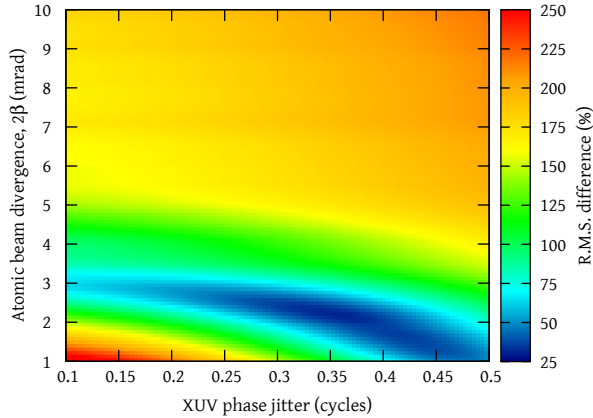


Figure 5.7: Root mean square difference between simulated and experimental contrasts assessed on the combined  $1s^2-1snp$   $n \in \{5, 6, 7\}$  measurements in He. A minimum is seen around beam angle  $\beta \approx 2.4$  mrad and and XUV jitter of  $\sim 0.4$  rad indicating that those are the most probable values for the experiment.

Ar spectroscopy by calculation of the root mean square (R.M.S.) over many wiggles. From these calculations an atomic beam angle has been estimated and the XUV phase jitter at this atomic beam angle was determined. The result of the assessment for the combined  $1s^2-1snp$   $n \in \{5, 6, 7\}$  measurements in He is given in Fig 5.7. It is assumed that this dataset has the best internal consistency, since the conditions during the helium measurements have been held as equal as possible.

The outcome of the assessment has resulted in the determination of an atomic beam divergence of 2.4(0.8) mrad (FWHM). The corresponding XUV phase jitter was 0.40(13), 0.46(9) and 0.41(10) cycles for the helium, neon and argon measurements respectively.

### 5.2.6 Estimation of contrasts in XUV spectroscopy

The values for XUV jitter and beam angle, obtained from the R.M.S. difference calculation, can be fed back into the calculation to obtain estimates of potential contrasts for various other atomic transitions. This is particularly interesting for 2-photon transitions, where the upper state typically has a large lifetime, which can be measured in a Doppler free or reduced regime.<sup>1</sup> For a certain atomic beam divergence and beam speed, the obtainable contrasts for various values of the XUV jitter can then be predicted.

The exercise has been done for ground state transitions in helium, neon and argon and the results presented in Fig. 5.8. It can be seen that the lower

<sup>1</sup>Note that in a crossed beam experiment in a counter propagating configuration with a pulsed atomic beam, one can still have a Doppler shift due to possible wavefront differences for the laser beams coming from opposite sides.

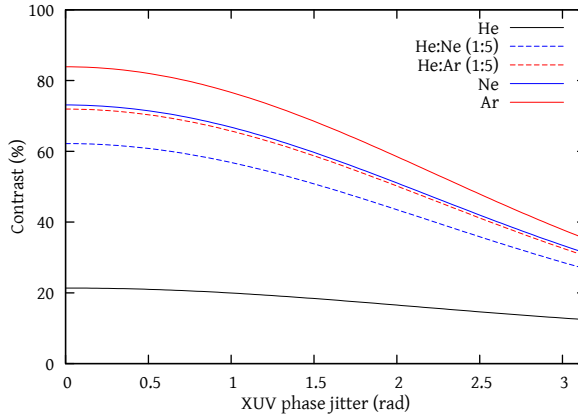


Figure 5.8: Calculated contrasts as a function of XUV phase jitter. It is seen that the speed of the atomic beam has a large impact on the contrasts that can be reached, but that the upper state lifetime, especially in He, plays an important role too. Upper states are: He 5p ( $t_{\text{spont}} \approx 7.7$  ns), Ne 5s ( $t_{\text{spont}} \approx 19.5$  ns), Ar 4d ( $t_{\text{spont}} \approx 168.0$  ns).

atomic beam velocities for a fixed atomic beam angle of 2.4 mrad, lead to a significant increase in signal contrast (pure helium versus seeded helium beams) at zero XUV jitter. The increase in contrast for neon and argon at zero XUV jitter is due to the longer excited state life times.

### 5.2.7 Extending contrast estimations to shorter wavelengths

Combinations of XUV phase jitter values together with Doppler broadening or, in the case of a Doppler-free configuration without, give predictions for maximally obtainable contrasts in XUV spectroscopy. In order to project these results out to shorter wavelengths, one has to take several properties of the HHG process into account as well, amongst others  $I_p$ ,  $U_p$  and thus the IR intensity needed to reach up to a certain wavelength given a certain gas in which HHG is performed.

This has been done for two-photon transitions up to 20 nm (an effectively infinite excited state lifetime is assumed compared to the delay of the two excitation pulses), for which the results are shown in Fig. 5.9. In this case the assumptions have been that the seed gas for the atomic beam (divergence 2.4 mrad) was argon, which minimizes Doppler broadening, and an intensity to phase coefficient (see equation (2.88)) of  $10^{-13}$  rad cm<sup>2</sup> W<sup>-1</sup> has been used as determined in [194] for Kr. A background ionisation of 15% has been assumed and 10% power fluctuations (worst case scenario) at the fundamental IR wavelength of 780 nm. The atomic beam profile and XUV phase noise shape have both been taken with a Gaussian distribution, which gives worst case results.

The determination of XUV jitter based solely on the HHG intensity to phase coefficient underestimates the HHG phase jitter. It was found that the phase noise was twice as large as expected from theory only. This may well

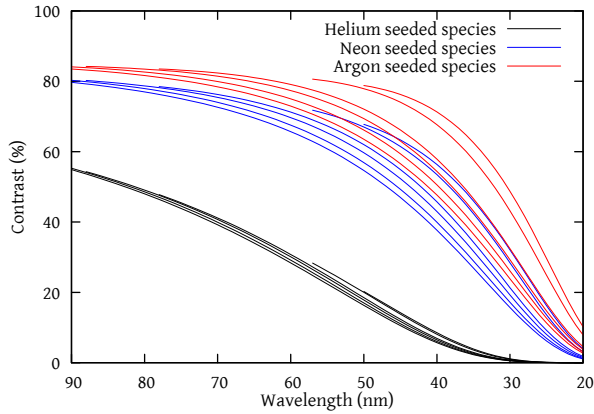


Figure 5.9: Calculated contrasts as a function of wavelength for Doppler-broadened signals and 10% power fluctuations in the IR on long-lived atomic transitions. The lines for the various seed gas groups are determined for several species of HHG gasses, from left to right: Rn, Xe, Kr, Ar, Ne, He. The cutoff of the lines at the left is due to the ionisation potential of the atoms, which determines the minimum wavelength that is generated in HHG.

be due to the fact that there is also a refractive index change induced by the first pulse, which is seen by the second pulse leading to additional phase jitter. This difference between a clean HHG calculation and the experimentally observed phase jitter, has been taken into account in the calculations as an experimentally determined multiplication factor.

In order to calculate the phase jitter for various HHG gasses, the electrical field and thus the intensity needed to reach the target wavelength was calculated by use of equations (2.75) and (2.76), taking the first ionisation potential of the various possible HHG gasses into account. Next the maximum phase jitter due to intensity fluctuations between the first and second HHG pulse has been determined using equation (2.88) multiplied by the afore mentioned factor. Equation (5.7) was used to determine the window function in order to calculate the contrasts.

The conclusion of these calculations is that a 10% contrast can still be obtained for longer lived transitions at 25 nm, with a power density that can be reached by our laser system, in a crossed beam experiment.

# 6. Frequency comb metrology on helium groundstate transitions

The first section of this chapter (6.1) has been published in Physical Review Letters [155]. The second part (6.2) gives a more detailed account of the theoretical aspects of some of the systematic effects appearing in the spectroscopy on ground state transitions in helium as described in the first section.

## 6.1 Extreme Ultraviolet Frequency Comb Metrology

**Abstract:** The remarkable precision of frequency-comb (FC) lasers is transferred to the extreme ultraviolet (XUV, wavelengths shorter than 100 nm), a frequency region previously not accessible to these devices. A frequency comb at XUV wavelengths near 51 nm is generated by amplification and coherent upconversion of a pair of pulses originating from a near-infrared femtosecond FC laser. The phase coherence of the source in the XUV is demonstrated using helium atoms as a ruler and phase detector. Signals in the form of stable Ramsey-like fringes with high contrast are observed when the FC laser is scanned over  $P$  states of helium, from which the absolute transition frequency in the XUV can be extracted. This procedure yields a  ${}^4\text{He}$  ionization energy at  $h \times 5\,945\,204\,212(6)$  MHz, improved by nearly an order of magnitude in accuracy, thus challenging QED calculations of this two-electron system.

### 6.1.1 Introduction

Mode-locked frequency-comb (FC) lasers [36,37] have revolutionized the field of precision laser spectroscopy. Optical atomic clocks using frequency combs are about to redefine the fundamental standard of frequency and time [75]. FC lasers have also vastly contributed to attosecond science by providing a way to synthesize electric fields at optical frequencies [277], made long distance absolute length measurements possible [278], and have recently been employed to produce ultracold molecules [279]. FC based precision spectroscopy on simple atomic systems has provided one of the most stringent tests of bound state quantum electrodynamics (QED) as well as upper bounds on the drift of fundamental constants [280]. Extending these methods into the extreme ultraviolet (XUV, wavelengths below 100 nm) spectral region is highly desirable since this would, for example, allow novel precision QED tests [281].

Currently the wavelength range below 120 nm is essentially inaccessible to precision frequency metrology applications due to a lack of power of single frequency lasers and media for frequency up-conversion. Spectroscopic studies on neutral helium using amplified nanosecond laser pulses [87,282] are notoriously plagued by frequency chirping during amplification and harmonic conversion which limits the accuracy. These kind of transient effects can be avoided if a continuous train of high power laser pulses (produced by a FC) can

be coherently up-converted. This would transfer the FC modes, at frequencies  $f_n = f_{\text{CEO}} + n f_{\text{rep}}$ , where  $f_{\text{CEO}}$  is the carrier-envelope offset frequency,  $f_{\text{rep}}$  is the repetition frequency of the pulses, and  $n$  an integer mode number, to the XUV. Similar to what was shown in the visible [283, 284], the up-converted pulse train could be used to directly excite a transition, with each of the up-converted modes acting like a single frequency laser.

By amplification of a few pulses from the train, and producing low harmonics in crystals and gasses, sufficient coherence has been demonstrated down to 125 nm to perform spectroscopic experiments [274, 275]. To reach wavelengths below 120 nm in the extreme ultraviolet or even x rays, high harmonic generation (HHG) has to be employed requiring nonlinear interaction at much higher intensities in the nonperturbative regime [176]. That HHG can be phase coherent to some degree is known [176, 285, 286], and recently XUV light has been generated based on upconversion of all pulses of a comb laser at full repetition rate [184, 185, 273, 287]. However, no comb structure in the harmonics has been demonstrated in the XUV, nor had these sources enough power to perform a spectroscopic experiment.

### 6.1.2 XUV frequency comb generation and spectroscopy

In this Letter we show that these limitations can be overcome, leading to the first absolute frequency measurement in the XUV. Instead of converting a continuous train of FC pulses, we amplify a pair of subsequent pulses from an IR frequency-comb laser with a double-pulse parametric amplifier (OPA) [177] to the milli-joule level. These pulses with time separation  $T = 1/f_{\text{rep}}$  can be easily upconverted into the XUV with high efficiency using HHG in a dilute gaseous medium, and used to directly excite a transition in atoms or molecules [see Figs. 6.1(a) and 6.1(c)]. This form of excitation with two pulses resembles an optical (XUV) variant of Ramsey spectroscopy [69, 274]. Excitation of an isolated (atomic or molecular) resonance with two (nearly) identical pulses produces a signal which is cosine-modulated according to  $\cos(2\pi(f_{\text{tr}}T) - \Delta\phi(f_{\text{tr}}))$ , where  $f_{\text{tr}}$  is the transition frequency and  $\Delta\phi(f_{\text{tr}})$  is the spectral phase difference between the two pulses at the transition frequency. Ideally, this spectral phase difference is just  $\Delta\phi(f) = q\phi_{\text{CE}} = 2q\pi \cdot f_{\text{CEO}}/f_{\text{rep}}$ , where  $q$  is the harmonic order under consideration and  $\Delta\phi_{\text{CE}}$  the carrier-envelope offset phase slip between subsequent pulses of the FC. In this case the cosine-modulated spectroscopy signal has a maximum whenever one of the modes of an up-converted frequency comb would be resonant. This statement remains true even if the amplification and harmonic up-conversion significantly distorts the electric field of the individual pulses as long as these distortions are common mode for each of them. Distortions that are not common mode need to be monitored and corrected for, in this experiment at a level of  $< 1/200$ th of the fundamental IR field period. The frequency accuracy of the method is not fundamentally limited by the accuracy of this correction since an error  $\delta$  in  $\Delta\phi(f)$  translates into a frequency error

$\Delta f = \delta/2\pi T$ . Therefore the error can be made arbitrarily small by increasing the time separation  $T$  between the pulses, provided the coherence time of the excited state allows this.

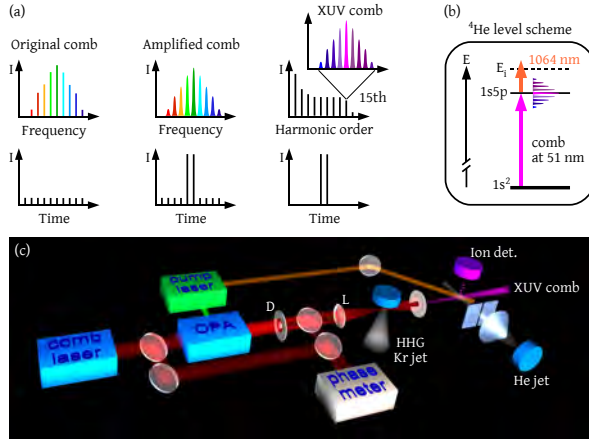


Figure 6.1: (a) Spectral and temporal structure of the generated light (left to right): FC of the continuous coherent pulse train from the FC laser, the cosine-modulated spectrum of a pair of amplified pulses, and odd harmonics of the amplified FC laser pulses each containing a cosine-modulated XUV comb corresponding to the XUV pulse pair. (b) Simplified  $^4\text{He}$  level scheme, XUV comb excitation at 51.5 nm from the  $1s^2$  ground state to the  $1s5p$  excited state and state-selective ionization by a pulse at 1064 nm. (c) Schematic of the experimental setup. D: beam mask, L: focusing lens,  $f = 50$  cm, I: iris to separate XUV from IR. The pump laser provides both the 532 nm for pumping the OPA as well as 1064 nm for ionization of helium.

### 6.1.3 Experimental setup

Phase coherent pulses near 773 nm are obtained from a Ti:sapphire frequency comb (repetition rate  $f_{\text{rep}}$  between 100 and 185 MHz), which is linked to a GPS-controlled rubidium clock (Stanford research PRS10) to reach a frequency stability on the order of  $10^{-11}$  after a few seconds of averaging. A bandwidth of 6 nm (rectangular spectrum, leading to  $\approx 300$  fs pulses after compression) is selected from the FC laser so that after up-conversion to the XUV only one state in helium is excited at a time. A noncollinear parametric double-pulse amplifier [177] is used to amplify two subsequent FC pulses (5.5–10 ns apart) at a repetition rate of 28 Hz. Parametric amplification intrinsically has small transient effects [195] so that differential pulse distortions are kept to a minimum. They are monitored using spectral interferometry with the unaltered FC pulses as a reference [177]. Wave front deformations in the amplified beam are reduced by spatial filtering. The differential phase shift from the amplifier and subsequent optics has a magnitude of typically 100 mrad in the IR. Spatial and spectral variations are at most 20–30 mrad. The IR beam is converted to a doughnut mode by a small disk mask (1.9 mm diameter compared to a beam diameter of 6 mm) to separate the XUV from the IR after HHG. The

remaining 1–2 mJ per pulse is focused in a pulsed krypton gas jet to  $< 5 \times 10^{13}$  W/cm<sup>2</sup> for HHG. This combination is chosen such that the 15th harmonic is exactly at the cutoff, so that higher harmonics are strongly suppressed. An iris of 0.8 mm diameter placed at 40 cm distance after the focus allows the XUV to pass without significant losses or beam distortion, but blocks the IR with a contrast ratio of 27:1. For the 15th harmonic at 51.5 nm generated in the krypton gas we estimate a yield of about  $1 \times 10^8$  photons per pulse. The resulting XUV beam intersects a low divergence beam of helium atoms at perpendicular angle to avoid a Doppler shift. This beam is generated in a supersonic pulsed expansion (backing pressure 3 bar) using a differential pumping stage containing two skimmers which limit the beam divergence to roughly 3–4 mrad. This is similar to the divergence of the XUV beam ( $< 2$  mrad). The second skimmer position can be adjusted to set the XUV-He beam angle. To investigate Doppler effects, helium can be seeded in heavier noble gases (partial pressure ratio 1:5). Pure helium results in a velocity of 2000(315) m/s, while seeding in neon and argon leads to a helium velocity of 830(200) and 500(250) m/s, respectively.

Helium atoms in the atomic beam are excited by the double pulse from the ground state into upper states which have spectral overlap with the HHG radiation [Fig. 6.1(b)]. After the double-pulse has passed, the excited state population is determined by state-selective ionization of the helium atoms using 60 ps, 1064 nm pulses from the OPA pump laser, followed by mass selective detection of the resulting ions in a time of flight spectrometer. Higher harmonics than the 15th are at least 10 times weaker, and produce a constant background signal of only 15% of the relevant spectroscopic signal due to direct ionization. The 13th and lower order harmonics are not resonant with any transition from the ground state of helium.

#### 6.1.4 Determination of the ionisation potential of helium

Figure 6.2 shows a typical recording of the <sup>4</sup>He ion signal, where the laser center frequency is tuned to the  $1s^2 \ ^1S_0 - 1s5p \ ^1P_1$  transition and the repetition frequency of the frequency comb is scanned. Recording such a trace takes about 20 000 laser shots, corresponding to ten minutes of continuous data taking. After correction for the measured IR phase shifts and XUV intensity, the data points are binned into 20 groups per Ramsey period. During a recording the pulse delay  $T$  is changed in steps of typically less than 1 attosecond every 28 laser shots, with a total change over a scan of less than 1 femtosecond.

By fitting the phase of the expected cosine function to this signal, we determine the transition frequency up to an integer multiple of the laser repetition frequency  $f_{\text{rep}}$ . The statistical error in the fit of a single recording is typically 1/50th of a modulation period. Depending on the repetition rate it amounts to a uncertainty of 2–3 MHz in the observed transition frequency, which is unprecedented in the XUV spectral region. Such scans are repeated many times to assess systematic effects. The dominant systematic shifts are

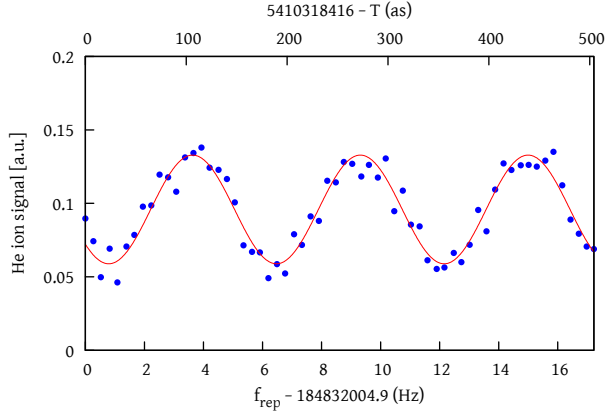


Figure 6.2: Measured excitation probability (blue circles) of helium at 51.5 nm on the  $1s^2\ ^1S_0 - 1s5p\ ^1P_1$  transition, normalized by the XUV pulse energy, as a function of the repetition rate  $f_{\text{rep}}$  of the frequency-comb laser. In this example  $f_{\text{EO}}$  is locked at 46.21 MHz, and a 1:5 He:Ne mixture is used for the atomic beam. The red line is a fit to the data.

Doppler shift and a differential phase shift of the XUV pulses due to changing levels of ionization of the HHG medium. The former is minimized by setting the XUV-helium beam angle perpendicular. It is evaluated by varying the speed of the helium beam and extrapolating the observed transition frequency to zero velocity. The ionization shift is found by varying the HHG medium density (assuming the ionized fraction remains constant) and extrapolating to zero density. The statistical error in the latter extrapolation dominates the final statistical error. Systematic errors in Doppler shift and ionization shift originate in the uncertainty of the helium velocity and ionization dynamics in the HHG medium, respectively. Other effects that are taken into account include recoil shifts, refractive index changes (Kerr effect) in the focusing lens for HHG and the entrance window to the vacuum setup, ac and dc-Stark effect and Zeeman shift. A summary of the error budget can be found in Table 6.1. Most recordings were made on the  $1s^2\ ^1S_0 - 1s5p\ ^1P_1$  transition at 51.5 nm. As a cross check also a series was measured on the  $1s^2\ ^1S_0 - 1s4p\ ^1P_1$  transition at 52.2 nm. The  $^4\text{He}$  ionization potential (up to an integer multiple of  $f_{\text{rep}}$ ) is derived from these measurements by adding the excited state ionization energy of the  $4p$  and  $5p$ . The energy of these states is known with an accuracy better than 20 kHz based on theoretical calculations [288].

To remove the ambiguity due to the periodic comb spectrum, we repeated this procedure for several repetition frequencies within the range of 100 MHz and 185 MHz. The correct “mode number” is found by plotting the possible ionization energies of the helium ground state against  $f_{\text{rep}}$  as shown in Fig. 6.3. A clear coincidence between the results for different repetition rates can be seen, leading to a new ground state ionization energy for  $^4\text{He}$  of 5 945 204 212(6) MHz by taking a weighted average over all measured frequencies at

Contribution	Size
Statistical error	3.7 MHz
Ionization shift	4.9 MHz
Doppler shift	500 kHz
dc-Stark shift	< 1 kHz
Signal from other levels	< 30 kHz
Zeeman shift	< 7 kHz
Total	6 MHz

Table 6.1: The major contributions to the error budget of the ionization potential expressed as frequencies.

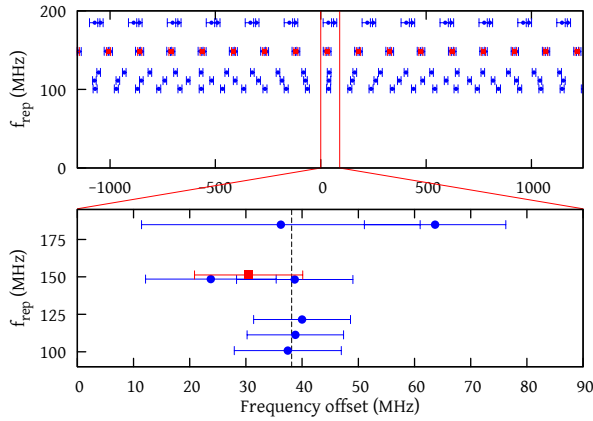


Figure 6.3: (top)  ${}^4\text{He}$  ground state ionization energy  $\pm n \times f_{\text{rep}}$  based on the  $1s^2\,{}^1S_0 - 1s5p\,{}^1P_1$  (blue circles) and the  $1s^2\,{}^1S_0 - 1s4p\,{}^1P_1$  transition (red squares). (bottom) Zoom at the coincidence point for all repetition frequencies. The vertical line at +38(6) MHz represents the weighted mean. All values are relative to the theoretical value of 5 945 204 174 MHz [88]. (square point slightly shifted up for visibility).

the coincidence location. This is in agreement with recent theoretical predictions of 5 945 204 174(36) MHz [88] and 5 945 204 175(36) MHz [203] within the combined uncertainty of theory and experiment. Compared to previous experiments employing single nanosecond duration laser pulses, we find good agreement with the value of 5 945 204 215(45) MHz [87] (using the most recent 2p state ionization energy [88], and corrected for a 14.6 MHz recoil shift that was previously not taken into account). However, there is a difference of nearly  $3\sigma$  compared to a competing result [282].

From the observed signal contrast (defined as the modulation amplitude divided by the average signal level) we can infer the temporal coherence of the HHG process. The contrast depends on several parameters: the upper state lifetime (natural linewidth), the time between the pulses, a difference

in XUV pulse energy of the two pulses, the frequency stability of the interference pattern, Doppler broadening of the transition, and the previously mentioned constant background from direct ionization due to the 17th and higher harmonics. The Doppler broadening is dominated by the effective atomic beam opening angle and the radial velocity of the beam. All these effects lead to a varying contrast depending on the helium velocity  $v$  and comb repetition frequency. For a high repetition rate ( $f_{\text{rep}} = 185$  MHz) and low  $v$  (helium seeded in argon), we find a fringe contrast of 55%, while on the other hand for  $f_{\text{rep}} = 100$  MHz and a pure helium beam (large  $v$ ) the contrast is below 5%. From these observed variations and a straight forward model for the visibility as a function of  $f_{\text{rep}}$  and atomic beam velocity, we estimate a phase jitter of 0.38(6) cycles in the XUV. To a large part this can be attributed to the timing noise of the driving IR pulses (0.014 cycles rms), leading to an estimated jitter in the XUV of 0.21 cycles. This noise in turn comes mostly from the radio frequency  $f_{\text{rep}}$  lock of the frequency-comb laser, which can be improved by locking the FC to an optical reference resonator.

### 6.1.5 Conclusion

In conclusion, we have demonstrated frequency-comb generation in the XUV and performed the first absolute frequency determination in this spectral region. Based on the contrast of the helium excitation signal we find that the excess phase noise in the HHG process used to generate the XUV comb is at most 0.3 optical cycles in the XUV. This means that the timing of the generated electric field of the XUV waveform of individual pulses is stable within less than 50 as, which is an important benchmark for both spectroscopy applications as well as ultrafast physics. The new value of the  $^4\text{He}$  ionization potential is in good agreement with theory [88, 203] and already almost an order of magnitude more accurate than the best previous results using single nanosecond laser pulses [87, 282]. Moreover, the accuracy of our method can readily be improved by orders of magnitude by increasing the time delay between the two pulses. One could, for example, perform high resolution spectroscopy on the  $1s - 2s$  two photon transition of hydrogenlike helium ions at 60 nm, which is very promising to perform QED tests beyond what has been possible so far in atomic hydrogen [281, 289]. The results show that as long as the carrier phase noise is kept low enough not to destroy the mode structure, comb generation should be extendable to the soft x-ray region. This may allow applications such as coherent XUV and x-ray imaging, precision QED tests of (highly) charged ions, to perhaps ultimately x-ray nuclear clocks.

This work was supported by the FOM through its IPP program “Metrology with Frequency Comb Lasers,” by the NWO, by the EU via the “Atlas” network, and by the Humboldt Foundation.

## 6.2 Appendix: Description of the systematic effects

In this section a selection of different effects is discussed in a more elaborate manner than previously possible in the published article [155]. Among them are the determination of the Stark shifts, Zeeman shifts and Recoil shifts.

### 6.2.1 Calculation of DC and AC Stark shifts

To determine the DC and AC Stark shifts (theory sections 2.8.1 and 2.8.1), the DC and AC field strengths in the interaction zone needs to be known. DC Stark shifts can be caused by residual fields of the extraction plates of the time of flight (TOF) mass spectrometer. The field is well approximated as a homogeneous field between two plates spaced by a distance  $d$ . The plates in our experiment are spaced 2.5 cm and a pulsed electrical potential of 85 Volts has been applied.

AC Stark shifts are present due to the presence of laser light during the excitation of the atomic transitions. Light at the excitation frequency of transitions from the ground state of the helium atoms is sufficiently weak that an AC Stark shift will be negligible. The electric field present at the fundamental of the HHG on the contrary, is very strong. The AC Stark shift due to the fundamental laser light has been measured, but a calculation of the AC Stark shift was done to confirm the measurement.

The determination of the field strength of the fundamental beam in the interaction zone is not straightforward. The AC Stark effect is linear in intensity, and due to this linearity, the average intensity of a pulsed source can be used to calculate the AC Stark shift. In the time-domain Ramsey excitation, pairs of pulses are used at an experiment rate of  $f_{\text{exp.}} = 28$  Hz to excite the transitions. The energy in a single IR laser pulse is therefore

$$E_{\text{IR pulse}} = \frac{P_{\text{avg.}}}{2f_{\text{exp.}}} \quad (6.1)$$

The measured power of the source can be used to calculate the intensity if the area of the beam is known as

$$I_{\text{avg.}} = \frac{E_{\text{IR pulse}}f_{\text{rep}}}{A} = \frac{P_{\text{avg.}}f_{\text{rep}}}{2Af_{\text{exp.}}} = \frac{P_{\text{avg.}}f_{\text{rep}}}{2\pi r^2f_{\text{exp.}}} \quad (6.2)$$

where  $A = \pi r^2$  is the beam area, and  $f_{\text{rep}}$  is the native frequency comb repetition rate, which is  $1/T$ , where  $T$  is the time between the two Ramsey pulses.

However, this assumes a top-hat intensity profile, which is not the case. Instead the fundamental beam has a Gaussian intensity profile. To determine the maximum intensity (the electric field where the Stark shift is largest) of this beam we need to relate the Gaussian beam profile to the rectangular beam profile. Taking the full width half maximum (FWHM) of the Gaussian intensity profile equal to  $2r$ , with  $r$  the radius, as compared to a beam with

a rectangular intensity profile, the maximum intensity of the Gaussian beam can be calculated via the normalised integrated Gaussian function

$$\frac{1}{2\pi w^2} \int_0^{2\pi} \int_0^\infty e^{-\frac{r^2}{2w^2}} r dr d\varphi = 1 \quad (6.3)$$

and the normalised rectangular function

$$\frac{1}{\pi w^2} \int_0^{2\pi} \int_0^\infty \text{rect}\left(\frac{x}{w}\right) r dr d\varphi = 1. \quad (6.4)$$

In this case the FWHM of the rectangular function ( $w$ ) is equal to the FWHM of the Gaussian function. The FWHM of the normalised Gaussian is  $2w_G \sqrt{2 \ln 2}$ , and it's height  $h_{\text{Gaus.}} = 1/(2\pi w^2)$ . The height of the rectangular is  $h_{\text{rect.}} = 1/(\pi w_r^2)$ . Under the aforementioned assumption we get the intensity ratio

$$\frac{h_{\text{Gaus.}}}{h_{\text{rect.}}} = \ln 2 \approx 0.693. \quad (6.5)$$

This means that we need to multiply the intensity, retrieved via the area  $A = \pi r^2 = \pi \text{FWHM}^2$  of the proposed rectangular beam with  $\approx 0.693$  to get the maximum intensity for the Gaussian beam.

The full-width half-maximum (FWHM) of a Gaussian laser beam can be measured sufficiently accurately with a knife edge or pinhole. We have applied a pinhole or iris measurement, where one measures the maximum power through an iris of radius  $r$ , that is then also centred on the beam. The radius  $r$  of the iris was determined with a calliper. The following equation (see [290] Eq. 2.18 modified) gives the power through a pinhole of radius  $r$

$$P(r) = \frac{\pi}{2} w_0^2 |E_0|^2 \left( 1 - e^{-\frac{2r^2}{w_0^2}} \right), \quad (6.6)$$

where  $w_0 = r/\sqrt{\ln(2)}$  is the beam waist parameter and  $E_0$  is the electrical field strength. The total power in the beam is given as

$$P_0 = \frac{\pi}{2} w_0^2 |E_0|^2 \quad (6.7)$$

and can be used to relate the measured power to the intensity too. Figure 6.4 shows the determined beam diameter.

In our particular case, the beam diameter was measured at a position close to the entrance of the vacuum system. The beam is focussed in the atomic beam used as HHG medium and simply diverges afterwards. The focal length (50 cm) for HHG has been taken as the source distance in the lens equation, while the distance from the HHG source to the helium atomic beam was measured to be about 53 cm, and was taken as the image distance. The ratio in distances equals the ratio in atomic beam diameters. The average power during

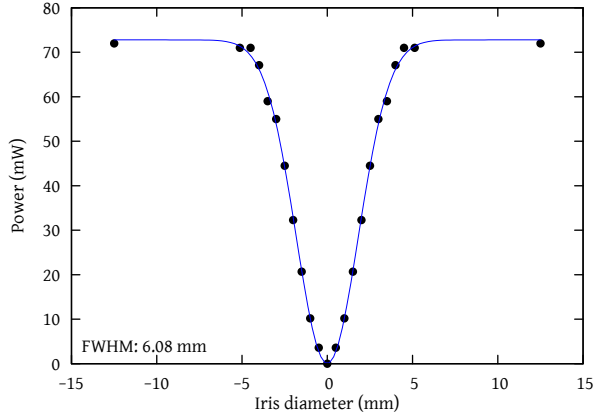


Figure 6.4: One of the two beam diameter measurements, yielding a beam diameter of 6.08 mm, the other yields 6.18 mm, leading to an average beam diameter of 6.13 mm at the focussing lens for HHG generation. The points are measurements, the line is the fit of function (6.6) to the data.

the Stark shift measurement was 100 mW IR at a wavelength of 773 nm with  $f_{\text{rep}} = 148.54$  MHz of the frequency comb. This leads to a maximum IR field in the interaction plane of the helium beam of 2.04 MV/m.

Table 6.2 gives the Stark shifts as they were calculated according to equations (2.103) and (2.107), with theoretical values from Theodosiou [216, 217], taking into account the experimental conditions present during the XUV frequency comb spectroscopy to determine the helium ground state energy. The values for the DC Stark shift correspond to the possible presence of residual fields due to the switched extraction field (1% of the field maximum of 3.4 kV/m). The AC Stark shift values correspond to the shift due to the fundamental laser field of 2.04 MV/m for the full IR beam in the interaction zone. It is estimated (by determination of the full beam power over the residual beam power through the vacuum system) that the Stark shift during the real experiment is at most  $1/27^{\text{th}}$  of the calculated value due to the presence of the beam block (see Fig. 2.7). Apart from a theoretical determination, a Stark shift measurement has been performed without the beam block resulting in 17.5 (6.0) MHz [178], with which the theoretical result of 14 MHz for the  $1s^2 \ ^1S_0 - 1s5p \ ^1P_1$  transition agrees well to within the experimental uncertainty.

### 6.2.2 Calculation of Zeeman shifts

The perturbation Hamiltonian for the Zeeman shift (Eq. (2.108)) immediately yields the shift in level energy for a given magnetic field. As noted the (low field) Zeeman shift for transitions between levels with equal  $M$  quantum number is zero (linearly polarised light  $\Delta M_J = 0$ , starting from  $M_J = 0$ ) if  $g_J$  of the levels are equal. In practice the light used for laser spectroscopy is never exactly linearly polarised. In case of the XUV spectroscopy done on helium  $1s^2$

atomic state	DC Stark shift (Hz)	AC Stark shift no shadow (MHz)	AC Stark shift shadow (MHz)
1s $^1S_0$ , M=0	0	-0.102	-0.004
4p $^1P_1$ , M=0	17	18.038	0.668
4p $^1P_1$ , M=±1	12	22.598	0.837
5p $^1P_1$ , M=0	91	13.968	0.517
5p $^1P_1$ , M=±1	61	22.061	0.817
6p $^1P_1$ , M=0	340	11.724	0.434
6p $^1P_1$ , M=±1	229	22.382	0.829
7p $^1P_1$ , M=0	1 022	9.915	0.367
7p $^1P_1$ , M=±1	688	22.903	0.848

Table 6.2: Stark shifts for several levels in helium, relative to the unperturbed level energy, under the experimental conditions of full IR illumination and residual fundamental IR illumination using the shadow to suppress the mentioned IR light in the interaction zone (see Fig. 2.7). For the DC Stark shift a residual field of 34 V/m is assumed (1% of the pulsed extraction field). Values for the experimental parameters are given in the main text. Theoretical values for the used Einstein A coefficients and level energies have been obtained from Theodosiou [216,217].

$^1S_0 - 1snp\ ^1P_1$ ,  $n \in 2, 3, 4 \dots$  transitions, the Lande g-factor  $g_J = 1$  for the levels involved. The measured magnetic field strength in the vacuum chamber was  $5 \times 10^{-5}$  Tesla due to the earth magnetic field.

As an upper bound we calculate the Zeeman shift that could be expected if we had fully single-handed circularly polarised light, say of the  $\sigma^+$  polarisation. In this case transitions with  $\Delta M = +1$  would have been excited and a Zeeman shift of the upper state of at most 7 kHz would have been present, which is insignificant. The fact that the efficiency of the high-harmonic generation process is strongly dependent on the polarisation state of the light, justifies the assumption that the amount of depolarised light is less than 1%, which means an even lower average shift is present than the maximum of 7 kHz.

### 6.2.3 Calculation of Recoil shifts

The recoil shift is usually calculated as

$$f_{\text{recoil}} = \frac{hf_{\text{obs.}}^2}{2m_a c^2}. \quad (6.8)$$

where  $f_{\text{obs.}}$  is the observed transition frequency in a spectroscopy experiment. In order to calculate recoil shifts from tabulated transition frequencies the substitution  $f_{\text{obs.}} = f_{\text{tr.}} + f_{\text{recoil}}$  is made, where  $f_{\text{tr.}}$  is the actual transition frequency, leading to the quadratic equation

$$\frac{h}{2m_a c^2} f_{\text{recoil}}^2 + \left( \frac{hf_{\text{tr.}}}{m_a c^2} - 1 \right) f_{\text{recoil}} + \frac{hf_{\text{tr.}}^2}{2m_a c^2} = 0. \quad (6.9)$$

atomic transition	$f_{\text{tr.}}$ (Hz)	$f_{\text{recoil}}$ (Hz)
$1s^2 \ ^1S_0 - 1s2p \ ^1P_1$	$5.130499 \times 10^{15}$	$14.59863 \times 10^6$
$1s^2 \ ^1S_0 - 1s4p \ ^1P_1$	$5.74110 \times 10^{15}$	$18.2803 \times 10^6$
$1s^2 \ ^1S_0 - 1s5p \ ^1P_1$	$5.81448 \times 10^{15}$	$18.7506 \times 10^6$
$1s^2 \ ^1S_0 - 1s2p \ ^1P_1$	$5.13023173 \times 10^{15}$	$19.3719766 \times 10^6$
$1s^2 \ ^1S_0 - 1s5p \ ^1P_1$	$5.81394205 \times 10^{15}$	$24.8794841 \times 10^6$

Table 6.3: Recoil shifts for transitions from the ground state to several excited states in  $^4\text{helium}$ . As a comparison values for  $^3\text{helium}$  are given below the ruler in the table. Transition frequencies (observed, Ritz wavelength for  $^3\text{helium}$ ) were taken from [291] and have been rounded after conversion to frequency. The recoil shift is given with the same number of significant digits as the input frequency and is also rounded. The  $^4\text{helium}$  mass is given as  $6.64647848 \times 10^{-27}$  kg and the  $^3\text{helium}$  mass as  $5.008234071 \times 10^{-27}$  kg [292]. Values for the other constants have been taken from the CODATA 2010 [84].

In order to compute recoil shifts from this equation, it is found that a high precision floating point library<sup>1</sup> needs to be used to obtain values absent of floating point errors<sup>2</sup>.

Tables 6.3 summarises the recoil shifts found for transitions from the ground state to several excited P states in  $^4\text{He}$ , and  $^3\text{He}$  calculated from the measured and calculated transition frequencies [291].

### 6.2.4 Calculation of second-order Doppler shifts

The second-order (relativistic) Doppler shift, Eq. (2.117) is to be added to the measured transition frequency because the atom sees a red-shifted laser beam due to its velocity. It has been calculated for the various speeds of the (seeded) helium atomic beam that were present in the spectroscopy experiment.

$$f_{\text{2nd order Doppler}} = \frac{f_0 v^2}{2c^2} \quad (6.10)$$

The transition frequency  $f_0$  is taken from the NIST atomic spectra database [291], while the velocity  $v$  of the atoms in the experiment was 2000(315) m/s in the unseeded helium beam. Usage of mixtures of 1:5 helium and neon or argon led to beam velocities of 830(200) and 500(250) m/s as reported in Sec. 6.1.3. The results of the calculation for several transitions from the ground state in  $^4\text{helium}$  are given in Table 6.4.

In principle the second-order Doppler effect also causes an asymmetric lineshape which must be taken into account. However in the presented experiment the second-order Doppler effect is not yet significant.

<sup>1</sup>I have used the “decimal” library of the Python programming language.

<sup>2</sup>Note that due to the large differences in the various terms even 96 bit floats have been found to yield inaccurate solutions of Eq (6.9).

atomic transition	$f_{\text{tr.}}$ (Hz)	$f_{\text{2nd order Doppler}}$ (Hz)		
		500 m/s	830 m/s	2000 m/s
$1s^2 \ ^1S_0 - 1s2p \ ^1P_1$	$5.130\,499 \times 10^{15}$	$7.14 \times 10^3$	$19.7 \times 10^3$	$114.2 \times 10^3$
$1s^2 \ ^1S_0 - 1s4p \ ^1P_1$	$5.741\,10 \times 10^{15}$	$7.98 \times 10^3$	$22.0 \times 10^3$	$127.8 \times 10^3$
$1s^2 \ ^1S_0 - 1s5p \ ^1P_1$	$5.814\,48 \times 10^{15}$	$8.09 \times 10^3$	$22.3 \times 10^3$	$129.4 \times 10^3$

Table 6.4: Second-order Doppler shifts for transitions from the ground state to several excited states in  $^4\text{helium}$ . Transition frequencies (observed) were taken from [291], while the atomic beam velocities have been taken from [155] (see Sec. 6.1.3)

### 6.2.5 Measurement of Ti:Sapphire frequency comb mode width

In order to establish the linewidth of the modes of the Ti:Sapphire frequency comb laser, we have set up a simple experiment in which a free running telecommunication laser with a linewidth in the order of 100 kHz was used, both at the fundamental and doubled optical frequency, to simultaneously make a heterodyne beat note with an  $\text{Er}^{3+}$ -fibre frequency comb laser and the Ti:Sapphire frequency comb laser used for the helium spectroscopy.

Both heterodyne beat notes have been simultaneously counted with synchronised counter gates, while the counter gate time was varied for the various measurement series. The heterodyne beat frequency of the Ti:Sapphire laser could be corrected for drifts of the telecommunication laser measured with the  $\text{Er}^{3+}$ -fibre frequency comb laser. The modes of the latter had a linewidth of about 400 kHz. The standard deviation of the corrected measurements of the Ti:Sapphire frequency comb beat frequency was determined. Additionally the measurements have been binned and a Gaussian function was fitted to the result to give a full width half maximum (FWHM) mode width at a given gate time.

Although this method can be improved upon, it gives a good indication of the mode width of the Ti:Sapphire laser, which was determined to be approximately between 1 and 2 MHz. An example of a binned measurement series (in this case 20 bins) is given in Fig. 6.5. An overview of the mode widths at the various gate times is given in Fig. 6.6.

### 6.2.6 Calculation of the probability of mode number coincidence

After the determination of the transition frequencies for the  $1s^2 \ ^1S_0 - 1snp \ ^1P_1$ ,  $n \in 4, 5$  transitions, each of the individual measurement series yielded a value for the ionisation energy of helium by addition of the calculated upper state energy. Because of the nature of the Ramsey comb measurement these values are modulo the repetition rate frequency  $f_{\text{rep}}$  of the frequency comb laser.

In order to determine the correct excitation mode numbers, a coincidence should be present among the measurements for the true ground state energy expressed in frequency  $f = E/h$ , with  $h$  Plancks constant, for the correct combination of mode numbers. Figure 6.3 (top) shows what we call a

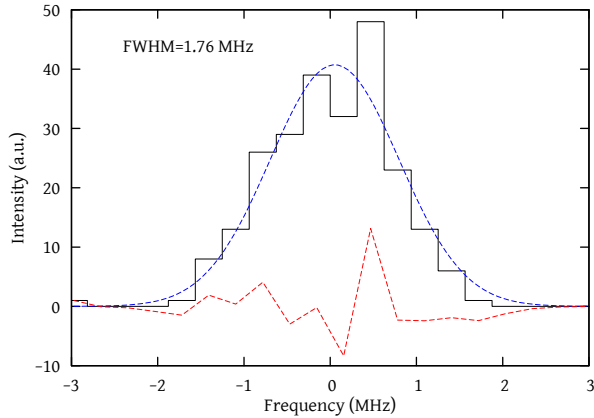


Figure 6.5: Example of a Ti:Sapphire frequency comb mode linewidth measurement. The recorded beat frequencies have been corrected for CW reference drift, the mean value was subtracted, and the values were binned in 20 bins (black). The full width half maximum (FWHM) was determined by fitting a Gaussian function to the data (blue dashed). The residual is plotted to assure no systematic effects have been overlooked (red dashed).

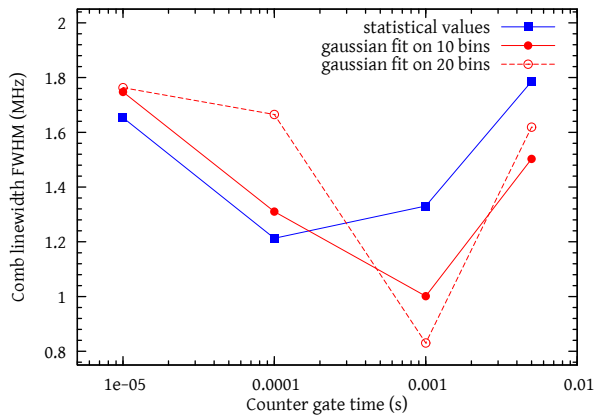


Figure 6.6: Overview of the determined Ti:Sapphire mode width as a function of counter gate time. The statistical value (standard deviation), 10 bin and 20 bin values have been derived from the same data set at the given gate time.

frequency vernier plot. The points on this plot where frequencies from all the measurements coincide, indicate the “true” value for the ionisation energy. It is noteworthy that some systematic effects show up as a deformation of the coincidence point in the vernier plot as a function of  $f_{\text{rep}}$  (e.g. linear shift with  $f_{\text{rep}}$ ).

One can “easily see” that there is a good coincidence at about 38 MHz above the theoretically calculated ground state frequency, but to give a more quantitative answer, the probabilities that the true ionisation energy is loc-

ated at a certain point on the frequency scale have been calculated. The calculation procedure is outlined here.

Each measured transition frequency comes with a statistical uncertainty. A normal distribution of the data has been assumed. The probability that the coincidence point lies around this transition frequency  $\mu_n = f_{\text{meas}_n} \bmod f_{\text{rep}}$ , for measurement  $n$ , is thus given by a Gaussian function

$$P_{\text{tr}_n}(f) = \frac{1}{\sigma_n \sqrt{2\pi}} e^{-\frac{(f - \mu_n)^2}{2\sigma_n^2}}, \quad (6.11)$$

with a standard deviation  $\sigma_n$ , which is the measurement uncertainty.

Because we can only have one correct mode number for each measurement series, the choice was made to calculate the probability at a certain frequency  $f$  only for the set of modes that are closest to this value. This is computationally favourable and is justified by the fact that Gaussian function is near zero at large values for  $(f - \mu_n)^2$ , which means that far off modes do not contribute significantly to the coincidence probability at certain  $f$ . The coincidence probability at  $f$  is now calculated as

$$P_C = \prod_n P_{\text{tr}_n}(f), \quad (6.12)$$

where  $\mu_n$  are the frequencies closest to  $f$ . The result for the measurement series to determine the ionisation energy of helium is given in Fig. 6.7, and shows that in a range of about  $\pm 1$  GHz around the theoretical value, the coincidence at 38 MHz is the most probable. We have therefore chosen this point as the measurement value of the ionisation energy of helium.

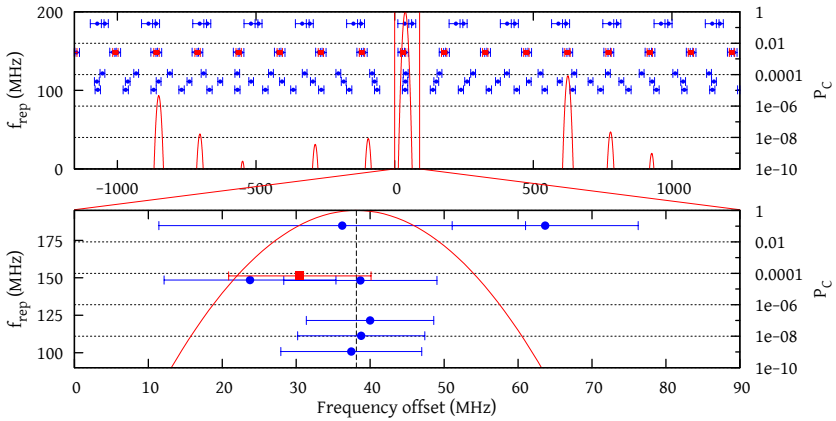


Figure 6.7: Measured helium ionisation energies. This graph includes (in red) the values of the coincidence probability of the measurement series and shows that the coincidence of measurements at 38 MHz is the most probable one within a range of  $\pm 1$  GHz



# 7. Effect of soil temperature on optical frequency transfer through unidirectional dense-wavelength-division-multiplexing fibre-optic links

Abstract: Results of optical frequency transfer over a carrier-grade dense-wavelength-division-multiplexing (DWDM) optical fibre network are presented. The relation between soil temperature changes on a buried optical fibre and frequency changes of an optical carrier through the fibre is modelled. Soil temperatures, measured at various depths by the Royal Netherlands Meteorology Institute (KNMI) are compared with observed frequency variations through this model. A comparison of a nine-day record of optical frequency measurements through the  $2 \times 298$  km fibre link with soil temperature data shows qualitative agreement. A soil temperature model is used to predict the link stability over longer periods (days-months-years). We show that optical frequency dissemination is sufficiently stable to distribute and compare e.g. rubidium frequency standards over standard DWDM optical fibre networks using unidirectional fibres.

## 7.1 Introduction

In recent years, fibre-optic connections in telecommunication networks have proven to be suitable for frequency comparisons and frequency distribution with high stability over long distances. In general the frequency of either a continuous-wave (CW) laser or a microwave reference is transmitted over an optical fibre and received at the remote site. Several experiments [293–299] have shown that frequency comparisons at or below the current accuracy level of the best atomic frequency references, a few times  $10^{-18}$  at  $>1000$  s [75, 76, 79, 300], are feasible over long-haul fibre connections. For example, the optical frequency of the 1S-2S transition in atomic hydrogen was recently measured with respect to a remote Cs frequency standard with  $4.5 \times 10^{-15}$  relative uncertainty, employing a 920 km long fibre-optic link performing at the  $4 \times 10^{-19}$  at 2000 s uncertainty level [298, 301].

Fibre-optic methods for remote frequency comparison can provide significantly better stability than current satellite-based methods. These include two-way satellite time and frequency transfer (TWSTFT) [302–304] and (carrier-phase) common-view global positioning system ((CP)/CV-GPS) comparisons [305–307]. The accuracy limits of satellite based methods are on the order of  $10^{-15}$  at one day [307–309], which is already insufficient to compare state-of-the-art cesium fountain clocks operating at less than  $5 \times 10^{-16}$  at  $\geq 3 \times 10^4$  seconds uncertainty level [310, 311].

Plans for high-resolution laser spectroscopy experiments at VU University Amsterdam LaserLaB and at Van Swinderen Institute, University of Groningen, would be greatly facilitated by direct frequency comparisons over an optical fibre-link at stability levels better than  $10^{-14}$  at  $< 1000$  s. For this purpose, a  $2 \times 298$  km fibre-optic connection between both laboratories has been established using a  $2 \times 295$  km DWDM channel provided by SURFnet. The top part of Fig. 7.1 gives an overview of the SURFnet fibre network in the Netherlands. The optical path between VU University Amsterdam and Van Swinderen Institute Groningen is marked in green. The bottom part shows the details of the optical path.

The link consists of two unidirectional fibres. Interferometric detection and active compensation of fibre length changes [312] is therefore not possible. However, it is possible to create a bidirectional path in the optical fibre, and implement a compensation system [299]. It must be noted that, in contrast to some of the other frequency comparison links [293,294,296–298], our link is part of a carrier-grade DWDM optical network in which the fibre is shared with other users, and several other wavelength channels are simultaneously used for data transfer.

The use of a standard DWDM channel enables us to characterise the performance of unidirectional transmission of optical frequency references in public transport networks carrying live network traffic. Here the performance is characterised in terms of frequency instability (Allan deviation). For long underground fibre links, the frequency instability has been attributed primarily to length changes induced by soil temperature variations. The main aim of this work is to provide quantitative insight into this phenomenon by modelling the soil-temperature-induced length variations and the resulting frequency instability of the fibre link, and by comparing measured frequency instabilities with predictions by the model.

Unidirectional frequency transfer will be useful for institutions and industries which require accurate and reliable time and frequency references. Optical frequency distribution may be used for calibration purposes, such as accurate length and, in the future, mass measurements (through the Josephson effect and the Watt balance) by referencing to the SI second.

This article is structured as follows. In Sec. 7.2 a model for the influence of temperature on the stability of fibre-optic frequency transfer is presented, along with a soil temperature model. In Sec. 7.3, we present our approach to determine the stability of the  $2 \times 298$  km optical frequency link, including details of the setups used in Amsterdam and Groningen, as well as technical details specific to the use of non-standard equipment in fibre networks carrying live data of other users. Results are discussed in Sec. 7.4, followed by conclusions and an outlook presented in Sec. 7.5.

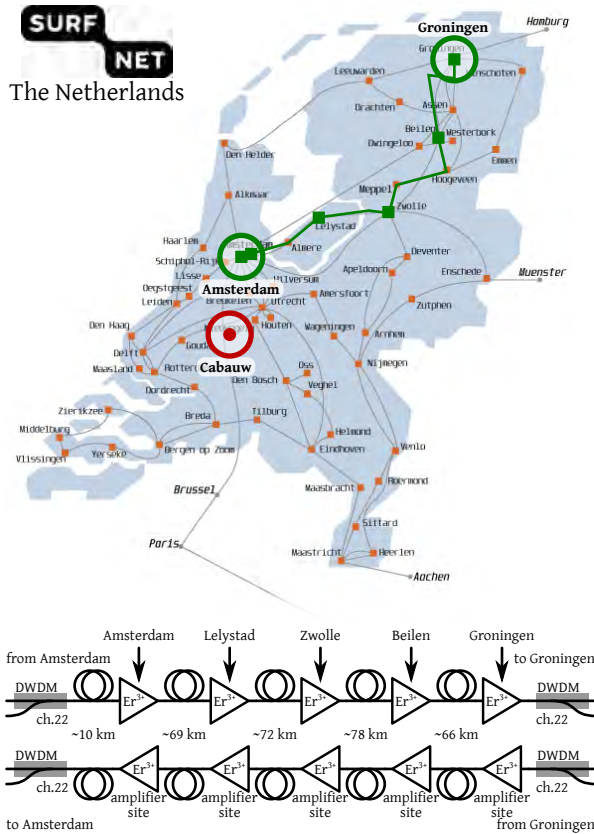


Figure 7.1: Top: Schematic map of the SURFnet fibre-optic network. The fibre link between VU University Amsterdam and Van Swinderen Institute Groningen (green line). Amplifier sites (green squares). The KNMI measurement site at Cabauw (red circle). Bottom: Schematic representation of the duplex fibre link between Amsterdam and Groningen in the SURFnet network (length:  $2 \times 295$  km). The unidirectional  $\text{Er}^{3+}$ -amplifiers are used by all active DWDM channels. In Amsterdam  $\sim 500$  m of intra-office fibre bridges the distance between the SURFnet node and the laboratory. In Groningen  $\sim 2$  km of additional underground fibre is needed to bridge the distance from the SURFnet node at the computing centre of the University of Groningen to the laboratory, adding to a total link length of  $2 \times 298$  km.

## 7.2 Theory: frequency stability of the fibre link and soil temperature

The phase  $\varphi$  accumulated by a monochromatic light wave guided along a certain path of length  $L$  and effective refractive index  $n$  can be written as

$$\varphi = \frac{\omega_0}{c} nL, \quad (7.1)$$

where  $\omega_0$  is the frequency of the light (in radians per second). Several physical processes can lead to phase (and thus frequency) variations in fibre-optic

links.

At short time scales ( $< 100$  s) environmental vibrations couple to the fibre and can therefore cause path length variations, e.g. via stress-induced refractive index variation, which may occur at frequencies up to tens of kHz. At time scales longer than 1 s, significant phase variations also occur because of thermal expansion of the fibre and thermally induced changes in the refractive index. These variations are typically slow and, for a fibre which is installed mainly underground in an outdoor environment, they are mostly affected by the diurnal and seasonal soil temperature cycles [313]. Our work is focused on the understanding of the long-term stability of fibre links in relation to such temperature variations.

The phase variations due to a time-varying temperature  $T$  are

$$\frac{d\varphi}{dt} = \frac{\omega_0}{c} \left( L \frac{\partial n}{\partial T} \frac{dT}{dt} + n \frac{\partial L}{\partial T} \frac{dT}{dt} \right). \quad (7.2)$$

We can express the relative length variations of the fibre as a function of temperature as

$$\frac{1}{L} \frac{\partial L}{\partial T} = \alpha_\Lambda, \quad (7.3)$$

where  $\alpha_\Lambda$  is the thermal expansion coefficient of the fibre. Furthermore it is customary to write

$$\frac{\partial n}{\partial T} = \alpha_n, \quad (7.4)$$

with  $\alpha_n$  the thermo-optic coefficient. Note that both  $\alpha_\Lambda$  and  $\alpha_n$  are weakly dependent on temperature, which we ignore here.

A typical (room-temperature) value of the thermal expansion coefficient of the fibre glass is  $\alpha_\Lambda = 5.6 \times 10^{-7} / ^\circ\text{C}$  [314]. The thermo-optic coefficient has a typical value of  $\alpha_n = 1.06 \times 10^{-5} / ^\circ\text{C}$  [314], and is therefore the main cause of phase variations due to temperature changes. Similar effects due to varying air pressure are approximately two orders of magnitude smaller [315] and have therefore not been included in the model.

Considering the heat flux in isotropic media (soil) for a vertical temperature gradient and varying temperature, and modelling the temperature variation as a sinusoidal periodic signal, Van der Hoeven and Lablans [316] derive the equation for the temperature of the soil at a certain depth  $z$  and time  $t$  as

$$T(z, t) = T_0 + A_{T_0} e^{-zC_\varphi} \sin \left( \frac{2\pi}{P_{T_0}} (t - t_0) - zC_\varphi \right), \quad (7.5)$$

where  $T_0$  is the average temperature at the surface ( $z = 0$ ),  $A_{T_0}$  is the amplitude of the temperature variation at the surface with period  $P_{T_0}$ , and  $t_0$  is an arbitrary time offset. The phase constant

$$C_\varphi = \frac{1}{C_s} \sqrt{\frac{\pi}{P_{T_0}}}, \quad (7.6)$$

includes the soil constant  $C_s$  which is determined by the thermal conductivity  $\lambda$ , the specific heat capacity  $C_m$ , and the mass density  $\rho$  of the soil according to

$$C_s = \sqrt{\lambda/\rho C_m}. \quad (7.7)$$

Equation (7.5) can be applied to both diurnal and annual variations in temperature. A remark must be made that accurate modelling of the soil temperature is delicate and involves, among others, the groundwater levels and groundwater freezing rates in winter [316].

In this model the amplitude of the temperature wave decreases exponentially with depth, while it undergoes a phase shift linear with depth. The equation is universal and can also be applied to other materials as long as the physical properties  $\lambda$ ,  $\rho$  and  $C_m$  are known.

With the help of Eq. (7.5), average frequency deviations  $\Delta f$  from the nominal frequency  $f_0 = \omega_0/2\pi$  can be calculated for any depth, using Eq. (7.2) for temperature differences  $\Delta T$  over a time interval  $\Delta t$  as

$$\Delta f = 2\pi f_0 \frac{L}{c} (\alpha_n + n\alpha_\Lambda) \frac{\Delta T}{\Delta t}. \quad (7.8)$$

### 7.3 Experimental methods

In order to characterise the frequency stability of the fibre link, two different methods are used. The first method consists of the one-way transmission of a C-band-wavelength CW laser, locked to a mode of an  $\text{Er}^{3+}$ -doped fibre frequency comb laser in Amsterdam. In Groningen, the transmitted laser frequency is measured using a similar frequency comb laser. Both frequency combs are locked to GPS-disciplined atomic clocks. Therefore, the stability of the optical frequency measurement in Amsterdam and in Groningen depends on the fibre link as well as the atomic clock stabilities. The second method employs a closed fibre loop Amsterdam – Groningen – Amsterdam. In this case the laser frequency can be compared with itself after its roundtrip through the fibre loop. The second method takes advantage of the fact that the laser frequency instability on the time scale of the measurement is much smaller than the instabilities introduced in the fibre loop.

Figure 7.2 gives an overview of the measurement setup that is used to characterise the frequency stability of the fibre link. A narrow-linewidth CW laser (Redfern Integrated Optics inc. (RIO) Planex, 3 kHz Lorentzian linewidth, 20 mW output power, and wavelength 1559.79 nm [ITU channel 22]) is phase-locked to the fibre frequency comb laser (Menlo Systems FC1500) and used as an absolute optical frequency reference. To verify the lock quality, the in-loop beat signal is counted. The optical reference frequency is sent to Groningen via the fibre link. The nominal length  $L$  of the fibre-link is  $2 \times 298$  km between the laboratories in Amsterdam and Groningen. The optical fibres of the pair are located in a fibre-bundle and thus follow nearly the same physical path.

In the SURFnet DWDM system, other wavelength channels transport 10 Gbps (non-return-to-zero amplitude modulation) and 100 Gbps (polarisation-multiplexed quadrature phase-shift keying) data. Nonlinear cross talk between these channels and the channel used for frequency transfer is avoided by limiting the average launch power to 0 dBm per span per wavelength, and to -4 dBm per wavelength when launched into dispersion compensation module. Intrachannel cross talk is avoided by reserving ITU channel 22 exclusively for the link Amsterdam–Groningen, i.e. this channel is not used in other segments of the DWDM system. We incorporated several measures to stabilise the power of the CW laser launched into the DWDM link. Firstly, the launch power is actively stabilised to  $(0 \pm 0.5)$  dBm using a variable optical attenuator controlled by a feedback loop. Secondly, wavelength stabilisation is needed as this prevents thermally induced mode hops to wavelengths that fall outside ITU channel 22, and which are converted to power jumps by the DWDM filters in the system. Apart from the phase lock to the frequency comb mentioned above, the temperature of the CW laser is stabilised by a two-stage temperature controller to within 10 mK. Mode hops are furthermore avoided by proper rf decoupling of the laser current control electronics from their electrical environment.

In Groningen the light is split. Part of the light is used in a frequency comparison against the local optical frequency standard (Menlo Systems FC1500), while the other part of the light is sent back to Amsterdam (received power 0–6 dBm). As pointed out above, the comparison of the frequency of the light after the roundtrip with the CW laser source reveals the noise contribution from the fibre link.

Both optical frequency combs are locked to rubidium (Rb) frequency standards (SRS FS725), which are disciplined to the 1 pulse per second output of GPS receivers (Amsterdam: Trimble Acutime 2000, Groningen: Navsync CW46). The combined instability of the GPS-receiver output and Rb clocks is transferred to the frequency comb lasers via the various rf locks used to stabilise the frequency comb laser repetition rate frequency  $f_{\text{rep}}$  and carrier envelope offset frequency  $f_{\text{CEO}}$ .

Figure 7.3 shows the details of the CW laser stabilisation setup. Part of the light of the diode is split off and fed to a fibre-based beat-note unit consisting of a DWDM filter to reject a large part of the frequency comb spectrum, a fused coupler, and a fibre-coupled photodiode ( $\sim 2$  GHz bandwidth, 50/125  $\mu\text{m}$  multi-mode fibre coupled) to detect the rf beat signal. The rf beat signal ( $f_{\text{beat}} = 60$  MHz) is bandpass filtered (filter bandwidth  $> 10$  MHz) and amplified before comparison with a signal generator (Agilent 33250A, referenced to the Rb clock), via counting phase detector electronics. Feedback on the diode laser phase is achieved via a fast PID controller acting directly onto the diode-laser injection current (bandwidth  $> 1$  MHz).

To verify proper CW-laser locking conditions during the experiment, the in-loop rf beat-frequency is recorded with a Rb-referenced counter. For dead-time-free counting of rf frequencies, either a quasi-continuous double Agilent

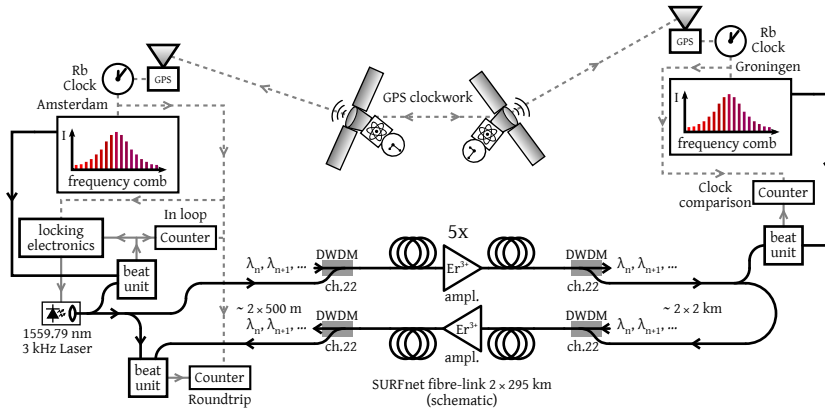


Figure 7.2: The Amsterdam - Groningen fibre link, overview of the experimental setup. This arrangement allows for optical-versus-GPS comparisons (essentially an fibre-optic frequency comparison of the GPS-linked Rb clocks in Amsterdam and Groningen), and for measurements of the roundtrip stability of the fibre-link in Amsterdam. Details of the CW laser lock setup are given in Fig. 7.3. The setup for the roundtrip analysis and for the optical versus Rb/GPS comparison are shown in detail in Fig. 7.4 and Fig. 7.5, respectively.

53132A counter setup is used, or an Agilent 53230A counter in a continuous reciprocal frequency counting mode.

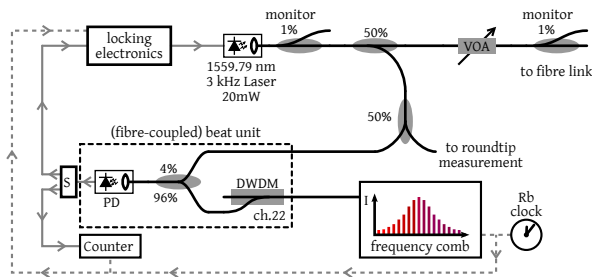


Figure 7.3: CW laser stabilisation setup (Amsterdam). The 1559.79 nm, 3 kHz (Lorentzian linewidth) diode laser is frequency stabilised by a phase-locked loop to a mode of the  $\text{Er}^{3+}$ -fibre frequency comb laser. The photo-diode signal of the fibre-coupled beat unit is amplified, filtered and split by a 3 dB power splitter (S) for input to the phase detector and the counter. The stabilisation setup is fully referenced to the GPS-disciplined Rb frequency standard. The monitor ports are used to observe optical power variations of the Planex laser before and after the variable optical attenuator (VOA), which regulates the laser power to a constant level before injection into the telecommunication network.

To characterise the stability of the fibre link, the setup of Fig. 7.4 is used. Light of the diode laser is split by a fused coupler. Part of the light is sent via the roundtrip Amsterdam - Groningen - Amsterdam, while another portion of the light is frequency shifted by an acousto-optic modulator (AOM). The output of the AOM is combined with the roundtrip optical signal after transmission by the fibre link (power  $\sim -3$  dBm) and the beat frequency is

detected with a fibre-coupled photo-diode. Apart from wideband ( $> 10$  MHz) RF filters the beat-note signal was not filtered. Any frequency variations introduced by the fibre link can be measured as frequency deviations from the AOM frequency, which is generated by a Rb-referenced DDS (Analog Devices AD9912).

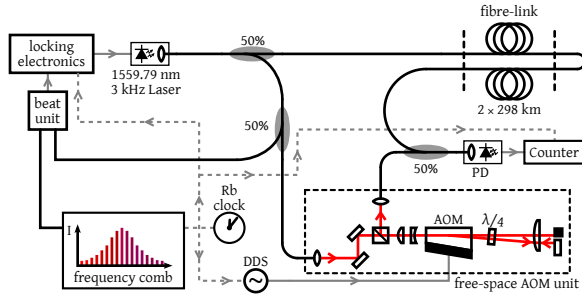


Figure 7.4: Experimental setup for the characterisation of the passive frequency stability of the fibre link (Amsterdam). For the long roundtrip measurements the free-space AOM unit (300 MHz) was replaced by a fibre-coupled AOM ( $-42$  MHz). In both cases the AOM was driven by a Rb-referenced DDS unit with a set accuracy of  $\sim 3.55 \mu\text{Hz}$ . Frequency deviations of the link are recorded with a Rb-referenced counter.

To measure the roundtrip stability two different AOM and counter setups were used during the experiments. Initially an Agilent 53230A counter in reciprocal continuous mode was used to count the beat frequency of a free-space double-pass AOM unit (300 MHz) to obtain the results of Sec. 7.4.2. The free-space AOM has a polarisation-dependent efficiency, which converts polarisation changes due to slowly changing fiber birefringence to unwanted power variations in the AOM output beam. To overcome this, the free-space AOM was later replaced by a polarisation insensitive fibre coupled AOM (frequency shift  $-42$  MHz). The lower frequency of this AOM allowed using a channel of a high-end zero-dead-time K+K FMX-50 counter to count the beat frequency (used to obtain the results of Sec. 7.4.1).

The remote (Groningen) optical frequency characterisation setup is depicted in Fig. 7.5. The link laser is amplified using a semiconductor optical amplifier, and guided to a free-space beat unit. The beat frequency is counted using a K+K FMX-50 counter. The frequency comb laser and counters are frequency referenced to the Rb-standard.

## 7.4 Measurements and simulations

Two series of measurements have been performed on the fibre link, namely an “optical-versus-GPS” measurement for which the optical frequency is measured simultaneously at Amsterdam and Groningen and compared, and a roundtrip measurement at the Amsterdam site (Fig. 7.2). It is known that soil temperature variations of the fibre may lead to significant frequency instability (see, for example, [317]). In this section, we present a model to describe

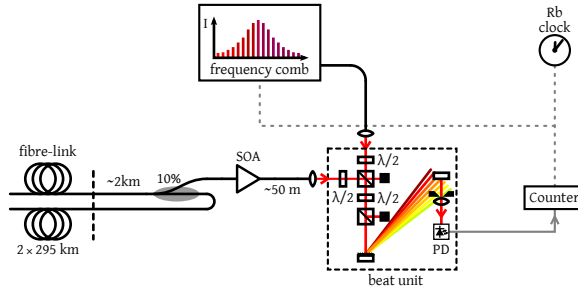


Figure 7.5: Experimental setup for the remote optical frequency measurement (Groningen). Of the received optical power 90% is sent back to Amsterdam. To improve the signal of the free-space beat unit, the link light is amplified with a BOA-6434 semiconductor optical amplifier (SOA). The amplified light is then combined with light from the fibre frequency comb laser in a free-space beat unit to obtain an rf beat between the nearest frequency comb mode and the CW link laser.

and predict the influence of soil temperature variations on the frequency stability of underground fibre links. The results of the temperature model are compared with actual soil temperature and link stability measurements.

Apart from the instability contributed by the fibre link, the stability of the frequency transfer is limited by three sources. First, the stability of the frequency comb laser is limited by the Rb/GPS rf reference oscillator used to control the parameters of the comb. This reference has a specified relative instability of  $< 10^{-11}$  at 1 second and below  $10^{-12}$  between  $10^3$  and  $10^5$  seconds, with a minimum around  $3 \times 10^{-13}$ . This long-term frequency instability is transferred to the CW link laser through the various rf locks in the setup.

The rflocks themselves also contribute to the frequency instability, which we assess as follows. Using a second, similar, CW laser (RIO Orion) locked to the frequency comb, and employing the virtual beat note technique [141], the combined instability of the locking electronics is determined to be  $< 9.1 \times 10^{-16}$  at 1 second. Thus, on time scales longer than 1s, the rf noise is effectively averaged out so that its influence on the link measurements may be neglected.

A second source of instability plays a role in the roundtrip measurements, for which a frequency drift of the laser source may lead to an apparent frequency shift of the (delayed) light transmitted by the fibre loop. Considering the 3.2 ms roundtrip propagation delay of the light over the fibre link, the (linear) drift of the frequency standard ( $10^{-11}$  at 1 s) only plays a role at the level of  $3.2 \times 10^{-14}$  at 1 s, decreasing as  $\sim 1/\tau_{\text{gate}}$ , the inverse of the counter gate time, due to the fractional time overlap  $(\tau_{\text{gate}} - \tau_{\text{roundtrip}}) / \tau_{\text{gate}}$  between reference and roundtrip light in the frequency comparison. This is one order of magnitude smaller than the typically measured link stability at 1 s, and averages down more rapidly with increasing  $\tau$ .

For the optical-versus-GPS comparison, a third source of instability is due to the fact that the Rb clocks in Amsterdam and Groningen are independently

locked to GPS time. Small intrinsic phase differences between GPS signals, received at geographically separated locations, thus propagate through the frequency locks, and may manifest itself as additional noise in the link frequency measurement.

#### 7.4.1 Fractional frequency transfer stability over a $2 \times 298$ km optical fibre link

The intrinsic frequency transfer stability of a fibre link is best measured on a closed loop, so that the frequency of the input signal can be directly compared with that of the roundtrip signal. Figure 7.6 shows the results of two roundtrip stability measurements. The first measurement is based on a 13-hour time series of frequency measurements acquired on 2012-07-06, using the free-space AOM unit (Fig. 7.4) while recording with the Agilent 53230A. For this dataset the absolute frequency of the roundtrip optical signal was calculated and used to determine the overlapping Allan deviation (ODEV).

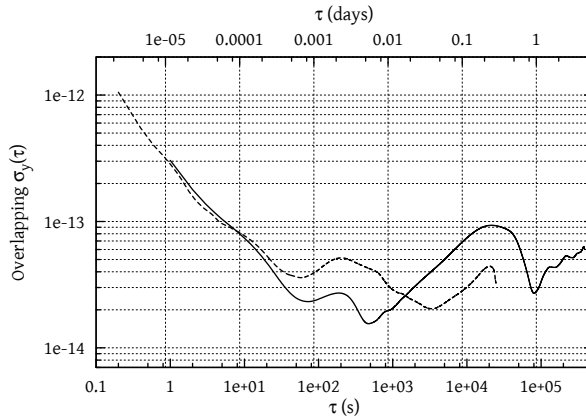


Figure 7.6: Comparison of two roundtrip stability measurements (overlapping Allan deviation (ODEV), here denoted as Overlapping  $\sigma_y(\tau)$ ) for averaging time  $\tau$ . Measurement of almost 9 days from 2013-09-30 to 2013-10-09 (solid, outliers due to accidental low beat signal in this period where taken out and replaced with the median of the dataset, see text). The peak at 0.5 days and dip at 1 day are typical for frequency deviations with a one-day period. Measurement of more than 13 hours performed at 2012-07-06, all data were included (dashed).

To compare the measurement with the soil temperature model, statistics on the scale of several days are needed. Therefore a longer roundtrip stability measurement took place from 2013-09-30 to 2013-10-09, using the fibre-coupled AOM while recording with the K+K FMX50 counter. This measurement contains a few periods during which the beat signal was too low for the FMX50 input circuits to record properly, leading to frequency outliers. Outliers were removed according to Chauvenets criterion ( $P = 0.5$ , 4102 data points (0.52% of the total set) removed) and were replaced with the median

of the dataset. We have verified that the ODEV statistics are not influenced significantly by this operation.

### 7.4.2 Clock transfer stability

In the previous section we established that for averaging periods of more than 10 s the frequency transfer instability of the link is  $< 1 \times 10^{-13}$ . Given the stability of the laboratory frequency standards (Rb clocks) it is therefore to be expected that a direct measurement of the link laser frequency at the remote site (Groningen) yields the mutual clock stability. During the 2012 measurement session, the absolute laser frequency at the remote site was recorded. The result of this measurement, together with the roundtrip stability and the stability of the link laser lock frequency are presented in Fig. 7.7.

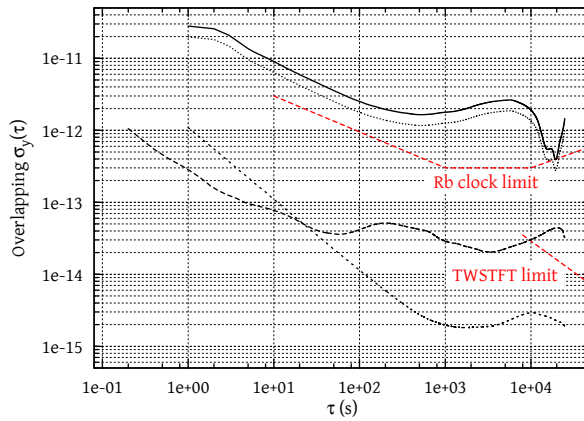


Figure 7.7: Comparison of ODEVs of the in-loop link laser stability relative to the frequency comb (short dash), the roundtrip stability (long dash), and the remote link laser frequency stability measured in Groningen (solid) of the 13 hour 2012 measurement series, divided by  $\sqrt{2}$  giving the Rb clock stabilities (dotted). The (red) straight dashed lines schematically indicate the Rb clock limit (SRS PRS10 datasheet), and the TWSTFT limit reported in [303].

The link laser frequency was determined with respect to the frequency comb, taking into account variations of  $f_{\text{rep}}$  and  $f_{\text{CEO}}$ . The determination of the absolute laser frequency is limited by the resolution of the  $f_{\text{rep}}$  counter to  $2.5 \times 10^{-13}/\text{s}$ . The maximum observable roundtrip instability is therefore about  $1 \times 10^{-15}/\text{s}$ . The observed instability is significantly higher, showing that the fibre may already influence the roundtrip stability at the second time scale.

The frequency of the laser used for the characterisation of the remote link was determined with respect to the nearest frequency comb mode. Together with the mode number determination, this directly delivers the remote absolute optical frequency. As can be seen in Fig. 7, the link laser frequency instability at the remote site is much larger than the total roundtrip instability. Therefore, the local frequency references are the limiting factor. This

means that we have effectively performed a frequency comparison between the GPS referenced Rb atomic clocks over the fibre link. Under the assumption of equal but independent clocks and frequency noise, the frequency instability is divided by  $\sqrt{2}$  to yield the stability of each individual setup and, thus, to enable the comparison with the instability of the Rb clock (Fig. 7). The measured performance is slightly worse than expected based on the Allan variance graph in the datasheet ( $< 10^{-12}$  at  $> 100$  s) of the clocks. This is possibly due to imperfect GPS reception, and/or uncorrelated frequency noise in the RF locks of the fibre combs to the Rb atomic clocks.

#### 7.4.3 Limits on frequency transfer stability due to soil temperature fluctuations

Based on coarse estimates we expected (soil) temperature fluctuations to have a major influence on the passive stability of the fibre link. The Royal Netherlands Meteorological Institute (KNMI) provided us with soil temperature measurements taken at the Cabauw site (see Fig. 7.1). Temperatures are measured at depths of 0, 2, 4, 6, 8, 12, 20, 30 and 50 cm every 12 seconds and averaged over 10 minute intervals. Out of five KNMI locations the site at Cabauw is the only location for which soil temperature data with such high temporal resolution is available in the Netherlands. The provided datasets consist of one set covering the 9 day link measurement with a 12 second time interval in October 2013 [318], and a 2 year dataset (2011, 2012) with a 10 minute interval [319].

Equation (7.8) is used to convert these temperature series to frequency deviations expected on a  $2 \times 298$  km fibre link with the given thermal expansion and thermo-optic coefficients. In the next sections we use these reference data to compare the link stability with the soil temperature model, Eq. (7.5).

#### Soil temperature and frequency transfer stability

The raw frequency data from the 9-day link stability measurement is compared to the frequency deviations as derived from the KNMI soil temperature dataset over the same time period. The first question that needs to be addressed is to what extent such a comparison, correlating temperature effects measured in locations separated by tens of kilometres, is meaningful. The Cabauw measurement site (Fig. 1) is located more than 40 km south of the (geographically) 200 km long trajectory of the fibre. Therefore the exact trends in soil temperature at the Cabauw site and along the fibre link can differ, due to local variations in solar irradiation and precipitation. Nevertheless, significant temperature correlations are expected as the different locations are relatively close, as seen from a meteorological and climatological point of view.

Figure 7.8 shows the roundtrip stability in comparison to the fibre-link stability calculated from the KNMI soil temperature data. KNMI aims at a rel-

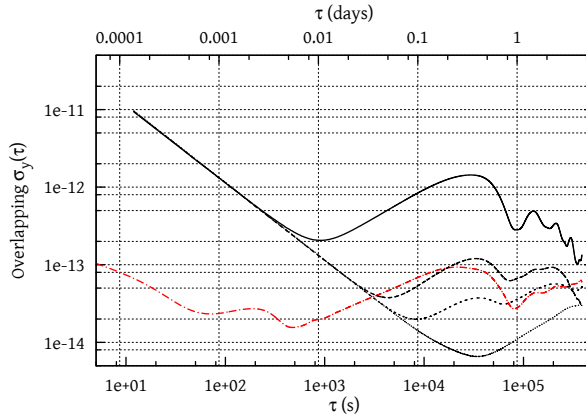


Figure 7.8: Fibre-link roundtrip stability (dash-dot) compared with roundtrip stabilities as calculated from the KNMI soil temperature measurements for different fibre depths: on the surface (solid curve), at 20 cm depth (long-dashed curve), at 30 cm depth (short-dashed curve), and at 50 cm depth (dotted curve). At shorter averaging times, the model curves display a  $1/\tau$  slope, which indicates that on shorter time scales temperature noise is significantly more prominent in the KNMI measurements than in the temperature-dependent link stability.

ative accuracy among sensors of 0.01 K and an absolute accuracy of 0.1 K. The noise in the soil temperature measurements amounts to a few mK. More accurate soil temperature observations will be difficult to make, let alone capturing all relevant variations along the optical path. All stabilities derived from soil temperature show a  $1/\tau$  slope for shorter time scales, which indicates the presence of white noise in the temperature measurements that does not appear in the fibre link instability. The noise levels at these time scales obscure frequency drift due to the daily temperature cycle. This cycle leads to the rising slope at longer time scales, with a local maximum at an averaging time of half a day. On even longer time scales, this instability cycle continues with a one-day period, and with local maxima decreasing in height over time. This is most clearly seen in the surface temperature curve.

The measured roundtrip stability curve shows averaging at short time scales less than 100 s, while at time scales larger than 1000 s frequency drifts due to the diurnal temperature cycle dominate the instability. For averaging times larger than  $4 \times 10^3$  s, the link measurement shows qualitative agreement with the KNMI data at depths of 20–30 cm. The origin of the level of instability at time scales less than  $4 \times 10^3$  s remains unclear. Possible causes are the several hundreds of meters of the fibre link located inside buildings, which are subject to significant and relatively fast temperature variations (due to e.g. airconditioning systems), while other factors like stress induced frequency fluctuations can not be entirely ruled out. We also considered the effect of polarisation mode dispersion, which we find to be negligible. For a worst-case differential group delay of  $0.2 \text{ ps}/\sqrt{\text{km}}$  the maximum polarisation-

dependent differential delay is  $\pm 5$  ps in our link. We typically observe polarisation changes of  $10^\circ$  per hour, leading to fractional frequency deviations smaller than  $1.5 \times 10^{-16}$ . This is negligible compared to the observed frequency instability.

The correlation between soil temperature and link frequency drift can be inferred from the temperature and frequency measurement time series. To this end, the roundtrip frequency deviations from the AOM frequency,  $\Delta f$ , are compared to the frequency deviations  $\Delta f_n$  due to soil temperature  $T_{\text{KNMI},n}$  at depth  $n$ , estimated using Eq. (7.8). Both datasets are averaged over two-hour windows to reduce noise levels. Figure 7.9 shows the raw data of the nine-day link measurement in comparison with  $\Delta f_n$  at 20 cm and 30 cm depth (2 hour averages).

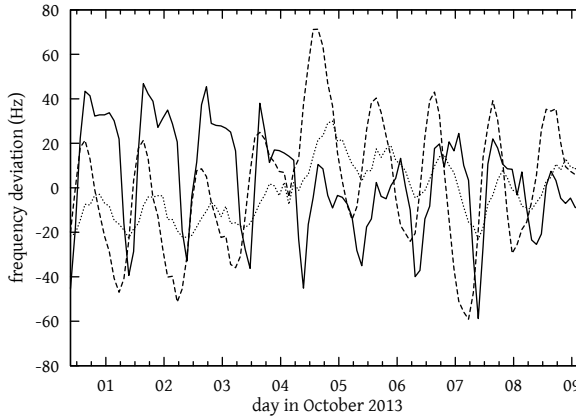


Figure 7.9: Frequency deviations after a roundtrip through the fibre link (solid) and frequency deviations calculated from the soil temperature data at 20 cm (dashed) and 30 cm depth (dotted).

The depth at which the fibre link is buried is not precisely known, and it furthermore may vary along the path of the link. An estimate of the 'effective' depth of the link may be obtained by assigning a weighting factor  $c_n \geq 0$  to each time series  $\Delta f_n$ , and minimising (by least squares fitting) the difference  $y$  between the measured and calculated frequency deviations

$$y = \Delta f - \sum_{n=0}^N c_n \Delta f_n(T_{\text{KNMI},n}) + f_{\text{offset}}. \quad (7.9)$$

The frequency offset parameter  $f_{\text{offset}}$  is needed to include a systematic offset between the link measurement data and the KNMI data. Such an offset may be caused by an overall relative temperature change between the fibre link path and the Cabauw site.

Figure 7.10 shows the variation of the fit parameters  $c_n$  and  $f_{\text{offset}}$  over time. These parameters and their time dependence are obtained as follows.

First, all input data (i.e. the measured frequency deviations and the frequency deviations estimated from soil temperature measurements) are averaged with a one-hour window. Of the averaged data sets, a 24-hour subset is taken (labeled by the median of the time stamps in the set), for which the coefficients  $c_n$  and  $f_{\text{offset}}$  are found by least-squares fitting. This last step is repeated for a 24-hour subset which is offset by six hours with respect to the previous subset, until the entire data set is covered. From Fig. 7.10 it follows that best agreement is found for an average fibre depth of about 30 cm. The least-squares fit method yields solutions which are generally well aligned in phase with the measured data (Fig. 7.9). However, Fig. 7.9 also shows that the agreement between the amplitude of the frequency deviations at 30 cm depth and the measured data is poor. The limited agreement may be partially caused by the contribution of fibre dispersion compensation modules which are located in equipment rooms rather than being buried underground. These modules are located in air-treated environments with stable temperatures and although the fibre length inside the modules is small compared to the fibre span, thermally induced length changes might have an appreciable effect. This effect will be subject to future study.

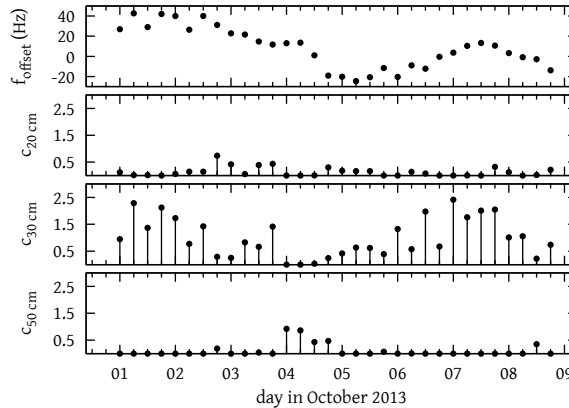


Figure 7.10: Fit parameters obtained by least-squares fitting to (partly overlapping) 24-hour subsets of roundtrip frequency data, with a spacing of six hours between each subset. Day of year represents the centre of the data range. (top) frequency offset for fit. (bottom three panels) Values of the  $c_n$  for the most important depths; the  $c_n$  found for the other depths are negligibly small. Averages and standard deviations over this dataset are  $f_{\text{offset}} = 8.1(20.3)$ ,  $c_{20\text{ cm}} = 0.13(0.17)$ ,  $c_{30\text{ cm}} = 1.01(0.72)$ , and  $c_{50\text{ cm}} = 0.10(0.24)$ .

In the time series of the link measurement (Fig. 7.9) the frequency deviations before 3 October and after 6 October appear to follow the predictions based on KNMI data, while between 3 October and 6 October the curves seem to be substantially less correlated. This discrepancy might be linked to the fact that during this period, the fibre-link path received considerably more precipitation on 3 October 2013 than the measurement site at Cabauw [320].

Moreover, solar irradiation differed substantially from day to day between Cabauw and the fibre link in this period [320]. It is conceivable that this led to local soil temperature variations along the fibre link and, thus, to the observed discrepancy. This behaviour illustrates the limited power of the temperature model for predicting or estimating instantaneous frequency variations based on soil temperature measurements.

#### A soil temperature model for frequency transfer stability estimation

Soil temperature data can be used to predict the long-term stability of fibre links, but it can be burdensome to obtain or construct long historical records. For example in 1961 soil temperature was measured 3 times a day [321]. Also, soil temperature is less often measured at meteorological measurement sites than other quantities. In the Netherlands KNMI has such data available for only four sites. In case of scarce soil temperature data, the sinusoidal soil temperature model (Eq. (7.5)) can be used to construct an artificial temperature cycle by superposition of a diurnal and an annual temperature cycle, which can be used to estimate the frequency transfer stability of fibre links. Such models can also be used to predict frequency transfer stability for various types of soil.

The amplitude of the diurnal temperature variation itself varies approximately sinusoidally during the year, and is given by

$$A_{T_{d,\text{year}}}(t) = T_{d,\text{year}} + A_{d,\text{year}} \sin\left(\frac{2\pi}{P_{\text{year}}}(t - t_{0,\text{year}})\right), \quad (7.10)$$

where  $T_{d,\text{year}}$  is the average diurnal temperature variation,  $A_{d,\text{year}}$  is the amplitude of the annual variation of the diurnal amplitude,  $P_{\text{year}}$  is the annual period, and  $t_{0,\text{year}}$  is used to shift the temperature cycle to fit the model to the long term measurement data of KNMI.

The total annual temperature cycle now becomes

$$T_{\text{annual}}(z, t) = T_0 + T_{\text{day}}(z, t, A_{T_{d,\text{year}}}(t)) + T_{\text{year}}(z, t), \quad (7.11)$$

where  $T_{\text{day}}$  and  $T_{\text{year}}$  are given by Eq. (7.5), but now with the amplitude  $A_{T_0}$  of the diurnal variation being a function of time.

We obtain a set of model parameters for Eq. (7.11) by fitting Eq. (7.5) to the data from Van der Hoeven and Lablans [316] as an estimate of the annual variations, and to the data from Woudenberg [321] to estimate the cycle of diurnal temperature variations. The soil constant was taken  $C_s = 7.5 \times 10^{-4}$ , which is representative for sand (being in a state between wet and dry), relatively dry loam, and clay [316]. The obtained average, amplitude and phase values are given in Table 7.1.

The soil temperatures resulting from the model are plotted in Fig. 7.11 and compared with the measured KNMI data set covering the year 2011. The plot compares the data at the surface and at 50 cm depth and shows that the

	Offset ( $^{\circ}\text{C}$ )	Amplitude ( $^{\circ}\text{C}$ )	$t_0$ (s)
Annual variation (surface)	10.2	8.8	$9.64 \times 10^6$
Annual day amplitude $A_{T_{d,\text{year}}}$	2.3	1.4	$7.94 \times 10^6$
Diurnal variation	0.0	$A_{T_{d,\text{year}}}(t)$	$3.67 \times 10^4$

Table 7.1: The parameters of the soil temperature model of Eq. (7.11) retrieved by a least-squares fit to data obtained from [316] and [321].

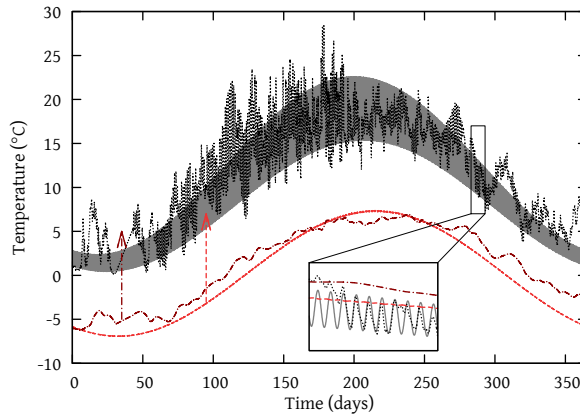


Figure 7.11: Annual variation of soil temperature at various depths. Modelled temperature at the surface (solid, appearing as a wide band due to diurnal variations which are not resolved at the time scale of the plot), and at 50 cm depth (dashed). Measured temperature at the surface (dotted) and at 50 cm depth (dash-dotted). Temperatures at 50 cm depth are offset by 10 degrees centigrade for visibility, arrows indicate true position. The inset shows a ten day subset of the data to visualise the diurnal variations of the surface temperature.

model is indeed in reasonable agreement with direct soil temperature measurements.

Figure 7.12 compares the frequency stability, computed using Eq. (7.8) and the soil temperature measurement series of 2011 and 2012, with that obtained from Eq. (7.8) and the sinusoidal model, Eq. (7.11). The most prominent feature is the discrepancy for 50 cm depth, likely due to fluctuations in weather conditions on long (days/weeks/months) time scales, which cause a higher instability at time scales between a day and half a year. These fluctuations are clearly visible in Fig. 7.11. This noise also leads to a smoothing of the strong minima in the frequency instability curves, which are a consequence of the sinusoidal temperature variations of the soil temperature model, Eq. (7.11). The stability at 200 cm depth was calculated from this model and shows that more deeply buried fibres offer a substantial stability improvement at the timescale of days, while the stability at the year scale is much closer to that of fibre buried closer to the surface.

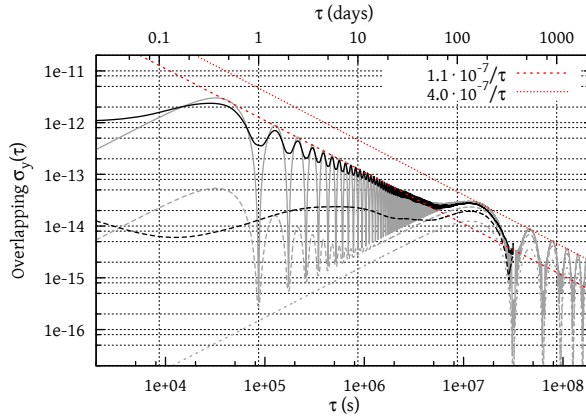


Figure 7.12: Frequency stability comparison between soil temperature measurements and the model (Eq. 7.11) at several depths. Surface measurement (solid), model (solid gray). 50 cm depth measurement (long-dash), model (long-dash gray). 200 cm depth model (short dash gray). The straight lines indicate the  $1/\tau$  behaviour with a maximum instability of  $2.6 \times 10^{-12}$  at half a day for the diurnal variation (dashed) and  $2.5 \times 10^{-14}$  at half a year for the annual variation (dotted) of the sinusoidal model.

## 7.5 Conclusions and outlook

We investigated the passive frequency stability of a  $2 \times 298$  km carrier-grade, unidirectional fibre link between VU University Amsterdam LaserLaB and Van Swinderen Institute, University of Groningen, using a single DWDM channel, and with live optical data traffic present in other DWDM channels. The observed frequency instability of the link lies in the range  $10^{-14}$  to  $10^{-13}$  for averaging times 10 to  $8 \times 10^5$  s. This result implies that such fibre links are well suited to distribute the frequency of commercial Rb atomic clocks with negligible loss of accuracy. A model for thermo-optical fibre length variation was developed which relates frequency variations to soil temperatures as a function of depth. We employed this model taking actual long-term soil temperature measurements as input, as well as predictions obtained from existing soil temperature models. We combined link frequency measurements with soil temperature measurements at the KNMI Cabauw site to show that the observed link stability corresponds to an average fibre depth of about 30 cm.

Qualitative agreement is found between the soil temperature model and KNMI measurements, while predictions of frequency stability based upon this model agree with actual roundtrip frequency measurements to within an order of magnitude. Although the predictive power of the soil-temperature model is limited, it does provide insight into the relation between soil temperature, fibre-optic path length variations and frequency-transfer stability. Our model thus allows estimating the passive frequency stability of fibre links for averaging times ranging from days to years, and allows to estimate up-

per bounds on the passive link instability. Such information will be useful for the design of future one-way frequency distribution systems based on underground fibre-optic infrastructure.

The presented results show that soil temperature fluctuations have a large impact on the passive frequency stability of optical carriers over underground fibre links for time scales longer than approximately 1000 seconds. The results of our study confirm the conclusions of previous work that fibre-optic infrastructure is sufficiently stable for one-way atomic clock frequency distribution over hundreds of kilometres distance, and with  $1 \times 10^{-13}$  relative instability [293, 295]. This level of instability compares favourably to the stability of commercial GPS-disciplined Rb clocks. The residual frequency variations are sufficiently small to back up the local oscillator of GPS-referenced clocks with indefinite holdover (provided a non-GPS-referenced master clock is used). This opens up the perspective of a terrestrial “flywheel” oscillator, embedded in the currently installed unidirectional fibre-optic telecommunications network, which can be used to back-up GPS-referenced oscillators during periods of GPS outage.

### Acknowledgement

This work was supported by the Netherlands Foundation for Fundamental Research of Matter (FOM) through the program “Broken Mirrors & Drifting Constants”. J.C.J.K. thanks the Dutch Organisation for Scientific Research (NWO) and the Dutch Technology Foundation (STW) for support.



## 8. Outlook

The development in technology with regard to frequency comb laser sources will be treated in the scope of three major subjects of this thesis. It can in general be said that the field is progressing fast in the direction of sub-Hz level combs and locking of lasers. Together with rapid developments in high-stability low-noise rf generation from frequency combs, enabling state of the art frequency standards, these developments will also enable the next level in spectroscopic accuracy in the XUV. Transfer techniques for such state of the art frequency standards are known, but their implementation in existing long-haul fibre networks is still an open research topic. Implementations for time transfer on the sub-ns level on the other hand, are a relatively novel terrain to be explored.

### 8.1 High-precision spectroscopy in the XUV

The frequency comb system to perform XUV spectroscopy has been extended by colleagues to work on multiple inter-pulse distances by use of a pump oscillator working at the same repetition rate as the frequency comb laser. The cumbersome delay line to create a double pump pulse has been replaced by fast pulse picking optoelectronics enabling subsequent amplification of pulse pairs at (almost) arbitrary intervals  $n/f_{\text{rep}}$ . In this way a full repetition rate spectrum can be built up by picking pulse pairs with variable inter pulse distance. Jonas Morgenweg has explained the advantages and detailed working of this system in his thesis [182].

First experiments on the simplest molecular systems ( $\text{H}_2$ ), used for QED testing as done in this thesis for helium, are in reach of this system, and with enhanced pump amplifier capacity much shorter wavelength ranges (down to the water window at 2 – 4 nm) come in reach at repetition rates up to 300 Hz [322]. A Doppler reduced near background-free two-photon spectroscopy method has been explored and demonstrated by Morgenweg and Barmes [137]. This method can be applied to do two-photon high resolution spectroscopy in the XUV via HHG too.

In the broader community competing groups have succeeded in doing spectroscopy with their full repetition rate enhancement cavity based approaches [183], although competing measurements on the ground state energy of the helium system have unfortunately not yet been published.

In the future optical locking of the frequency comb lasers will become a key issue again when the limits of the Ti:Sapphire frequency comb system will be reached in the XUV spectroscopy. Especially for measurements on the 1S–2S transition in  $\text{He}^+$  ions where the Ramsey pulses have to be separated by long time spans will need this technology to push the limits of the XUV frequency comb system to the kHz level. To reach this goal the mode linewidth of the Ti:Sapphire comb now used for the Ramsey-comb method has to be re-

duced to kHz or narrower modes from the current 1–2 MHz. In order to perform state of the art sub-Hz optical locking a sub-Hz level CW laser has been installed in the lab. Means for frequency doubling of this 1542.4 nm laser to the near infrared have partially been described in this thesis (Chapter 3), which will be used to lock the Ti:sapphire frequency comb to in the future.

Currently the fibre integration of various components has been shown to be very useful and user friendly. However, when the laser systems start to approach the Hz level in the IR, these concepts will have to be reviewed and actively stabilised fibre based optical frequency dissemination systems will need to be employed in order to push the performance of the frequency comb lasers even further.

## 8.2 Semiconductor frequency comb laser sources

It is exactly in the area of high frequency stability performance where integrated optical components might play a key role in the future. Due to the possibility of integration of active optical components like CW and mode-locked lasers, optical amplifiers, together with non-linear components, active and passive optical devices like modulators, wavelength selection and couplers, photo diodes and possibly even driver and control electronics needed for complete stabilisation of a frequency comb laser, such technology can enable very compact metrology laser sources. Integrating various means for phase stabilised optical frequency transfer from and to the chip yields integrated frequency comb and CW lasers that can be cross-locked on-chip to Hz level lasers and deliver ultra-stable RF as an output too.

Other opportunities for such small semiconductor lasers lie in the telecommunications area. Several encoding methods using phase-amplitude modulation will favour narrow linewidth frequency comb lasers whose individual comb lines can be spatially separated on chip and sent to individual modulators. In this way information densities can be obtained that lie closer to Shannon's limit. This will optimise the use of available bandwidth in optical telecommunication systems.

Indeed, such integrated per comb-line modulator is capable of performing electric field synthesis in the optical wavelength range. Such systems might boost research in quantum chemistry by enabling potential energy surface control in large molecules and might eventually find applications in the chemical or pharmaceuticals industry. A novel development that is interesting for the field of molecular spectroscopy in particular are quantum cascade mode-locked lasers. Recent developments show that these semiconductor lasers can be optically locked to stable CW lasers, yielding an interesting tool for far-infrared spectroscopy [323].

## 8.3 Time and frequency transfer techniques

Some of the research in this thesis shows that optical networks as deployed in the Netherlands can already be used to improve upon traditional time dis-

semination concepts. The passive stability of these networks surpasses the accuracy of simple rubidium clocks, which are currently used in many applications, for example in mobile telecommunication. Methods for stable time transfer based on the results in this thesis are under development and will be available for commercial applications on relatively short time scale. That there is a need for such technology can be seen from the ongoing efforts in next generation internet standards for time transfer (NTP, PTP, PTPv2, White Rabbit). As an example, the varying bit rates of network segments in 100 Gbit Ethernet routing is a problem that is not yet solved fully by suppliers of 100G equipment and such standards might in the future include means for syntonisation and time transfer in order to solve such problems.

Currently the limits of electronic synchronisation methods are being pushed to the sub-ps level at the second time scale, while reference measurements on electronic systems can be performed that can determine the delay stability of devices towards the attosecond level. It is in this perspective that the now somewhat exotic tools of optical frequency comparison at the highest level [298, 299, 324, 325] can soon start to take over the role of satellite based methods for frequency and time comparison of atomic standards. Networks can then be fully syntonised and time synchronised by a single optical time standard. Chip based CW and frequency comb lasers and active phase stabilisation of optical networks might start to play an important role in such networks.

In the field of fundamental physics these technologies are of main importance for high-accuracy tests of physical theories, like the hypothesis of possibly varying fundamental constants [326, 327], or the search for fifth forces [328, 329]. Optical clocks, fibre-based frequency comparisons, high-accuracy frequency comb spectroscopy will possibly bring new physical phenomena in view.

*And further, by these, my son, be admonished: of making many books there is no end; and much study is a weariness of the flesh. Let us hear the conclusion of the whole matter: Fear God, and keep his commandments: for this is the whole duty of man.*

(Ecclesiastes 12:12,13) [1]



# Appendices



# A. Equations, notations and derivations

Without too much comments some mathematical relations referred to in this thesis are recalled, some notations used are clarified, and derivations that would have interfered with the main text are presented here.

## A.1 $N$ sample variance

The  $N$  sample variance of frequency measurements is defined as

$$\sigma^2(N, T, \tau) = \frac{1}{N} \sum_{i=1}^N \left( \bar{y}_i - \frac{1}{N} \sum_{j=1}^N \bar{y}_j \right)^2, \quad (\text{A.1})$$

where  $N$  is the number of samples  $y_i$ ,  $T$  is the time interval between the samples and  $\tau$  the duration of the measurement of the samples, giving rise to a dead time  $t - \tau$ . However, this estimator is biased for any kind of frequency noise and a finite number of samples. An unbiased estimator for the case of white frequency noise when  $T = \tau$  (zero dead time), is given by [99]

$$\sigma^2(N, T, \tau) = \frac{1}{N-1} \sum_{i=1}^N \left( \bar{y}_i - \frac{1}{N} \sum_{j=1}^N \bar{y}_j \right)^2. \quad (\text{A.2})$$

The relation between the average of the  $N$ -sample variance (A.2) and the one sided spectral density of the fractional frequency fluctuations  $S_y(f)$  defined in Eq. (2.11), is given by

$$\begin{aligned} \langle \sigma_y^2(N, T, \tau) \rangle = \\ \frac{N}{N-1} \int_0^\infty S_y(f) \left( \frac{\sin \pi \tau f}{\pi \tau f} \right)^2 \left[ 1 - \left( \frac{\sin N \pi T f}{N \sin \pi T f} \right)^2 \right] df, \end{aligned} \quad (\text{A.3})$$

where  $\sigma_y$  denotes the two-sample Allan variance.

## A.2 Error estimation based on $\chi^2$ distributions

For a chi-squared distribution  $\chi^2$  the sample variance  $s^2$  with a number of degrees of freedom (df.) can be related to the true variance  $\sigma^2$  of the distribution via the equation

$$\chi^2 = \frac{(\text{df.})s^2}{\sigma^2}. \quad (\text{A.4})$$

The number of degrees of freedom is easily determined as  $N/2$  for an even number  $N$  of data samples, used only once each to estimate the Allan variance, e.g. if sample 1 and 2, 3 and 4, and so on are used. If, however, we

include a variance determined by samples 2 and 3, the sample variance calculated for this point is not independent from the other two, which means that we cannot assume (df.) to be 3. Various authors have used analytical and simulation techniques to estimate (df.) [103, 330]. The analytical (Lesage, Audoin and Yoshimura [102, 331, 332]) and simulation based (empirical) results of Howe [103] are given in table A.2<sup>1</sup>, as a function of the dominant noise type characterized by the slope alpha in the Allan variance graph (see Table A.1). Note here that the values of  $R(n)$  for  $\alpha = 1, -1$  are empirically determined <sup>2</sup>.

$\alpha$	$\sigma_y^2(\tau)$	mod. $\sigma_y^2(\tau)$	$R(n)$
-2	$h_{-2} \frac{2\pi^2}{3} \tau$	$h_{-2} \frac{2\pi^2}{3} \tau R(n)$	0.824
-1	$h_{-1} 2 \ln(2)$	$h_{-1} 2 \ln(2) R(n)$	0.647
0	$h_0 \frac{1}{2\tau}$	$h_0 \frac{R(n)}{2\tau}$	0.5
1	$h_1 \frac{1.038 + 3 \ln(2\pi f_h \tau)}{4\pi^2 \tau^2}$	$h_1 \frac{3.37}{4\pi^2 \tau^2}$	$\frac{3.37}{1.038 + 3 \ln(2\pi f_h \tau)}$
2	$h_2 \frac{3f_h}{4\pi^2 \tau^2}$	$h_2 \frac{3f_h}{4n\pi^2 \tau^2}$	$\frac{1}{n}$

Table A.1: Noise types  $\alpha$  and the slopes for the Allan variance and modified Allan variance including their ratio  $R(n)$  where  $n$  is the sample size. The constants  $h_\alpha$  are intensity coefficients indicating the strength of the noise (see [103]). In some cases the result relies on the hardware cutoff frequency  $f_h$  in order to achieve convergence. The ratio  $R(n) = \text{mod. } \sigma_y^2(\tau) / \sigma_y^2(\tau)$  relates the slopes of the variances and is given for the limit value  $n \rightarrow \infty$ . In a single case the slope depends on the number of samples  $n$  averaged to obtain a software defined  $\tau = n\tau_0$ . Note that the equation for white phase noise  $\alpha = 2$  for the modified Allan deviation cannot be true since in the property of the modified deviation is that the slopes for  $\alpha = 1$  and  $\alpha = 2$  in the modified version are distinguishable. This error possibly stems from untracked errata in Sullivan [333].

<sup>1</sup>Errata are found in NIST Technical Note 1337 [333], take note to track a single erratum throughout the document.

<sup>2</sup>see Sullivan [333] and the numerous errata therein.

$\alpha$	empirical (df.) [103]
-2	$\frac{N-2}{m} \frac{(N-2)^2 - 3m(N-1) + 4m^2}{(N-3)^2}$
-1	$\left. \begin{array}{l} \frac{2(N-2)^2}{2.3N-4.9} \quad \text{for } m=1 \\ \frac{5N^2}{4m(N+3m)} \quad \text{for } m \geq 2 \end{array} \right\}$
0	$\left( \frac{3(N-1)}{2m} - \frac{2(N-2)}{N} \right) \frac{4m^2}{4m^2+5}$
1	$\exp \left[ \ln \left( \frac{N-1}{2m} \right) \ln \left( \frac{(2m+1)(N-1)}{4} \right) \right]^{\frac{1}{2}}$
2	$\frac{(N+1)(N-2m)}{2(N-m)}$
$\alpha$	analytical (df.) for $m=1$ [103]
-2	$N-2$
-1	$\frac{2(N-2)^2}{2.3N-4.9}$
0	$\frac{2(N-2)^2}{3N-7}$
1	unknown
2	$\frac{18(N-2)^2}{35N-88}, \quad \text{for } N \geq 4$

Table A.2: Number of degrees of freedom (df), for common noise types  $\alpha$  (see Table 2.1).  $N$  is the number of samples in the set, (df.) is then given for an effective sample time  $\tau = m\tau_0$  where frequency data for  $m$  samples are combined. Analytical values were only available for  $m=1$ .

### A.3 From Maxwell's equations to the wave equation

Maxwell's equations [334], which fully describe classical electromagnetic fields can be written as

$$\nabla \cdot \mathbf{E} = \frac{1}{\epsilon_0} \rho, \tag{A.5a}$$

$$\nabla \cdot \mathbf{B} = 0, \tag{A.5b}$$

$$\nabla \times \mathbf{E} = -\frac{\partial \mathbf{B}}{\partial t}, \tag{A.5c}$$

$$\nabla \times \mathbf{B} = \mu_0 \mathbf{J} + \mu_0 \epsilon_0 \frac{\partial \mathbf{E}}{\partial t}, \tag{A.5d}$$

where  $\mathbf{E}$  is the electric field strength,  $\rho$  the electric charge density,  $\mathbf{B}$  the magnetic flux density and  $\mathbf{J}$  the electric current density.  $\epsilon_0$  and  $\mu_0$  are the permit-

tivity and permeability of free space.

In matter several effects give rise to charge and current densities [335]. The polarisation  $\mathbf{P}$  leads to a bound electric charge density  $\rho_b = -\nabla \cdot \mathbf{P}$  and a change in  $\mathbf{P}$  leads to an electric polarisation current density  $\mathbf{J}_p = \frac{\partial \mathbf{P}}{\partial t}$ , the magnetisation  $\mathbf{M}$  leads to a bound electric current density  $\mathbf{J}_b = \nabla \times \mathbf{M}$ , from which we now write the electric charge and current densities as

$$\rho = \rho_f + \rho_b = \rho_f - \nabla \cdot \mathbf{P}, \quad (\text{A.6})$$

$$\mathbf{J} = \mathbf{J}_f + \mathbf{J}_b + \mathbf{J}_p = \mathbf{J}_f + \nabla \times \mathbf{M} + \frac{\partial \mathbf{P}}{\partial t}. \quad (\text{A.7})$$

Wave equations of the fields are obtained by switching from the magnetic flux density  $\mathbf{B}$  to the magnetic field intensity  $\mathbf{H}$  through the relation

$$\mathbf{H} = \frac{1}{\mu_0} \mathbf{B} - \mathbf{M}. \quad (\text{A.8})$$

The relation

$$\mathbf{D} = \varepsilon_0 \mathbf{E} + \mathbf{P}, \quad (\text{A.9})$$

between the electric field intensity  $\mathbf{E}$  and the electric displacement  $\mathbf{D}$  is given for the sake of completeness. Separating  $\mathbf{E}$  and  $\mathbf{H}$  by application of the curl to equations (A.5c) and (A.5d) the wave equations

$$\begin{aligned} \nabla^2 \mathbf{E} - \mu_0 \varepsilon_0 \frac{\partial^2 \mathbf{E}}{\partial t^2} &= \frac{1}{\varepsilon_0} \nabla \rho_f + \mu_0 \frac{\partial \mathbf{J}_f}{\partial t} + \mu_0 \frac{\partial}{\partial t} (\nabla \times \mathbf{M}) \\ &\quad + \mu_0 \frac{\partial^2 \mathbf{P}}{\partial t^2} - \frac{1}{\varepsilon_0} \nabla (\nabla \cdot \mathbf{P}) \end{aligned} \quad (\text{A.10a})$$

and

$$\begin{aligned} \nabla^2 \mathbf{H} - \mu_0 \varepsilon_0 \frac{\partial^2 \mathbf{H}}{\partial t^2} &= -\nabla \times \mathbf{J}_f - \frac{\partial}{\partial t} \nabla \times \mathbf{P} \\ &\quad + \mu_0 \varepsilon_0 \frac{\partial^2 \mathbf{M}}{\partial t^2} - \nabla (\nabla \cdot \mathbf{M}) \end{aligned} \quad (\text{A.10b})$$

are obtained. Although these equations look somewhat bloated with source factors, compared to what is normally presented, it should be noted that these equations are in their most general form, and no assumptions have yet been made with respect to the medium in which the electromagnetic field resides.

Anisotropic electric<sup>3</sup> media are described by the electric susceptibility  $\chi_e$  in the form of tensors relating  $\mathbf{P}$  and  $\mathbf{E}$ . The non-linear material responses can be described by letting  $\mathbf{P}$  depend on higher orders  $n$  of  $\mathbf{E}$ . In general

$$\mathbf{P} = \varepsilon_0 \sum_{n=1}^{\infty} \chi_e^{(n)} \mathbf{E}^n, \quad (\text{A.11})$$

<sup>3</sup>The equation is equally valid for dielectric and conducting media.

where  $\mathbf{E}$  can be a linear combination of electrical fields. For isotropic electric media with a linear response this equation reduces to

$$\mathbf{P} = \varepsilon_0 \chi_e \mathbf{E} \quad (\text{A.12})$$

where  $\chi$  can be complex and is in general frequency dependent, the imaginary part represents dielectric losses.

The same holds for anisotropic magnetic media, of which the ferrimagnetic materials play an important role in non-reciprocal optical devices like isolators and Faraday rotators. The magnetic susceptibility  $\chi_m$  relates  $\mathbf{M}$  and  $\mathbf{H}$  and non-linear responses can be described as well using

$$\mathbf{M} = \sum_{n=1}^{\infty} \chi_m^{(n)} \mathbf{H}^n, \quad (\text{A.13})$$

in this case the imaginary part of  $\chi_m$ . For isotropic magnetic media with a linear response the equation reduces to

$$\mathbf{M} = \chi_m \mathbf{H}, \quad (\text{A.14})$$

where  $\chi_m$  can have an imaginary part to account for magnetic losses.

For completeness the relation between the permittivity  $\varepsilon$ , relative permittivity  $\varepsilon_r$  and  $\chi_e$  and between the permeability  $\mu$ , relative permeability  $\mu_r$  and  $\chi_m$  are given

$$\varepsilon \equiv \varepsilon_0 (1 + \chi_e) = \varepsilon_0 \varepsilon_r, \quad (\text{A.15})$$

$$\mu \equiv \mu_0 (1 + \chi_m) = \mu_0 \mu_r. \quad (\text{A.16})$$

In vacuum  $\rho$  and  $\mathbf{J}$  are zero, and rewriting (A.5) yields the free-space wave equation for the electric field

$$\nabla^2 \mathbf{E} - \mu_0 \varepsilon_0 \frac{\partial^2 \mathbf{E}}{\partial t^2} = 0, \quad (\text{A.17})$$

which has as one of the solutions the plane travelling wave in the  $\mathbf{k}$  direction [336]

$$\mathbf{E}(\mathbf{r}, t) = E_0 \cos(\mathbf{k} \cdot \mathbf{r} - \omega t + \varphi) \hat{\mathbf{n}}, \quad (\text{A.18})$$

$$\hat{\mathbf{k}} \cdot \hat{\mathbf{n}} = 0, \quad (\text{A.19})$$

$$\mathbf{B}(\mathbf{r}, t) = \frac{E_0}{c} \cos(\mathbf{k} \cdot \mathbf{r} - \omega t + \varphi) (\hat{\mathbf{k}} \times \hat{\mathbf{n}}), \quad (\text{A.20})$$

where  $E_0$  is the field strength,  $\mathbf{k}$  the wave vector,  $\hat{\mathbf{n}}$  polarization vectors,  $\mathbf{r}$  is the position vector and  $\varphi$  an arbitrary phase of the wave. This means that both the  $\mathbf{E}$  and  $\mathbf{B}$  fields are perpendicular to  $\mathbf{k}$ .

#### A.4 Determination of the mode ambiguity range

Determination of the mode numbers  $m$  on measurement of an optical frequency with a frequency comb typically yields an ambiguous result since there are multiple solutions possible for the set of equations (2.53) of Sec. 2.4.1

$$f_{l_1} = \pm f_{\text{CEO}_1} + m_1 f_{\text{rep}_1} \pm f_{\text{beat}_1}, \quad (\text{A.21a})$$

$$f_{l_2} = \pm f_{\text{CEO}_2} + m_2 f_{\text{rep}_2} \pm f_{\text{beat}_2}, \quad (\text{A.21b})$$

$$|\Delta f_{l_1, l_2}| = |f_{l_1} - f_{l_2}| \equiv 0, \quad (\text{A.21c})$$

The smallest interval  $n f_{\text{rep}_1}$  over which an unambiguous solution is defined is determined by

$$\begin{aligned} n (f_{\text{rep}_2} - f_{\text{rep}_1}) &= f_{\text{rep}_1}, \\ \frac{n}{n+1} &= \frac{f_{\text{rep}_1}}{f_{\text{rep}_2}} \end{aligned} \quad (\text{A.22})$$

from which we can see that large  $n$  can be reached by a small fractional  $f_{\text{rep}}$  change between the measurements or becomes infinite if the fractional  $f_{\text{rep}}$  change is non integer. For integer fractional  $f_{\text{rep}}$  change

$$n = \frac{f_{\text{rep}_1}}{f_{\text{rep}_2} - f_{\text{rep}_1}} \quad (\text{A.23})$$

the frequency interval is approximately proportional to the fractional frequency change.

In practice the fractional stability of the lasers in the time between the two frequency determinations is crucial. If either  $f_l$ ,  $f_{\text{rep}}$  or  $f_{\text{CEO}}$  drifts by more than the fractional  $f_{\text{rep}}$  change between the two measurements, Eq. (A.21a) yields values around 0 for large amounts of frequencies. In practice a change in  $f_{\text{rep}}$  in the order of 0.1% to 1% will lead to an unambiguously defined frequency within  $1000 f_{\text{rep}}$  to  $100 f_{\text{rep}}$ . Resolving the ambiguity on such a coarse wavelength scale can typically be done with a normal spectrum analyser, and thus allows for an unambiguous determination of the laser frequency  $f_l$ .

#### A.5 Second order DC Stark shift in helium

Here slightly more detail on the derivation of the second order Stark shift is given after Hertel [162]. For a linear Stark shift the perturbation leads to first order correction

$$\begin{aligned} \Delta E_k^{(1)} &= \langle \gamma J M_k | V_{\text{el}} | \gamma J M_k \rangle \\ &= eE \langle \gamma J M_k | r C_{10}(\theta) | \gamma J M_k \rangle \\ &= eE \langle \gamma_k | r | \gamma_k \rangle \langle J M_k | C_{10}(\theta) | J M_k \rangle \end{aligned} \quad (\text{A.24})$$

of the energy of level  $k$ , which can be separated in a radial part ( $\langle \gamma_k | r | \gamma_k \rangle$ ) and a spherical part ( $\langle J M_k | C_{10}(\theta) | J M_k \rangle$ ), with  $C_{10}(\theta)$  a spherical harmonic

function. To obtain a value for the radial part of the wave equation the following integral is evaluated

$$\langle Y_k | r | Y_k \rangle = \langle nl_k | r | nl_k \rangle = \int_0^\infty R_{nl_k}(r) R_{nl_k}(r) r^3 dr, \quad (\text{A.25})$$

where  $R_{nl}(r)$  are the radial wave functions of the atom for quantum numbers  $n$  and  $l$ .<sup>4</sup> The spherical part of the wave function can be calculated by means of  $3j$  symbols.

However, for the helium atom, a calculation of the second order perturbation is needed to obtain values for the Stark shift resulting in

$$E_k^{(2)} = E_k^{(0)} + \langle k | V_{\text{el}} | k \rangle + \sum_{j \neq k} \frac{|\langle j | V_{\text{el}} | k \rangle|^2}{E_k^{(0)} - E_j^{(0)}}. \quad (\text{A.26})$$

The first order shift  $E_k^{(1)} = \langle k | V_{\text{el}} | k \rangle = 0$  drops out of this equation, and instead a correction for each coupling level  $j$  to level  $k$  needs to be taken into account. Because the helium atom has a strong  $LS$  coupling ( $V_{LS} \gg V_{\text{el}}$ ) the spherical wave function is written (in quantum numbers) as  $|LSJM\rangle$  which leads to

$$\begin{aligned} \Delta E_k^{(2)} &= E_k - E_k^{(0)} \\ &= \sum_{j \neq k} \frac{|\langle j | V_{\text{el}} | k \rangle|^2}{E_k^{(0)} - E_j^{(0)}} \\ &= \sum_{j \neq k} \frac{|\langle \gamma LSJM_j | V_{\text{el}} | \gamma LSJM_k \rangle|^2}{E_k^{(0)} - E_j^{(0)}}, \end{aligned} \quad (\text{A.27})$$

where the wave functions are expanded into a radial and spherical part, yielding for the interaction (Hertel equation 8.57)

$$\begin{aligned} \langle \gamma LSJM_j | V_{\text{el}} | \gamma LSJM_k \rangle &= \\ &= eE \langle nl_j | r | nl_k \rangle \sqrt{(2J_j + 1)(2J_k + 1)(2L_j + 1)(2L_k + 1)} \times \delta_{M_j M_k} \delta_{L_j L_k \pm 1} \\ &\quad \times (-1)^{M_k - S_k} \begin{pmatrix} J_j & J_k & 1 \\ -M_k & M_k & 0 \end{pmatrix} \begin{Bmatrix} L_j & L_k & 1 \\ J_k & J_j & S_k \end{Bmatrix} \begin{pmatrix} L_j & 1 & L_k \\ 0 & 0 & 0 \end{pmatrix} \\ &= eE z_{kj}. \end{aligned} \quad (\text{A.28})$$

Inserting (A.28) into (A.27) yields the second order Stark shift as

$$\Delta E_k^{(2)} = |eE|^2 \sum_{j \neq k} \frac{|z_{kj}|^2}{E_k^{(0)} - E_j^{(0)}}, \quad (\text{A.29})$$

where  $z_{kj}$  is a measure for the strength of the transition.

<sup>4</sup>see Hertel [162] §2.8.5 how to solve this equation, and §2.8.2 on the atomic units used.

## A.6 On the notation of the helium atomic state

When reading literature on spectroscopy of helium, one immediately notices the various notations of the atomic states that are used. In this thesis I have followed a modern convention, in which the atomic state is notated in a complete manner. The basics of this notation are covered here.

As we have seen, the atomic state depends on several quantum numbers  $nlm$ . The principal quantum numbers  $n$  for each electron as well as the orbital momentum  $l$ , denoted s,p,d,..., are unique for each electron. The atomic state is therefore typically written as

$$n_1 l_1 n_2 l_2 \dots n_i l_i \quad (\text{A.30})$$

where each electron  $i$  is denoted. If multiple electrons are in the same configuration this is typically denoted as a power. For example, we have a 3 electron atom in it's ground state, this is written as  $1s^2 2s$ , which is the ground state of lithium. Closed shells are sometimes omitted or replaced by the abbreviation of the atom for which this is the full shell, in case of the previous example [He]2s. The abbreviation is however typically done for elements with more than 10 electrons to avoid an excessive number of filled shells in the notation<sup>5</sup>.

The combination of orbital momentum quantum numbers,  $l$ , gives a total orbital momentum  $L$  and the combination of spins quantum numbers,  $s$ , of the electrons, a total spin  $S$ , which is then again combined to give a total angular momentum quantum number  $J$ . This reasoning is of course only valid if the chosen basis set of the quantum state is orthogonal. Fortunately helium is an atom in which this so called spin-orbit coupling (also known as LS-coupling or Russel-Saunders coupling regime) is a valid description of the atomic state and we will thus write

$$S = \sum_{i=1}^n s_i, \quad L = \sum_{i=1}^n l_i, \quad J = L + S. \quad (\text{A.31})$$

These three parameters can now be combined in the term symbol  $^{2S+1}L_J$ . The ground state of helium is now denoted  $1s^2 \ ^1S_0$  (a singlet state) and an excited state could be  $1s3p \ ^3P_2$  (a triplet state).

In the equations for the Stark shift the magnetic quantum number  $M$  appears. This is the magnetic sublevel of the angular momentum  $L$  and range from  $-L$  to  $+L$  in integer steps. Conservation of energy, momentum and angular momentum, makes that for an atomic excitation between equal  $M$ , the magnetic moment of the photon should be  $q = 0$ , implying linearly polarised light. Circularly polarised light ( $q = \pm 1$ ) can excite transitions with  $\Delta M = \pm 1$ .

<sup>5</sup>E.g. for Thorium we write the groundstate [Rn]6d<sup>2</sup>7s<sup>2</sup> in stead of  $1s^2 2s^2 2p^6 3s^2 3p^6 3d^{10} 4s^2 4p^6 4d^{10} 5s^2 5p^6 4f^{14} 5d^{10} 6s^2 6p^6 6d^2 7s^2$ .

## B. A historical overview of the ionisation energy of helium

The title of this appendix is somewhat remarkable, how could the ionisation energy of helium have changed over time? Although there is ample speculation about temporal changes in fundamental constants, the title does not refer to these phenomena. Rather, it refers to the accuracy and resolution with which the ionisation energy of helium has been observed and calculated from the time that helium was discovered. Please note that this overview cannot be considered complete, but hopefully it does provide an interesting read about the historical developments concerning the helium ionisation energy, to which this thesis also made a contribution.

### B.1 Introduction

With the discovery of helium goes the name of Pierre Jules César Janssen [49], who first observed it as a bright yellow line at 587.49 nm near the D<sub>1</sub> and D<sub>2</sub> sodium lines during the solar eclipse on August 18, 1868. Later that year, on October 20, Norman Lockyer [337] observed the same line, which he named D<sub>3</sub>. Lockyer then investigated the hydrogen lines together with Edward Frankland [337], and the two concluded that this line could not be measured in the laboratory, indicating that it might belong to a new element. Who termed the name helium [338], which has a “metallic” ending, is unclear, although the best guess is Lockyer [339].

Luigi Palmieri first detected helium on earth, during spectroscopic measurements on lava samples from mount Vesuvius<sup>1</sup>. In 1895 Lord Ramsay<sup>2</sup> then succeeded in extracting, purifying and identifying helium from samples of clèveite, observing the D<sub>3</sub> line by use of an electrical discharge through the extracted gas. Mr. Crookes measured the D<sub>3</sub> line at a wave-length<sup>3</sup> of 587.49 millionths of a millimetre. Ramsay makes a remark about the visibility of violet lines in the helium spectra, speculating in the conclusion of his paper that helium might be an atom belonging to the group of argon due to apparent equal behaviour in the purification process [341]. He further concludes that if this is the case the atomic mass should be 4 or 8 (giving argon a weight of 20 or 40). Ramsay cites in this work part of a letter from William Francis Hillebrand who claims to have seen additional lines in the spectra, but attributed these to Nitrogen. In the second part of the paper [342] Ramsay then marks a difference in weight of the gas from various sources and distinctly different spectral features from the lighter gas samples.

---

<sup>1</sup>Supposedly in 1882, a trustworthy source document would be welcome.

<sup>2</sup>The Swedish chemists Nils Abraham Langlet and Per Teodor Cleve independently discovered helium in cleveite in 1895 too, no trustworthy source is yet available to the author.

<sup>3</sup>historical, see [340]

Although from the beginning the gas was electrically excited (typically by means of a Ruhmkorff coil or high voltage DC discharge) in order to produce the spectra, most of these excitations took place in glass tubes, sometimes using photographic plates and sometimes only by measuring directly the spacings between the visible lines of a reference gas and helium. These first observers could simply not have seen any parts of the spectrum below a few hundred nanometre due to the construction of the sources and spectrographs.

The initial availability of helium was limited, since the gas could only be extracted from uranium rich minerals. In 1903 state geologist Erasmus Haworth and David F. McFarland together with Hamilton P. Cady of the university of Kansas analysed unidentified contents from natural gas sources in the U.S.A. [343]. In 1905 they identified a 1.84% fraction of the well of Dexter as helium [344]. The gas became available to a wider public and in a better purified form only after about 10 years and was still a gas without a use. When it became clear around 1917 that it was of importance to the Allied forces for the filling of blimps and balloons, production took off only after establishment of helium production plants from 1919 on [345].

It took until 1924 to observe the single photon lines from the groundstate of He I and He II in the XUV directly, requiring a special construction of a vacuum discharge source connected to a much optimized vacuum spectrograph, with gratings specially ruled for the XUV spectroscopic region [346].

In the quest for a better understanding of the helium atom, theoretically important because of its three particle nature<sup>4</sup>, the determination of the ground state energy (or, otherwise stated, the first ionisation energy) is a long lasting tradition. This quest for an ever more precise and accurate metrology has at times yielded important results, such as the discovery of the Lamb shift, pushing the developments in the field of three particle quantum electrodynamics (QED).

Although ideally this review would contain all possible determinations of the ionisation energy of helium, it focusses on spectroscopy where the excitation takes place directly from the ground state. The theoretical accuracy<sup>5</sup>, rapidly increases for higher principle quantum number  $n$  and is normally much better than any experimental value obtained from extrapolating a Rydberg series. Therefore the theoretical ionisation energy of those higher lying states is frequently used as a reference to calculate the total ionisation energy from a measured transition frequency to this higher lying state.

---

<sup>4</sup>Up to this date there are no methods to analytically solve the three particle problem, theorists therefore use perturbation theories like higher order QED and would like to know the region of validity for these theories.

<sup>5</sup>It is problematic to give the accuracy because one needs to know all next order QED contributions. Theorists therefore try to estimate which QED terms of the next higher order are likely to dominate the contribution, and give an estimation of the upper bound based on such values.

## B.2 Interpretation of a historical value

It is not directly clear how a value given in a dated reference should be interpreted. For one, the view on the best unit to present values in has changed over time. Secondly, the known values of physical constants have changed and improved over time. The latter not only influences results obtained from calculations, but has, in certain cases, also an influence on a measured value e.g. via the calibration procedures for the instrumentation used. This makes that retrieval of a contemporary value needs to be traceable from historical values of the constants, and, in some cases, maybe even exact knowledge of the used instruments. This sort of information is obviously not always available.

In the early publications the error on the result is not always present. In these cases we take a standard deviation of one unit of the least significant digit. Each value has been converted to a contemporary value of the energy. These contemporary values have been used in paragraph B.4 to make a comparison of the accuracy and resolution of the literature values. All contemporary values are given as a frequency, which, multiplied by Planck's constant<sup>6</sup> ( $h = 6.626\,069\,57(29) \times 10^{-34}$  J s), give the ionisation energy of helium. During the conversion to a contemporary value, as many significant digits as possible are preserved. The final result of the conversion is truncated to one additional significant digit, in order to enable the reader to judge the round off error of the conversion.

Unless specifically noted in the sections below treating each reference, the following conversions have been applied. The ionisation energy in units of Volt (V), a remarkable unit of energy but apparently common at the time, has been understood by the author to be equivalent to the electron Volt (eV). The ionisation energy can therefore be converted to a frequency according to

$$f = \frac{Ve}{h}, \quad (\text{B.1})$$

where  $V$  is the value of the energy in (e)V,  $e$  the elementary charge ( $e = 1.602\,176\,565(35) \times 10^{-19}$  C),  $h$  is Planck's constant and  $f$  the resulting frequency in Hz.

The values of the ionisation energy in wavenumbers can be converted to a frequency according to

$$f = 100\tilde{\nu}c, \quad (\text{B.2})$$

where  $\tilde{\nu}$  is the wavenumber in  $\text{cm}^{-1}$  and  $c$  the speed of light ( $c = 299\,792\,458$   $\text{m s}^{-1}$ ).

## B.3 Measured and calculated values of the ionisation energy

In this section the actual historical overview of the ionisation energy is presented. For each entry in Table B.1 to Table B.3 a paragraph with notes has

<sup>6</sup>The values of the constants have been taken from the CODATA 2010 values as published in [84], which is available from the NIST website.

been compiled, including peculiarities found in the articles and methods of calculation of the contemporary value where they differ from the default methods.

In general the following conventions hold for the tables: a \* in the reference field indicates that the reference was not available to the author. The quoted value and uncertainty are as given in the reference, as is the unit. The “type”, indicates how the ground state energy has been derived, or if a value was re-evaluated or corrected. The frequency column contains the recalculated value in the currently prevailing unit Hz in order to make comparisons possible. Remarks are made by the author when needed.

### B.3.1 <sup>4</sup>Helium measurements

Table B.1 presents an overview of ionisation energy determinations of <sup>4</sup>He. References from this table are then treated separately to tell more about the methods involved in the measurement.

#### J. Franck, 1920 [347]

Lyman [346] mentions this value, copied from the work of Franck and Knipping[347], with which Lyman compares his results. The resonance potential (ionisation energy) had been determined to lie at 25.3 Volt. The discrepancy lies in the measurement of Franck and Knipping through systematics in the measurement method. “Considerations of this nature have led Franck [356] to review the interpretation of his experimental data” and the source of error was found. A corrected value then agrees with the observation of Lyman.

Earlier Kappenman [357] had already noted that his results had to be corrected by 1.1 Volt “to bring them in agreement with accepted results.” In this case being the voltages named by Franck and Knipping, among others with the ionisation potential of 25.3 Volt.

#### Landolt-Börnstein tabellen, 1923 [348]

Kellner[349] mentions this value, copied from the Landolt-Börnstein tabellen. I take this value to be computed from spectroscopic line series measurements, and therefore file it in table B.1. It should be noted that the given resolution is rather high, and higher than that of the first direct spectroscopic observation of the transitions from the ground state obtained by Lyman [346], although the value deviates at the  $3 \times 10^{-2}$  level.

#### T. Lyman, 1924 [346]

Lyman makes notes about several of the methods used to observe spectral lines at short wavelengths. First he has received from Prof. R. W. Wood, a series of gratings ruled with different depths and on different engines. Results from among others Millikan, are confirmed “for it appears that a lightly ruled grating gives a stronger spectrum in the region of extremely short wave-lengths”. Woods new driving mechanism of the dividing engine (a part

reference	published value	uncertainty	unit	type	frequency (Hz)	remarks
Franck, 1920 [347]*	25.3	—	V	Voltage	$6.117(24) \times 10^{15}$	given in Lyman [346]
Landolt, 1923 [348]*	24.4735	—	V	Series limit	$5.917666(24) \times 10^{15}$	given in Kellner [349] pag. 93
Lyman, 1924 [346]	198298	—	cm <sup>-1</sup>	Series limit	$5.944824(29) \times 10^{15}$	Series wavelengths accurate to $\times 10^{-4}$
Hopfield, 1930 [350]	198314.4	0.5	cm <sup>-1</sup>	Series limit	$5.9453161(149) \times 10^{15}$	
Herzberg, 1958 [351]	198310.82	0.15	cm <sup>-1</sup>	Series limit	$5.94520881(449) \times 10^{15}$	
Martin, 1960 [352]	198310.81	0.15	cm <sup>-1</sup>	Series limits	$5.94520851(449) \times 10^{15}$	from assessment of measurements
Baig, 1984 [353]	504.2591	0.0004	Å	Series limit	$5.9452067(47) \times 10^{15}$	$n > 11$ assessed
Baig, 1984 [353]a	198310.91	—	cm <sup>-1</sup>	Re-evaluation	$5.94521151(29) \times 10^{15}$	calculated by Eikema [354]
Eikema, 1993 [354]	198310.66	0.03	cm <sup>-1</sup>	Line + theory	$5.94520402(89) \times 10^{15}$	
Eikema, 1993 [354]a	171134.89	0.03	cm <sup>-1</sup>	Correction	$5.94520406(89) \times 10^{15}$	corrected by Pinkert
Eikema, 1996 [355]	5130495040	175	cm <sup>-1</sup>	Line + theory	$5.9452041925(1738) \times 10^{15}$	ionisation potential not in article
Eikema, 1996 [355]a	5130495040	175	cm <sup>-1</sup>	Correction	$5.9452041720(1738) \times 10^{15}$	corrected by Pinkert
Eikema, 1997 [87]	198310.6672	0.0015	cm <sup>-1</sup>	Line + theory	$5.9452042367(449) \times 10^{15}$	
Eikema, 1997 [87]a	5130495083	45	MHz	Line + theory	$5.9452042148(450) \times 10^{15}$	corrected by Pinkert
Bergeson, 1998 [282]	5945204356	48	MHz	Line + theory	$5.9452043560(480) \times 10^{15}$	possible residual Doppler shift
Kandula, 2010 [155]	5945204212.14	6.20	MHz	2 Lines + theory	$5.94520421214(620) \times 10^{15}$	
Kandula, 2011 [178]						see Kandula, 2010

Table B.1: Measured <sup>4</sup>helium ionisation energies. An explanation for the columns is found in Sec. B.3.

of the grating ruling machines) “has succeeded in greatly reducing the intensity of the false spectra”.

To “put the matter beyond question” on the  $4N(1/2^2 + 1/m^2)$  series, Lyman wants to use a continuous discharge contrary to the previously used disruptive discharge, which is prone to errors due to impurities which give additional spectral lines. In order to obtain a continuous discharge in the spectral region<sup>7</sup> of  $\lambda$  1200 to  $\lambda$  1700 the design of a discharge tube of Paschen is used in which “the discharge from the interior of a hollow cylindrical cathode is viewed end on.” The vacuum spectrograph itself is connected to the discharge source via a small hole in order to obtain a high enough vacuum, the length of the spectrograph is 1 meter.

The main result is a fully confirmed  $OS-mP$  series with the principal line at  $\lambda$  584.40, by use of both a continuous and disruptive discharge, of which the plate is reproduced in the article. Some peculiarities of the plate are the line at  $\lambda$  600.3, which cannot be accounted for by Lyman. The line at  $\lambda$  591.5 is attributed to a singlet doublet transition, but we can now say that this is most probably the  $1s^2\ ^1S_0 - 1s2p\ ^3P_1$  line that has been seen. Lyman states: “I think it unlikely that it is due to an impurity.” Lyman also observes two lines (and possibly more) of the He II series.

Lyman notes the discrepancy between the previously accepted value of the ionisation potential of 25.3 Volts against the series limit at 24.5 Volts. This value has apparently been calculated up to only three digits for reasons of comparison, since “the wave-lengths are probably correct to one or two tenth of a unit”. In table 1, a wave-length of  $OS = 198,298$  is found as series limit for the principle series, which has even an additional digit on the ionisation potential, yielding in current numbers a voltage of 24.5858 V, which is slightly higher than the value given for comparison by Lyman and more accurate.

It is specifically noted that “several sources have furnished the helium that has been employed” but that the results were independent of the source of the gas. A peculiar remark is made about the presence of hydrogen in the discharge. Lyman alpha and beta lines were entirely invisible but lines at 1215.7 and 1025.8 have been observed, which lead Lyman to think that a trace of hydrogen might have been present. Another conclusion might be that more lines of He II have been seen, which are positioned at almost exactly the expected wavelengths (lying 0.6 Å lower than the values that Lyman gives) as suggested from Table 1 in the article as well.

#### J. J. Hopfield, 1930 [350]

Hopfield is in the search for the effects of the presence of helium on spectra of other gases and this article is a mere by-product of that research. The machine used is a vacuum spectrograph (radius of curvature of the grating is 50 cm) and the gas discharge source are separated by a slit, which allows

<sup>7</sup>The wavelengths are given in Ångström, the notation is historical.

to maintain a “fairly large difference of pressure” between both sides of the instrument.

Table 1 gives an overview of the ten measured lines of the  $1^1S-n^1P$  although the value of the ionisation potential is retrieved from a fit to the first three members of the series. Further results are mainly on the  $\text{He}_2$  molecular spectra.

#### G. Herzberg, 1958 [351]

This capital result is the first measurement with a high enough accuracy to determine the Lamb shift of the ground state of helium experimentally. The determination of the ionisation potential is an integral part of this measurement, and an improved experimental value is retrieved. Another important aspect is the fact that not only  $^4\text{He}$  has been measured, but also  $^3\text{He}$ , yielding accurate values for the isotope shifts of various lines.

#### W. C. Martin, 1960 [352]

Martin gives an extended overview of all literature values available on helium. For the ionisation potential he mainly relies on the result from Herzberg in the uncertainty, although an independent assessment of the series limits was performed, yielding basically the same energy. The value given and inaccuracy have been taken from Table 2 in [352].

#### M. A. Baig *et. al.*, 1984 [353]

Baig *et. al.* have concentrated on the measurement of the high principal quantum numbers in the  $1s^2 - 1snp$   $n > 11$  series and has recalculated the ionisation potential based on his results, comparing with a wide range of theoretical results through a series approximation. The accuracy is  $0.16 \text{ cm}^{-1}$  which is one hundredth of a wavenumber less accurate than the results from Herzberg [351]. The obtained values compare within the error margin.

#### Re-evaluation, 1984 [353]a

Eikema re-evaluates Baig *et. al.*, the resulting value having one additional digit, but no series fitting accuracy is given. The error given for the contemporary value is therefore that of the single line accuracy of Baig,  $0.16 \text{ cm}^{-1}$  as quoted by Eikema, which is consistent with figure 3 in [354].

#### K. S. E. Eikema *et. al.*, 1993 [354]

Eikema measures the  $1s^2 \ ^1S_0 - 1s2p \ ^1P_1$  transition at 58.4 nm at high accuracy to be  $171\,134.89(3) \text{ cm}^{-1}$ . This measurement is the first laser-based measurement of helium from the ground state. He uses the experimental term value for the upper state energy from Sansonetti [358] Table II ( $27175.77234(14) \text{ cm}^{-1}$ ) to come to a value for the energy of the ionisation potential. The two electron part of the QED terms is shown to exist by this measurement. Due

to the fact that a single line is measured, it is particularly simple to recalculate the groundstate energy when the calculation or measurement accuracy of the upper state energy has improved.

The transition was induced in a crossed atomic beam setup to reduce Doppler effects. The excitation light was generated by a pulsed dye laser ( $\sim 5$  ns pulse length) that was calibrated with an  $I_2$  absorption spectrum. The dye laser was first doubled in frequency to the UV, and subsequently the fifth harmonic was generated in a gas pulse to reach the required 58.4 nm for excitation of helium.

The theoretical Lamb shift ( $1.3745(10) \text{ cm}^{-1}$ ) given in this article has been calculated as follows. The  $\Delta E_{L1,2}$  one and two electron QED terms ( $1.519836$  and  $-0.140402 \text{ cm}^{-1}$ ) from Table 3 in Drake [359] were added to the theoretical ground state energy ( $198310.662801 \text{ cm}^{-1}$ ) from Drake [360], this is the  $1^1S$  level energy ( $-198312.04224 \text{ cm}^{-1}$ ) not including QED effects as stated in the article. From this value the theoretical value of Baker [361] ( $198310.66774(4) \text{ cm}^{-1}$ ) is subtracted. The accuracy comes from the  $10^{-3} \text{ cm}^{-1}$  inaccuracy of the results of Baker [361] due to expected values of  $O\alpha^4$  corrections. The route via the ionisation potential has most probably been taken due to the fact that Baker includes an improved value of the Bethe logarithm in his result for the ground state energy.

#### Corrected value, 1993 [354]a

The result of Eikema is corrected for the recoil shift [155] of -14.6 MHz of the transition frequency. A second correction due to improved calculation of the  $1s2p^1P_1$  level ( $2.7175771929(13) \times 10^4 \text{ cm}^{-1}$ ) by Yerokhin [88] leads to an improved ionisation energy, which differs about 44 MHz from the previous value, well within the experimental error of 899 MHz.

#### K. S. E. Eikema *et. al.*, 1996 [355]

An important measurement of the  $1s^2^1S_0 - 1s2p^1P_1$  transitions in  $^3\text{He}$  and  $^4\text{He}$ , determines a new value for the isotope shift after the measurement of Herzberg [351] almost 40 years back. The measurement sets a new limit to test the accuracy of QED theory. It is of importance that the isotope shift has been deduced much more accurate (7 MHz) than the actual transition frequencies although it should be corrected for recoil shifts.

The theoretical Lamb shift ( $1.3755(10) \text{ cm}^{-1}$ ) has been calculated by taking the ground state energy ( $-5\,945\,204\,108.44(1\,820) \text{ MHz}$ ) from table XI in Drake [362] subtracting the  $\Delta E_{L1,2}$  values ( $45\,560(1\,820)$  and  $-4\,208(-)$  MHz) and the  $O(mc^2\alpha^6 \ln \alpha)$  correction from Drake [363] Table II ( $30.666\,344 \text{ MHz}$ ). The value of the ground state energy derived by Baker [361] ( $(198310.66774(4) \text{ cm}^{-1})$ ,  $5\,945\,204\,252.93(1.19) \text{ MHz}$ ) is then added. The route via the ionisation potential has most probably been taken due to the fact that Baker includes an improved value of the Bethe logarithm in his result for the ground state energy.

An ionisation energy, which is not named in this article, has been derived by taking the theoretical value from Drake [362] ( $814709152.36(1.8)$  MHz) for the upper state. This level energy has been derived according to the method named in the book.

#### Corrected value, 1996 [355]a

An improved and corrected value of the ionisation potential can be derived by taking a recent theoretical value ( $2.7175771929(13) \times 10^4 \text{ cm}^{-1}$ ,  $814709146.464$  (389) MHz) for the upper state from Yerokhin [88]. A correction for a missing recoil shift [155] of  $-14.6$  MHz to the transition frequency has been applied as well. The total shift of the ionisation potential is  $-20.5$  MHz.

#### K. S. E. Eikema *et. al.*, 1997 [87]

As in his previous measurements, Eikema excites the  $1s^2 \ ^1S_0 - 1s2p \ ^1P_1$  transition at a wavelength of  $58.4$  nm. An etalon, locked to an iodine stabilised helium-neon laser provides a reference for a CW ring dye laser operating on a fundamental wavelength of  $584$  nm. The light is then amplified in a pulsed dye laser to about  $220$  mJ,  $6.5$  ns with a bandwidth of  $90-95$  MHz. This pulsed laser output is frequency doubled ( $100$  mJ,  $292$  nm) and then upconverted to  $58.4$  nm at the  $5^{\text{th}}$  harmonic in a  $\text{C}_2\text{H}_2$  or  $\text{N}_2$  pulsed gas jet. A crossed beam setup with a pulsed and skimmed supersonically expanding He jet was used to reduce Doppler width, the skimmer geometries have been optimized for a symmetric Doppler broadened profile. Excited atoms are ionised by the UV light and detected in a time of flight setup. The XUV bandwidth is assessed by use of a chirp measurement setup, and determined to be about  $250$  MHz, due to the fact that the chirp was measured the actual uncertainty in the spectroscopy due to chirp is only about  $10$  MHz.

The main results are the  $1s^2 \ ^1S_0 - 1s2p \ ^1P_1$  transition frequency ( $5\ 130\ 495\ 083(45)$  MHz) of the  $^4\text{He}$  isotope. Together with the already very accurately determined isotope shift for  $^3\text{He}$  ( $263\ 410(7)$  MHz) [355], this yields an improved value of the transition frequency of that isotope as well. Together with theoretical values from Drake [362] for  $^4\text{He}$  and from a private communication with Drake for the theoretical values of the isotope shift, the ground state energy ( $198\ 310.6672(15) \text{ cm}^{-1}$ ) can be derived which includes the improved value for the Bethe logarithm of Baker [361].

#### Corrected value, 1997 [87]a

An improved and corrected value of the ionisation energy has been derived by taking a recent theoretical value ( $2.7175771929(13) \times 10^4 \text{ cm}^{-1}$ ) for the upper state from Yerokhin [88]. A correction for a missing recoil shift [155] of  $-14.6$  MHz to the transition frequency has been applied as well. The total correction to the original ionisation energy is  $-21.9$  MHz.

S. D. Bergeson *et. al.*, 1998 [282]

Bergeson measures the  $1^1S - 2^1S$  transition at 120 nm, and makes use of a Ti:Sapphire laser to seed a pulsed dye amplifier. The pulses are doubled in frequency twice and then upconverted further via a three-wave mixing process in a gas cell. The pulse length at 120 nm is estimated to be 3 ns. The spectroscopy setup is of a crossed beam type, where the 120 nm radiation is focused into the (pulsed?) helium jet, retro-reflected and refocused in the interaction area. Important details of this setup are not given, namely how the atomic beam has been skimmed, and how accurate the angular alignment has been. The angle between the incoming and retro-reflected beams is of importance as well as the difference in focal conditions, because any error in it can lead to a systematic Doppler shift despite the use of a two-photon transition.

The main result is a first direct measurement of the  $1^1S - 2^1S$  transition frequency of 4 984 872 315(48) MHz.

The width of the measured transition has been attributed to the line-width of the laser combined with frequency chirp present in the pulses, although part of this width can come from Doppler effects. Contrary to what the authors believed at that time, the two-photon excitation method used does not completely exclude Doppler shifts or broadening. Any misalignment of the two counter-propagating beams will lead to a Doppler shift when an atomic beam is used. Those residual Doppler effects were overlooked and not evaluated., and are most probably the cause of the large deviation ( $\sim 3\sigma$ ) of the ionisation potential from the result of Kandula [155].

D. Z. Kandula, 2010 [155]

This measurement is treated in chapter 6 of this thesis. The individual measurements of the transition frequencies result in a comparison with the ground state in Fig 3. of [155] and are given in table B.2. The ground state energy is compared with the theoretical value ( $198\,310.665\,1(12)\text{ cm}^{-1}$  corresponding to 5 945 204 174(36) MHz) from Yerokhin [88]. The upper state energies for the transition frequency calculation are taken from Morton [288]. The  $1s4p$  upper state energy is 204 397 210.76(2) MHz and the  $1s5p$  upper state energy is 130 955 541.84(1) MHz.

The obtained transition frequencies are weighted averages where the measurement sessions were treated as independent probability distributions. After rounding the values published in [178] are obtained. For the ground state energy calculation, the upper state energies were added to the individual measurements and a weighted average was calculated over all values giving a ground state energy of 5945204212.139841 MHz with a statistical error of 3.688967 MHz (Table I of [155]) which are rounded according to the total error.

date	$f_{\text{rep}}$ (MHz)	transition frequency (MHz)	standard deviation (MHz)
31 March 2009	148.24	5740806993.723802	9.627609
26 March 2009	148.24	5814248670.832916	10.354866
8 April 2009	100.75	5814248669.606191	9.521412
15 April 2009	121.53	5814248672.143160	8.623418
20 April 2009	111.28	5814248670.951601	8.592003
5 June 2009	184.83	5814248695.833862	12.583185
8 June 2009	184.84	5814248668.375237	24.795339
11 June 2009	148.54	5814248655.916435	11.622794
average	—	5814248671.617290	3.993772

Table B.2: Individual transition frequencies as found in Fig. 3 of Kandula [155]. The top section represents the measurement on the  $1s^2\ ^1S_0 - 1s4p\ ^1P_1$  transition, the bottom section those on the  $1s^2\ ^1S_0 - 1s5p\ ^1P_1$  transition. The last line of the bottom section gives the average for the transition frequency calculated from the table.

#### D. Z. Kandula, 2011 [178]

This publication describes in greater detail the experimental procedures and analysis of systematic effects involved in the spectroscopy of Kandula [155].

#### B.3.2 $^3\text{He}$ measurements

Only a few measurements of the  $^3\text{He}$  groundstate have been performed. The main importance lies in the possibility to determine the scaling properties of QED calculations, although calculations become more difficult due to hyperfine splitting of the energy levels. Table B.3 presents these measured values.

#### G. Herzberg, 1958 [351]

This is the first measurement of the groundstate energy of  $^3\text{He}$  derived from a series limit determined from transitions excited from the groundstate. This makes it possible for the first time to accurately compare theory and measurement for the isotope shift in helium and the ground state energy.

#### K. S. E. Eikema *et. al.*, 1996 [355]

An important measurement of the  $1s^2\ ^1S_0 - 1s2p\ ^1P_1$  transitions in  $^3\text{He}$  and  $^4\text{He}$ , determines a new value for the isotope shift after the measurement of Herzberg almost 40 years back. The measurement sets a new limit to test the accuracy of QED theory.

The main results are the  $1s^2\ ^1S_0 - 1s2p\ ^1P_1$  transition frequency (5 130 495 040(175) MHz) of the  $^4\text{He}$  isotope. Together with the already very accurately determined isotope shift for  $^3\text{He}$  (263 410(7) MHz) this yields an improved value of the  $1s^2\ ^1S_0 - 1s2p\ ^1P_1$  transition frequency of  $^3\text{He}$  of 5 130 231 630(175) MHz.

reference	published value	uncertainty	unit	type	frequency (Hz)	remarks
Herzberg, 1958 [351]	198300.3	0.15	cm <sup>-1</sup>	Series limit	$5.9448934(44) \times 10^{15}$	ionisation potential not in article
Eikema, 1996 [355]	5130231630	175	MHz	Line + theory	$5.944890673(175) \times 10^{15}$	
Eikema, 1997 [87]	198301.8808	0.0015	cm <sup>-1</sup>	Line + theory	$5.9449408271(449) \times 10^{15}$	Contains an error, see text Corrected by Eikema and Pinkert
Eikema, 1997 [87]a	5944890711	45	MHz	Line + theory	$5.944890711(45) \times 10^{15}$	

Table B.3: Measured <sup>3</sup>helium ionisation energies. An explanation for the columns is found in Sec. B.3.

reference	published value	uncertainty	unit	type	frequency (Hz)	remarks
Kellner, 1927 [349]	23.750	0.001	V	Schrödinger equation	$5.74272(24) \times 10^{15}$	where $h = c$ , the speed of light
Slater, 1927 [364]	24.35	0.01	V	Schrödinger equation	$5.8878(24) \times 10^{15}$	
Hylleraas, 1929 [201]	-1.45162	—	4R <i>h</i>	Schrödinger equation	$5.943033(131) \times 10^{15}$	
Kabir, 1957 [365]	198310.35	0.2	cm <sup>-1</sup>	Schrödinger equation	$5.94519472(599) \times 10^{15}$	
Sucher, 1958 [366]	198310.31	—	cm <sup>-1</sup>	QED	$5.94519352(29) \times 10^{15}$	
Drake, 1999 [367]	5945204225.9	91.1	MHz	QED	$5.94520422590(9110) \times 10^{15}$	
Korobov, 2001 [368]	5945204223	42	MHz	QED	$5.9452042230(420) \times 10^{15}$	
Pachucki, 2006 [206]	5945204174	36	MHz	QED	$5.9452041740(360) \times 10^{15}$	
Drake, 2008 [203]	5945204175	36	MHz	QED	$5.9452041750(360) \times 10^{15}$	
Yerokhin, 2010 [88]	198310.6651	0.0012	cm <sup>-1</sup>	QED	$5.9452041737(359) \times 10^{15}$	

Table B.4: Calculated <sup>4</sup>helium ionisation energies. An explanation for the columns is found in Sec. B.3.

The isotope shift for  $^3\text{He}$  and  $^4\text{He}$  was calculated by Drake in a private communication to be 263411.24(10.00) MHz. In this private communication Drake further gives an extrapolation equation for small deviations of the nuclear charge radius  $R$  of  $^3\text{He}$  around 1.95 fm as  $\Delta E = 263\,411.24(10) + 41.145(R - 1.95)$  MHz. In addition a table with contributions to the isotope shift was communicated. The error of 10 MHz in these comes from the  $E_{L1}$  term in the ground state energy isotope shift.

An ionisation energy, not found in the article, for  $^3\text{He}$  is now calculated analogue to that of  $^4\text{He}$ . For the upper state energy of  $^4\text{He}$  the value from Drake [362] (814 709 152.36(1.8) MHz) is taken. This value is corrected for the isotope shift for the upper state given in the private communication (50 108.921 MHz). The upper state energy of  $^3\text{He}$  then becomes 814 659 043.439(1.8) MHz. The ionisation energy is calculated by adding the upper state value to the transition frequency and is 5 944 890 673(175) MHz.

K.S.E.Eikema *et. al.*, 1997 [87]

A new measurement of the  $^4\text{He } 1s^2 \ ^1S_0 - 1s2p \ ^1P_1$  transition. The value of the ionisation potential for  $^3\text{He}$  is calculated by use of the isotope shift measurement of Eikema [355].

K.S.E.Eikema *et. al.*, 1997 [87]a

In [87] the isotope shift measurement is used to calculate the ionisation potential for  $^3\text{He}$  from the value of  $^4\text{He}$ . However, due to an unfortunate combination of circumstances the excited state isotope shift was not included (private communication with K. S. E. Eikema), leading to an error of nearly a wavenumber. In addition the differential recoil shift is included here.

The correct  $^3\text{He}$  ground state ionisation energy derived from the measurements is calculated here. For the upper state ( $1s2p \ ^1P_1$ ) energy of  $^4\text{He}$  the value from Drake [362] (814709152.36(1.8) MHz) is taken. We need to correct this value for the isotope shift of the upper state given in the private communication (see appendix C) with Drake (50108.921 MHz). The upper state energy of  $^3\text{He}$  then becomes (814659043.439(1.8) MHz). The  $^3\text{He } 1s^2 \ ^1S_0 - 1s2p \ ^1P_1$  transition frequency (5 130 231 668(45) MHz) is calculated from the  $^4\text{He}$  transition frequency (5 130 495 083(45) MHz) by subtracting the measured isotope shift (263 410(7) MHz) and the differential recoil shift (4.8 MHz,  $^4\text{He}$  14.6 MHz,  $^3\text{He}$  19.4 MHz). The ionisation energy of  $^3\text{He}$  is then calculated by adding the upper state energy, resulting in 5 944 890 711(45) MHz.

## B.4 Graphical representations of the ionisation potential history

The experimental data from the previous sections is graphically represented in two figures (Fig. B.1 and B.2). Only  $^4\text{helium}$  results are shown because that presents the most complete data and gives the best indication of the accuracy that has been obtained.

Parallel to the experiments, also the theoretical values for the ionisation potential have improved dramatically over the years. It is beyond the scope of this thesis to give a full overview, but the main results are compiled in Table B.4. The theoretical accuracy (expressed as a fraction) is included as well in Fig. B.1 and B.2 for a comparison.

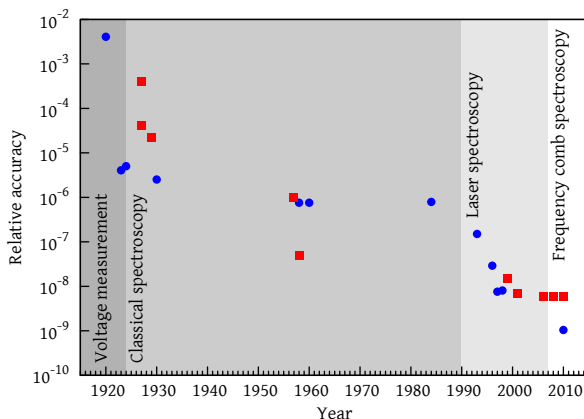


Figure B.1: Graphical representation of the projected accuracy for measurement and theory over the past century. In blue the measurement accuracy of the various experiments, in red the (estimated) accuracy of the calculations of the ground state energy of helium.

Figure B.1 presents the accuracy of the measurements over the past century. First it is seen that there are two periods with a remarkable improvement of the measurement accuracy in the XUV energy region. The first rapid improvement happened when Lyman started observing XUV spectra of helium in 1924. This improves the accuracy with approximately three orders of magnitude over the voltage measurement from Franck [347]. The Landolt-Börstein tabellen present a value with a resolution of  $\sim 2 \times 10^{-6}$  already in 1923, however, the value is off by  $\sim 3 \times 10^{-2}$ .

The next big improvement in measurement accuracy comes with the advent of pulsed XUV laser systems. This time the accuracy improves by approximately an order of magnitude each successive improvement cycle of the laser system, which reaches its limit at about 45 MHz accuracy. The latest generation experiments use a frequency comb to increase the measurement accuracy even further. Based on amplification of two frequency comb laser pulses (as described in this thesis in Chapter 6) an accuracy of 6 MHz has been achieved. Further progress using the so called “Ramsey-comb” method is expected to improve the accuracy to the kHz level, which would mean an unprecedented relative accuracy of  $10^{-12}$  (or better) in the XUV.

Figure B.2 present the most recent measurement and theory results in a linear graph. The current best theoretical value for the ground state energy from Yerokhin [88] has been used as a reference. Interestingly the theoretical

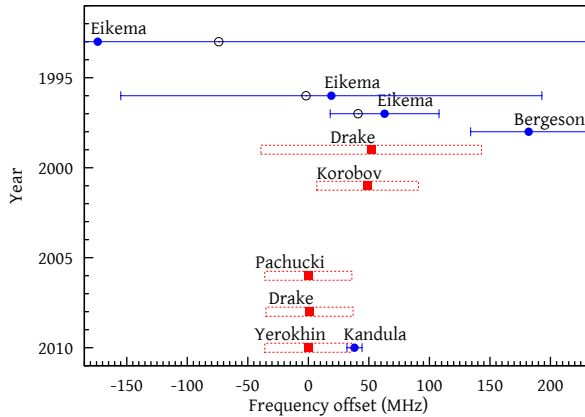


Figure B.2: Graphical representation of the ground state energy in the laser spectroscopy era. In blue (solid circle) the original published values with their error bar are shown for the various experiments. The black open circles represent corrected values as given in the tables. In red the values of calculations of the ground state energy of helium are shown. The errorbox on the theory values indicates that the given uncertainty is an estimation.

results from Drake and Korobov are closer to the current measurement value than the more recent calculations from Pachucki and Yerokhin. The shifts in earlier measurement values are mainly due to use of a more recent upper state energy value and inclusion of the recoil shift.

## B.5 Conclusion

The historical overview presented in this appendix is far from complete, and only the beginning of an full account of the measurements and theory development involving the ground state of helium. However, already from the current overview it is clear that great progress has been made over the almost 100 years that spectroscopy on helium has been performed. It is the intent of the author of this thesis to make a more complete review of helium and its spectroscopy in the future. Therefore any comments, corrections or other information of interest on this subject is highly appreciated. I would also like to thank Jeroen Koelemeij for allowing me the time to work on this overview.



## C. Private communication G. W. F. Drake

In this appendix the copy of the private communication of Gordon Drake to Wim Vassen from the archive of the latter, is reproduced with kind permission of both. This is the private communication that is referred to as reference 14 of Eikema [355] and reference 16 of Eikema [87]. The handwriting is of Wim Vassen. It is to be noted that this document is purely reproduced for its historical value. Calculations on QED have improved since 1994, especially due to improved methods for calculation of the Bethe logarithm (see e.g. [369]). Also take in mind that CODATA values may have changed since then.

Return-Path: <a36@server.uwindsor.ca>  
 Received: from server.uwindsor.ca by hardy (4.1/SMI-4.0)  
 id AA03208; Fri, 12 Aug 94 05:58:24 +0200  
 Received: by server.uwindsor.ca (931110.SGI.ANONFTP/931108.SGI.AUTO.ANONFTP)  
 for wim@nat.vu.nl id AA14322; Thu, 11 Aug 94 23:57:42 -0400  
 From: a36@server.uwindsor.ca (Drake G)  
 Message-Id: <9408120357.AA14322@server.uwindsor.ca>  
 Subject: He isotope shift  
 To: wim@nat.vu.nl (Wim Vassen)  
 Date: Thu, 11 Aug 94 23:57:40 EDT  
 X-Mailer: ELM [version 2.3 PL11]  
 Status: R

$263402 \approx 1.73 \text{ fm}$   
 $263418 \approx 2.12 \text{ fm}$

Dear Wim:

As promised, I have calculated the isotope shift for the  
 1 1S - 2 1P transition of helium. Assuming a nuclear radius  
 of 1.673 fm for  $^4\text{He}$ , the isotope shift is

$$\Delta E = 263411.24(10) + 41.145 (R - 1.95) \text{ MHz}$$

$R = 1.93(.20) \text{ fm}$

$m \approx 1.9506$

$263411.26(13)$

where  $R$  is the nuclear radius of  $^3\text{He}$  in the neighborhood of  
 1.95 fm. Your experimental value of 263.50(5) GHz lies  
 higher by about two standard deviations. The accuracy is  
 not quite sufficient to provide a useful measure of  $R$ , but it  
 still provides an interesting comparison with theory for the  
 other mass-dependent corrections to the isotope shift. Below  
 is a tabulation of the various contributions. The various con-  
 tributions are as defined in G. W. F. Drake and Z.-C. Yan,  
 Phys. Rev. A 46, 2378 (1992). A more extended discussion is  
 contained in the review article G. W. F. Drake in "Long Range  
 Casimir Forces: Theory and Recent Experiments in Atomic  
 Systems", Edited by F. S. Levin and D. Micha (Plenum, New  
 York, 1993). I am sending a reprint of this article by mail.  
 See also E. Riis et al. Phys. Rev. A 49, 207 (1994).

The only significant source of theoretical uncertainty is the  
 Lamb shift contribution of 3.65(10) MHz for the 1 1S state.  
 The  $\pm 0.10$  MHz uncertainty is an estimate of uncalculated terms.  
 All other terms have converged to the figures quoted.

Best regards,  
 Gordon Drake.

Contributions to the  $^3\text{He} - ^4\text{He}$  isotope shift  
 for each state, relative to  $\text{He}+(1s)$  (MHz).

Contribution	1 1S	2 1P
Enr	-266668.081	-36543.219
EM(1)	-46922.728	-13582.334
EM(2)	44.266	15.835
Exel	0.758	-0.629
Est	0.000	0.003
(ERR)M	50.624	2.784
(ERR)X	-17.458	-1.235
Enuc	-10.609	-0.023
EL(1)	3.65(10)	-0.086
EL(2)	-0.584	-0.017
Total	-313520.16(10)	-50108.921

$^4\text{He} \begin{cases} 1S_0 & 29.619 \text{ MHz} \\ 1P_1 & 0.060 \text{ MHz} \end{cases}$

$^3\text{He} \begin{cases} 1S_0 & 40.228 \text{ MHz} \\ 1P_1 & 0.083 \text{ MHz} \end{cases}$

Isotope shift 263411.24(10)

Department of Physics, University of Windsor  
 Windsor, Ontario N9B 3P4, Canada.  
 e-mail: A36@server.uwindsor.ca  
 Tel: (519) 253-4232 Ext. 2656

# Bibliography

- [1] *The Holy Bible: King James Version*. Available from various publishers and on the web, 1611.
- [2] Roger Bacon. *Opus Majus*. 1267.
- [3] M. Lavoisier. *Traité élémentaire de chimie*. 1789.
- [4] D. Mendelejeff. Ueber die Beziehungen der Eigenschaften zu den Atomgewichten der Elemente. *Zeitschrift für Chemie*, pages 405–406, 1869.
- [5] J. J. Thomson. Cathode rays. *The London, Edinburgh, and Dublin Philosophical Magazine and Journal of Science*, 44(269):293–316, October 1897.
- [6] H. Geiger, John Harling, and E. Marsden. On a diffuse reflection of the  $\alpha$ -particles. *Proceedings of the Royal Society of London. Series A, Mathematical and Physical Sciences*, 82(557):495–500, Juli 1909.
- [7] R. A. Millikan. The isolation of an ion, a precision measurement of its charge, and the correction of Stokes's law. *Physical Review*, 32:349–397, 1911.
- [8] R. A. Millikan. On the elementary electrical charge and the Avogadro constant. *Physical Review*, 2(2):109–143, 1913.
- [9] M. Louis de Broglie. Recherches sur la théorie des quanta. *Annales de Physique*, 10(3):22–128, 1925.
- [10] Claus Jönsson. Elektroneninterferenzen an mehreren künstlich hergestellten Feinspalten. *Zeitschrift für Physik*, 161:454–474, 1961.
- [11] N. Bohr. On the constitution of atoms and molecules. *The London, Edinburgh, and Dublin Philosophical Magazine and Journal of Science*, 26:1–25, 1913.
- [12] E. Schrödinger. Quantisierung als Eigenwertproblem; (Erste Mitteilung). *Annalen der Physik*, 384(4):361–376, 1926.
- [13] E. Rutherford. Collisions of  $\alpha$  particles with light atoms. IV. an anomalous effect in nitrogen. *Philosophical Magazine*, 37(222):581–587, 1919.
- [14] J. Chadwick. Possible existence of a neutron. *Nature*, 129(3252):312, February 1932.
- [15] Mary K. Gaillard, Paul D. Grannis, and Frank J. Sciulli. The standard model of particle physics. *Review of Modern Physics*, 71:S96–S111, 1999.
- [16] ATLAS Collaboration. Observation of a new particle in the search for the standard model Higgs boson with the ATLAS detector at the LHC. *Physics Letters B*, 716:1–29, 2012.
- [17] CMS Collaboration. Observation of a new boson at a mass of 125 GeV with the CMS experiment at the LHC. *Physics Letters B*, 716:30–61, 2012.
- [18] Roy J. Glauber. One hundred years of light quanta, December 2005. Nobel Lecture.
- [19] *Job 28:2*. In [1], 1611.
- [20] Harry Edwin Burton. The optics of Euclid. *Journal of the Optical Society of America*, 35(5):357–372, May 1945.
- [21] Max Herzberger. Optics from Euclid to Huygens. *Applied Optics*, 5:1383–1393, 1966.
- [22] Ibn al Haytham (Alhazen). *Kitāb al-Manāzīr (Book of Optics)*. 1021.
- [23] James Clerk Maxwell. *A Treatise on Electricity and Magnetism*. Clarendon Press, Oxford, 1873.
- [24] Max Planck. Ueber das Gesetz der Energieverteilung im Normalspectrum. *Annalen der Physik*, 309:553–563, 1901.
- [25] A. Einstein. Über einen die Erzeugung und Verwandlung des Lichtes betreffenden heuristischen Gesichtspunkt. *Annalen der Physik*, 322:132–148, 1905.
- [26] A. Einstein. Zur Theorie der Lichterzeugung und Lichtabsorbtion. *Annalen der Physik*, 325:199–206, 1906.
- [27] F. J. Dyson. The radiation theories of Tomonaga, Schwinger, and Feynman. *Physical Review*, 75(3):486–502, Februari 1949.
- [28] A. Einstein. Zur Quantentheorie der Strahlung. *Physikalische Zeitschrift*, 18:121–128, 1917.
- [29] A. L. Schawlow and C. H. Townes. Infrared and optical masers. *Physical Review*, 112(6):1940–1949, Dec 1958.

- [30] F. Russell Petersen, Kenneth M. Evenson, Donald A. Jennings, Joseph F. Wells, Kenya Goto, and Juan J. Jiménez. Far infrared frequency synthesis with stabilised CO<sub>2</sub> lasers: Accurate measurements of the water vapor and methyl alcohol laser frequencies. *IEEE Journal of Quantum Electronics*, QE-11(10):838–843, October 1975.
- [31] V. P. Chebotayev, V. M. Klementyev, M. V. Nikitin, B. A. Timchenko, and V. F. Zakharyash. Comparison of frequency stabilities of the Rb standard and of the He-Ne/CH<sub>4</sub> laser stabilized to the  $e$  line in methane. *Applied Physics B*, 36:59–61, 1985.
- [32] K. Nakagawa, M. de Labachellerie, Y. Awaji, and M. Kourogi. Accurate optical frequency atlas of the 1.5- $\mu$ m bands of acetylene. *Journal of the Optical Society of America B*, 13(12):2708–2714, December 1996.
- [33] T. W. Hänsch and B. Couillaud. Laser frequency stabilization by polarization spectroscopy of a reflecting reference cavity. *Optics Communications*, 35(3):441–444, December 1980.
- [34] R. W. P. Drever, J. L. Hall, F. V. Kowalski, J. Hough, Ford G. M., A. J. Munley, and H. Ward. Laser phase and frequency stabilization using an optical resonator. *Applied Physics B*, 31:97–105, 1983.
- [35] T. Kessler, C. Hagemann, C. Grebing, T. Legero, U. Sterr, F. Riehle, M.J. Martin, L. Chen, and J. Ye. A sub-40-mHz-linewidth laser based on a silicon single-crystal optical cavity. *Nature Photonics*, 6:687–692, 2012.
- [36] R. Holzwarth, Th. Udem, T. W. Hänsch, J. C. Knight, W. J. Wadsworth, and P. St. J. Russell. Optical frequency synthesizer for precision spectroscopy. *Physical Review Letters*, 85(11):2264–2267, 2000.
- [37] Scott A. Diddams, David J. Jones, Jun Ye, Steven T. Cundiff, John L. Hall, Jinendra K. Ranka, Robert S. Windeler, Ronald Holzwarth, Thomas Udem, and T. W. Hänsch. Direct link between microwave and optical frequencies with a 300 THz femtosecond laser comb. *Physical Review Letters*, 84(22):5102–5105, 2000.
- [38] A. Apolonski, A. Poppe, G. Tempea, Ch. Spielmann, Th. Udem, R. Holzwarth, T. W. Hänsch, and F. Krausz. Controlling the phase evolution of few-cycle light pulses. *Physical Review Letters*, 85(4):740–743, 2000.
- [39] Jinendra K. Ranka, Robert S. Windeler, and Andrew J. Stentz. Visible continuum generation in air silica microstructure optical fibers with anomalous dispersion at 800 nm. *Optics Letters*, 25:25, 2000.
- [40] Chris Bennett. Egyptian dates: The Egyptian civil calendar. Website: [http://www.tyndalehouse.com/Egypt/ptolemies/chron/egyptian/chron\\_lnk\\_calendars.htm](http://www.tyndalehouse.com/Egypt/ptolemies/chron/egyptian/chron_lnk_calendars.htm). retrieved: 03-05-2013 14:03.
- [41] J. L. Heiberg. *Claudii Ptolemaei - Opera Quae Exstant Omnia*. B. G. Teubneri, 1898.
- [42] Maren Schentuleit. *The Carlsberg Papyri 9: Aus der Buchhaltung des Weinmagazins im Edfu-Tempel. Der demotische P. Carlsberg 409*. Museum Tusulanum Press, 2006.
- [43] Dr. Eduard Mahler. *Handbuch der jüdischen Chronologie*. Buchhandlung Gustav Fock, G. m. b. H., Leipzig, 1916.
- [44] Nachum Dershowitz and Edward M. Reingold. Calendrical calculations. *Software Practice and Experience*, 20(9):899–928, September 1990.
- [45] Mark E. Cohen. *The Cultic Calendars of the Ancient Near East*. CDL Press, Bethesda Maryland, 1993.
- [46] Louay J. Fatoohi, F. Richard Stephenson, and Stetha S. Al-Dargazelli. The Babylonian first visibility of the lunar crescent: Data and criterion. *Journal for the History of Astronomy*, 30(98):51–72, Februari 1999.
- [47] M. Heydari-Malayeri. A concise review of the Iranian calendar. *Arxiv*, page 0409620v2, 2004. arXiv:astro-ph/0409620v2; 2006 version on website of Observatoire de Paris.
- [48] George A. Davis. The so-called royal stars of Persia. *Popular Astronomy*, 53:149–159, 1945.
- [49] R. K. Kochhar. French astronomers in India during the 17th–19th centuries. *Journal of the British Astronomical Association*, 101(2):95–100, 1991.
- [50] N. Sivin. Cosmos and computation in early Chinese mathematical astronomy. *T'oung Pao*, 55:1–73, 1969.
- [51] John M. Steele. Predictions of eclipse times recorded in Chinese history. *Journal for the*

- History of Astronomy*, 29(96):275–285, August 1998.
- [52] Xueshun Liu. *The first known Chinese calendar: A reconstruction by the synchronic evidential approach*. PhD thesis, The University of British Columbia, 2005.
- [53] Helmer Aslaksen. The mathematics of the Chinese calendar. Technical report, Department of Mathematics; National University of Singapore, 2010.
- [54] Steven Roland Gullberg. *The cosmology of Inca huacas*. PhD thesis, James Cook University, 2009.
- [55] Anthony F. Aveni. Archaeoastronomy in the ancient Americas. *Journal of Archeological Research*, 11(2):149–191, June 2003.
- [56] *Codex Dresdensis*. 1200–1250. Dresdner Mayahandschrift.
- [57] Charles H. Smiley. The antiquity and precision of Mayan astronomy. *Journal of the Royal Astronomical Society of Canada*, 54(5):222–227, 1960.
- [58] Gerald S. Hawkins. Stonehenge: A neolithic computer. *Nature*, 202:1258–1261, June 1964.
- [59] Herbert E. Stone. The purpose of Stonehenge. *Man*, 25:69–72, May 1925.
- [60] Nils-Axel Mörner and Bob G. Lind. Stonehenge has got a younger sister Ales stones in Sweden decoded. *International Journal of Astronomy and Astrophysics*, 2:23–27, 2012.
- [61] David Trevarthen. Illuminating the monuments: Observation and speculation on the structure and function of the cairns at Balnuaran of Clava. *Cambridge Archeological Journal*, 10(2):295–315, April 2000.
- [62] Alexander Jones. Callendria I: New Callippic dates. *Zeitschrift für Papyrologie und Epigraphik*, 129:141–158, 2000.
- [63] Michael A. Lombardi. First in a series on the evolution of time measurement: Celestial, flow, and mechanical clocks. *IEEE Instrumentation and Measurement Magazine*, pages 45–51, August 2011.
- [64] J. M. Steele and F. R. Stephenson. Astronomical evidence for the accuracy of clocks in pre-jesuit China. *Journal for the History of Astronomy*, 29(94):35–48, Februari 1998.
- [65] Warren A. Marrison. The evolution of the quartz crystal clock. *Bell Systems Technical Journal*, 27(3):510–588, July 1948.
- [66] Pierre Curie and Jacques Curie. Développement, par pression, de l'électricité polaire dans les cristaux hémihédres à faces inclinées. *Comptes Rendus Hebdomadaires des Séances de l'Académie des Sciences*, XCI:294–297, 1880.
- [67] Jaques Chauvin, Patrick Weber, Jean-Pierre Aubry, Frederic Lefebvre, Fabrice Sthal, Serge Galliou, Enrico Rubiola, and Xavier Vacheret. A new generation of very high stability BVA oscillators. In *Proceedings of the IEEE International Frequency Control Symposium & 21<sup>th</sup> European Frequency and Time Forum*, pages 1261–1268, 2007.
- [68] I. I. Rabi. Space quantization in a gyrating magnetic field. *Physical Review*, 51:652–654, April 1937.
- [69] N. F. Ramsey. A new molecular beam resonance method. *Physical Review*, 76(7):996–996, Oct 1949.
- [70] Norman F. Ramsey. A molecular beam resonance method with separated oscillating fields. *Physical Review*, 78(6):695–699, June 1950.
- [71] L. Essen and J. V. L. Parry. A caesium resonator. *Nature*, 176(4476):280–282, August 1955.
- [72] Bureau International des Poids et Mesures. Unité SI de temps (seconde). Website: <http://www.bipm.org/fr/CGPM/db/13/1/>. retrieved: 17-10-2012 17:58.
- [73] Consultative Committee for Time and Frequency. Consultative Committee for Time and Frequency (CCTF) 14th meeting (April 1999). Technical report, Bureau International des Poids et Mesures, 1999.
- [74] Norman F. Ramsey. History of atomic clocks. *Journal of Research of the National Bureau of Standards*, 88(5), September–October 1983.
- [75] T. Rosenband, D. B. Hume, P. O. Schmidt, C. W. Chou, A. Brusch, L. Lorini, W. H. Oskay, R. E. Drullinger, T. M. Fortier, J. E. Stalnaker, S. A. Diddams, W. C. Swann, N. R. Newbury, W. M. Itano, D. J. Wineland, and J. C. Bergquist. Frequency ratio of  $\text{Al}^+$  and  $\text{Hg}^+$  single-ion optical clocks; metrology at the 17<sup>th</sup> decimal place. *Science*, 319(5871):1808–1812, 2008.

- [76] C. W. Chou, D. B. Hume, J. C. J. Koelemeij, D. J. Wineland, and T. Rosenband. Frequency comparison of two high-accuracy  $\text{Al}^+$  optical clocks. *Physical Review Letters*, 104:070802, Februari 2010.
- [77] N. Huntemann, M. Okhapkin, B. Lipphardt, S. Weyers, Chr. Tamm, and E. Peik. High-accuracy optical clock based on the octupole transition in  $^{171}\text{Yb}^+$ . *Physical Review Letters*, 108:090801, Feb 2012.
- [78] P. G. Westergaard, J. Lodewyck, L. Lorini, A. Lecallier, E. A. Burt, M. Zawada, J. Millo, and P. Lemonde. Lattice-induced frequency shifts in Sr optical lattice clocks at the  $10^{-17}$  level. *Physical Review Letters*, 106:210801, May 2011.
- [79] N. Hinkley, J. A. Sherman, N. B. Phillips, M. Schioppo, N. D. Lemke, K. Beloy, M. Pizzocaro, C. W. Oates, and A. D. Ludlow. An atomic clock with  $10^{-18}$  instability. *Science*, 341:1215–1218, 2013.
- [80] Stephan Falke, Nathan Lemke, Christian Grebing, Burghard Lipphardt, Stefan Weyers, Vladislav Gerginov, Nils Huntemann, Christian Hagemann, Ali Al-Masoudi, Sebastian Häfner, Stefan Vogt, Uwe Sterr, and Christian Lisdat. A strontium lattice clock with  $3 \times 10^{-17}$  inaccuracy and its frequency. *Arxiv*, 2013.
- [81] J. Millo, R. Boudot, M. Lours, P. Y. Bourgeois, A. N. Luiten, Y. Le Coq, Y. Kersalé, and Santarelli G. Ultra-low-noise microwave extraction from fiber-based optical frequency comb. *Optics Letters*, 34:3707–3709, 2009.
- [82] T. M. Fortier, C. W. Nelson, A. Hati, F. Quinlan, J. Taylor, H. Jiang, C. W. Chou, T. Rosenband, N. Lemke, A. Ludlow, D. Howe, C. W. Oates, and S. A. Diddams. Sub-femtosecond absolute timing jitter with a 10 GHz hybrid photonic-microwave oscillator. *Applied Physics Letters*, 100:231111, 2012.
- [83] Tara M. Fortier, Franklyn Quinlan, Archita Hati, Craig Nelson, Jennifer A. Taylor, Yang Fu, Joe Campbell, and Scott A. Diddams. Photonic microwave generation with high-power photodiodes. *Optics Letters*, 38:1712–1714, 2013.
- [84] Peter J. Mohr, Barry N. Taylor, and David B. Newell. CODATA recommended values of the fundamental physical constants: 2010. *Review of Modern Physics*, 84(4):1527–1605, October–December 2012.
- [85] Randolf Pohl, Aldo Antognini, François Nez, Fernando D. Amaro, François Biraben, João M. R. Cardoso, Daniel S. Covita, Andreas Dax, Satish Dhawan, Luis M. P. Fernandes, Adolf Giesen, Thomas Graf, Theodor W. Hänsch, Paul Indelicato, Lucile Julien, Cheng-Yang Kao, Paul Knowles, Eric-Olivier Le Bigot, Yi-Wei Liu, A. M. Lopes, José, Livia Ludhova, Cristina M. B. Monteiro, Françoise Mulhauser, Tobias Nebel, Paul Rabinowitz, Joaquim M. F. dos Santos, Lukas A. Schaller, Karsten Schuhmann, Catherine Schwob, David Taqqu, João F. C. A. Veloso, and Franz Kottmann. The size of the proton. *Nature*, 466:213–217, July 2010.
- [86] Aldo Antognini, François Karsten Schuhmann Nez, Fernando D. Amaro, François Biraben, João M. R. Cardoso, Daniel S. Covita, Andreas Dax, Satish Dhawan, Marc Diepold, Luis M. P. Fernandes, Adolf Giesen, Andrea L. Gouvea, Thomas Graf, Theodor W. Hänsch, Paul Indelicato, Lucile Julien, Cheng-Yang Kao, Paul Knowles, Franz Kottmann, Eric-Olivier Le Bigot, Yi-Wei Liu, José A. M. Lopes, Livia Ludhova, Cristina M. B. Monteiro, Françoise Mulhauser, Tobias Nebel, Paul Rabinowitz, Joaquim M. F. dos Santos, Lukas A. Schaller, Catherine Schwob, David Taqqu, João F. C. A. Veloso, Jan Vogelsang, and Randolf Pohl. Proton structure from the measurement of 2s-2p transition frequencies of muonic hydrogen. *Science*, 339:417–420, January 2013.
- [87] K. S. E. Eikema, W. Ubachs, W. Vassen, and W. Hogervorst. Lamb shift measurement in the  $1^1\text{S}$  ground state of helium. *Physical Review A*, 55(3):1866–1884, Mar 1997.
- [88] Vladimir A. Yerokhin and Krzysztof Pachucki. Theoretical energies of low-lying states of light helium-like ions. *Physical Review A*, 81:022507, 2010.
- [89] Bureau International des Poids et Mesures. Définition de l'unité de temps (seconde). Website: <http://www.bipm.org/fr/CIPM/db/1956/1/>. retrieved: 17-10-2012 17:53.
- [90] Michael A. Lombardi. The evolution of time measurement, part 4: The atomic second. *IEEE Instrumentation and Measurement Magazine*, pages 47–51, Februari 2012.
- [91] Ian Mills, Terry Quinn, Barry Taylor, Richard David, Marc Himbert, and Jörg Stenger. Draft

- chapter 2 for SI brochure, following redefinitions of the base units, September 2010.
- [92] W. Markowitz, R. Glenn Hall, L. Essen, and J.V.L. Parry. Frequency of cesium in terms of ephemeris time. *Physical Review Letters*, 1(3):105–107, August 1958.
- [93] R. A. Nelson, D. D. McCarthy, S. Malys, J. Levine, B. Guinot, H. F. Fliegel, R. L. Beard, and T. R. Bartholomew. The leap second: its history and possible future. *Metrologia*, 38:509–529, 2001.
- [94] S. Aoki, B. Guinot, G. H. Kaplan, H. Kinoshita, D. D. McCarthy, and P. K. Seidelmann. The new definition of universal time. *Astronomy and Astrophysics*, 105:359–361, 1982.
- [95] E. F. Arias and W. Lewandowski. Modern applications of timescales. *Metrologia*, 48:Foreword, 2011.
- [96] Bureau International des Poids et Mesures. International atomic time. Website: <http://www.bipm.org/en/scientific/tai/tai.html>. retrieved: 27-06-2012 11:40.
- [97] Samir S. Soliman and Mandyam D. Srinath. *Continuous and discrete signals and systems*. Prentice-Hall International Inc., second edition, 1998.
- [98] Algi L. Lance, Wendell D. Seal, and Frederik Labaar. Phase noise and AM noise measurements in the frequency domain. *Infrared and Millimeter Waves*, 11:239–289, 1984.
- [99] Jaques Rutman. Characterization of phase and frequency instabilities in precision frequency sources: Fifteen years of progress. *Proceedings of the IEEE*, 66(9):1048–1075, September 1978.
- [100] D. W. Allan. Statistics of atomic frequency standards. *Proceedings of the IEEE*, 54(2):221–230, 1966.
- [101] James A. Barnes, Andrew R. Chi, Leonard S. Cutler, Daniel J. Healey, David B. Leeson, Thomas E. McCunigal, Jr. Mullen, James A., Warren L. Smith, Richard L. Sydnor, Robert F. C. Vessot, and Gernot M. R. Winkler. Characterization of frequency stability. *IEEE Transactions on Instrumentation and Measurement*, IM-20(2):105–120, May 1971.
- [102] Patrick Lesage and Claude Audoin. Characterization of frequency stability: Uncertainty due to the finite number of measurements. *IEEE Transactions on Instrumentation and Measurement*, 22(2):157–161, June 1973.
- [103] D. A. Howe, D. W. Allan, and J. A. Barnes. Properties of signal sources and measurement methods. In *Proceedings of the 35<sup>th</sup> Annual Symposium on Frequency Control*, 1981.
- [104] Samuel R. Stein. *Precision Frequency Control*, volume 2, chapter 12, Frequency and Time – Their Measurement and Characterization, pages 191–232, 399–416. Academic Press, New York, 1985.
- [105] C. A. Greenhall and W. J. Riley. Uncertainty of stability variances based on finite differences. In *Proceedings of the 35<sup>th</sup> Annual Precise Time and Time Interval (PTTI) Meeting*, pages 267–279, 2003.
- [106] D. A. Howe and T. K. Peppler. Very long-term frequency stability: Estimation using a special-purpose statistic. In *Proceedings of the 2003 IEEE International Frequency Control Symposium and PDA Exhibition Jointly with the 17<sup>th</sup> European Frequency and Time Forum*, pages 233–238, 2003.
- [107] D. A. Howe and T. N. Tasset.  $\widehat{\text{Theo}}_1$  characterization of very long-term frequency stability. In *Proceedings of the 18<sup>th</sup> European Frequency and Time Forum*, pages 581–587, 2004.
- [108] T. N. Tasset, D. A. Howe, and Percival D. B.  $\widehat{\text{Theo}}_1$  confidence intervals. In *Proceedings of the IEEE International Ultrasonics, Ferroelectrics, and Frequency Control Joint 50<sup>th</sup> Anniversary Conference*, pages 725–728. IEEE, 2004.
- [109] D. A. Howe, J. McGee-Taylor, and Tasset T.  $\widehat{\text{Theo}}_H$  bias-removal method. In *Proceedings of the IEEE Frequency Control Symposium*, 2006.
- [110] D. A. Howe.  $\widehat{\text{Theo}}_H$ : a hybrid, high-confidence statistic that improves on the Allan deviation. *Metrologia*, 43:S322–S331, 2006.
- [111] Jennifer A. McGee and David. A. Howe.  $\widehat{\text{Theo}}_H$  and Allan deviation as power-law noise estimators. *IEEE Transactions on Ultrasonics, Ferroelectrics and Frequency Control*, 54(2):448–452, February 2007.
- [112] Jennifer A. Taylor and David A. Howe. Fast  $\widehat{\text{Theo}}_{BR}$ : A method for long data set stability analysis. *IEEE Transactions on Ultrasonics, Ferroelectrics and Frequency Control*, 57(9):2091–2094,

- September 2010.
- [113] François Vernotte. Application of the moment condition to noise simulation and to stability analysis. *IEEE Transactions on Ultrasonics, Ferroelectrics and Frequency Control*, 49:508–513, 2002.
  - [114] W. J. Riley. *Handbook of Frequency Stability Analysis*. US Government Printing Office, 2008. NIST Special Publication 1065.
  - [115] R. W. Boyd. *Nonlinear optics*, chapter 2.1. In [370], 2nd edition, 2003.
  - [116] David J. Griffiths. *Introduction to Electrodynamics*, chapter 9.4. In [371], 3rd edition, 1999.
  - [117] Eugene Hecht. *Optics*, chapter 3.5.1. Addison-Wesley, 4th edition, 2002.
  - [118] D. Marcuse. Pulse distortion in single-mode fibers. *Applied Optics*, 19(10):1653–1660, May 1980.
  - [119] Sergei A. Akhmanov, Victor A. Vysloukh, and Anatoly S. Chirkin. *Optics of femtosecond laser pulses*. American Institute of Physics, New York, 1992.
  - [120] S. M. Witte. Terawatt-intensity few-cycle laser pulses - optical parametric chirped pulse amplification and frequency comb spectroscopy, 2007. equation 2.21.
  - [121] S. M. Witte. *Terawatt-intensity few-cycle laser pulses - Optical parametric chirped pulse amplification and frequency comb spectroscopy*. PhD thesis, Vrije Universiteit Amsterdam, 2007.
  - [122] John Kerr. XL. a new relation between electricity and light: Dielectric media birefringent. *Philosophical Magazine Series 4*, 50(332):337–348, 1875.
  - [123] John Kerr. XXIV. on reflection of polarized light from the equatorial surface of a magnet. *Philosophical Magazine Series 5*, 5(30):161–177, 1878.
  - [124] J. A. Armstrong, N. Bloembergen, J. Ducuing, and P. S. Pershan. Interactions between light waves in a nonlinear dielectric. *Physical Review*, 127(6):1918–1939, 1962.
  - [125] N. Bloembergen and P. Lallemand. Complex intensity-dependent index of refraction, frequency broadening of stimulated Raman lines, and stimulated Rayleigh scattering. *Physical Review Letters*, 16(3):81–84, Januari 1966.
  - [126] Tan Jun Yu and Chang Hee Nam. Carrier-envelope phase stabilization of femtosecond lasers by the direct locking method. *Progress in Quantum Electronics*, 36:541–565, 2012.
  - [127] K. D. Froome. Microwave harmonic generator capable of frequencies in excess of 600 Gc./s. *Nature*, 193:1169–1170, March 1962.
  - [128] M. Kourogi, K. Nakagawa, and M. Ohtsu. Wide-span optical frequency comb generator for accurate optical frequency difference measurement. *IEEE Journal of Quantum Electronics*, 29:2693–2701, 1993.
  - [129] Th. Udem, J. Reichert, T. W. Hänsch, and M Kourogi. Accuracy of optical frequency comb generators and optical frequency interval divider chains. *Optics Letters*, 23(17):1387–1389, September 1998.
  - [130] Motonobu Kourogi, Kazuhiro Imai, Bambang Widiatmoko, and Motoichi Ohtsu. Generation of expanded optical frequency combs. *Topics in Applied Physics*, 79:315–335, 2001.
  - [131] J. Reichert, R. Holzwarth, Th. Udem, and T. W. Hänsch. Measuring the frequency of light with mode-locked lasers. *Optics Communications*, 172:59–68, 1999.
  - [132] P. Maddaloni, P. Cancio, and P. De Natale. Optical comb generators for laser frequency measurement. *Measurement Science and Technology*, 20:052001, 2009.
  - [133] P. Del’Haye, A. Schliesser, O. Arcizet, T. Wilken, Holzwarth R., and T. J. Kippenberg. Optical frequency comb generation from a monolithic microresonator. *Nature*, 450:1214–1217, December 2007.
  - [134] T. Kippenberg, R. Holzwarth, and S. A. Diddams. Microresonator-based optical frequency combs. *Science*, 332:555–559, 2011.
  - [135] L.-S. Ma, Z. Bi, A. Bartels, L. Robertsson, M. Zucco, R. S. Windeler, G. Wilpers, C. Oates, L. Hollberg, and S. A. Diddams. Optical frequency synthesis and comparison with uncertainty at the  $10^{-19}$  level. *Science*, 303:1843, March 2004.
  - [136] L. A. M. Johnson, P. Gill, and H. S. Margolis. Evaluating the performance of the NPL femtosecond frequency combs: agreement at the  $10^{-21}$  level. *Metrologia*, 52(1):62, 2015.
  - [137] Itan Barmes, Stefan Witte, and K. S. E. Eikema. Spatial and spectral coherent control with

- frequency combs. *Nature Photonics*, 7(1):38–42, January 2013.
- [138] R. W. Boyd. *Nonlinear optics*, chapter 1.2. In [370], 2nd edition, 2003.
- [139] Kerry J. Vahala. Optical microcavities. *Nature*, 424(6950):839–846, Aug 2003.
- [140] T. Herr, K. Hartinger, J. Riemensberger, C. Y. Wang, E. Gavartin, R. Holzwarth, M. L. Gorodetsky, and T. J. Kippenberg. Universal formation dynamics and noise of Kerr-frequency combs in microresonators. *Nature Photonics*, 6:480–487, 2012.
- [141] H. R. Telle, B. Lipphardt, and J. Stenger. Kerr-lens, mode-locked lasers as transfer oscillators for optical frequency measurements. *Applied Physics B*, 74:1–6, 2002.
- [142] Enrico Rubiola and Vincent Giordano. Correlation-based phase noise measurements. *Review of Scientific Instruments*, 71(8):3085–3091, August 2000.
- [143] John G. Hartnett, Travis Povey, and Stephen Parker. A transposed frequency technique for phase noise and frequency stability measurements. *Arxiv*, pages 1–6, 2012.
- [144] Chih-Hao Li, Andrew J. Benedict, Peter Fendel, Alexander G. Glenday, Franz X. Kärtner, David F. Phillips, Dimitar Sasselov, Andrew Szentgyogyi, and Ronald L. Walsworth. A laser frequency comb that enables radial velocity measurements with a precision of  $1 \text{ cm s}^{-1}$ . *Nature*, 452:610–612, April 2008.
- [145] Tilo Steinmetz, Tobias Wilken, Constanza Araujo-Hauck, Ronald Holzwarth, Theodor W. Hänsch, Luca Pasquini, Antonio Manescau, Sandro D’Odorico, Michael T. Murphy, Thomas Kentscher, Wolfgang Schmidt, and Thomas Udem. Laser frequency combs for astronomical observations. *Science*, 321:1335–1337, September 2008.
- [146] S. Hannemann, E. J. Salumbides, S. Witte, R. Th. Zinkstok, E.-J. van Duijn, K. S. E. Eikema, and W. Ubachs. Frequency metrology on the  $\text{Mg } 3s^2 \ ^1S \rightarrow 3s4p \ ^1P$  line for comparison with quasar data. *Physical Review A*, 74(1):012505, 2006.
- [147] S. Hannemann, E. J. Salumbides, S. Witte, R. T. Zinkstok, E.-J. van Duijn, K. S. E. Eikema, and W. Ubachs. Frequency metrology on the  $\text{EF } ^1\Sigma_g^+ \leftarrow X \ ^1\Sigma_g^+(0, 0)$  transition in  $\text{H}_2$ , HD, and  $\text{D}_2$ . *Physical Review A*, 74:062514, 2006.
- [148] S. Hannemann, E. J. Salumbides, and W. Ubachs. Reducing the first-order doppler shift in a sagnac interferometer. *Optics Letters*, 32(11):1381–1383, June 2007.
- [149] A. L. Wolf, S. A. van den Berg, C. Gohle, E. J. Salumbides, W. Ubachs, and K. S. E. Eikema. Frequency metrology on the  $4s \ ^2S_{1/2} - 4p \ ^2P_{1/2}$  transition in  $^{40}\text{Ca}^+$  for a comparison with quasar data. *Physical Review A*, 78:032511, 2008.
- [150] Jinjun Liu, Edcel J. Salumbides, Urs Hollenstein, Koelemeij Jeroen C. J., K. S. E. Eikema, W. Ubachs, and Frédéric Merkt. Determination of the ionization and dissociation energies of the hydrogen molecule. *The Journal of Chemical Physics*, 130:174306, 2009.
- [151] E. J. Salumbides, V. Maslinskas, I. M. Dildar, A. L. Wolf, E.-J. van Duijn, K. S. E. Eikema, and W. Ubachs. High-precision frequency measurement of the 423-nm Ca I line. *Physical Review A*, 83:012502, 2011.
- [152] R. van Rooij, J. S. Borbely, J. Simonet, M. D. Hoogerland, K. S. E. Eikema, R. A. Rozendaal, and W. Vassen. Frequency metrology in quantum degenerate helium: Direct measurement of the  $2 \ ^3S_1 \rightarrow 2 \ ^1S_0$  transition. *Science*, 333(6039):196–198, July 2011.
- [153] Scott A. Diddams, Leo Hollberg, and Vela Mbele. Molecular fingerprinting with the resolved modes of a femtosecond laser frequency comb. *Nature*, 445:627–630, Februari 2007.
- [154] A. L. Wolf, S. A. van den Berg, W. Ubachs, and K. S. E. Eikema. Direct frequency comb spectroscopy of trapped ions. *Physical Review Letters*, 102(22):223901, June 2009.
- [155] D. Z. Kandula, C. Gohle, T. J. Pinkert, W. Ubachs, and K. S. E. Eikema. Extreme ultraviolet frequency comb metrology. *Physical Review Letters*, 105(6):063001, August 2010.
- [156] Ian Coddington, William C. Swann, and Nathan R. Newbury. Coherent multiheterodyne spectroscopy using stabilized optical frequency combs. *Physical Review Letters*, 100:013902, Januari 2008.
- [157] Fritz Keilmann, Christoph Gohle, and Holzwarth Ronald. Time-domain mid-infrared frequency-comb spectrometer. *Optics Letters*, 29(13):1542–1544, July 2004.
- [158] A. Bartels, A. Thoma, C. Janke, T. Decorsy, A. Dreyhaupt, S. Winnerl, and M. Helm. High-resolution THz spectrometer with kHz scan rates. *Optics Express*, 14(1):430–437, Januari 2006.

- [159] Takuro Ideguchi, Antonin Poisson, Guy Guelachvili, Nathalie Picqué, and Theodor W. Hänsch. Adaptive real-time dual-comb spectroscopy. *Nature Communications*, 5:3375, 2014.
- [160] B. Bernhardt, E. Sorokin, P. Jacquet, R. Thon, T. Becker, I. T. Sorokina, N. Picqué, and T. W. Hansch. Mid-infrared dual-comb spectroscopy with  $2.4 \mu\text{m}$   $\text{Cr}^{2+}:\text{ZnSe}$  femtosecond lasers. *Applied Physics B*, 100:3–8, 2010.
- [161] Arthur Hipke, Samuel A. Meek, Takuro Ideguchi, Theodor W. Hänsch, and Nathalie Picqué. Broadband Doppler-limited two-photon and stepwise excitation spectroscopy with laser frequency combs. *Physical Review A*, 90:011805(R), 2014.
- [162] Ingolf V. Hertel and Claus-Peter Schulz. *Atome, Moleküle und optische Physik*, volume 1. Springer, 2008. ISBN 978-3-540-30613-9.
- [163] Christopher C. Gerry and Peter L. Knight. *Introductory Quantum Optics*. Cambridge University Press, 1st edition, 2005.
- [164] David J. Griffiths. *Introduction to Quantum Mechanics*, chapter 9. Pearson Prentice Hall, 2nd edition, 2005. see Sec. 9.1 and Problem 9.15.
- [165] R. Th. Zinkstok. *Direct frequency comb spectroscopy in the vacuum ultraviolet*. PhD thesis, Vrije Universiteit Amsterdam, 2008.
- [166] D. J. Wineland, J. J. Bollinger, W. M. Itano, and D. J. Heinzen. Squeezed atomic states and projection noise in spectroscopy. *Physical Review A*, 50(1):67–88, July 1994.
- [167] Bernard Yurke, Samuel L. McCall, and John R. Klauder.  $\text{SU}(2)$  and  $\text{SU}(1,1)$  interferometers. *Physical Review A*, 33(6):4033–4054, June 1986.
- [168] R. Th. Zinkstok. *Direct frequency comb spectroscopy in the vacuum ultraviolet*, 2008. Chapter 3.4.
- [169] S. M. Witte. Terawatt-intensity few-cycle laser pulses - optical parametric chirped pulse amplification and frequency comb spectroscopy, 2007. Chapter 2.3.
- [170] R. Teets, J. Eckstein, and T. W. Hänsch. Coherent two-photon excitation by multiple light pulses. *Physical Review Letters*, 38(14):760–764, Apr 1977.
- [171] D. E. Roberts and E. N. Fortson. Rubidium isotope shifts and hyperfine structure by two-photon spectroscopy with a multimode laser. *Optics Communications*, 14(3):332–335, July 1975.
- [172] Younan Tang, Dingyuan abd Xia, Bochuang Wu, and Chuangtai Chen. Growth of a new UV nonlinear optical crystal:  $\text{KBe}_2(\text{BO}_3)\text{F}_2$ . *Journal of Crystal Growth*, 222:125–129, 2001.
- [173] Chun Zhou, Teruto Kanai, Xiaoyang Wang, Yong Zhu, Chuangtian Chen, and Shuntaro Watanabe. Generation of ultrashort 25- $\mu\text{J}$  pulses at 200 nm by dual broadband frequency doubling with a thin  $\text{KBe}_2\text{BO}_3\text{F}_2$  crystal. *Optics Express*, 20(13):13684–13691, June 2012.
- [174] Hongwei Huang, Chuangtian Chen, Xiaoyang Wang, Yong Zhu, Guiling Wang, Xin Zhang, Lirong Wang, and Jiyong Yao. Ultraviolet nonlinear optical crystal:  $\text{CsBe}_2\text{BO}_3\text{F}_2$ . *Journal of the Optical Society of America B*, 28(9):2186–2190, September 2011.
- [175] P. B. Corkum. Plasma perspective on strong field multiphoton ionization. *Physical Review Letters*, 71(13):1994–1997, 1993.
- [176] M. Lewenstein, Ph. Balcou, M. Yu. Ivanov, Anne L’Huillier, and P. B. Corkum. Theory of high-harmonic generation by low-frequency laser fields. *Physical Review A*, 49(3):2117–2132, 1994.
- [177] D. Z. Kandula, A. Renault, Ch. Gohle, A. L. Wolf, S. Witte, W. Hogervorst, W. Ubachs, and K. S. E. Eikema. Ultrafast double-pulse parametric amplification for precision ramsey metrology. *Optics Express*, 16(10):7071–7082, May 2008.
- [178] Dominik Z. Kandula, Christoph Gohle, Tjeerd J. Pinkert, Wim Ubachs, and Kjeld S. E. Eikema. XUV frequency-comb metrology on the ground state of helium. *Physical Review A*, 84:062512, 2011.
- [179] T. J. Pinkert, D. Z. Kandula, C Gohle, I. Barmes, J. Morgenweg, and K. S. E. Eikema. Widely tunable extreme UV frequency comb generation. *Optics Letters*, 36(11):2026–2028, June 2011.
- [180] J. Morgenweg and K. S. E. Eikema. Tailored pulse sequences from an 880 nm pumped  $\text{Nd}:\text{YVO}_4$  bounce amplifier. *Optics Letters*, 37(2):208–210, Januari 2012.
- [181] Jonas Morgenweg and Kjeld S. E. Eikema. Ramsey-comb spectroscopy: Theory and signal

- analysis. *Physical Review A*, 89:052510, 2014.
- [182] Jonas Morgenweg. *Ramsey-comb spectroscopy*. PhD thesis, VU University, Amsterdam, 2014.
- [183] Arman Cingöz, Dylan C. Yost, Thomas K. Allison, Axel Ruehl, Martin E. Fermann, Ingmar Hartl, and Jun Ye. Direct frequency comb spectroscopy in the extreme ultraviolet. *Nature*, 482:68–71, Februari 2012.
- [184] Christoph Gohle, Thomas Udem, Maximilian Herrmann, Jens Rauschenberger, Ronald Holzwarth, Hans A. Schuessler, Ferenc Krausz, and Theodor W. Hänsch. A frequency comb in the extreme ultraviolet. *Nature*, 436(7048):234–237, July 2005.
- [185] R. Jason Jones, Kevin D. Moll, Michael J. Thorpe, and Jun Ye. Phase-coherent frequency combs in the vacuum ultraviolet via high-harmonic generation inside a femtosecond enhancement cavity. *Physical Review Letters*, 94(19):193201, 2005.
- [186] J. Seres, E. Seres, D. Hochhaus, B. Ecker, D. Zimmer, V. Bagnoud, T. Kuehl, and C. Spielmann. Laser-driven amplification of soft X-rays by parametric stimulated emission in neutral gases. *Nature Physics*, 6(6):455–461, June 2010.
- [187] A. M. Perelomov, V. S. Popov, and M. V. Terent'ev. Ionization of atoms in an alternating electric field. *Sovjet Physics JETP*, 23(5):924–934, November 1966.
- [188] M. V. Ammosov, N. B. Delone, and V. P. Kraĭnov. Tunnel ionization of complex atoms and of atomic ions in an alternating electromagnetic field. *Sovjet Physics JETP*, 64(6):1191–1194, December 1986.
- [189] L. V. Keldysh. Ionisation in the field of a strong electromagnetic wave. *Sovjet Physics JETP*, 20(5):1307–1314, May 1965.
- [190] H. R. Reiss. Theoretical methods in quantum optics: S-matrix and Keldysh techniques for strong-field processes. *Progress in Quantum Electronics*, 16:1–71, 1992.
- [191] J. H. Eberly, J. Javanainen, and K. Rzazewski. Above-threshold ionization. *Physical Review E*, 204(5):331–381, 1991.
- [192] Pascal Salières, Anne L'Huillier, and Maciej Lewenstein. Coherence control of high-order harmonics. *Physical Review Letters*, 74(19):3776–3779, May 1995.
- [193] M. Lewenstein, P. Salières, and A. L'Huillier. Phase of the atomic polarization in high-order harmonic-generation. *Physical Review A*, 52(6):4747–4754, December 1995.
- [194] Chiara Corsi, Angela Pirri, Emiliano Sali, Alessandra Tortora, and Marco Bellini. Direct interferometric measurement of the atomic dipole phase in high-order harmonic generation. *Physical Review Letters*, 97(2):023901, Jul 2006.
- [195] A. Renault, D. Z. Kandula, S. Witte, A. L. Wolf, R. T. Zinkstok, W. Hogervorst, and K. S. E. Eikema. Phase stability of terawatt-class ultrabroadband parametric amplification. *Optics Letters*, 32(16):2363–2365, August 2007.
- [196] Dominik Zbigniew Kanduła. *XUV frequency comb metrology and the ground state of helium*. PhD thesis, Vrije Universiteit, Amsterdam, December 2011.
- [197] E. Rutherford. The scattering of  $\alpha$  and  $\beta$  particles by matter and the structure of the atom. *Philosophical Magazine*, 21(125):669–688, 1911.
- [198] Stephen Gasiorowitz. *Quantum Physics*, chapter 18. Wiley, 1996.
- [199] Ingolf V. Hertel and Claus-Peter Schulz. *Atome, Moleküle und optische Physik*, chapter 3.3. Volume 1 of [162], 2008. ISBN 978-3-540-30613-9.
- [200] Egil A. Hylleraas. Über den Grundzustand des Heliumatoms. *Zeitschrift für Physik*, 48(7–8):469–494, 1928.
- [201] Egil A. Hylleraas. Neue Berechnung der Energie des Heliums im Grundzustande, sowie des tiefsten Terms von Ortho-Helium. *Zeitschrift für Physik*, 54(5–6):347–366, 1929.
- [202] W. Heisenberg. Über den anschaulichen Inhalt der quantentheoretischen Kinematik und Mechanik. *Zeitschrift für Physik*, 43:172–198, 1927.
- [203] G. W. F. Drake and Zong-Chao Yan. High-precision spectroscopy as a test of quantum electrodynamics in light atomic systems. *Canadian Journal of Physics*, 86(1):45–54, JAN 2008.
- [204] Gordon W. F. Drake, editor. *Handbook of Atomic, Molecular and Optical Physics*. Springer Handbooks. Springer, 2nd edition, 2006.
- [205] Krzysztof Pachucki.  $\alpha^4\mathcal{R}$  corrections to singlet states of helium. *Physical Review A*, 74:022512, 2006.

- [206] Krzysztof Pachucki. Helium energy levels including  $m\alpha^6$  corrections. *Physical Review A*, 74(6):062510, DEC 2006.
- [207] Krzysztof Pachucki and Vladimir A. Yerokhin. Reexamination of the helium fine structure. *Physical Review A*, 79(6):062516, JUN 2009.
- [208] K. Pachucki, V. A. Yerokhin, and P. Cancio Pastor. Quantum electrodynamic calculation of the hyperfine structure of  $^3\text{He}$ . *Physical Review A*, 85:042517, 2012.
- [209] J. Stark. Beobachtungen über den Effekt des elektrischen Feldes auf Spektrallinien. I. Quereffekt. *Annalen der Physik*, 348(7):965–982, 1914.
- [210] Paul S. Epstein. Zur theorie des Starkeffectes. *Annalen der Physik*, 355(13):489–520, 1916.
- [211] E. Schrödinger. Quantisierung als Eigenwertproblem; (Dritte Mitteilung: Störungstheorie, mit anwendung auf den Starkeffect der Balmerlinien). *Annalen der Physik*, 385(13):437–490, 1926.
- [212] W. Pauli jr. Über das Wasserstoffspektrum vom Standpunkt der neuen Quantenmechanik. *Zeitschrift für Physik*, pages 336–363, 1926.
- [213] Paul S. Epstein. The Stark effect from the point of view of Schroedinger's quantum theory. *Physical Review*, 28:695–710, 1926.
- [214] Igor I. Sobelman. *Atomic Spectra and Radiative Transitions*. Springer-Verlag, Berlin, Heidelberg, New York, 1979. ISBN: 3-540-09082-7, 0-387-09082-7.
- [215] Ingolf V. Hertel and Claus-Peter Schulz. *Atome, Moleküle und optische Physik*, volume 2, chapter 8.5.4. Springer, 2010. ISBN 978-3-642-11972-9.
- [216] Constantine E. Theodosiou. Transition probabilities for the helium singly excited states  $1snl^{1,3}l$  with  $n = 2 - 21$  and  $l = 0 - 5$ . *Atomic Data and Nuclear Data Tables*, 36:97–127, 1987.
- [217] Constantine E. Theodosiou. Lifetimes of singly excited states in He I. *Physical Review A*, 30(6):2910–2921, December 1984.
- [218] W. L. Wiese, M. W. Smith, and Glennon B. M. *Atomic Transition Probabilities Volume I, Hydrogen Through Neon*, volume I. US Government Printing Office, 1966.
- [219] A. Einstein. Zur Elektrodynamik bewegter Körper. *Annalen der Physik*, 17:891–921, 1905.
- [220] Stephen Gourley. Binomial expansion, power series, limits, approximations, fourier series. lecture notes (online), 2007.
- [221] A. Einstein. Über die Möglichkeit einer neuen Prüfung des Relativitätsprinzips. *Annalen der Physik*, 23:197–198, 1907.
- [222] Jonas Morgenweg, Itan Barmes, and Kjeld S. E. Eikema. Ramsey-comb spectroscopy with intense ultrashort laser pulses. *Nature Physics*, 10:30–33, Januari 2013.
- [223] Nathan R. Newbury and William C. Swann. Low-noise fiber-laser frequency combs. *Journal of the Optical Society of America B*, 24(8):1756–1770, August 2007.
- [224] Orazio Svelto. *Principles of Lasers*, chapter 9.2.4. Plenum Press, 4th edition, 1998.
- [225] Fred L. Walls and Andrea DeMarchi. RF spectrum of a signal after frequency multiplication; measurement and comparison with a simple calculation. *IEEE Transactions on Instrumentation and Measurement*, IM-24(3):210–217, Sept. 1975.
- [226] Agilent Technologies, Inc. *Agilent E8241A/44A/51A/54A PSG Family Performance Signal Generator - Data Sheet*, 2002. document no. 5988-2412EN.
- [227] Travis C. Briles, Dylan C. Yost, Arman Cingöz, Jun Ye, and Thomas R. Schibli. Simple piezoelectric-actuated mirror with 180 kHz servo bandwidth. *Optics Express*, 18(10):9739–9746, May 2010.
- [228] A. Bartels, C. W. Oates, L. Hollberg, and S. A. Diddams. Stabilization of femtosecond laser frequency combs with subhertz residual linewidths. *Optics Letters*, 29:1081, 2004.
- [229] T. R. Schibli, I. Hartl, D. C. Yost, M. J. Martin, A. Marcinkevičius, M. E. Fermann, and J. Ye. Optical frequency comb with submillihertz linewidth and more than 10W average power. *Nature Photonics*, 2:355, June 2008.
- [230] R. V. Pound. Electronic frequency stabilization of microwave oscillators. *Review of Scientific Instruments*, 17(11):490–505, November 1946.
- [231] K. Nakagawa, A. S. Shelkovich, T. Katsuda, and M. Ohtsu. Absolute frequency stability of a diode-laser-pumped Nd:YAG laser stabilized to a high-finesse optical cavity. *Applied*

- Optics*, 33(27):6383–6386, September 1994.
- [232] Redfern Integrated Optics Inc. Product brief: RIO Planex™ external cavity laser. [www.rio-inc.com](http://www.rio-inc.com), Jan 2012.
- [233] Christopher J. Erickson, Marshal Van Zijll, Greg Doermann, and Dallin S. Durfee. An ultrahigh stability, low-noise laser current driver with digital control. *Review of Scientific Instruments*, 79:073107, 2008.
- [234] K. G. Libbrecht and J. L. Hall. A low-noise high-speed diode current laser driver. *Review of Scientific Instruments*, 64(8):2133–2135, Aug 1993.
- [235] Wei Zhang, Zhenyu Xu, Michel Lours, Rodolphe Boudot, Yann Kersalé, Andre N. Luiten, Yann Le Coq, and Giorgio Santarelli. Advanced noise reduction techniques for ultra-low phase noise optical-to-microwave division with femtosecond fiber combs. *IEEE Transactions on Ultrasonics, Ferroelectrics and Frequency Control*, 58(5):900–908, May 2011.
- [236] J. J. McFerran, E. N. Ivanov, A. Bartels, G. Wilpers, Oates C. W., S. A. Diddams, and L. Hollberg. Low-noise synthesis of microwave signals from an optical source. *Electronic Letters*, 41(11):650–651, May 2005.
- [237] E. A. Donley, T. P. Heaven, F. Levi, M. O. Tataw, and S. R. Jefferts. Double-pass acousto-optic modulator system. *Review of Scientific Instruments*, 76:063112, 2005.
- [238] C. Randy Giles and Emmanuel Desurvire. Modeling erbium-doped fiber amplifiers. *Journal of Lightwave Technology*, 9(2):271–283, Februari 1991.
- [239] C. R. Giles, E. Desurvire, and Simpson J. R. Transient gain and cross talk in erbium-doped fiber amplifiers. *Optics Letters*, 14(16):880–882, August 1989.
- [240] C. R. Giles and Emmanuel Desurvire. Propagation of signal and noise in concatenated erbium-doped fiber optical amplifiers. *Journal of Lightwave Technology*, 9(2):147–154, Februari 1991.
- [241] Emmanuel Desurvire and Jay R. Simpson. Amplification of spontaneous emission in erbium-doped single-mode fibers. *Journal of Lightwave Technology*, 7(5):835–845, May 1989.
- [242] DJ Jones, SA Diddams, JK Ranka, A Stentz, RS Windeler, JL Hall, and ST Cundiff. Carrier-envelope phase control of femtosecond mode-locked lasers and direct optical frequency synthesis. *Science*, 288(5466):635–639, APR 28 2000.
- [243] H. S. Margolis, G. P. Barwood, G. Huang, H. A. Klein, S. N. Lea, K. Szymaniec, and P. Gill. Hertz level measurement of the optical clock frequency in a single  $^{88}\text{Sr}^+$  ion. *Science*, 306:1355–1358, 2004.
- [244] Petr Balling, Petr Křeň, Pavel Mašika, and S. A. van den Berg. Femtosecond frequency comb based distance measurement in air. *Optics Express*, 17(11):9300–9313, May 2009.
- [245] S. Anantathanasarn, R. Nötzel, P. J. van Veldhoven, F. W. M. van Otten, Y. Barbarin, G. Servanton, T. de Vries, E. Smalbrugge, E. J. Geluk, T. J. Eijkemans, E. A. J. M. Bente, Y. S. Oei, M. K. Smit, and J. H. Wolter. Wavelength controlled InAs/InP quantum dots for telecom laser applications. *Microelectronics Journal*, 37:1461–1467, 2006.
- [246] Z. G. Lu, J. R. Liu, S. Raymond, P. J. Poole, P. J. Barrios, and D. Poitras. 312-fs pulse generation from a passive C-band InAs/InP quantum dot mode-locked laser. *Optics Express*, 16(14):10835–10840, July 2008.
- [247] Ricardo Rosales, Kamel Merghem, Anthony Martinez, A. Akrouf, J.-P. Tourrenc, Alain Accard, Francois Lelarge, and Abderrahim Ramdane. InAs/InP quantum-dot passively mode-locked lasers for 1.55- $\mu\text{m}$  applications. *IEEE Journal on Selected Topics in Quantum Electronics*, 17(5):1292–1301, September/October 2011.
- [248] E. U. Rafailov, M. A. Cataluna, W. Sibbett, N. D. Il'inskaya, Yu. M. Zadiranov, A. E. Zhukov, V. M. Ustinov, D. A. Livshits, A. R. Kovsh, and N. N. Ledenstov. High-power picosecond and femtosecond pulse generation from a two-section mode-locked quantum-dot laser. *Applied Physics Letters*, 87:081107, 2005.
- [249] E. U. Rafailov, M. A. Cataluna, and W. Sibbett. Mode-locked quantum-dot lasers. *Nature Photonics*, 1:395–401, July 2007.
- [250] Kevin W. Holman, David J. Jones, Jun Ye, and Erich P. Ippen. Orthogonal control of the frequency comb dynamics of a mode-locked laser diode. *Optics Letters*, 28(23):2405–2407, December 2003.

- [251] S. A. Diddams, M. Kirchner, T. Fortier, D. Braje, A. M. Weiner, and L. Hollberg. Improved signal-to-noise ratio of 10 GHz microwave signals generated with a mode-filtered femto-second laser frequency comb. *Optics Express*, 17(5):3331–3340, march 2009.
- [252] Tatiana Habruseva, Shane O’Donoghue, Natalia Rebrova, Douglas A. Reid, Liam P. Barry, Stephen P. Hegarty, Dmitrii Rachinskii, and Guillaume Huyet. Quantum-dot mode-locked lasers with dual mode optical injection. *IEEE Photonics Technology Letters*, 22(6):359–361, March 2010.
- [253] N. K. Fontaine, R. P. Scott, J. Cao, A. Karalar, W. Jiang, K. Okamoto, J. P. Heritage, B. H. Kolner, and S. J. B. Yoo. 32 phase  $\times$  32 amplitude optical arbitrary waveform generation. *Optics Letters*, 32(7):865–867, April 2007.
- [254] H. Schmeckebeier, G. Fiol, C. Meuer, D. Arsenijević, and D. Bimberg. Complete pulse characterization of quantum-dot mode-locked lasers suitable for optical communication up to 160 Gbit/s. *Optics Express*, 18(4):3415–3425, 2010.
- [255] S. Arahira, H. Takahashi, K. Nakamura, H. Yaegashi, and Y. Ogawa. Polarization-, wavelength-, and filter-free all-optical clock recovery in a passively mode-locked laser diode with orthogonally pumped polarization-diversity configuration. *IEEE Journal of Quantum Electronics*, 45(5):476–487, may 2009.
- [256] H. Takara, T. Ohara, K. Mori, K. Sato, E. Yamada, Y. Inoue, T. Shibata, M. Abe, T. Morioka, and K.-I. Sato. More than 1000 channel optical frequency chain generation from single supercontinuum source with 12.5 GHz channel spacing. *Electronic Letters*, 36(25):2089–2090, 2000.
- [257] T. Kuri, T. Nakasyotani, H. Toda, and K.-I. Kitayama. Characterizations of supercontinuum light source for WDM millimeter-wave-band radio-on-fiber systems. *IEEE Photonics Technology Letters*, 17(6):1274–1276, june 2005.
- [258] T. Kuri, H. Toda, J.J.V. Olmos, and K. Kitayama. Reconfigurable dense wavelength-division-multiplexing millimeter-waveband radio-over-fiber access system technologies. *Journal of Lightwave Technology*, 28(16):2247–2257, aug,15, 2010.
- [259] Rui Zhou, Sylwester Latkowski, John O’Carroll, Richard Phelan, Liam P. Barry, and Prince Anandarajah. 40 nm wavelength tunable gain-switched optical comb source. *Optics Express*, 19(26):B415–B420, December 2011.
- [260] W. Shieh, H. Bao, and Y. Tang. Coherent optical OFDM: theory and design. *Optics Express*, 16(2):841–859, January 2008.
- [261] Martijn J. R. Heck, Edcel J. Salumbides, Amandine Renault, Erwin A. J. M. Bente, Yok-Siang Oei, Meint K. Smit, René van Veldhoven, Richard Nötzel, Kjeld S. E. Eikema, and Wim Ubachs. Analysis of hybrid mode-locking of two-section quantum dot lasers operating at 1.5  $\mu\text{m}$ . *Optics Express*, 17(20):18063–18075, September 2009.
- [262] Martijn J. R. Heck, Amandine Renault, Erwin A. J. M. Bente, Yok-Siang Oei, Meint K. Smit, Kjeld S. E. Eikema, Wim Ubachs, Sanguan Anantathanasarn, and Richard Nötzel. Passively mode-locked 4.6 and 10.5 GHz quantum dot laser diodes around 1.55  $\mu\text{m}$  with large operating regime. *IEEE Journal on Selected Topics in Quantum Electronics*, 15(3):634–643, May/June 2009.
- [263] Martijn J. R. Heck, Erwin A. J. M. Bente, Barry Smalbrugge, Yok-Siang Oei, Meint K. Smit, Sanguan Anantathanasarn, and Richard Nötzel. Observation of Q-switching and mode-locking in two-section InAs/InP (100) quantum dot lasers around 1.55  $\mu\text{m}$ . *Optics Express*, 15(25):16292–16301, December 2007.
- [264] S. Anantathanasarn, R. Nötzel, P. J. van Veldhoven, F. W. M. van Otten, Y. Barbarin, G. Servanton, T. de Vries, E. Smalbrugge, E. J. Geluk, T. J. Eijkemans, E. A. J. M. Bente, Y.-S. Oei, M. K. Smit, and J. H. Wolter. Lasing of wavelength-tunable (1.55  $\mu\text{m}$  region) InAs/InGaAsP/InP (100) quantum dots grown by metal organic vapor-phase epitaxy. *Applied Physics Letters*, 89(7):073115, August 2006.
- [265] M. S. Tahvili, L. Du, M. J. R. Heck, R. Nötzel, M. K. Smit, and E. A. J. M. Bente. Dual-wavelength passive and hybrid mode-locking of 3, 4.5 and 10 GHz InAs/InP(100) quantum dot lasers. *Optics Express*, 20(7):8117–8135, March 2012.
- [266] Govind P. Agrawal and N. Anders Olsson. Self-phase modulation and spectral broadening

- of optical pulses in semiconductor laser amplifiers. *IEEE Journal of Quantum Electronics*, 25(11):2297–2306, November 1989.
- [267] Petr Balling, Marc Fischer, Philipp Kubina, and Ronald Holzwarth. Absolute frequency measurement of wavelength standard at 1542nm: acetylene stabilized DFB laser. *Optics Express*, 13(23):9169–9201, November 2005.
- [268] R. Prasanth, J. E. M. Haverkort, A. Deepthy, E. W. Bogaart, J. J. G. M. van der Tol, E. A. Patent, G. Zhao, Q. Gong, P. J. van Veldhoven, R. Nötzel, and J. H. Wolter. All-optical switching due to state filling in quantum dots. *Applied Physics Letters*, 84(20):4059–4061, May 2004.
- [269] Tadhg Healy, Fatima C. Garcia Gunning, and Andrew D. Ellis. Multi-wavelength source using low drive-voltage amplitude modulators for optical communications. *Optics Express*, 15(6):2981–2986, March 2007.
- [270] F. Krausz and M. Ivanov. Attosecond physics. *Review of Modern Physics*, 81(1):163–234, January 2009.
- [271] M. Bellini, C. Lyngå, A. Tozzi, M. B. Gaarde, T. W. Hänsch, A. L’Huillier, and C.-G. Wahlström. Temporal coherence of ultrashort high-order harmonic pulses. *Physical Review Letters*, 81(2):297–300, 1998.
- [272] I. Lontos, S. Cavalieri, C. Corsi, R. Eramo, S. Kaziannis, A. Pirri, E. Sali, and M. Bellini. Ramsey spectroscopy of bound atomic states with extreme-ultraviolet laser harmonics. *Optics Letters*, 35(6):832–834, March 2010.
- [273] D. C. Yost, T. R. Schibli, J. Ye, J. L. Tate, J. Hostetter, M. B. Gaarde, and K. J. Schafer. Vacuum-ultraviolet frequency combs from below-threshold harmonics. *Nature Physics*, 5(11):815–820, 2009.
- [274] Stefan Witte, Roel Th. Zinkstok, Wim Ubachs, Wim Hogervorst, and Kjeld S. E. Eikema. Deep-ultraviolet quantum interference metrology with ultrashort laser pulses. *Science*, 307(5708):400–403, Jan 2005.
- [275] Roel Th. Zinkstok, Stefan Witte, Wim Ubachs, Wim Hogervorst, and Kjeld S. E. Eikema. Frequency comb laser spectroscopy in the vacuum-ultraviolet region. *Physical Review A*, 73(6):061801(R), 2006.
- [276] Yu. Ralchenko, A.E. Kramida, J. Reader, and NIST ASD Team (2008), 2008. NIST Atomic Spectra Database (version 3.1.5), [Online]. Available: <http://physics.nist.gov/asd3> [2010, August 25].
- [277] A. Baltuska, Th. Udem, M. Uiberacker, M. Hentschel, E. Goulielmakis, C. Gohle, R. Holzwarth, V. S. Yakoviev, A. Scrinzi, T. W. Hänsch, and F. Krausz. Attosecond control of electronic processes by intense light fields. *Nature*, 421(6923):611–615, Feb 2003.
- [278] I. Coddington, W. C. Swann, L. Nenadovic, and N. R. Newbury. Rapid and precise absolute distance measurements at long range. *Nature Photonics*, 3(6):351–356, June 2009.
- [279] K.-K. Ni, S. Ospelkaus, M. H. G. de Miranda, A. Pe’er, B. Neyenhuis, J. J. Zirbel, S. Kotochigova, P. S. Julienne, D. S. Jin, and J. Ye. A high phase-space-density gas of polar molecules. *Science*, 322:231–235, October 2008.
- [280] T. W. Hänsch, J. Alnis, P. Fendel, M. Fischer, C. Gohle, M. Herrmann, Holzwarth R., N. Kolachevsky, Th. Udem, and M. Zimmermann. Precision spectroscopy of hydrogen and femtosecond laser frequency combs. *Philosophical Transaction of the Royal Society A*, 363:2155–2163, August 2005.
- [281] M. Herrmann, M. Haas, U. D. Jentschura, F. Kottmann, D. Leibfried, G. Saathoff, C. Gohle, A. Ozawa, V. Batteiger, S. Knunz, N. Kolachevsky, H. A. Schussler, T. W. Hansch, and T. Udem. Feasibility of coherent XUV spectroscopy on the 1S–2S transition in singly ionized helium. *Physical Review A*, 79(5):052505, May 2009.
- [282] S. D. Bergeson, A. Balakrishnan, K. G. H. Baldwin, T. B. Lucatorto, J. P. Marangos, T. J. McIlrath, T. R. O’Brian, S. L. Rolston, C. J. Sansonetti, Jesse Wen, N. Westbrook, C. H. Cheng, and E. E. Eyler. Measurement of the He ground state Lamb shift via the two-photon  $1^1S - 2^1S$  transition. *Physical Review Letters*, 80(16):3475–3478, Apr 1998.
- [283] Adela Marian, Matthew C. Stowe, Daniel Felinto, and Jun Ye. Direct frequency comb measurements of absolute optical frequencies and population transfer dynamics. *Physical Review Letters*, 95(2):023001, 2005.

- [284] P. Fendel, S. D. Bergeson, Th. Udem, and T. W. Haensch. Two-photon frequency comb spectroscopy of the 6s–8s transition in cesium. *Optics Letters*, 32(6):701–703, MAR 15 2007.
- [285] Raulo Zerneck, Carlo Altucci, Marco Bellini, Mette B. Gaarde, T. W. Hänsch, Anne L’Huillier, Claire Lyngå, and C.-G. Wahlström. Phase-locked high-order harmonic sources. *Physical Review Letters*, 79(6):1006–1009, 1997.
- [286] Stefano Cavalieri, Roberto Eramo, Marzia Materazzi, Chiara Corsi, and Marco Bellini. Ramsey-type spectroscopy with high-order harmonics. *Physical Review Letters*, 89(13):133002, 2002.
- [287] A. Ozawa, J. Rauschenberger, Ch. Gohle, M. Herrmann, D. R. Walker, V. Pervak, A. Fernandez, R. Graf, A. Apolonski, R. Holzwarth, F. Krausz, T. W. Hänsch, and Th. Udem. High harmonic frequency combs for high resolution spectroscopy. *Physical Review Letters*, 100(25):253901, JUN 27 2008.
- [288] D. C. Morton, Q. X. Wu, and G. W. F. Drake. Energy levels for the stable isotopes of atomic helium ( $^4\text{He}$  I and  $^3\text{He}$  I). *Canadian Journal of Physics*, 84(2):83–105, February 2006.
- [289] M. Fischer, N. Kolachevsky, M. Zimmermann, R. Holzwarth, Th. Udem, T. W. Hänsch, M. Abgrall, J. Grunert, I. Maksimovic, S. Bize, H. Marion, F. Pereira Dos Santos, P. Lemonde, G. Santarelli, P. Laurent, A. Clairon, C. Salomon, M. Haas, U. D. Jentschura, and C. H. Keitel. New limits on the drift of fundamental constants from laboratory measurements. *Physical Review Letters*, 92(23):230802, 2004.
- [290] Tjeerd J. Pinkert. Characterisation of high brightness laser diodes at 970 nm for end pumped ultrafast lasers. Internship report, Max-Born-Institut, für Nichtlineare Optik und Kurzzeitspektroskopie, Februari 2007.
- [291] Yu. Ralchenko, A. Kramida, J. Reader, E.B. Saloman, J.E. Sansonetti, J.J. Curry, J.R. Fuhr, L. Podobedova, W.L. Wiese, and K. Olsen. NIST atomic spectra database version 4. Website: [http://physics.nist.gov/PhysRefData/ASD/lines\\_form.html](http://physics.nist.gov/PhysRefData/ASD/lines_form.html). retrieved: 16-07-2012 10:30.
- [292] J. S. Coursey, D. J. Schwab, and R. A. Dragoset. Atomic weights and isotopic compositions. Website: [http://physics.nist.gov/cgi-bin/Compositions/stand\\_alone.pl?ele=He](http://physics.nist.gov/cgi-bin/Compositions/stand_alone.pl?ele=He). retrieved: 16-07-2012 10:20.
- [293] P. A. Williams, W. C. Swann, and N. R. Newbury. High-stability transfer of an optical frequency over long fiber-optic links. *Journal of the Optical Society of America B*, 25(8):1284–1293, August 2008.
- [294] O. Lopez, A. Amy-Klein, C. Daussy, C. Chardonnet, F. Narbonneau, M. Lours, and G. Santarelli. 86-km optical link with a resolution of  $2 \times 10^{-18}$  for RF frequency transfer. *The European Physics Journal D*, 48:35–41, 2008.
- [295] K. Jaldehag, S.-C. Ebenhag, P. O. Hedekvist, and C. Rieck. Time and frequency transfer using asynchronous fiber-optical networks: progress report. In *Proceedings of the 41st Annual Precise Time and Time Interval (PTTI) Meeting*, pages 383–396, 2009.
- [296] G. Grosche, O. Terra, K. Predehl, R. Holzwarth, B. Lipphardt, F. Vogt, U. Sterr, and H. Schnatz. Optical frequency transfer via 146 km fiber link with  $10^{-19}$  relative accuracy. *Optics Letters*, 34(15):2270–2272, August 2009.
- [297] Miho Fujieda, Motohiro Kumagai, Shigeo Nagano, Atsushi Yamaguchi, Hidekazu Hachisu, and Ido Tetsuya. All-optical link for direct comparison of distant optical clocks. *Optics Express*, 19(17):16498–16507, August 2011.
- [298] K. Predehl, G. Grosche, S. M. F. Raupach, S. Droste, O. Terra, J. Alnis, Th. Legero, T. W. Hänsch, Th. Udem, R. Holzwarth, and H. Schnatz. A 920-kilometer optical fiber link for frequency metrology at the 19<sup>th</sup> decimal place. *Science*, 336:441–444, April 2012.
- [299] Olivier Lopez, Adil Haboucha, Bruno Chanteau, Christian Chardonnet, Anne Amy-Klein, and Giorgio Santarelli. Ultra-stable long distance optical frequency distribution using the internet fiber network. *Optics Express*, 20(21):23518–23526, October 2012.
- [300] B. J. Bloom, T. L. Nicholson, J. R. Williams, S. L. Campbell, M. Bishof, X. Zhang, W. Zhang, S. L. Bromley, and J. Ye. An optical lattice clock with accuracy and stability at the  $10^{-18}$  level. *Nature*, 506:71–75, Februari 2014.
- [301] Arthur Matveev, Christian G. Parthey, Katharina Predehl, Janis Alnis, Axel Beyer, Ronald Holzwarth, Thomas Udem, Tobias Wilken, Nikolai Kolachevsky, Michel Abgrall, Daniele

- Rovera, Christophe Salomon, Philippe Laurent, Gesine Grosche, Osama Terra, Thomas Legero, Harald Schnatz, Stefan Weyers, Brett Altschul, and Theodor W. Hänsch. Precision measurement of the hydrogen 1S–2S frequency via a 920-km fiber link. *Physical Review Letters*, 110:230801, June 2013.
- [302] D. W. Hanson. Fundamentals of two-way time transfer by satellite. In *Proceedings of the 43<sup>th</sup> Annual Symposium on Frequency Control*, pages 174–178, 1989.
- [303] Victor Zhang, Thomas E. Parker, Joseph Achkar, Andreas Bauch, Luca Lorini, Demetrios Matsakis, Dirk Piester, and Daniele G. Rovera. Two-way satellite time and frequency transfer using 1 Mchip/s codes. In *Proceedings of the 41<sup>st</sup> Annual Precise Time and Time Interval (PTTI) Meeting*, pages 371–382, 2009.
- [304] D. Piester, A. Bauch, L. Breakiron, D. Matsakis, B. Blanzano, and O. Koudelka. Time transfer with nanosecond accuracy for the realization of international atomic time. *Metrologia*, 45(1):185–198, 2008.
- [305] David. W. Allan and Marc A. Weiss. Accurate time and frequency transfer during common-view of a GPS satellite. In *Proceedings of the 34<sup>th</sup> Annual Frequency Control Symposium*, pages 334–346, 1980.
- [306] Victor S. Zhang, Thomas E. Parker, and Marc A. Weiss. Multi-channel GPS/GLONASS common-view between NIST and USNO. In *Proceedings of the 2000 IEEE/EIA International Frequency Control Symposium and Exhibition*, pages 598–606, 2000.
- [307] Michael. A. Lombardi, Lisa M. Nelson, Andrew N. Novick, and Victor S. Zhang. Time and frequency measurements using the global positioning system. *Cal Lab Magazine The International Journal of Metrology*, 8:26–33, 2001.
- [308] Kristine M. Larson and Judah Levine. Carrier-phase time transfer. *IEEE Transactions on Ultrasonics, Ferroelectrics and Frequency Control*, 46(4):1001–1012, July 1999.
- [309] Alison Brown, Randy Silva, and Ed Powers. A GPS receiver designed for carrier-phase time transfer. In *Proceedings of ION National Technical Meeting, January 2000, Anaheim, CA*, 2000.
- [310] S. Weyers, V. Gerginov, N. Nemitz, R. Li, and K. Gibble. Distributed cavity phase frequency shifts of the caesium fountain PTB-CSF2. *Metrologia*, 49(1):82–87, 2011.
- [311] Thomas P. Heavner, Elizabeth A. Donley, Filippo Levi, Giovanni Costanzo, Thomas E. Parker, Jon H. Shirley, Neil Ashby, Stephan Barlow, and S. R. Jefferts. First accuracy evaluation of NIST-F2. *Metrologia*, 51(1):174–182, 2014.
- [312] Long-Sheng Ma, Peter Jungner, Jun Ye, and John L. Hall. Delivering the same optical frequency at two places: accurate cancellation of phase noise introduced by an optical fiber or other time-varying path. *Optics Letters*, 19(21):1777–1779, November 1994.
- [313] Elimoel A. Elias, Rogerio Cichota, Hugo H. Torriani, and Quirijn de Jong van Lier. Analytical soil-temperature model: Correction for temporal variation of daily amplitude. *Soil Science Society of America Journal*, 68:784–788, May–June 2004.
- [314] K.-C. Lin, C.-J. Lin, and W.-Y. Lee. Effects of gamma radiation on optical fibre sensors. *IEE Proceedings Optoelectronics*, 151(1):12–15, Februari 2004.
- [315] Gorachland Ghosh and Hiroyoshi Yajima. Pressure-dependent sellmeier coefficients and material dispersions for silica fiber glass. *Journal of Lightwave Technology*, 16(11):2002–2005, November 1998.
- [316] P. C. T. van der Hoeven and W. N. Lablans. Grondtemperaturen. Technical report, KNMI, 1992. Wetenschappelijke Rapporten; WR-92-05.
- [317] Ragne Emardson, Per Olof Hedekvist, Mattias Nilsson, Sven-Christian Ebenhag, Kenneth Jaldehag, Per Jarlemark, Carsten Rieck, Jan Johansson, Leslie R. Pendrill, Peter Löthberg, and Håkan Nilsson. Time transfer by passive listening over a 10-Gb/s optical fiber. *IEEE Transactions on Instrumentation and Measurement*, 57(11):2495–2501, November 2008.
- [318] Made available by KNMI.
- [319] Koninklijk Nederlands Meteorologisch Instituut (KNMI). Cesar, Cabauw experimental site for atmospheric research. <http://www.cesar-observatory.nl/>.
- [320] Koninklijk Nederlands Meteorologisch Instituut (KNMI). KNMI DataCentrum. <https://data.knmi.nl/>.
- [321] Dr. J. P. W. Woudenberg. Vergelijkende metingen van de grondtemperatuur te De Bilt in

1961. Technical report, KNMI, 1966.
- [322] Daniel W. E. Noom, Stefan Witte, Jonas Morgenweg, Robert K. Altmann, and K. S. E. Eikema. High-energy, high-repetition-rate picosecond pulses from a quasi-CW diode-pumped Nd:YAG system. *Optics Letters*, 38(16):3021–3023, August 2013.
- [323] B ereng ere Argence, Bruno Chanteau, Olivier Lopez, Daniele Nicolodi, Michel Abgrall, Christian Chardonnet, Christophe Daussey, Beno t Darqui , Yann Le Coq, and Anne Amy-Klein. Quantum cascade laser frequency stabilisation at the sub-Hz level. *Arxiv*, page 1412.2207v1, 2014.
- [324] Bo Ning, Peng Du, Dong Hou, and Jianye Zhao. Phase-fluctuation compensation for long-term transfer of stable radio frequency over fibre link. *Optics Express*, 20(27):28447–28454, December 2012.
- [325] Michael J. Peng, Patrick T. Callahan, Amir H. Nejadmalayeri, Stefano Valente, Ming Xin, Lars Gr uner-Nielsen, Eric M. Monberg, Man Yan, John M. Fini, and Franz X. K artner. Long-term stable, sub-femtosecond timing distribution via a 1.2-km polarization-maintaining fiber link: approaching  $10^{-21}$  link stability. *Optics Express*, 21(17):19982–19989, August 2013.
- [326] J. Bagdonait , W. Ubachs, M. T. Murphy, and J. B. Whitmore. Analysis of molecular hydrogen absorption toward QSO B0642–5038 for a varying proton-to-electron mass ratio. *The Astrophysical Journal*, 786:10, 2014.
- [327] J. Bagdonait , W. Ubachs, M. T. Murphy, and J. B. Whitmore. Constraint on a varying proton-electron mass ratio 1.5 billion years after the big bang. *Physical Review Letters*, 114:071301, 2015.
- [328] E. J. Salumbides, Koelemeij J. C. J., J. Komasa, K. Pachucki, K. S. E. Eikema, and W. Ubachs. Bounds on fifth forces from precision measurements on molecules. *Physical Review D*, 87:112008, 2013.
- [329] E. J. Salumbides, W. Ubachs, and V. I. Korobov. Bounds on fifth forces at the sub-  length scale. *Journal of Molecular Spectroscopy*, 300:65–69, 2014.
- [330] Kazuyuki Yoshimura. Degrees of freedom of the estimate of the two-sample variance in the continuous sampling method. *IEEE Transactions on Instrumentation and Measurement*, 38(6):1044–1049, December 1989.
- [331] P. Lesage and C. Audoin. Characterization and measurement of time and frequency stability. *Radio Science*, 14(4):521–539, June 1979.
- [332] Kazuyuki Yoshimura. Characterization of frequency stability: Uncertainty due to the autocorrelation of the frequency fluctuations. *IEEE Transactions on Instrumentation and Measurement*, 27(1):1–7, March 1978.
- [333] D. B. Sullivan, D. W. Allan, D. A. Howe, and F. L. Walls. Characterization of clocks and oscillators. Technical report, NIST, 1990. NIST Technical Note 1337, Publicly downloadable PDF file includes numerous corrections to the articles.
- [334] David J. Griffiths. *Introduction to Electrodynamics*, chapter 7.3.3. In [371], 3rd edition, 1999.
- [335] David J. Griffiths. *Introduction to Electrodynamics*, chapter 7.3.5. In [371], 3rd edition, 1999.
- [336] David J. Griffiths. *Introduction to Electrodynamics*, chapter 9.2.2. In [371], 3rd edition, 1999.
- [337] Edward Frankland and J. Norman Lockyer. Preliminary note of researches on gaseous spectra in relation to the physical constitution of the sun. *Proceedings of the Royal Society of London*, 17:288–291, 1869.
- [338] Sir William Thomson. Inaugural address of Sir William Thomson. *Nature*, 4(92):262–270, August 1871.
- [339] William B. Jensen. Why helium ends in “-ium”. *Journal of Chemical Education*, 81(7):944, July 2004.
- [340] William Ramsay. On a gas showing the spectrum of helium, the reputed cause of  $D_3$ , one of the lines in the coronal spectrum. preliminary note. *Proceedings of the Royal Society of London*, 58:65–67, 1895.
- [341] William Ramsay. Helium, a gaseous constituent of certain minerals. part I. *Proceedings of the Royal Society of London*, 58:81–89, 1895.
- [342] William Ramsay. Helium, a gaseous constituent of certain minerals. part II – density.

- Proceedings of the Royal Society of London*, 59:325–330, 1895.
- [343] D. F. McFarland. Composition of gas from a well at Dexter, Kan. *Transactions of the Kansas Academy of Science*, 19:60–62, 1903.
- [344] James J. Bohning, , and Lois W. Sierra. *The discovery of helium in natural gas*. The American Chemical Society, 2000.
- [345] Dave (dangrdave). The Fort Worth helium plant. Website: <https://fortworthstockyard.wordpress.com/2011/05/20/the-fort-worth-helium-plant/>, May 2011. retrieved: 06-01-2015 18:12.
- [346] T. Lyman. The spectrum of helium in the extreme ultra-violet. *The Astrophysical Journal*, 60(1):1–14, jul 1924.
- [347] J. Franck and P. Knipping. Über die Anregungsspannungen des Heliums. *Zeitschrift für Physik*, 1(4):320–332, 1920.
- [348] Landolt-Börnstein. *Tabellen*. 5th edition, 1923. Bd. II, S. 825.
- [349] Georg W. Kellner. Die Ionisierungsspannung des Heliums nach der Schrödingerschen Theorie. *Zeitschrift für Physik*, 44(1–2):91–109, 1927.
- [350] J. J. Hopfield. New ultra-violet spectrum of helium. *The Astrophysical Journal*, 72(3):133–145, oct 1930.
- [351] G. Herzberg. Ionization potentials and Lamb shifts of the ground states of  $^4\text{He}$  and  $^3\text{He}$ . *Proceedings of the Royal Society of London. Series A, Mathematical and Physical Sciences*, 248(1254):309, 1958.
- [352] William C. Martin. Energy levels and spectrum of neutral helium ( $^4\text{He}$  I). *Journal of Research of the National Bureau of Standards - A. Physics and Chemistry*, 64(1):19–28, 1960.
- [353] M. A. Baig, J. P. Connerade, C. Mayhew, G. Noeldeke, and M. J. Seaton. On the principle series of helium. *Journal of Physics B*, 17:L383–L387, 1984.
- [354] K. S. E. Eikema, W. Ubachs, W. Vassen, and W. Hogervorst. First laser excitation of the  $^4\text{He}$   $1^1\text{S} - 2^1\text{P}$  resonance line at 58 nm. *Physical Review Letters*, 71(11):1690–1692, sep 1993.
- [355] K. S. E. Eikema, W. Ubachs, W. Vassen, and W. Hogervorst. Precision measurements in helium at 58 nm: Ground state Lamb shift and the  $1^1\text{S} - 2^1\text{P}$  transition isotope shift. *Physical Review Letters*, 76(8):1216–1219, February 1996.
- [356] J. Franck. Bemerkungen über Anregungs- und Ionisierungsspannung des Heliums. *Zeitschrift für Physik*, 11(1):155–160, 1922.
- [357] Fabian M. Kannenstine. Formation and life of metastable helium. *The Astrophysical Journal*, 55:345–354, 1922.
- [358] Craig J. Sansonetti, J. D. Gillaspay, and C. L. Cromer. Precise experimental test of calculated two-electron Lamb shifts in helium. *Physical Review Letters*, 65(20):2539–2542, November 1990.
- [359] G. W. F. Drake. High precision variational calculations for the  $1s^2\ ^1\text{S}$  state of  $\text{H}^-$  and the  $1s^2\ ^1\text{S}$ ,  $1s2s\ ^1\text{S}$  and  $1s2s\ ^3\text{S}$  states of helium. *Nuclear Instruments and Methods in Physics Research*, B31:7–13, 1988.
- [360] G. W. F. Drake and A. J. Makowski. High-precision eigenvalues for the  $1s2p\ ^1\text{P}$  and  $^3\text{P}$  states of helium. *Journal of the Optical Society of America B*, 5(10):2207–2214, October 1988.
- [361] J. D. Baker, R. C. Forrey, J. D. Morgan III, R. N. Hill, M. Jeziorska, and J. Schertzer. Theoretical estimates of the  $1^1\text{S}$  and  $2^1\text{S}$  Lamb shifts in helium. *Bulletin of the American Physical Society*, 38(3):1127, May 1993.
- [362] G. W. F. Drake. *Long-Range Casimir Forces: Theory and Recent Experiments on Atomic Systems*, chapter High Precision Calculations for the Rydberg States of Helium, pages 107–217. Plenum Press, New York, 1993.
- [363] G. W. F. Drake, I. B. Khriplovich, A. I. Milstein, and A. S. Yelkhovskiy. Energy corrections of order  $mc^2\alpha^6\ln\alpha$  in helium. *Physical Review A*, 48(1):R15–R17, jul 1993.
- [364] J. C. Slater. The structure of the helium atom. I. *Proceedings of the National Academy of Sciences of the United States of America*, 13:423–430, 1927.
- [365] P. K. Kabir and E. E. Salpeter. Radiative corrections to the ground-state energy of the helium atom. *Physical Review*, 108(5):1256–1263, 1957.
- [366] J. Sucher. Energy levels of the 2-electron atom to order  $\alpha^3$  ry - ionization energy of helium.

- Physical Review*, 109(3):1010–1011, 1958.
- [367] G. W. F. Drake. High precision theory of atomic helium. *Physica Scripta*, T83:83–92, 1999.
- [368] Vladimir Korobov and Alexander Yelkhovsky. Ionization potential of the helium atom. *Physical Review Letters*, 87(19):193003, November 2001.
- [369] G. W. F. Drake and S. P. Goldman. Bethe logarithms for Ps, H, and heliumlike atoms. *Canadian Journal of Physics*, 77(11):835–845, Februari 2000.
- [370] R. W. Boyd. *Nonlinear optics*. Academic Press, 2nd edition, 2003.
- [371] David J. Griffiths. *Introduction to Electrodynamics*. Pearson Education, 3rd edition, 1999.

# List of publications

The following publications are included in this thesis as (parts of) chapters.

D. Z. Kandula, C. Gohle, T. J. Pinkert, W. Ubachs, and K. S. E. Eikema. *Extreme ultraviolet frequency comb metrology*. Physical Review Letters, 105(6):063001, August 2010. (Chapter 6)

T. J. Pinkert, D. Z. Kandula, C. Gohle, I. Barmes, J. Morgenweg, and K. S. E. Eikema. *Widely tunable extreme UV frequency comb generation*. Optics Letters, 36(11):2026–2028, June 2011. (Chapter 5)

T. J. Pinkert, E. J. Salumbides, M. S. Tahvili, W. Ubachs, E. A. J. M. Bente, and K. S. E. Eikema. *Frequency comb generation by CW laser injection into a quantum-dot mode-locked laser*. Optics Express, 20(19):21357–21371, September 2012. (Chapter 4)

T. J. Pinkert, O. Böll, L. Willmann, G. S. M. Jansen, E. A. Dijck, B. G. H. M. Groeneveld, R. Smets, F. C. Bosveld, W. Ubachs, K. Jungmann, K. S. E. Eikema, and J. C. J. Koelemeij. *Effect of soil temperature on optical frequency transfer through unidirectional dense-wavelength-division-multiplexing fiber-optic links*. Applied Optics, 54(4):728–738, Februari 2015. (Chapter 7)

Other publications to which the author contributed.

D. Z. Kandula, C. Gohle, T. J. Pinkert, W. Ubachs, and K. S. E. Eikema. *XUV frequency-comb metrology on the ground state of helium*. Physical Review A, 84(6):062512, December 2011.



# Summary

The basis of this thesis are frequency comb lasers, either as an essential part of the experiments or as the experiment themselves. Frequency comb lasers allow a tight link between optical and rf frequencies. In this way, optical frequencies can be measured with the accuracy of the best available clocks. This has enabled a variety of applications, including precision spectroscopy of atoms and molecules for tests of fundamental physics or other purposes, optical atomic clocks, and physics on attosecond time scales. Frequency comb lasers in our lab allow absolute optical frequency measurements with a relative uncertainty of about  $10^{-12}$ , determined by the precision of the main frequency standard in the lab, a GPS referenced rubidium atomic clock.

The first three introductory chapters of this thesis describe the theory needed to understand the later parts of this thesis. This includes theory about frequency stability measurements, the principles of optical frequency combs, high-order harmonic generation and atomic spectroscopy. It also treats the development and testing of short-term narrow linewidth diode lasers, optical fibre amplifiers, optical fibre coupled beat units and direct digital synthesizer units.

In Ch. 4 is described how hybridly mode-locked quantum dot semiconductor lasers, produced at the TUE, were injected with CW laser light. The injected light is modulated in the microwave-driven saturable absorption section of the quantum dot laser, thereby forming a frequency comb that is amplified in the laser medium. In this manner a miniature frequency comb generator was realised. A characterisation of these devices reveals that the quantum dot laser material is suitable for accurate, narrow linewidth (100 kHz) frequency comb generation.

Chapter 5 forms an introduction to the work in Ch. 6, which describes high resolution spectroscopy in the XUV performed on transitions from the ground state of helium. Spectroscopy on helium is of interest because it offers a test of quantum electrodynamic (QED) theory. After hydrogen, helium is the next more complex atom where QED can be tested, including electron-electron effects. Theoretically bound state QED effects are usually formulated as a power series of  $\alpha$ , the fine structure constant, and  $Z$ , the nuclear charge. Because convergence of this power series is not proven, experimental verification of the calculations is vital for further developments of theoretical approaches to many-body QED calculations. The high resolution spectroscopy on helium was performed with an amplified frequency comb laser, using the Ramsey excitation scheme. We have determined the ground state energy of helium, which is most influenced by QED effects, to be  $h \times 5\,945\,204\,212(6)$  MHz. The experimental determination of this energy is now six times more precise than the value provided by theory, which calls for a better theoretical calculation.

Finally, the components described in Ch. 3 are used in Ch. 7 to perform experiments on the frequency transfer stability of a  $2 \times 298$  km optical fibre link between Amsterdam and Groningen. Relative frequency deviations added by the link to a continuous wave laser frequency, mainly due to temperature fluctuations of the optical fibre, are at the level of  $10^{-13}$ . This enables a direct comparison of the two rubidium standards at the VU LaserLaB and the Van Swinderen Institute. An attempt was made to improve the frequency transfer by means of a simple soil temperature model together with the temperature measurements of KNMI at the Cabauw site. Although no improvement was seen, the model can be used to predict the order of magnitude of the maximum expected frequency deviations on optical fibre links without active length stabilisation.

# Samenvatting

Het fundament van dit proefschrift wordt gevormd door frequentiekam-lasers, dan wel als essentieel onderdeel van de experimenten, dan wel als onderwerp van het experiment zelf. Frequentiekam-lasers maken een precieze verbinding tussen optische en rf frequenties mogelijk. Op die manier kunnen optische frequenties met de nauwkeurigheid van de beste atoomklokken worden gemeten. Dit heeft een spectra aan toepassingen mogelijk gemaakt, waaronder precisie spectroscopie aan atomen en moleculen voor het testen van fundamentele natuurkunde of andere doeleinden, optische atoomklokken, en natuurkunde op de tijdschaal van een attoseconde. Frequentiekam-lasers in ons laboratorium maken het meten van absolute optische frequenties mogelijk met een relatieve nauwkeurigheid van  $10^{-12}$ , bepaald door de precisie van de belangrijkste frequentiestandaard in het laboratorium, een aan het GPS gerefereerde rubidium atoomklok.

De eerste drie introductiehoofdstukken van dit proefschrift beschrijven de noodzakelijke theorie om de latere hoofdstukken te kunnen begrijpen. Hierbij inbegrepen zijn theorie over metingen aan frequentiestabiliteit, de principes van optische frequentiekammen, hogere orde harmonische generatie en atoomspectroscopie. Ook behandelen zij het ontwikkelen en testen van op korte tijdschalen smalbandige diodelasers, optische glasvezelversterkers, glasvezelgekoppelde optische heterodyne meningenheden en direct digitale synthese eenheden.

In Hoofdstuk 4 wordt beschreven hoe hybride modengekoppelde kwantum-punthalfgeleiderlasers, geproduceerd aan de TUE, met continu laserlicht werden geïnjecteerd. Het geïnjecteerde licht wordt door de microgolfgedreven verzadigbare absorptiesectie van de kwantumpunt laser gemoduleerd, hetgeen de vorming van een frequentiekam ten gevolge heeft die wordt versterkt in het lasermedium. Op deze manier werd een miniatuur frequentiekamgenerator gerealiseerd. Een karakterisatie van deze apparaten laat zien dat het kwantumpunt medium geschikt is voor het genereren van nauwkeurige, smalbandige (100 kHz) frequentiekamgeneratie.

Hoofdstuk 5 vormt een inleiding op het werk van Hoofdstuk 6, alwaar hoge resolutie spectroscopie in het XUV op overgangen vanuit de grondtoestand in helium wordt beschreven. Spectroscopie aan helium is van belang omdat het een test van de Kwantum Elektrodynamische (KED) theorie mogelijk maakt. Na waterstof is helium het volgende iets complexere atoom waar KED kan worden getest, inclusief de elektron-elektron effecten. In de theorie worden gebonden KED effecten normaliter geformuleerd als een machtreeks van  $\alpha$ , de fijnstructuurconstante, en  $Z$ , de kernlading. Omdat de convergentie van deze machtreeks niet is bewezen, is experimentele verificatie van de berekeningen vitaal voor het verder ontwikkelen van theoretische methoden voor

meerdeeltjes KED berekeningen. De hoge-resolutie spectroscopie aan helium is uitgevoerd met behulp van een versterkte frequentiekamleraser, waarbij de Ramsey excitatiemethode werd gebruikt. We hebben de grondtoestandsenergie van helium, die het meest beïnvloed wordt door KED effecten, bepaald op  $h \times 5\,945\,204\,212(6)$  MHz. De experimentele bepaling is nu zes maal nauwkeuriger dan de theoretische waarde, hetgeen vraagt om een betere theoretische berekening.

Als laatste worden de onderdelen die zijn beschreven in Hoofdstuk 3, gebruikt in Hoofdstuk 7 om de frequentieoverdrachtsstabiliteit van een  $2 \times 298$  km optische glasvezelverbinding tussen Amsterdam en Groningen te onderzoeken. De door de verbinding toegevoegde relatieve frequentieafwijkingen aan een continuegolf laserfrequentie, met name door temperatuursveranderingen van de glasvezel, zijn in de orde van grootte van  $10^{-13}$ . Dit maakt een directe vergelijking van de twee rubidium standaarden in het VU LaserLaB en het Van Swinderen Instituut mogelijk. Er werd een poging ondernomen om de frequentieoverdracht te verbeteren door de toepassing van een eenvoudig grondtemperatuurmodel samen met de grondtemperatuurmetingen van het KNMI op de Cabauw locatie. Ondanks dat geen verbetering werd gezien kan het model gebruikt worden om de grootteorde van de maximaal te verwachten frequentieafwijkingen op optische glasvezelverbindingen zonder actieve lengtecompensatie te voorspellen.





# Dankwoord

Bovenal dank ik mijn Heer, Jezus Christus, door wie ik, gered van zonde en dood, leef.

Liefste Esther, je hebt veel avonden alleen doorgebracht als ik weer eens te hard aan het werk was. Dat heb je me nooit kwalijk genomen. Dank je wel voor jouw liefde, steun en hulp, waardoor dit proefschrift er nu ligt. Ik hoop jou in de toekomst meer te kunnen helpen en er meer voor je te zijn.

Pap en Mam, het heeft een tijdje geduurd, maar nu is het zover. Dank jullie voor al jullie liefde en hulp. Onder andere met al die spulletjes die heen en weer gesleept moesten worden tussen kamer en kamer en flat.

Kjeld, dank je voor de mogelijkheid mijn onderzoek te doen in jouw onderzoeksgroep. Blijkbaar had je genoeg vertrouwen in zo'n Twentse elektrotechnisch ingenieur uit het Avereesterland om je lasers en atomen aan mij toe te vertrouwen. Ik hoop dat ik dat vertrouwen niet al te veel geschaad heb. Mijn laser en natuurkunde kennis is in elk geval erg toegenomen. Ik kijk met veel plezier terug op een mooie tijd met leuke (maar soms frustrerende) experimenten in een zeer luxueus uitgerust lab met zeer waarschijnlijk (hier wat academische voorzichtigheid) de hoogste concentratie aan frequentiekamlers in Nederland.

Wim (U), bij jou kon ik af en toe binnenlopen voor een goed advies en een opinie over mijn ideeën.

Dominik und Christoph, ihr habt mich warm empfangen im Labor. Von euch hab ich viel gelernt, unter anderem das Arbeiten mit einem großartigen Lasersystem. Ich schätze es sehr mit euch zusammengearbeitet zu haben und würde das gerne noch einmal machen, vielleicht kann ich euch jetzt auch etwas beibringen.

Anna Lisa, de wat stille collega bij die andere ( $\text{Ca}^+$ ) opstelling, ook jouw aanwezigheid droeg altijd bij aan de goede sfeer in het lab.

Jonas, Itan jullie kwamen halverwege mijn promotietijd in het lab. Ik hoop de XUV laser goed genoeg te hebben overgedragen, alhoewel er al gauw van alles aan verbeterd werd. Dank voor jullie hulp bij het meten aan helium, neon en argon; alleen was het niet gelukt.

Jonas, Itan, ihr seid während meiner Doctorandenzeit ins Labor gekommen. Ich hoffe euch das XUV-Lasersystem gut genug übertragen zu haben, obwohl schon schnell eine Menge Verbesserungen durchgeführt wurde. Danke für eure Hilfe beim Vermessen von Helium, Neon und Argon; alleine wäre es mir nicht gelungen.

Edcel and Saeed, we have tried to tame some stubborn lasers. Together with your efforts this work has even delivered an article. Sylwester, thank you sincerely for your constructive comments on the article.

Axel, danke für das Übertragen von deinen Kenntnisse über Glasfasern. Sie haben dem Labor keine Windeier gelegt, und ich habe deine Kenntnisse inzwischen auch an andere Leute in unsere Abteilung weitergeben können.

Matthijs, jij kwam, zag, en overwon de glasvezels in je bachelorproject. Samen met de inspanningen van Olivier en Lorenz (Kernfysisch Versneller Instituut, Groningen) kon daardoor de verbinding naar Groningen tot stand komen. Met jullie allen was het prettig samenwerken.

Jeroen, de “Atomen, Moleculen en Lasers” spin in het glasvezelweb van Nederland, zonder jou geen  $2 \times 298$  km glas tussen Groningen en Amsterdam. Ook wil ik je bedanken voor de vele discussies die we hadden over de juiste interpretatie van alle gegevens.

Fred, jij was meteen bereid de grondtemperaturen gemeten bij het KNMI te delen, waarvoor mijn hartelijke dank.

Sjaak, Rob, jullie hebben beide op een heel eigen manier geholpen de experimenten tot een succes te maken. Zonder jullie inzet was het niet mogelijk geweest. Sjaak, die kast staat er nog steeds hoor!

Ziyu, ik hoop dat mijn ideeën over trouwen nog steeds correct zijn, dank je wel voor de fijne gesprekken tijdens de lunch en na werktijd. (You should be able to read this in Dutch by now.)

Overige groepsleden, ook jullie hartelijk dank voor gesprekken en discussies aan de koffietafel en tijdens borrels, voor vragen (over L...) en meedenken met de experimenten. Het is fijn om je thuis te voelen in je vakgroep.